Applied Computational Electromagnetics Society

Journal

Special Issue on ACES 2011 Conference

Guest Editors: C. J. Reddy and Erik Vedeler

December 2011

Vol. 26 No. 12

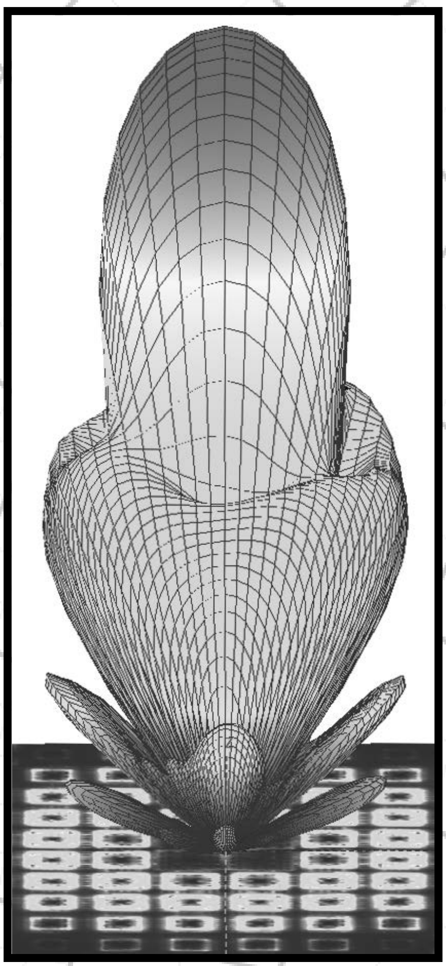

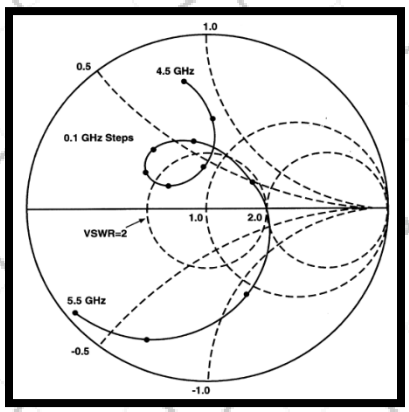

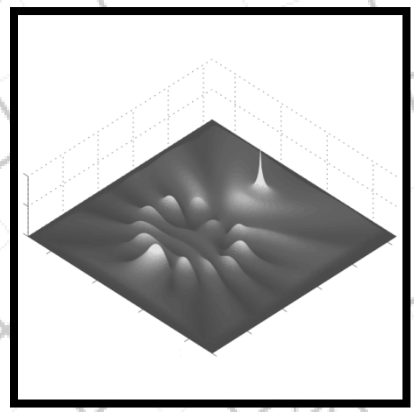

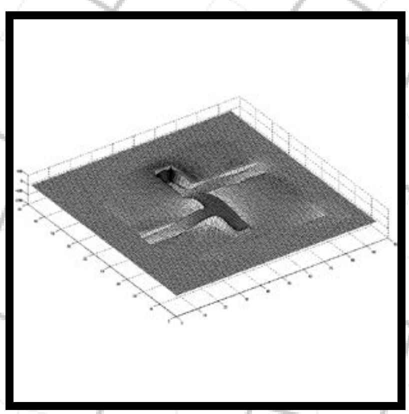

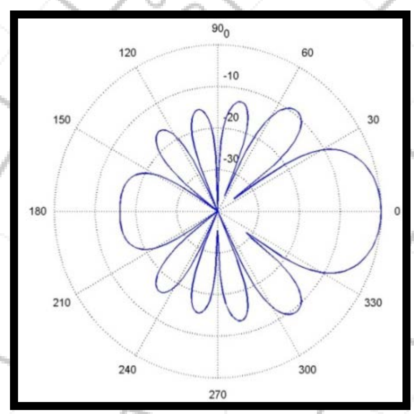

ISSN 1054-4887

GENERAL PURPOSE AND SCOPE: The Applied Computational Electromagnetics Society ***(ACES)*** Journal hereinafter known as the ***ACES Journal*** is devoted to the exchange of information in computational electromagnetics, to the advancement of the state-of-the art, and the promotion of related technical activities. The primary objective of the information exchange is to inform the scientific community on the developments of new computational electromagnetics tools and their use in electrical engineering, physics, or related areas. The technical activities promoted by this publication include code validation, performance analysis, and input/output standardization; code or technique optimization and error minimization; innovations in solution technique or in data input/output; identification of new applications for electromagnetics modeling codes and techniques; integration of computational electromagnetics techniques with new computer architectures; and correlation of computational parameters with physical mechanisms.

SUBMISSIONS: The ***ACES Journal*** welcomes original, previously unpublished papers, relating to applied computational electromagnetics. Typical papers will represent the computational electromagnetics aspects of research in electrical engineering, physics, or related disciplines. However, papers which represent research in applied computational electromagnetics itself are equally acceptable.

Manuscripts are to be submitted through the upload system of ***ACES*** web site http://aces.ee.olemiss.edu See "Information for Authors" on inside of back cover and at ***ACES*** web site. For additional information contact the Editor-in-Chief:

Dr. Atef Elsherbeni
Department of Electrical Engineering
The University of Mississippi
University, MS 386377 USA
Phone: 662-915-5382
Email: atef@olemiss.edu

SUBSCRIPTIONS: All members of the Applied Computational Electromagnetics Society are entitled to access and download the ***ACES Journal*** any published journal article available at http://aces.ee.olemiss.edu. Printed issues of the ***ACES Journal*** are delivered to institutional members. Each author of published papers receives a printed issue of the ***ACES Journal*** in which the paper is published.

Back issues, when available, are $50 each. Subscription to ***ACES*** is through the web site. Orders for back issues of the ***ACES Journal*** and change of address requests should be sent directly to ***ACES*** office at:

Department of Electrical Engineering
The University of Mississippi
University, MS 386377 USA
Phone: 662-915-7231
Email: aglisson@olemiss.edu

Allow four weeks advance notice for change of address. Claims for missing issues will not be honored because of insufficient notice, or address change, or loss in the mail unless the ***ACES*** office is notified within 60 days for USA and Canadian subscribers, or 90 days for subscribers in other countries, from the last day of the month of publication. For information regarding reprints of individual papers or other materials, see "Information for Authors".

LIABILITY. Neither ***ACES***, nor the ***ACES Journal*** editors, are responsible for any consequence of misinformation or claims, express or implied, in any published material in an ***ACES Journal*** issue. This also applies to advertising, for which only camera-ready copies are accepted. Authors are responsible for information contained in their papers. If any material submitted for publication includes material which has already been published elsewhere, it is the author's responsibility to obtain written permission to reproduce such material.

APPLIED COMPUTATIONAL ELECTROMAGNETICS SOCIETY JOURNAL

Special Issue on ACES 2011 Conference

Guest Editors
C. J. Reddy and Erik Vedeler

December 2011
Vol. 26 No. 12
ISSN 1054-4887

The ACES Journal is abstracted in INSPEC, in Engineering Index, DTIC, Science Citation Index Expanded, the Research Alert, and to Current Contents/Engineering, Computing & Technology.

The illustrations on the front cover have been obtained from the research groups at the Department of Electrical Engineering, The University of Mississippi.

DECEMBER 2011 REVIEWERS

Ahmed Abdelrahman
Shirook Ali
Mohamed Bakr
Sami Barmada
Adalbert Beyer
Indira Chatterjee
Michael Chryssomallis
Jorge Costa
Randy Haupt
Fernando Las-Heras
Zhuo Li
Ivor Morrow
Marco Mussetta
Andrew Peterson
C. J. Reddy
Harvey Schuman
Rui Wang
Fan Yang
Kezhong Zhao

THE APPLIED COMPUTATIONAL ELECTROMAGNETICS SOCIETY

JOURNAL

Vol. 26 No. 12 December 2011

TABLE OF CONTENTS

Performance of Single and Double T-matched Short Dipole Tag Antennas for UHF RFID Systems

Toni Björninen [1], Atef Z. Elsherbeni [2], and Leena Ukkonen [1]

[1] Department of Electronics, Rauma Research Unit
Tampere University of Technology, Rauma, FI-26100, Finland
toni.bjorninen@tut.fi, leena.ukkonen@tut.fi

[2] Department of Electrical Engineering
University of Mississippi, University, MS 38677-1848, USA
atef@olemiss.edu

Abstract **─** The impact of tag antenna and chip impedance tolerances on power transfer between these components is investigated analytically. Means for efficient computation of the minimum and maximum power transmission coefficient under given impedance tolerances are developed. The presented sensitivity analysis is employed to quantify the design uncertainty of single and double T-matched short dipole tag antennas for UHF RFID systems. The simulated and measured performance of the two tag antennas is analyzed and compared.

IndexTerms **─** Double T-matching, impedance matching, passive UHF RFID, tag antenna, T-matching.

I. INTRODUCTION

In radio-frequency identification (RFID) systems, electromagnetic interaction between a reader and electronic labels, designated as RFID tags, is employed to identify objects. In ultra high frequency (UHF) RFID systems, the mechanism of the interaction is most commonly wave propagation and the RFID tags are antennas loaded with a microchip. Passive RFID tags, which are studied in this article, scavenge energy for their operation from the incident electromagnetic field sent by the reader. In addition to capturing energy with on-chip rectification, the chip stores a unique electronic product code to label the tagged object, demodulates commands from the reader and creates a response to the reader's queries. Tag's response is created by switching the chip impedance between two values while the reader illuminates the tag with a single-frequency electromagnetic field. As a result, the tag's response is modulated in the load-dependent component of the electromagnetic field scattered from the tag antenna [1].

As the passive RFID tags are not equipped with an energy source, maximizing the power delivery from the tag antenna to the chip is often the principal goal in tag design. However, the boundary conditions for the design are stringent. For a globally operable UHF RFID tag, good antenna performance is required over a broad, 10% fractional bandwidth (from 860 MHz to 960 MHz), while compact and low-profile antenna structures are preferred for seamless integration with objects. Thus, small antenna features are a crucial tag antenna design aspect. Furthermore, the unit cost of the tag antenna needs to be minimal when labelling a large asset base with RFID tags. To achieve cost-savings in the antenna manufacturing, most commonly the complex conjugate impedance matching between the tag antenna and the chip is arranged by designing the tag antenna geometry so that appropriate antenna impedance is achieved together with the desired radiation characteristics. In this process computational electromagnetics is extensively employed.

Dipole-type tag antennas are popular in UHF RFID systems. They benefit from being structurally simple radiators with omnidirectional radiation pattern, which allows the detection of

Submitted On: April 27, 2011
Accepted On: June 26, 2011

1054-4887

dipole tags from all directions in a plane normal to the tag. Moreover, clever size reduction and impedance matching techniques for them have also been extensively investigated in general context [2-5] as well as for RFID applications [6-8]. This article focuses on RFID tag antenna design verification based on impedance tolerances and on the performance comparison of single and double T-matched short dipole tags.

The rest of the article is organized as follows. Section II introduces the concept of power transmission coefficient and discusses the efficient computation of its limits under given source and load impedance variations. In Section III, the simulation based design of single and a double T-matched short dipole tag antennas is discussed and the prototype antennas as well as simulation results are presented. Section IV focuses on experimental verification of the simulation-based designs and presents the comparison of the simulation and measurement results. Finally, conclusions are drawn in Section V.

II. IMPACT OF IMPEDANCE TOLERANCES ON POWER TRANSFER

Power transfer from the tag antenna to the chip can be analyzed by considering two complex impedances connected with a transmission line with negligible electrical length. In this case, the ratio of the power available from the tag antenna (P_{tag}) and the power reflected back (P_{rfl}) from the antenna-chip interface due to impedance mismatch is given by [10]

$$\frac{P_{rfl}}{P_{tag}} = \left|\frac{Z_{ic} - Z_a^*}{Z_{ic} + Z_a}\right|^2, \tag{1}$$

where Z_a=R_a+jX_a and Z_{ic}=R_{ic}+jX_{ic} are the antenna and chip impedances, respectively and $(\cdot)^*$ denotes complex conjugation. As the delivered power to the chip is the difference P_{ic}=P_{tag}–P_{rfl}, using (1), the power transmission coefficient (τ) between the tag antenna and chip is expressed as

$$\tau = \frac{P_{ic}}{P_{tag}} = 1 - \frac{P_{rfl}}{P_{tag}} = \frac{4R_a R_{ic}}{\left|Z_a + Z_{ic}\right|^2}. \tag{2}$$

In practice, neither the tag antenna nor the chip impedance is known exactly and due to the nonlinearity of (2) it is difficult to predict the magnitude of the impact of impedance variations on the power transfers without a more rigorous analysis. Thus, it is of practical interest to evaluate the maximum deviation of τ from its nominal value while assuming the tag antenna and the chip impedances lie in the neighborhood of their nominal values Z_{a0}=R_{a0}+jX_{a0} and Z_{ic0}=R_{ic0}+jX_{ic0}, respectively. For the purposes of the presented analysis, these neighbourhoods are defined below as rectangles in the chip and antenna impedance planes.

Let $0<p,r<\infty$, $0<q,s<\infty$, and $0<\varepsilon<\min(p,r)$ and consider sets defined as

$$D_\varepsilon = \left\{ (x,y) \in R^2 : x \geq \varepsilon,\ y \in R \right\},$$

$$\begin{aligned}\Lambda_{pq} = \{(x,y) \in R^2 : &\left|R_{ic0} - x\right| \leq pR_{ic0}, \\ &\left|X_{ic0} - y\right| \leq q\left|X_{ic0}\right|\} \cap D_\varepsilon,\end{aligned} \tag{3}$$

$$\begin{aligned}\Lambda_{rs} = \{(x,y) \in R^2 : &\left|R_{a0} - x\right| \leq rR_{a0}, \\ &\left|X_{a0} - y\right| \leq s\left|X_{a0}\right|\} \cap D_\varepsilon.\end{aligned}$$

Under these definitions, Λ_{pq} and Λ_{rs} are rectangles centered at the nominal chip and tag antenna impedances, respectively, and restricted in the half-plane containing the positive resistances. The size of these rectangles is determined by the parameter pairs (p,q) and (r,s) with r and p defining the percentage tolerance in R_a and R_{ic}, respectively, and the parameters s and q defining the percentage tolerance in X_a and X_{ic}, respectively. In the special case $0<p,r<1$, the set D_ε along with the positive and arbitrarily small number ε could be dropped from the definition (3), as in this case the imaginary axis, where (2) is not necessarily well-defined, is always excluded from the sets Λ_{pq} and Λ_{rs}. However, as discussed in Section III, large values of p and r may be needed in evaluation of platform-tolerance of RFID tags based on the analysis presented in the Section II A. Therefore, p and q are not considered upper bounded, but rather the set D_ε is used to keep (2) well-defined in Λ_{pq}, Λ_{rs}. Moreover, these sets are nonempty and closed by definition. These properties are also required in the presented analysis.

A. Minimum τ under given impedance tolerances

Treating τ first as a function of the chip impedance only, while considering the antenna impedance fixed and calculating the directional derivative of τ along a vector u point from the perfect conjugate match impedance point $(R_{a0},-X_{a0})$ to an arbitrary point $(R_{ic}, X_{ic})\in D$, one finds

$$D_u\tau = -\frac{4R_{a0}(R_{a0}+R_{ic})\left((R_{a0}-R_{ic})^2+(X_{a0}+X_{ic})^2\right)}{\left((R_{a0}+R_{ic})^2+(X_{a0}+X_{ic})^2\right)^2} < 0,\ \forall (R_{ic},X_{ic})\in D\setminus\{(R_{a0},-X_{a0})\}. \quad (4)$$

This shows that τ is a strictly decreasing function of the chip impedance in D towards directions away from the perfect conjugate match impedance point $(R_{a0},-X_{a0})$, where it attains its maximum value τ=1. Equation (4) also implies the uniqueness of this maximum within D.

Starting from (2), it is shown that the chip impedances corresponding to a constant τ define a circle with center point $P(\tau)$ and radius $r(\tau)$ given by

$$P(\tau)=\left(R_{a0}\frac{2-\tau}{\tau},-X_{a0}\right)$$
$$\text{and}\quad r(\tau)=2R_{a0}\frac{\sqrt{1-\tau}}{\tau}. \quad (5)$$

This circle always encloses the perfect conjugate match impedance point $(R_{a0},-X_{a0})$, where τ is maximized. Since a rectangle can always be enclosed in a circle touching one of its corners, particularly the rectangle Λ_{pq} defined in equation (3) can always be enclosed in a constant τ circle touching one of its corners.

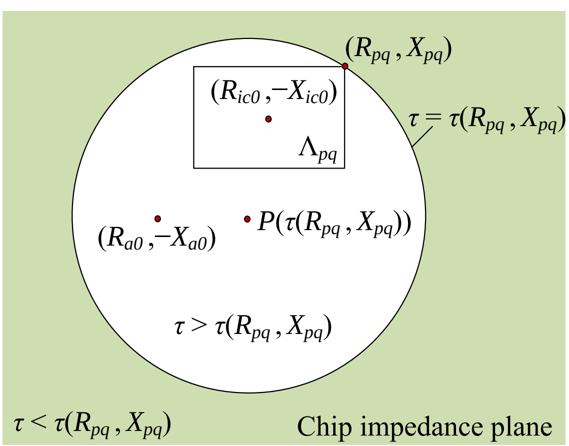

Fig. 1. A constant power transmission coefficient circle enclosing the uncertainty rectangle Λ_{pq} in the chip impedance plane.

To elaborate on the implications of this geometric observation, let (R_{pq},X_{pq}) be the corner discussed above. As the perfect conjugate match impedance point $(R_{a0},-X_{a0})$ is always contained in the circle (5), equation (4) then guarantees that at any point in Λ_{pq}, except for (R_{pq},X_{pq}), it holds $\tau>\tau(R_{pq},X_{pq})$. This means that the minimum value of τ in Λ_{pq} is always attained at a corner of the rectangle Λ_{pq}. This is illustrated in Fig. 1.

As seen from equation (2), the expression of τ is symmetric with respect to pairs (R_a,X_a) and (R_{ic},X_{ic}). Therefore, all the above conclusions of τ as a function of the chip impedance are valid also when τ is treated as a function of the tag antenna impedance, while considering the chip impedance fixed. Consequently, for all $(R_{ic},X_{ic};R_a,X_a)\in\Lambda_{pqrs}=\Lambda_{pq}\times\Lambda_{rs}$, one obtains

$$\begin{aligned}\tau(R_{ic},X_{ic};R_a,X_a) &\ge \tau(R_{pq},X_{pq};R_a,X_a)\\ &\ge \tau(R_{pq},X_{pq};R_{rs},X_{rs}),\\ &=\tau_{min},\end{aligned} \quad (6)$$

where (R_{pq},X_{pq}) is a corner of Λ_{pq} and (R_{rs},X_{rs}) is a corner of Λ_{rs}. Obviously, as the lower bound for τ obtained in (6) is actually the function itself evaluated at a point in Λ_{pqrs}, τ_{min} is necessarily a minimum of τ within this set.

In practice, this value is calculated as the minimum of τ evaluated at the 16 corners of the 4-dimensional rectangle Λ_{pqrs}. Equation for τ_{min} is given in (7), where the minimum is considered for all the possible sign combinations. Compared with a direct numerical search through a 4-dimensional search grid, much less computations – only 16 evaluations of τ – are needed to find τ_{min} with this approach. This allows tag antenna designers to perform rapid worst-case tag performance estimation for a large number of frequency points in practical times.

B. Maximum τ under given impedance tolerances

Treating τ first as a function of the chip impedance only, while considering the antenna impedance fixed, one immediately discovers that the maximum value of τ in Λ_{pq} is one, if the

$$\tau_{min} = \min_{+/-}\frac{4\chi_\varepsilon(1\pm r)\chi_\varepsilon(1\pm p)R_{a0}R_{ic0}}{\left(\chi_\varepsilon(1\pm r)R_{a0}+\chi_\varepsilon(1\pm p)R_{ic0}\right)^2+\left(X_{a0}\pm s|X_{a0}|+X_{ic0}\pm q|X_{ic0}|\right)^2},\quad \chi_\varepsilon(x)=\begin{cases}\varepsilon, & x\le 0\\ x, & x>0\end{cases} \quad (7)$$

perfect conjugate match impedance point $(R_{a0},-X_{a0})$ is contained in Λ_{pq}. Otherwise, $(R_{ic},X_{ic}) \in \Lambda_{pq}$ and $(R_{a0},-X_{a0}) \in D/\Lambda_{pq}$ can be joined with a straight line $L(R_{ic},X_{ic})$ crossing the boundary of Λ_{pq}, as illustrated in Fig. 2.

As shown in (4), in $\Lambda_{pq} \subset D$, τ is decreasing towards every direction from the perfect conjugate match impedance point $(R_{a0},-X_{a0})$. From the fact that this holds in particular in the direction along the line $L(R_{ic},X_{ic})$, it follows that in the intersection $L(R_{ic},X_{ic}) \cap \Lambda_{pq}$, τ attains its maximum at the

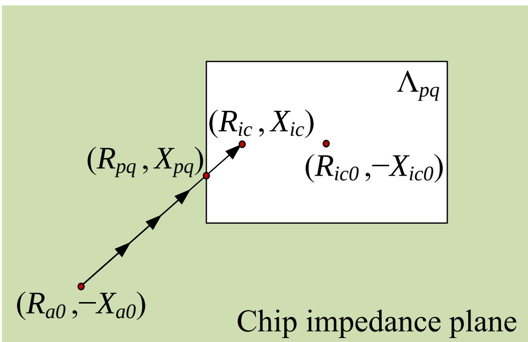

Fig. 2. The perfect conjugate match impedance point joined with a line to an arbitrary point in the chip impedance tolerance rectangle. Arrows indicate the direction of decreasing τ.

boundary of Λ_{pq}. Furthermore, the collection of the subsets of Λ_{pq} for which this is true is actually the whole set Λ_{pq}:

$$\bigcup_{(R_{ic},X_{ic}) \in \Lambda_{pq}} \left\{ L(R_{ic}, X_{ic}) \cap \Lambda_{pq} \right\} = \Lambda_{pq}. \tag{8}$$

Thus, if the perfect conjugate match impedance point $(R_{a0},-X_{a0})$ is not contained in Λ_{pq}, then the maximum of τ in Λ_{pq} is necessarily attained at its boundary.

Since the expression of τ is symmetric with respect to pairs (R_a,X_a) and (R_{ic},X_{ic}), the same conclusions hold if τ is treated as a function of the antenna impedance, while considering the chip impedance fixed. Based on this observation, a chain of inequalities similar to (6) can be developed as described below.

Let $\partial\Lambda_{pq}$ and $\partial\Lambda_{rs}$ be the boundaries of Λ_{pq} and Λ_{rs}, respectively and suppose that $(R_{a0},-X_{a0}) \notin \Lambda_{pq}$ and $(R_{ic0},-X_{ic0}) \notin \Lambda_{rs}$. Under these assumptions

$$\begin{aligned} \tau(R_{ic}, X_{ic}; R_a, X_A) &\le \tau(R_{pq}, X_{pq}; R_a, X_a) \\ &\le \tau(R_{pq}, X_{pq}; R_{rs}, X_{rs}), \\ &= \tau_{max}, \end{aligned} \tag{9}$$

for all $(R_{ic},X_{ic};R_a,X_a) \in \Lambda_{pqrs}$, with $(R_{pq},X_{pq}) \in \partial\Lambda_{pq}$ and $(R_{rs},X_{rs}) \in \partial\Lambda_{rs}$. As the upper bound for τ obtained in (9) is actually the function itself evaluated at a point in Λ_{pqrs}, τ_{max} is necessarily a maximum of τ within this set and it is attained in the Cartesian product $\partial\Lambda_{pq} \times \partial\Lambda_{rs}$. Finally, if $(R_{a0},-X_{a0}) \in \Lambda_{pq}$ or $(R_{ic0},-X_{ic0}) \in \Lambda_{rs}$, then $\tau_{max}=1$.

Based on this theoretical insight, the maximum of τ under given impedance tolerances can be evaluated much more efficiently compared with a direct numerical search through a 4-dimensional grid, since only a very limited subset – the Cartesian product $\partial\Lambda_{pq} \times \partial\Lambda_{rs}$ – of the 4-dimensional rectangle Λ_{pqrs} needs to be considered. With this approach, e.g. a search grid of size $n \cdot n \cdot n \cdot n$ is reduced to significantly smaller grid of size $4n \cdot 4n$, which means a $1-16/n^2$ relative size reduction.

III. TAG DESIGNS AND SIMULATION RESULTS

The frontend circuitry of an RFID chip is composed of capacitors, diodes and semiconductor switches, making the input impedance of the IC capacitive, as well as frequency and power dependent [11-13]. On the other hand, the input impedance of a short dipole tag antenna, operating below the fundamental resonance frequency of the antenna, is capacitive [2] and needs to be transformed to be inductive in order to conjugate match the tag antenna with the chip. This can be done using T-matching [6-9], which in practice is realized by forming a short circuit current path parallel to the antenna terminals. With the standard (single) T-matching this means adding a conductor loop in the structure around the antenna terminals. With the embedded T-matching, the short circuit current path is formed by a slot, which inscribed in the structure around the antenna terminals. The input impedance of a T-matched short dipole with a fixed length is then controlled by the shape of the short circuit current path. For example, with the commonly used rectangular path, the antenna input impedance can be controlled with only two parameters; the length and width of the rectangle.

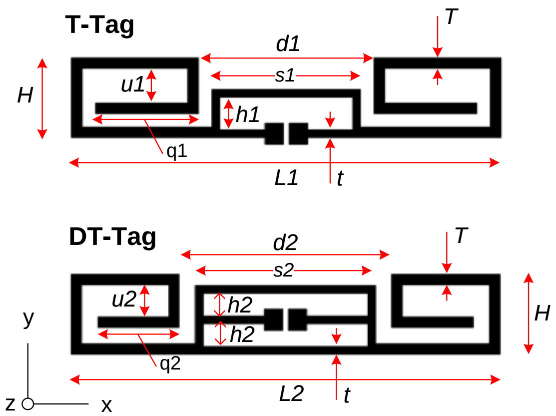

	$H = 15$	$T = 2$	$t = 1.5$
T-Tag	$L1 = 80.7$ $d1 = 33$	$h1 = 6.1$ $u1 = 6.5$	$S1 = 28$ $q1 = 19.4$
DT-Tag	$L2 = 80.7$ $d2 = 40$	$h2 = 4.2$ $u2 = 6$	$S2 = 34$ $q2 = 15.4$

Fig. 3. Layout of the designed T-matched tag antenna (top) and double T-matched tag (bottom). Values of the geometrical parameters are in millimeters.

Further degrees of freedom in the T-matching approach may be added by means of multiple T-matching stages [6]. In references [7-8] complex dipole antenna configurations with modified double-T matching approaches have been proposed. On the other hand, the present study focuses on a judicious performance comparison of fairly basic dipole antenna configurations with standard (single) T-matching and its simplest possible extension to double T-matching by addition of another identical loop.

The comparison is done using quarter wave dipole tag antennas with the same foot-print size and very similar radiating geometry. The structure of these tags is shown in Fig. 3. The chip used in both tag designs is the Higgs-3 UHF RFID IC by Alien Technology with the input impedance measured at the wake-up power of the chip [14]. The conjugate of this impedance, i.e. the target for the antenna impedance, is shown in Fig. 4. Ansoft high frequency structure simulator (HFSS) was employed in the antenna design.

Substrate material for the antenna designs is Rogers RT/duroid 5880 with the thickness of 3.175 mm, relative permittivity 2.2, and loss tangent 0.0009. This material was chosen due to its well-known microwave properties to reduce the design uncertainties and thereby yield more reliable comparison between the studied antennas. However, for tag antennas aimed for mass markets, thin low cost plastic films are a preferred choice for antenna substrate.

Since it is known that with the standard T-matching approach, good complex conjugate matching at a single frequency can be achieved, the design goal for the T-matched tag (T-Tag) was good performance within the US RFID band centered at 915 MHz. With the added degree of freedom in the impedance tuning with the double T-matching approach, a broader operational bandwidth is expected of DT-Tag. Therefore, a more challenging design goal with good antenna radiation characteristics together with more than 50% power transfer between the antenna and the chip throughout the global UHF RFID frequencies from 860 MHz to 960 MHz was considered.

The initial simulations showed that in practice, the added degree of freedom in the double T-matching approach manifests itself as a non-monotonic frequency response of the antenna reactance. This achievable feature allows a small dip to be tailored in the antenna reactance response to reduce its total variation over a range of frequencies. The reactance response of T-Tag, however, is inherently monotonic. This suggests that the expected broader operable bandwidth of DT-Tag may be realized by utilizing the local reactance dip in the tag antenna impedance in order to create a dual-frequency impedance matching.

In both tag antenna designs, the spiraled dipole arms are used to increase the electrical size of the antenna through the current alignment principle [4] and thus the fundamental resonance frequency of the antennas is much affected by the shape of the arms. Therefore, the related parameters *H*, *T*, *q1* and *q2* and *u1* and *u2* were first chosen in such a way that the fundamental resonance of the tag antennas with lengths *L1* and *L2* set to 80 mm (close to quarter wavelength) occurred slightly above 1 GHz. In this way, a gradual reactance slope favorable for the design was achieved over the frequencies of interest with both antennas. After this initial step, DT-Tag was optimized for the expected broadband operation, by varying the parameters *L2*, *h2*, and *s2* with *L2*

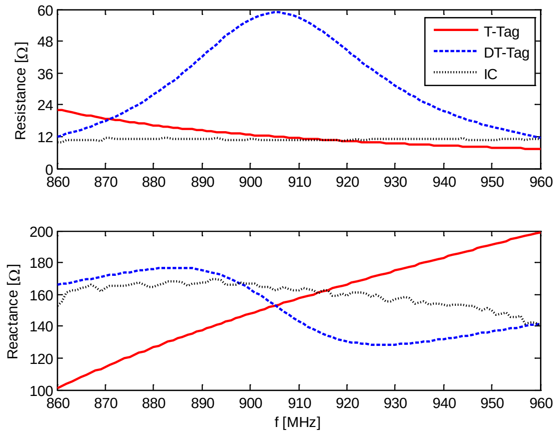

Fig. 4. Simulated tag antenna impedance and conjugate of the measured chip impedance.

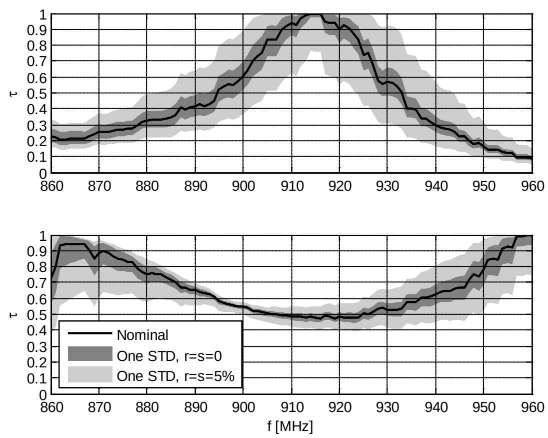

Fig. 5. Power transmission coefficient of T-Tag (top) and DT-Tag (bottom).

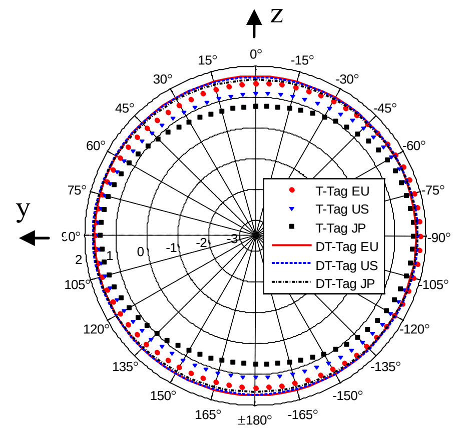

Fig. 6. Simulated tag antenna gain (dBi) yz-plane.

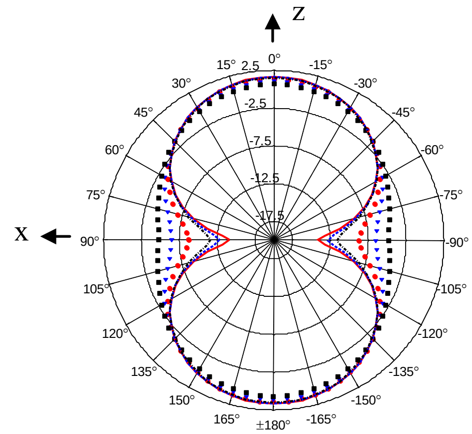

Fig. 7. Simulated tag antenna gain (dBi) xz-plane.

restricted in the neighborhood of the quarter wave length.

Before optimizing the T-matching loop of T-Tag, the parameter *L1* was set equal to *L2* to achieve exactly the same antenna foot-print size for both tags and thereby enable fair comparison between them. Then the parameters *h1* and *s1*, where optimized to satisfy the design goal for T-Tag: good performance within the US RFID band. The built-in genetic optimizer of HFSS version 12 was used in the design.

The optimized antenna impedance of T-Tag and DT-Tag is shown together with the conjugate of the chip impedance (antenna design target) in Fig. 4. The corresponding power transmission coefficients are presented in Fig. 5 with solid "Nominal" curve. These simulation results predict that the T-Tag is well matched near 915 MHz with both resistance and reactance close to their target values. For DT-Tag the same holds in edges of the studied frequency range. In the mid-band, the DT-Tag is also reasonably matched, despite the seemingly large antenna resistance compared with the chip resistance. This is understood by examining the power transmission coefficient given in (2) as a function of the antenna resistance. With small reactance mismatch, the optimal value for resistance is $R_a \approx R_{ic}$, but beyond this value, the increasing numerator $4R_aR_{ic}$ limits the decrease in τ. For reactance mismatch the rate of decrease in τ is determined solely by the square expression in the denominator. This explains the more rapid decrease of τ for the T-Tag, despite the good resistance match in the studied frequency range.

The Monte Carlo simulation method used in the chip impedance measurement [14] gives the chip resistance and reactance as means of Gaussian distributions with known standard deviations. The two uncertainty envelopes shown in Fig. 5 are based on 0% and 5% percentage tolerance in the simulated antenna impedance and the one standard deviation uncertainty for the measured chip resistance and reactance. In order to use the analysis from Section II to calculate the minimum and maximum power transmission coefficient under these impedance uncertainties, the standard deviations were first transformed into percentage tolerances. The envelope minimum is obtained from (7) and the maximum with direct numerical search through the set $\partial\Lambda_{pq}\times\partial\Lambda_{rs}$ defined in Section II.

In Fig. 5, the 0% case (r=s=0) represents a hypothetic perfectly successful simulation-based design and the 5% case (r=s=0.05) represents a more realistic scenario, which could be achieved with good modeling practices. In this study, tolerances beyond 5% were not considered, since the goal of the simulations is to provide judicious performance comparison between the two antennas on a platform with well-known dielectric properties. However, with larger antenna impedance tolerances, the analysis presented in Section II.A can be used for evaluating the platform-tolerance of RFID tags in terms of the minimum τ under variations in the tag antenna impedance when the tag is attached on different items with different electromagnetic properties.

As seen from Figs. 6-7, both antennas have an omnidirectional radiation pattern in yz-plane (the dipole H-plane) and an 8-shaped pattern in xz-plane (the dipole E-plane). Moreover, both antennas are linearly polarized in yz-plane with predominantly x-directed electric field component. It can also be observed from Figs. 6-7, that the gain of T-Tag decreases slightly with frequency in the yz-plane, while the minimum gain in xz-plane is increasing, whereas the gain pattern of DT-tag is less affected by frequency. However, in the yz-plane the gains of the two antennas are of the same order.

These results show that the matching network does not affect much on the radiation properties of the antenna and thus, the comparison of the antennas' performance in terms of the matching approach is fair.

All the tag measurements discussed in the next Section were conducted in the forward direction corresponding to the direction of the z-axis in Figs. 6-7. In this particular direction, the forward gain of DT-tag is found to be approximately constant at 1.6 dBi, while for T-Tag, the gain decreases from 1.5 dBi at 860 MHz to $G_{fwd} \approx 0.7$ dBi at 960 MHz.

IV. MEASUREMENT RESULTS AND DISCUSSION

In order to verify the tag designs experimentally, the simulated and measured empty space read range is compared. Here it is assumed that the read range is limited by IC's wake-up power and Friis' simple transmission equation [15] is used in the calculations. This simple formulation may not be sufficient for estimating the read range in complex real-life environments [16] and in some applications with strong tag-to-tag coupling the receiver sensitivity may be limiting the read range [17]. However, in a controlled measurement environment, the empty space read range allows direct comparison between the measurements and simulations and thereby provides a method for design verification. In the present study, the main goal of the experimental work is to add assurance for the simulation-based conclusions about the performance of the compared tags.

To characterize the forward link performance of the designed tags experimentally, the transmitted threshold power (P_{th}) was measured for each tag. This is the minimum transmitted continuous wave power at which a valid response to Electronic Product Code (EPC) Generation 2 protocol's *query* command is received from the tag under test. The threshold measurement was conducted in the forward direction in a compact anechoic cabinet with a linearly polarized transmitter antenna. During the measurement, the tag antennas were carefully aligned to match the polarization of the reader to minimize the link loss due to polarization mismatch. In addition, the path loss (L_{fwd}) from the generator's output port to the input port of an equivalent isotropic antenna placed at the tag's location was measured using the calibration procedure of the measurement device. This allows the compensation of any possible multipath effects in the measurements space, as described below.

According to Friis' simple transmission equation:

$$P_{ic,sens} = \tau G_{tag} L_c G_{tx} \left(\frac{\lambda}{4\pi d} \right)^2 P_{th*}, \tag{10}$$

where $P_{ic,sens}$ is the wake-up power of the chip, P_{th*} is the equivalent transmitted threshold power that would be measured in the perfect empty space conditions, L_c is the cable loss from the generator's output (matched to the cable) to the input port of the transmitting antenna (matched to the cable), the gain of the transmitting antenna and the tag antenna are G_{tx} and G_{tag}, respectively, and the separation between these antennas is d. On the other hand, in the real measurement it holds

$$P_{ic,sens} = \tau G_{tag} L_{fwd} P_{th}. \tag{11}$$

Thus, multiplying the measured transmitted threshold power with the factor Λ defined as

$$P_{th*} = \Lambda P_{th}, \quad \text{with} \quad \Lambda = \frac{L_{fwd}}{L_c G_{tx} \left(\frac{\lambda}{4\pi d} \right)^2}, \tag{12}$$

the measured P_{th} is mapped to the value that would have been obtained in empty space.

On the other hand, assuming that the measurement was conducted in empty space, the theoretical read range is

$$\begin{aligned} d_{tag} &= \frac{\lambda}{4\pi} \sqrt{\frac{\tau G_{tag} L_c G_{tx} P_{tx,EIRP}}{P_{ic,sens}}} \\ &= \frac{\lambda}{4\pi} \sqrt{\frac{\tau G_{tag} L_c G_{tx} P_{th*}}{P_{ic,sens}}} \sqrt{\frac{P_{tx,EIRP}}{P_{th*}}} \\ &= d \sqrt{\frac{EIRP / G_{tx} / L_c}{P_{th*}}}, \end{aligned} \tag{13}$$

where $P_{tx,EIRP}$ is the transmitted power corresponding to the regulated equivalent isotropically radiated power (*EIRP*). The theoretical empty space read range is now obtained by expressing P_{th*} in terms of P_{th} and L_{fwd} from (12) and substituting this into (13). As a result we get,

$$d_{tag}^{m} = \frac{\lambda}{4\pi} \sqrt{\frac{EIRP}{L_{fwd} P_{th}}}, \tag{14}$$

where the superscript *m* indicates that this value is based on measurements.

For comparison between the measurements and simulations, the theoretical empty space read range can be calculated with Friis' simple transmission equation using the simulated power transmission coefficient (τ), tag antenna gain in the forward direction (G_{fwd}), and the chip sensitivity ($P_{ic,sens}$ = −18 dBm) provided by the manufacturer. Under these definitions, the simulated value is given by

$$d_{tag}^{s} = \frac{\lambda}{4\pi} \sqrt{\frac{\tau G_{fwd} EIRP}{P_{ic,sens}}}. \tag{15}$$

Comparison of the measured and simulated theoretical empty space read ranges with European power regulation (EIRP = 3.28W) is shown in Fig. 8.

Simulation results, in Figs. 4-5, predict good reactance matching for DT-Tag at both ends of the studied frequency range, while the tag antenna gain was observed to remain approximately constant. This agrees with the measured frequency response shown in Fig. 8, with peak performance at the edges of the measured frequency range and slightly weaker performance in the middle. The simulated reactance of T-Tag, shown in Fig. 4, increases monotonically through the studied frequencies and consequently, good conjugate impedance matching is achieved only in the neighborhood of 915 MHz. This agrees with the measured frequency response, shown in Fig. 8. Simulations also predict a decreasing slope in the tag antenna gain versus frequency, which agrees with the measured frequency response as well; T-Tag's performance decays faster towards the higher end of the measured frequency range. In addition, both tag antenna designs are verified within 5% impedance tolerances through the majority of the studied frequency points. This provides further assurance for the performance comparison between them.

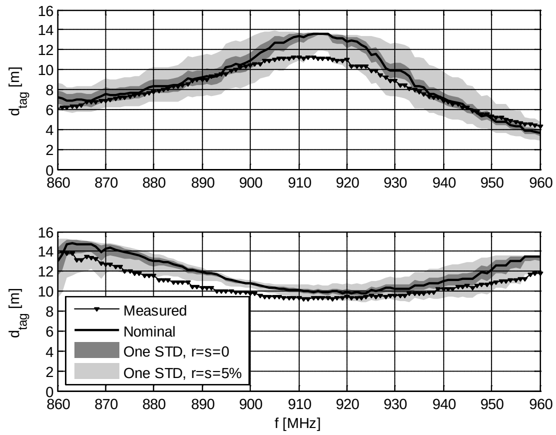

Fig. 8. Theoretical empty space read range of T-Tag (top) and DT-Tag (bottom) in the forward direction.

V. CONCLUSIONS

The impact of tag antenna and chip impedance tolerances on power transfer between these components was investigated analytically. Means for efficient computation of the minimum and maximum power transmission coefficient under given impedance tolerances were developed and a closed-form expression for the minimum value was derived. This analysis provides tools for tag antenna designers to validate their designs.

The presented sensitivity analysis was employed to quantify the design uncertainty of single and double T-matched short dipole tags. Both, the simulation-based and experimental comparisons of these tags showed that the bandwidth of a standard T-matched tag can be significantly improved with the double T-matching approach. Importantly, the modification of the standard T-matching to double-T matching requires only a minimal structural modification, which in our study did not increase the antenna foot-print size.

ACKNOWLEDGMENT

This research work was funded by the Finnish Funding Agency for Technology and Innovation (TEKES), Academy of Finland, Centennial Foundation of Finnish Technology Industries, Tampere Doctoral Programme in Information Science and Engineering (TISE), HPY Research Foundation, and Nokia Foundation.

REFERENCES

[1] D. Dobkin, *The RF in RFID: Passive UHF RFID in Practice*, Newline, 2008.

[2] R. C. Hansen, *Electrically Small, Superdirective, and Superconducting Antennas*, Wiley, 2006.

[3] J. Rashed and C.-T. Tai, “A New Class of Resonant Antennas,” *IEEE Trans. Antennas Propagat.*, vol. 39, pp. 1428-1430, Sep. 1991.

[4] S. R. Best and J. D. Morrow, “On the Significance of Current Vector Alignment in Establishing the Resonant Frequency of Small Space-Filling Wire Antennas,” *IEEE Antennas Wireless Propag. Lett.,* vol. 2, pp. 201-204, 2003.

[5] A. Harmouch and H. A. Al Sheikh, “Miniaturization of the Folded-Dipole Antenna [Antenna Designer's Notebook],” *IEEE Antennas Propag. Mag.*, vol. 51, no. 1, pp. 117-123, Feb. 2009.

[6] G. Marrocco, “The Art of UHF RFID Antenna Design: Impedance-Matching and Size-Reduction Techniques,” *IEEE Antennas Propag. Mag.,* vol. 50, no. 1, pp. 66-79, Feb. 2008.

[7] C. Cho, H. Choo, and I. Park, “Broadband RFID Tag Antenna with Quasi-Isotropic Radiation Pattern,” *IET Electronics Letters,* vol. 41, no. 20, pp. 1091-1092, 29 Sept. 2005.

[8] J. Tan and X. Li, “Wideband Double-UT RFID Tag Antenna Design,” *IEEE Asia Pacific Conference on Circuits and Systems (APCCAS)*, pp. 1256-1259, Nov. 30 - Dec. 3, 2008.

[9] D. D. Deavours, “Improving the Near-Metal Performance of UHF RFID Tags,” *IEEE International Conference on RFID*, pp.187-194, 14-16 Apr. 2010.

[10] K. Kurokawa, “Power Waves and the Scattering Matrix,” *IEEE Trans. Microw. Theory*, vol. 13, no. 2, pp. 194-202, Mar. 1965.

[11] G. De Vita and G. Iannaccone, “Design Criteria for the RF Section of UHF and Microwave Passive RFID Transponders,” *IEEE Trans. Microw. Theory*, vol. 53, no. 9, pp. 2978-2990, Sept. 2005.

[12] J.-P. Curty, N. Joehl, C. Dehollain, and M. J. Declercq, “Remotely Powered Addressable UHF RFID Integrated System,” *IEEE J. Solid-State Circuits*, vol. 40, no. 11, pp. 2193- 2202, Nov. 2005.

[13] C.-H. Loo, K. Elmahgoub, F. Yang, A. Z. Elsherbeni, D. Kajfez, A. A. Kishk, T. Elsherbeni, L. Ukkonen, L. Sydanheimo, M. Kivikoski, S. Merilampi, and P. Ruuskanen, “Chip Impedance Matching for UHF RFID Tag Antenna Design,” *Progress In Electromagnetics Research (PIER)*, vol. 81, pp. 359-370, 2008.

[14] T. Björninen, M. Lauri, L. Ukkonen, L. Sydänheimo, A. Z. Elsherbeni, and R. Ritala, ”Wireless Measurement of UHF RFID Chip Impedance,” *Proc. 32nd Antenna Measurement Techniques Association (AMTA) Symposium*, pp. 35-40, Atlanta, GA, USA, 10-15 Oct. 2010.

[15] H. T. Friis, “A Note on a Simple Transmission Formula,” *Proc. IRE*, vol. 34, no. 5, pp. 254-256, May 1946.

[16] G. Marrocco, E. Di Giampaolo, and R. Aliberti “Estimation of UHF RFID Reading Regions in Real Environments,” *Antennas Propag. Mag.*, vol. 51, no. 6, pp. 44-57, Dec. 2009.

[17] H. Yojima, Y. Tanaka, Y. Umeda, O. Takyu, M. Nakayama, and K. Kodama “Analysis of Read Range for UHF Passive RFID Tags in Close Proximity with Dynamic Impedance Measurement of Tag ICs,” *IEEE Radio and Wireless Symposium (RWS)*, pp. 110-113, Phoenix, AZ, USA, 16-19 Jan. 2011.

[18] Voyantic Ltd., Espoo, Finland: http://www.voyantic.com/

Toni Björninen received the M.Sc. degree in Electrical Engineering from Tampere University of Technology (TUT), Tampere, Finland, in 2009. He is currently a Researcher at the Wireless Identification and Sensing Systems research group, Rauma Research Unit, Department of Electronics, TUT, where he is working toward the Ph.D. degree in Electrical Engineering.

He has authored publications on passive RFID tag antennas and printable electronics for microwave applications. His research interests include antennas for RFID systems and wireless sensing, and modeling of electromagnetics.

Dr. Atef Z. Elsherbeni is a Professor of Electrical Engineering and Associate Dean of Engineering for Research and Graduate Programs, the Director of The School of Engineering CAD Lab, and the Associate Director of The Center for Applied Electromagnetic Systems Research (CAESR) at The University of Mississippi. In 2004, he was appointed as an adjunct Professor, at The Department of Electrical Engineering and Computer Science of the L.C. Smith College of Engineering and Computer Science at Syracuse University. In 2009, he was selected as Finland Distinguished Professor by the Academy of Finland and TEKES. Dr. Elsherbeni is the co-author of the books, “The Finite Difference Time Domain Method for Electromagnetics With MATLAB Simulations”, SciTech 2009, “Antenna Design and Visualization Using Matlab”, SciTech, 2006, “MATLAB Simulations for Radar Systems Design”, CRC Press, 2003, “Electromagnetic Scattering Using the Iterative Multiregion Technique”, Morgan & Claypool, 2007, “Electromagnetics and Antenna Optimization using Taguchi's Method”, Morgan & Claypool, 2007, and the main author of the chapters “Handheld Antennas” and “The Finite Difference Time Domain Technique for Microstrip Antennas” in Handbook of Antennas in Wireless Communications, CRC Press, 2001. Dr. Elsherbeni is a Fellow member of the Institute of Electrical and Electronics Engineers (IEEE) and a Fellow member of The Applied Computational Electromagnetic Society (ACES). He is the Editor-in-Chief for ACES Journal.

Leena Ukkonen received the M.Sc. and Ph.D. degrees in Electrical Engineering from Tampere University of Technology (TUT), Tampere, Finland, in 2003 and 2006, respectively.

She is currently leading the Wireless Identification and Sensing Systems research group at the Rauma Research Unit, Department of Electronics, TUT. She also holds Adjunct Professorship in the Aalto University School of Science and Technology, Espoo, Finland. She has authored over 100 scientific publications in the fields of RFID antenna design and industrial RFID applications. Her research interests are focused on RFID antenna development for tags, readers and RFID sensors.

FEKO/NEC2 Simulation of Candidate Antennas for the Long Wavelength Array (LWA)

Nassissie Fekadu [1, 2] and Amir I. Zaghloul [1, 3]

[1] Virginia Polytechnic Institute and State University
Blacksburg, VA 24061-2000, USA
nfekadu@vt.edu , amirz@vt.edu

[2] Noblis
3150 Fairview Park Drive
Falls Church, VA 22042-4504, USA
nassissie.fekadu@noblis.org

[3] US Army Research Laboratory
Adelphia, MD 20783, USA
amir.zaghloul@us.army.mil

Abstract **─** This paper presents FEKO and NEC-2 simulations done on three dipole-like structures; the big blade, the tied-fork and the fork antenna. These antenna elements are considered for the design of the long wavelength array (LWA). The LWA is an interferometer under construction in New Mexico, USA for astronomical observations in the 20 - 80 MHz spectrum. This paper presents the simulation results of a co-polarized antenna gain patterns, impedance values, and mutual couplings for each candidate elements. Coupling results from FEKO and NEC-2 simulations are compared with measurement result of the big blade antenna. The paper also presents S-parameters for 25 elements of the tied-fork antennas.

Index Terms **─** Blade, dipole-like structures, FEKO, fork, mutual coupling, and tied-fork.

I. INTRODUCTION

The long wavelength array (LWA) is a radio interferometer telescope array under construction in New Mexico, USA for astronomical observation in the 20-80 MHz radio spectrum, within a total range of 10 MHz (ionospheric cut off) to 88 MHz [1, 2]. The array will consist of 53 electrically steered phased array stations. Each station will be constructed using 256 cross-dipole type antennas. The array will cover maximum baselines (distances between stations) up to 400 km of which core stations of 17 are within the center 10 km [3]. The station array has a pseudo-random arrangement that enables large aperture achievement with relatively fewer antenna elements while maintaining low sidelobe levels [4]. The objective of the LWA is to achieve long wavelength imaging with angular resolution and sensitivity comparable to existing instruments operating at shorter wavelengths [5].

Each station will have an elliptical shape with an axial ratio of 1.1:1 (110m in the N-S direction and 100m in E-W direction). This structure enables observation toward declinations that appear in the southern sky of New Mexico. Furthermore, it provides the ability to observe the inner galaxy region. The dimensions of the station array are chosen to balance sampling of a large field efficiently and calibration across the field of view (FOV) [5]. The array spacing d, is 5m which is 0.33λ at 20MHz and 1.33λ at 80MHz. Aliasing at the highest frequency for periodic arrays is avoided by using spacing, $d < 0.5\lambda$. To avoid aliasing at 80 MHz, the number of antenna elements required for the LWA would have to increase by a factor of three which is economically

Submitted On: July 22, 2010
Accepted On: March 17, 2011

prohibitive [5]. Hence, a pseudo-random array arrangement is used to avoid aliasing at the highest frequency.

The number of elements in a station is arbitrarily chosen to be 256, a power of 2. The number of elements can be anywhere between 50 to 2500; however, it is constrained by requirements such as the baseline which affects image quality and the logistics associated with acquiring land, transporting the data, and maintenance of the equipment [5].

The choice of individual element design depends on whether the design meets technical requirements as well as cost limitations. The technical requirements for the LWA interferometer include [5]:

- Sensitivity on the order of arcseconds resolution of 8" and 2" at 20MHz and 80 MHz, respectively
- Field of view of 8° and 2 ° at 20 MHz and 80 MHz, respectively
- Broad and slowly-varying patterns over the tuning range
- Dimensions on the order of ½ λ at the highest frequency for alias-free beamforming
- Large tuning range for large impedance bandwidth

The technical requirements for candidate elements include [6]:

- Frequency range of 20-80 MHz (3-88 MHz desired)
- Stable, sky noise dominance of 6dB over the frequency range
- Zenith angle coverage, $z \leq 74°$ ($z \leq 80°$ is desired), to detect bright transients near the galactic center
- Good axial ratio for circular polarization (This requirement refers to the cross-polarization isolation)
- Durability for 15 year lifespan

The candidate antennas for the LWA system are dipole-like structures. Even though dipoles inherently have narrow impedances, the limitation does not apply to frequencies below 300MHz. Potential and dominant noise contribution comes from natural Galactic noise, not the instrument used [5].

This paper presents FEKO and NEC-2 simulations of the candidate antennas; the big blade, the tied-fork, and the fork antennas. FEKO is an electromagnetic (EM) analysis software suite based on the method of moments (MoM). NEC-2 (the numerical electromagnetic code version 2) is a public domain code also based on the method of moments. Simulation results from this paper as well as measurement data from other studies show the candidate antennas to be comparable in performance. All three candidates have also shown to meet technical requirements for the element design [2].

Section 2 describes the topology of the three candidate dipole type antennas. Sections 3 and 4 present design specification and design process of the LWA, respectively. Section 5 presents the parameters used for simulating the individual antennas as well as the results of the simulation, including the results from the S-parameter simulation of the 25-element array of tied-fork antennas. Section 6 provides the analysis of the results, and Section 7 summarizes the paper.

II. DESCRIPTION OF CANDIDATE ANTENNAS

Each stand of the candidate antennas has two dipoles with collocated feed points oriented at right angles to each other.

The big blade is a complex structure made of two linearly polarized cross dipoles. The element is made of aluminum sheets. Even though the overall performance of this antenna is comparable with the other candidates, since it takes a total of 13,000 elements to construct the entire array system, it makes this candidate unfavorable with respect to cost. The big blade antenna dimensions are shown in Figure 1 and its images from FEKO and NEC-2 simulations are given in Figure 2.

The tied -fork antenna is made of strands of wire that represent the skeletal outline of the big blade. It also has two bars that run across the strands. Since the fork antenna does not involve the use of the aluminum sheet, it is less costly than the complex big blade structure. The tied-fork antenna dimensions are presented in Fig. 1 and its images from FEKO and NEC-2 simulations are shown in Fig. 2.

Like the tied-fork, the fork antenna is made of 3 strands of wire that represent the skeletal outline of the big blade. This antenna is a cost effective candidate. It is also less susceptible to wind effects [7]. The fork antenna dimensions are presented in Fig. 1 and its images from FEKO and NEC-2

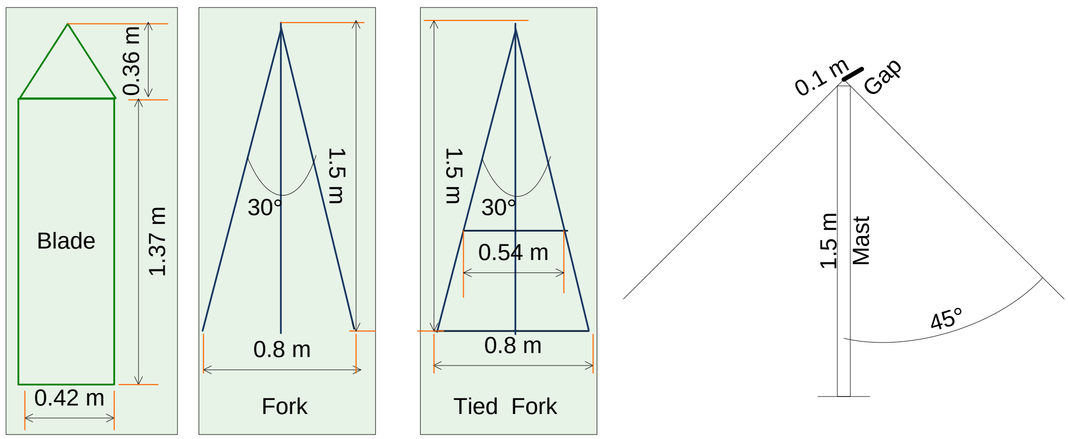

Fig. 1. Big blade, tied fork, and fork antenna dimensions.

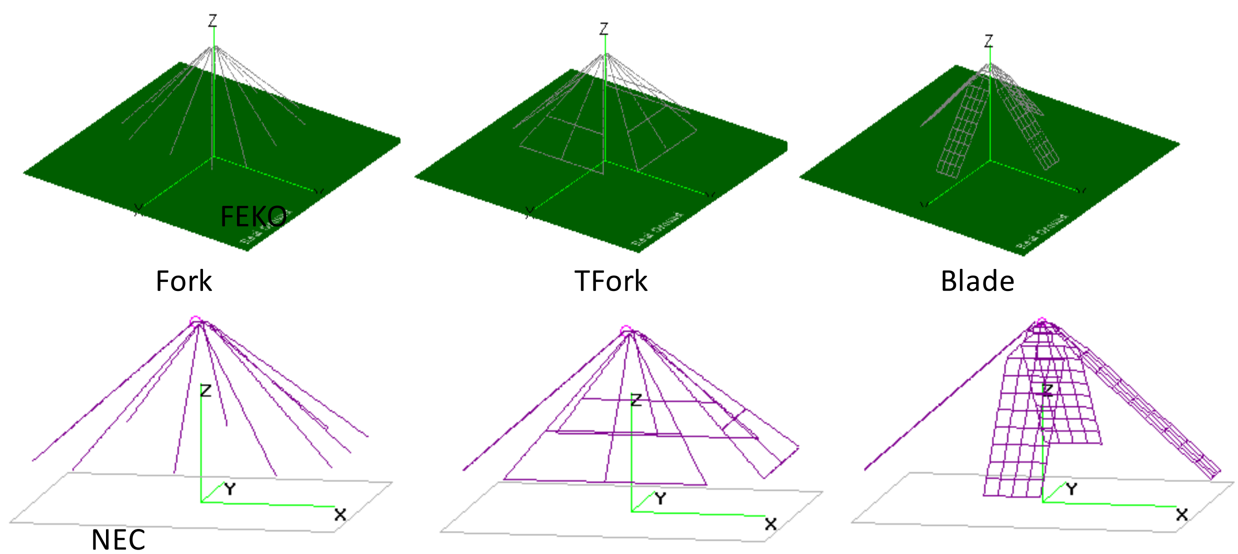

Fig. 2. Big blade, tied fork, and fork images from FEKO and NEC-2 simulations.

simulations are shown in Fig. 2.

III. DESIGN SPECIFICATIONS

The LWA is designed for long-wavelength astrophysics and ionospheric research [5]. The LWA addresses a wide range of research interests including cosmic evolution, solar science, and space weather. Detailed and specific objectives for the LWA are described in [8]. The underlining expectation of the LWA is that it should be able to perform comparably to existing instruments operating in shorter wavelengths with respect to resolution and sensitivity. That is resolution in the order of arcseconds and sensitivity in the orders of mili-janskys, where 1 Jansky= $(10^{-26}\ \mathrm{W})/(\mathrm{m}^2\ \mathrm{Hz}^{-1})$, are desired [5]. This means an improvement of several orders of magnitude over existing instruments operating below 100 MHz [5].

In order to achieve the long wavelength imaging required for the exploration of various scientific frontiers, parameters such as dimensions of stations, resolution, collecting area, sensitivity, and field of view (FOV) are considered in the design process. An overview of these parameters is provided here. However, for detailed description and design processes please refer to [5] and [8]. The key design parameters of the LWA stations are collecting area and dimensions of the station beam [5]. Collecting area contributes to image sensitivity while dimensions of the beam constraint image FOV.

Resolution (R) is the system's ability to distinguish between two very close, adjacent and independent objects in the sky. The largest structure that can be imaged by the system is a function of the observational wavelength and the minimum baseline. It is the finest detail an instrument is capable of showing. It is calculated as, $R= (\lambda/D)*(648000/\pi)$, where D is the maximum baseline (400km).

The process of determining the collecting area involves using sufficient number of sources that are detected above a certain flux within the FOV to calibrate the image against the effects of the ionosphere. The effective collecting area of a LWA station is given by $A= \gamma N_a \xi A_{eo} (\lambda,\theta,\phi)$ where γ accounts for aggregate mutual coupling, N_a is the number of elements and A_{eo} is the collecting area of a single antenna in isolation [8].

FOV is the area of the sky being observed. Dimensions of the station array determine the width of the station beam which in turn determines the field of view. The image quality over larger FOV is limited by atmospheric variance in it. The usable FOV is determined by spacings between antennas and it is affected significantly by the ionosphere. The FOV of the LWA can be defined as the area bounded by the half-power beamwidth of a station beam and is calculated as $FOV= 4.12\psi_o^2 (\lambda/4m)^2 (D/100m)^{-2} \sec\theta$ [deg^2] where, ψ_o =1.02 for a uniformly excited circular array and D is the station mean diameter. For detail derivation of the parameters, please refer to [8].

The sensitivity of a radiotelescope is a measure of the weakest source of radio emission that can be detected; hence, it is directly related to the errors of measurement [9]. Many factors affect sensitivity including the nature of the source signal, antenna characteristics, receiver performance (LWA has Galactic-noise limited receiver), resolution, the medium between the source and the antenna system (atmospheric conditions that are frequency dependent), image forming characteristics, and the size of the region of the sky observed. Sensitivity is parameterized using system temperature where high system temperature value indicates low sensitivity. Sensitivities are calculated for a given integration time. Sensitivity is proportional to the size of the beam, integration time, and total observation bandwidth. It can be improved after observations by averaging channels together. The sensitivity of observation varies across the FOV where it declines away from the center position of the main beam.

IV. DESIGN PROCESS

In general, for short wavelength design if technical issues are overcome, costs will be a major obstacle [8]. Simulations and prototype testing were performed to choose the design of the antenna elements. Each antenna element needed to achieve large tuning range to be considered for the design of the LWA. Previously, low frequency telescopes used antennas that have inherently large impendence bandwidth such as conical spirals [8]. Since the design of the LWA calls for a large number of antennas, such complex and expensive structures are not suitable for the LWA. Hence, simple wire dipoles (folded dipoles) that have inherently narrow impedance bandwidth are chosen. This does not pose significant problems for systems operating below 300 MHz. This is because the natural Galactic noise dominates over the noise contribution of the electrons attached to the antennas [5]. Prototypes of the antennas are used to measure the radio frequency interference environment in the desired frequency band and the result show stable sky noise dominance of 6dB over the frequency range.

The choice of 256 stands distributed over roughly 100m diameter (110mx100m ellipse) balances the desire to efficiently sample large FOV required to image several sources across the sky against the difficulty of ionospheric calibration across the wide FOV [5]. The LWA will be able to image wide FOVs with sufficient diversity of baselines [8]. This choice will also balance cost against quality of image calibration over a broad range of frequencies and zenith angles [8].

Even though it is desirable to have a small number of stations to simplify the process of obtaining land, transporting data, and maintaining instruments since image quality requires diversity of baselines the argument calls for a larger number of stations. The station numbers (53) were chosen based on prior experience and guidance from previous large array systems [5].

The maximum baseline of 400km was chosen in order to obtain the resolution values required to observe detailed structures of extragalactic radio galaxies and avoid confusion that arises due to unresolved sources or due to plausible long hours of integration times (interval over which data collected are averaged to reduce background noise) [5]. This baseline yields the desired resolution; 8'' at 20 MHz and 2'' at 80 MHz.

Optimization of antenna positions for a pseudorandom station configuration was performed and details of it are found in [10]. Pseudorandom antenna distributions are susceptible to mutual coupling effects. Current simulation does not consider effects of coupling for the LWA; future effort will be focused to include effects of coupling. Furthermore, the effects will be studied when the first station is built [8].

As mentioned earlier, the primary receiving element of the LWA is a fixed stand that incorporates two broadband, crossed, linearly-polarized dipoles. The signal from every antenna is processed by a direct-sampling receiver consisting of an analog receiver and an analog-to-digital converter. Beams are formed using a time-domain delay-and-sum architecture, which allows the entire 10–88 MHz passband associated with each antenna to be processed as a single wideband data stream. A finite impulse response filter which is used to introduce coarse delay is also used to introduce corrections for polarization and other frequency-dependent effects. The raw linear polarizations are transformed into calibrated standard orthogonal circular polarizations, and the signals are then added to the signals from other antennas processed similarly [11].

V. SIMULATION PARAMETERS AND RESULTS

This section presents the parameters used and the results obtained from FEKO and NEC-2 simulations. MATLAB scripts are used to generate the antenna models used in the two simulation tools.

Figure 3 shows co-polarized gain patterns in E- and H-planes along with axial ratios of the candidate antennas at 38MHz, 74 MHz, and 80 MHz. The axial ratio resulting from a pair of dipoles can be approximated from the difference between the E- and H-plane gain patterns at each elevation angle for a single dipole [12]. Axial ratios are calculated from the co-polarized gain patterns using AR (θ, ϕ) = |GE,co (θ, ϕ) – GH,co (θ, ϕ)|, where (θ, ϕ) are observation angles and GE,co and GH,co are co-polarized gain patterns in the E- and H-planes, respectively, of a single dipole expressed in dB. Since the maximum cross-polarized gains for all antenna structures from both simulation tools are very low, their plots are not included in the paper.

Figure 4 presents impedance values obtained for each isolated dipole-like structure. A reference input impedance of 50 Ω is assumed when calculating the S-parameters in all cases in both FEKO and NEC-2 simulations. Figure 5 shows the S-parameters obtained for two identical elements of each of the antenna types. Dynamic matching at different frequencies would achieve better performance for the significant portion of the required frequency bands instead of the narrow band observed for the S11 values. In Fig. 6, the big blade antenna measurement data from [13] is compared with big blade simulations of NEC-2 and FEKO. A spacing of 6m between two big blade antennas is used when calculating S21.

Figures 7 and 8 present mutual coupling between elements in a periodic 5X5, or 25-element array of tied-fork antennas for the center element and an edge element, respectively, for a range of frequencies. In this coupling calculation all the elements in the array but one are terminated with 50Ω impedance and one of the elements (the edge or the center element) is excited.

A conducting ground screen (3mx3m) that can prevent loss through absorption and isolate the antenna from variable ground conditions to stabilize the system temperature will be used in the field. However, it is not included for this simulation. The measurement setup also did not include the ground screen (Fig. 6). Real ground conditions, permittivity, ε_r = 13, and conductivity, σ =0.005 S/m, are used in all cases of the simulation in this study. Based on [14], a wire radius (r_w) = 0.0099 m is used in all cases. A segment length of ~ 8* r_w is used for NEC-2 simulations and a segment length of ~5*r_w is used for FEKO simulations. The choice of the length of the segments is based on [15] and the final adjustments are made by trial and error. The feed point is assumed to be 1.5 m above the ground for all candidate antenna types. A 0.1m feed point width is used for all antenna types.

FEKO and NEC-2 simulation results for the co-polarized E-plane and H-plane gain patterns of the big blade, tied fork, and fork antenna (Fig. 3) at 38 MHz, 74 MHz, and 80 MHz are fairly comparable. The H-plane patterns maintain their shape with increased beamwidth as the frequency increases. However, the E-plane patterns exhibit sidelobes at the higher frequencies. The tied fork antenna has the maximum axial ratio for all frequency ranges. The big blade has the lowest axial ratio in all frequencies at all elevation angles.

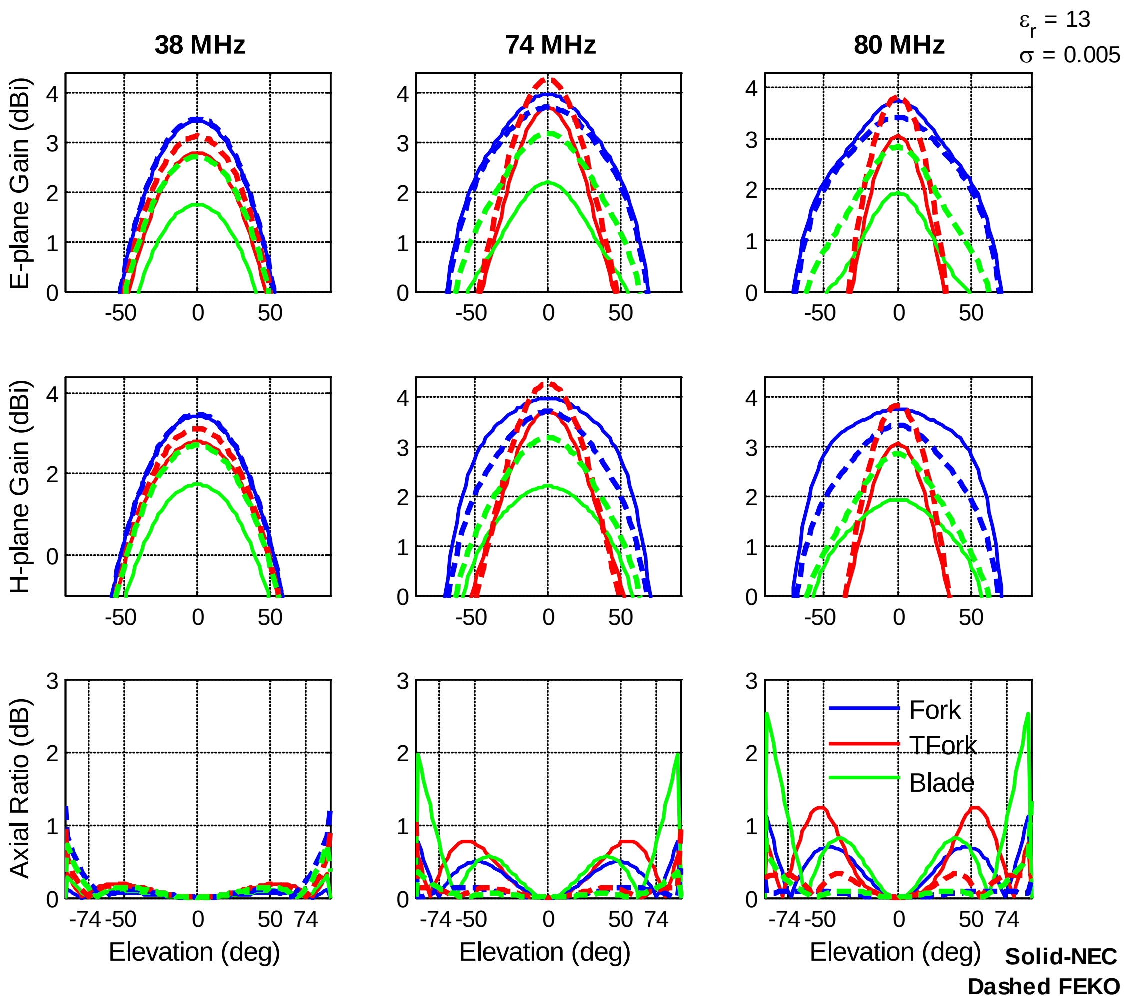

Fig. 3. Co-polarized gain patterns and axial ratios at 38, 74, and 80 MHz.

Impedance values (Fig. 4) obtained from the simulations show that for all the three element types FEKO simulations results are slightly higher, particularly for higher frequencies than NEC-2 simulations. Overall, the fork antenna has higher impedance values than the other two antennas. There is a spike seen around 55 MHz for the fork antenna, and it is assumed to be a simulation artifact. The tied-fork and fork antenna exhibit higher resonant frequencies as compared to the big blade.

For the mutual coupling calculation of two antennas side by side, a spacing of 6 m between the elements is used; this is because the available measurement data is for 6m spacing. However, 5 m spacing is considered for the LWA design. The mutual coupling measurement of the big-blade [13] is comparable with NEC-2 and FEKO simulations results.

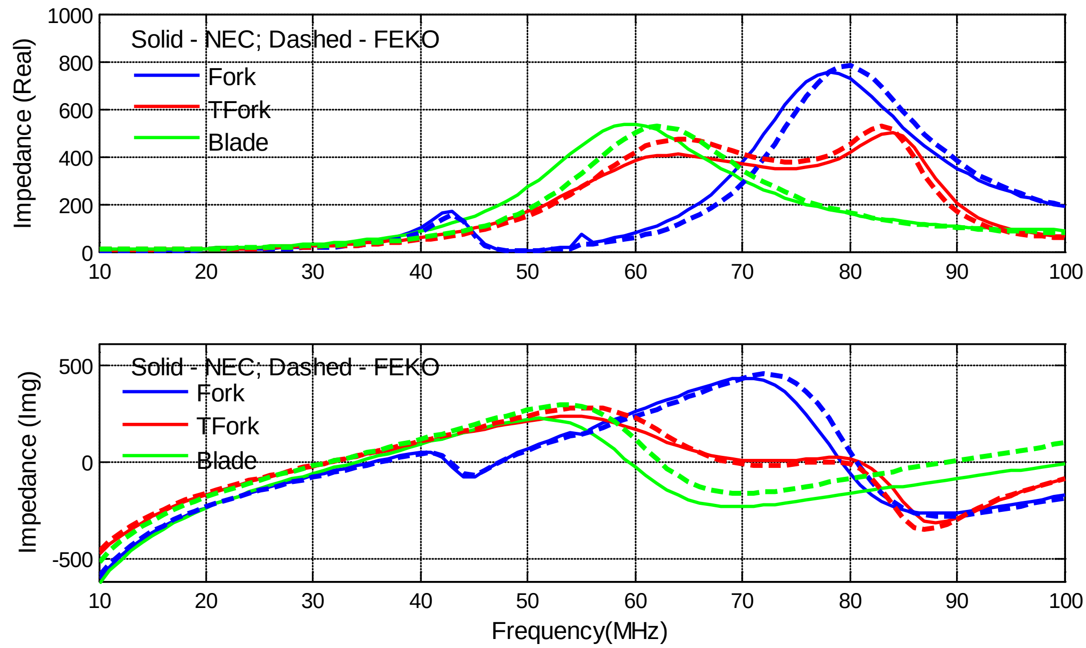

Fig. 4. Big blade, tied-fork, and fork antenna impedances for isolated elements.

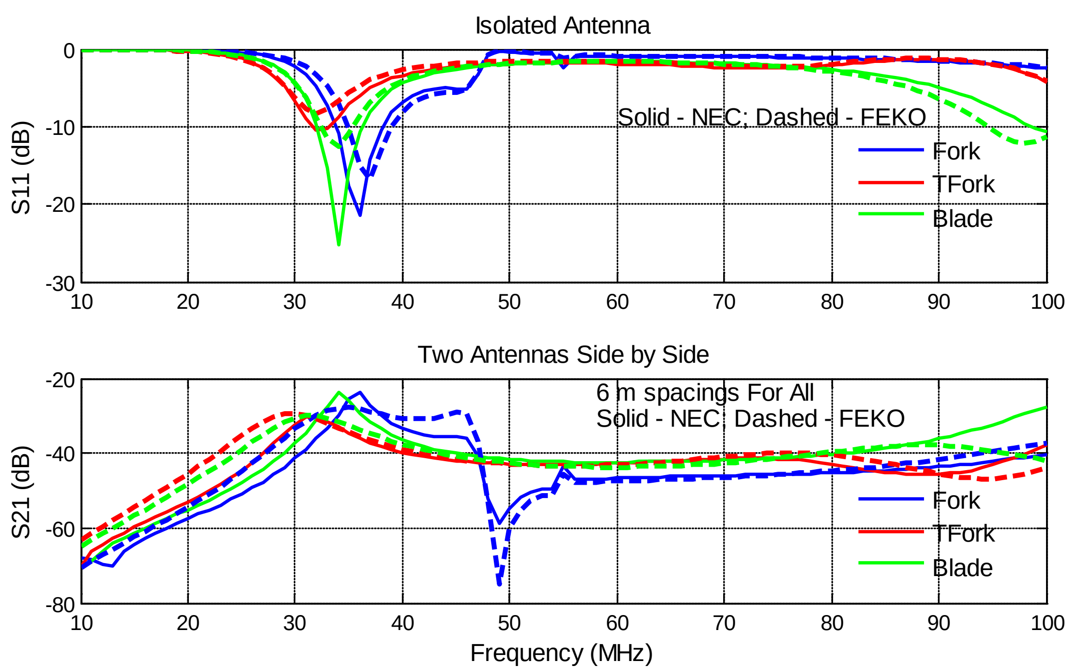

Fig. 5. Big blade, tied-fork, and fork antenna S-parameters.

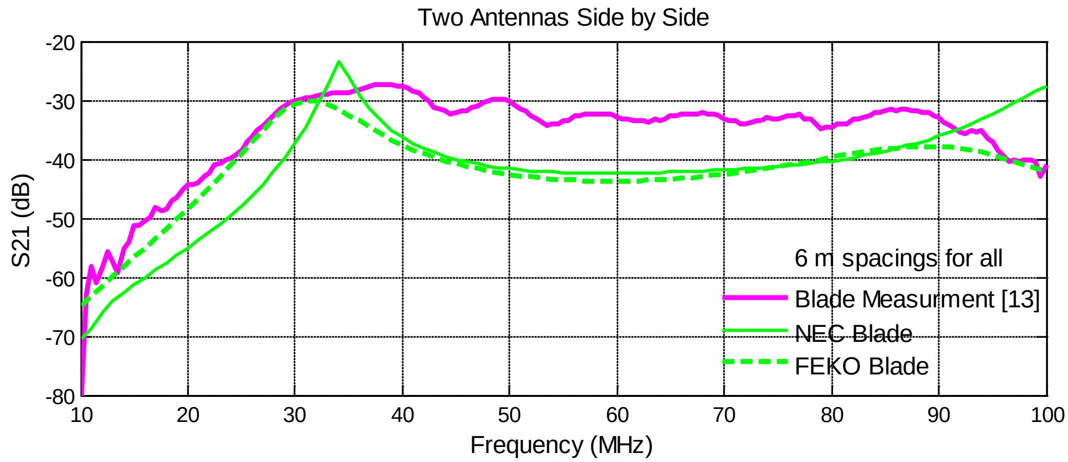

Fig. 6. Measurement data and simulation results of the big blade antenna coupling.

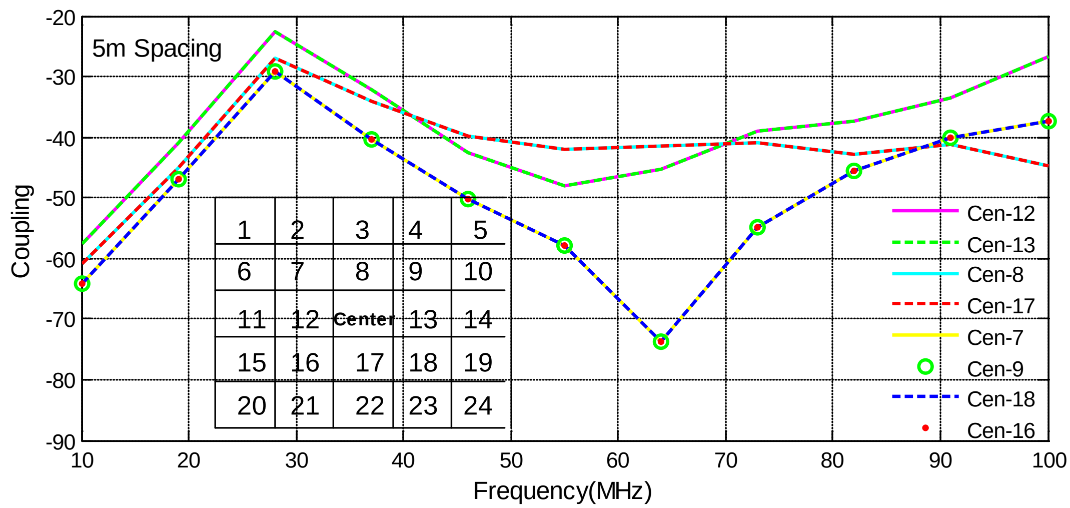

Fig. 7. S-parameters for 5x5 tied-fork antennas – center element.

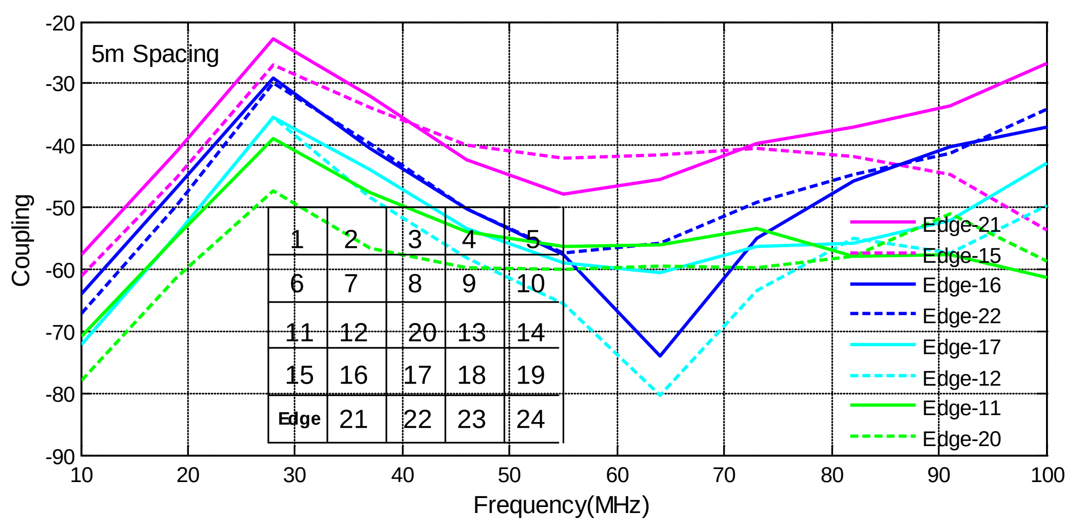

Fig. 8. S-parameters for 5x5 tied-fork antennas – edge element.

VI. ANALYSIS

The LWA candidate antennas maintain good performance over the required 20 – 80 MHz frequency range if a dynamic input impedance matching is applied for frequency and scan angle changes. This study did not consider antenna performance optimization. Even though, the tied-fork antenna and the fork antenna have simpler topology, they exhibit comparable RF properties to the complex big blade structure.

The co-polarized gain patterns of the antennas in both planes exhibit a single, wide beamwidth lobe with the maximum towards zenith. However, the H-plane patterns better maintain their shape and provide increased beamwidth up to higher frequencies than the E-plane patterns, which develop sidelobes at higher frequencies. The fork antenna seems to be better in keeping its shape at all frequencies. The co-polarized gain patterns are plotted only for E-plane since it is assumed the performance of this plane to be worse than other planes [16].

The beam patterns of the three structures have axial symmetry of 1.2 dB or less for elevation angles down to ± 74 ° from zenith for all frequencies. For higher frequencies, the FEKO simulation results show 1dB or less for all frequencies at these elevations.

The simulated impedance values of the simpler topology antennas are generally higher and shifted down in frequency when compared to the simulated response of the big blade antenna. The big blade exhibits larger impedance bandwidth as compared to the other two antennas.

The S-parameters for the 25 tied-fork antennas show that coupling effects are not prominent enough to cause concern. The worst condition, a coupling of -23 dB, is observed for both center and edge cases at 28 MHz at a distance of 5m when the antennas are in parallel. For the same distance if the antennas are placed diagonally from each other, the coupling is only about -27 dB. This is because the induced current is largest when the two antennas are parallel. The coupling results are obtained by exciting one element (center or the edge) and terminating all the other elements with 50 Ω. Note that parallel implies the maximum radiation is aligned along the line of separation, hence a higher coupling. For all the calculation, the unexcited antenna is terminated with a load of 50Ω.

VII. CONCLUSION

FEKO and NEC-2 simulation results of the big blade, tied-fork, and fork antennas are presented in this paper. The candidate antennas exhibit similar characteristics with slight differences in impedance and gain values. The simulation results obtained in this study are in agreement with the measurement provided in [2]. The S-parameters for the 25 tied-fork antennas indicate that coupling is not a concern. However, further analysis is needed to rule it out completely as an important factor affecting pattern.

A dynamic input impedance matching is recommended for the required range of frequencies to obtain optimum performance of the station.

ACKNOWLEDGEMENT

The authors wish to acknowledge the support of Dr. S. Ellingson of Virginia Polytechnic Institute and State University, Dr. N. Kassim, Emil J. Polisensky, Ken Stewart and Henrique Schmitt of the Navy Research Laboratory in providing the measurement data needed for the analysis presented in this paper.

REFERENCES

[1] N. Paravastu, B. Hicks, P. Ray, and W. Erickson, “A New Candidate Active Antenna Design for the Long Wavelength Array”, *Long Wavelength Array Memo*, no. 88, May 2007.

[2] W. C. Erickson, “Tests on Large Blade Dipoles,” *Long Wavelength Array Memo*, no. 36, May 2006.

[3] Retrieved May 31, 2010, from http://lwa.nrl.navy.mil/.

[4] A. Kerkhoff, “The Calculation of Mutual Coupling between Two Antennas and its Application to the Reduction of Mutual Coupling Effects in a Pseudo-Random Phased Array,” *Long Wavelength Array Memo*, no. 103, August 2007.

[5] S. W. Ellingson, T. E. Clarke, A. Cohem, N. E. Kassim, Y. Pihlstrom, L. J Rickard, and G.B. Taylor, “The Long Wavelength Array (invited paper),” *Proc. IEEE*, vol. 97, no. 8, pp. 1421-1430, August 2009.

[6] C. Janes, J. Craig, and L. Rickard, “The Long Wavelength Array System Technical Requirements, Version: Draft #10,” *Long Wavelength Array Memo*, no. 160, Feb. 2009.

[7] B. Hicks et al., “Specmaster: A Simple Spectrum Monitoring Tool,” *Long Wavelength Array Memo*, no. 74, Jan 2007.

[8] T. E. Clarke, “Scientific Requirements for the

Long Wavelength Array," *Long Wavelength Array Memo*, no. 117, Nov. 19, 2007.

[9] W. N. Christiansen and J. A. Högbom, Radiotelescopes, Cambridge University Press, New York, 1969.

[10] L. Kogan and A. Cohen, "A 110 m x 100 m Elliptical Station Design Optimized to Minimize Sidelobes," *Long Wavelength Array Memo*, no. 150, Jan 8, 2009.

[11] P. Henning et.al, "The First Station of the Long Wavelength Array," *Long Wavelength Array Memo*, no. 171, August, 2010.

[12] A. Kerkhof and S. Ellingson, "A Wideband Planar Dipole Antenna for Use in the Long Wavelength Demonstrator Array (LWDA)," *Long Wavelength Array Memo*, no. 18, July 2005.

[13] B. Erickson, H. Schmitt, and E. Polisensky, "Report on Mutual Coupling and Impedance Measurements on Large Blade Dipoles," *Long Wavelength Array Memo*, no. 53, Aug. 2006.

[14] A. Kerkhoff, "Comparison of Dipole Antenna Designs for the LWA," *Long Wavelength Array Memo*, no. 102, Aug 2007.

[15] D. B. Davidson, *Computational Electromagnetics for RF and Microwave Engineering,* Cambridge University Press, New York, 2005.

[16] S. Ellingson, "A Design Study Comparing LWA Station Arrays Consisting of Thin Inverted-V Dipoles," *Long Wavelength Array Memo, no.* 75, January 2008.

Nassissie Fekadu received the B.Sc. degree in Electrical and Computer Engineering from Virginia Tech, Blacksburg, VA in 1999, and the M.S degree in Astronomy from San Diego State University, San Diego, CA in 2005. She is currently working on the Ph.D. degree at Virginia Tech, Falls Church, VA. From 1999-2002, she worked as an RF Engineer at MCI WorldCom Wireless Solutions (Reston, VA), Comsearch (Reston, VA), and Invertix Corporation (Annandale, VA). From 2005-2006 she was a Test and Commissioning Engineer for Andrew Corporation. From 2006-2007 she was a Senior Consultant with Booz-Allen Hamilton, McLean, VA. She has been with Noblis since 2007 as Senior Staff and works as a system engineer to provide technical support to the Federal Aviation Administration (FAA). Her research interests include antennas & propagation, radio astronomy, and wireless communications.

Amir I. Zaghloul is with Virginia Tech and the US Army Research Lab (ARL) on a joint research arrangement. He has been with the Bradley Department of Electrical and Computer Engineering at Virginia Tech since 2001, prior to which he was at COMSAT Laboratories for 24 years performing and directing R&D efforts on satellite communications and antennas. He is a Life Fellow of the IEEE, Fellow of the Applied Computational Electromagnetics Society (ACES), and Associate Fellow of The American Institute of Aeronautics and Astronautics (AIAA). He is a member of Commissions A, B, and Chair of Commission C of the US national Committee (USNC) of the International Union of Radio Science (URSI). He was the general chair of the 2005 "IEEE International Symposium on Antennas and Propagation and USNC/URSI Meeting," held in Washington, D.C., and served as an Ad Com member of the IEEE AP Society in 2006-2009. He also served on the IEEE Publication Services and Products Board and on the Editorial Board of "The Institute." He is a Distinguished Lecturer for the IEEE Sensors Council. He received several research and patent awards, including the Exceptional Patent Award at COMSAT and the 1986 Wheeler Prize Award for Best Application Paper in the IEEE Transactions on Antennas and Propagation.

Dr. Zaghloul received the Ph.D. and M.A.Sc. degrees from the University of Waterloo, Canada in 1973 and 1970, respectively, and the B.Sc. degree (Honors) from Cairo University, Egypt in 1965, all in Electrical Engineering.

Electromagnetic Launch Vehicle Fairing and Acoustic Blanket Model of Received Power using FEKO

Dawn H. Trout [1,2], James E. Stanley [2], and Parveen F. Wahid[1]

[1] Department of Electrical Engineering and Computer Science
University of Central Florida, Orlando, FL32816, USA
dawn.h.trout@knights.ucf.edu, Parveen.Wahid@ucf.edu

[2] Kennedy Space Center
KSC, FL 32899, USA
dawn.h.trout@nasa.gov
james.e.stanley@nasa.gov

***Abstract*─** Evaluating the impact of radio frequency transmission in vehicle fairings is important to electromagnetically sensitive spacecraft. This study employs the multilevel fast multipole method (MLFMM) from a commercial electromagnetic tool, FEKO, to model the fairing electromagnetic environment in the presence of an internal transmitter with improved accuracy over industry applied techniques. This fairing model includes material properties representative of acoustic blanketing commonly used in vehicles. Equivalent surface material models within FEKO were successfully applied to simulate the test case. Finally, a simplified model is presented using the Nicholson Ross Weir derived blanket material properties. These properties are implemented with the coated metal option to reduce the model to one layer within the accuracy of the original three layer simulation.

***Index Terms* ─** FEKO, MLFMM, Nicholson Ross Weir, resonant cavity.

I. INTRODUCTION

With multiple contributions from the range and surrounding radio frequency (rf) emitters, defining the electromagnetic environment for spacecraft can be a daunting task [1]. Determining the environment inside the vehicle fairing presents further challenges as field distribution within the cavity is influenced by resonances which require a full wave solution to achieve a desired accuracy. An added concern is that most spacecraft transmitters are in the GHz frequency range making the structures electrically large and memory requirements a constraint for many of the 3D electromagnetic simulation tools available. Recent research with hybrid physical optics and near-field to far-field transformations, as well as the use of parallelized fast multilevel codes with non-uniform rational B-spline surfaces, have had demonstrated success in modeling complex, electrically large structures [2-3]. This study is focused on solutions to electrically large internal cavity problems related to structures with layers of acoustic blanketing.

In this paper, two structural cases are evaluated: a three layer model, and a one layer model. The three layer model of a vehicle fairing with layered acoustic blanketing materials characterized by thin surface approximations is first presented [4]. For comparison and validation purposes the test case from [5] is summarized here and used as the evaluation data. Next, an equivalent one-layer model is developed using material properties predicted with S-parameters measurement and implemented into the FEKO standard coating option.

II. FAIRING FIXTURE

A fairing test fixture is shown in Figure 1. It is a scaled version with a height of 2 meters and a diameter of 0.6 meters and with industry grade

Submitted On: August 7, 2011
Accepted On: November 23, 2011

aluminum foil lining on the Lexan outer shell [6]. This fixture is representative of typical launch vehicles. The fairing has three sections bolted together and a metal frame outer support structure. Double ridge guide horns were used for transmit and receive and were placed at the bottom and top of the fairing fixture, respectively [7].

Lining materials were added to the inside of the test fixture to simulate typical acoustic blankets inside vehicle fairings. Kapton is commonly used in space applications for its favorable thermal insulating properties. DuPont's Kapton 160XC, designed to maintain a surface resistance of 377 ohms with inherent RF absorption properties, is utilized as the outer blanket layers while standard ½ inch foam is used as the internal layer.

The test results from this fairing fixture with acoustic blanketing are used for comparison with the three layer and one layer computational models presented here. The goal is to obtain an equivalent one layer model that has similar test data correlation as the three layer model.

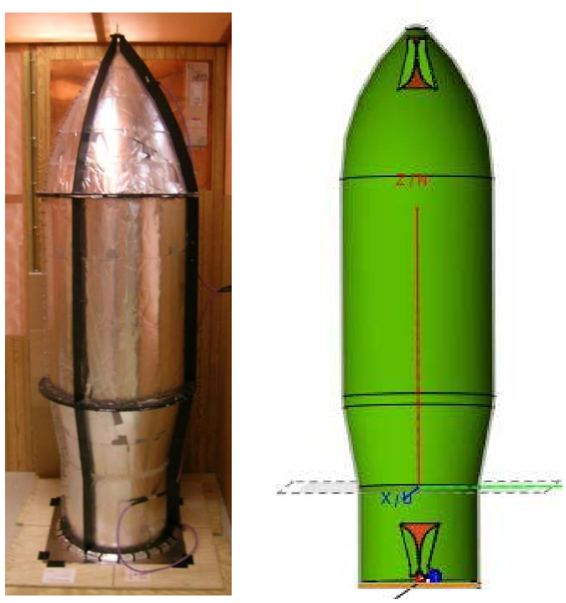

Fig. 1. Test fixture with CAD model.

III. THREE LAYER MODEL

A commercial computational electromagnetic software tool, EM Software Systems, FEKO is utilized in this study. The multilevel fast multipole method (MLFMM) feature is implemented to extend the method of moments (MoM) technique to higher frequencies. MoM is directly implemented for near elements and iterations are used to achieve the desired overall convergence criteria. Figure 2 demonstrates the adequacy of this approach for an aluminum cavity represented by an impedance sheet using both the MoM and MLFMM techniques. The field distribution and power received at 1 GHz using a surface impedance of 0.015 ohms reveals excellent agreement.

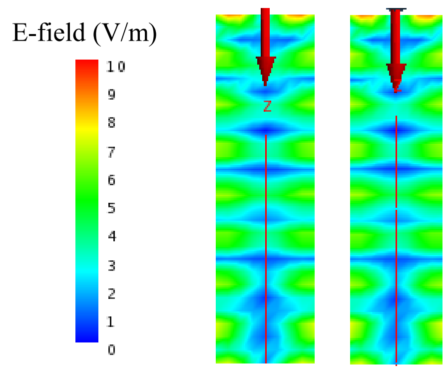

Fig. 2. Field distribution of an aluminum fairing using MLFMM (a) and MoM (b) techniques.

Comparable results were found with FEKO's lossy metal feature which has a similar implementation as the impedance sheet. FEKO evaluates the input material properties, such as permittivity and conductivity, to obtain a representative impedance term, Z_s, which is then added to the standard electric field integral equations used for perfect electric conductor (PEC) structures as in (1) [8, 9].

$$E_{s,tan} - Z_s J_s = -E_{i,tan}, \qquad (1)$$

where:

$\vec{E}_i$ is the field due to an impressed source in the absence of the scatterer, $\vec{E}_s$ is the scattered field, and J_s is the equivalent current density.

The double ridge guide horns were implemented in the simulation using antenna pattern models presented in [4] of the EMCO 3115 horn developed within FEKO. Replacing the horn model with the horn pattern affords a significant savings in computational resources. In addition, parallelization of the FEKO code via pre-conditioners, such as the sparse approximate inverse, supports solutions for detailed electrically large structures as those considered here. [10].

A combined blanketing and composite fairing structure model was presented in [11]. In this paper, it is desired to first represent the layers separately for direct test comparison. Figure 3 depicts the separate test fixture layers and the composite model used within FEKO.

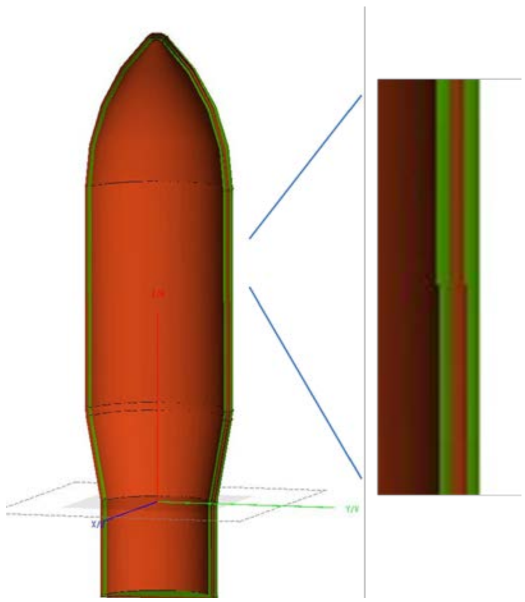

Fig. 3. FEKO model with acoustic blankets.

The aluminum foil outer layer and acoustic blanketing layers were represented within FEKO as described below:

- The fairing outer walls were represented as a single layer lossy metal with a thickness representing the industry aluminum foil that lined the prototype fairing (0.127 mm thick).
- The Kapton acoustic blanket sheets are modeled with a surface impedance based on industry data at the model frequency.
- The gaps between the impedance sheets represent the foam layer.
- Free space is required on both sides of the impedance sheet thus a thin layer of free space is implemented between the Kapton layer and the aluminum foil outer layer

Figure 4 shows a comparison of received power between the computational and the test results. The data compares well, with the average variation of 2.43 dB from test data. This is a reasonable result for a test article to model comparisons given uncaptured variations present in the test set-up. The selection of this frequency range is related to the waveguide measurements used in the equivalent one layer approach described in the following section.

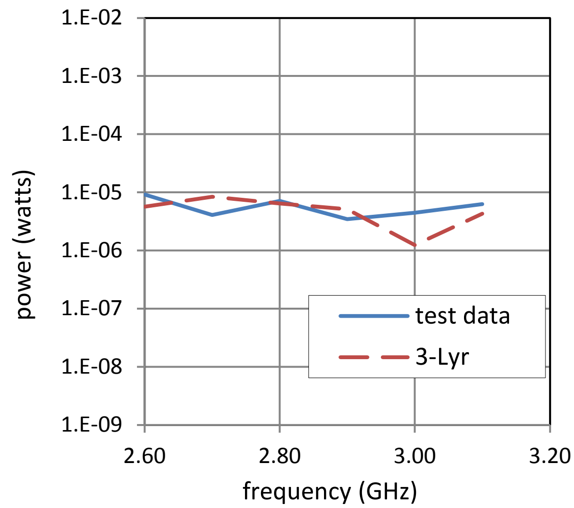

Fig. 4. Comparison of received power using computational and test results for the acoustic blanket model.

IV. EQUIVALENT ONE LAYER MODEL

It is desirable to further reduce the required computational resource and run-time requirements of the three layer structure with an electrically large cavity model and simulation by using an equivalent one layer model. Another reason to form a one layer equivalent model is the limited availability of vehicle CAD models with blanket configuration information. It should be noted that the following equivalent layer technique is not needed for simulating waveguide structures in general as there are finite element codes available that precisely model these layers and complex materials in such structures with no simplification [12-13]. This effort uses the waveguide equivalent model to later implement the layered material effects in the computationally intensive electrically large cavity structures where dimensions can be greater than 100 times the transmit wavelength and exact representation of blankets not feasible with existing software packages on available platforms.

A. Methodology selection

Truncation of the scalar Green's function implemented with the addition theory series in MLFMM introduces an error that can be controlled in open structures, but difficult to achieve sufficiently accurate results in electrically large reflective cavities [14]. This residual error can, in effect, numerically excite the cavity. Thus, convergence is improved by using layer representations that characterize the material absorption. The absorbing impedance sheets used in the three layer model require a layer of free space on either side; consequently, the one layer model requires a different material representation that can readily be combined with the metallic outer layer. The difficulty in representing the entire vehicle in one layer is the contrast between properties of the aluminum layer and that of the acoustic blankets. Accordingly, an option was used to apply the blanket properties as a coating to the metal outer layer. Material properties of the lossy metals and dielectrics are available in the FEKO material tree. Dielectrics can then be selected as a thin dielectric sheet (TDS) with specified thickness. The coatings were selected from the TDS single layer option. The TDS is implemented within FEKO in a similar way as the impedance sheet in (1) with the Z_s term described in given by [6].

$$Z_s = \frac{1}{j\omega(\varepsilon_2 - \varepsilon_1)\mathrm{d}} \,. \tag{2}$$

A TDS is required to be geometrically or electrically thin (approximately 1/10 the smallest element or wavelength, respectively). Due to the this requirement, an inherent limitation is often encountered in the computation when the automatic mesh routine generates fine elements to accurately characterize the respective geometries. However, if the coating is geometrically small with respect to the majority of the elements, the geometrically thin constraint driven by these fine elements is effectively ignored in the model solution. A FEKO utility will perform a validate check, and will return a solution with warnings only. It is also important to note that the electrically thin constraint is relative to a wavelength in the interfacing medium, but the layer does not have to be electrically small relative to a wavelength of the layer itself [9]. Nevertheless, it is often the situation that the actual thickness of the blankets cannot be represented in a coating, and an equivalent method must always be demonstrated and evaluated.

B. Sample S-parameter measurement

The one layer coating model constraint drives the need to alternately represent the three layer blanket model in a waveguide with a one layer TDS. The Nicholson Ross Weir (NRW) technique is used to derive an equivalent permittivity of the entire layered blanket using S-parameter measurements. A blanket sample was placed in an S-Band waveguide. The S-parameters were then measured with a vector network analyzer as in Fig. 5. These parameters are used in an equation to determine the transmission coefficient and then evaluated in expression (3) to obtain an approximate value of the equivalent permittivity of a homogenous sample with the same length. As most launch vehicle blanketing materials are non-magnetic, setting the permeability, μ_r, to one simplifies the permittivity determination. Moreover, the TDS implementation requires the permeability to be continuous with the surrounding media.

$$\varepsilon_r = \frac{\lambda_0^2}{\mu_r}\left(\frac{1}{\lambda_c^2} - \left[\frac{1}{2\pi L}\ln\left(\frac{1}{T}\right)\right]^2\right), \tag{3}$$

where: λ_0 is the freespace wavelength for the desired frequency, λ_c, is the waveguide cut-off wavelength, L is the sample length, and T is the transmission coefficient determined by the measured S-parameters [15].

Fig. 5. Material sample test fixture.

Determining the permittivity of a homogeneous sample using waveguide measurements and computational models has been verified as being effective in the literature [16]. In this paper, the NRW technique is used to determine a first level approximation of an equivalent permittivity that would apply to a dielectric block with the same measured S-parameters, although the sample itself is layered. Full wave analysis is then used to modify the permittivity at each frequency until a sufficiently close approximation of the S-parameters is found. This equivalent permittivity data is then used to construct the coating in the one layer model of the fairing.

C. Waveguide sample models

A three layer MoM model was first constructed in FEKO as shown in Fig. 6 to emulate the actual S parameter measurement set-up.

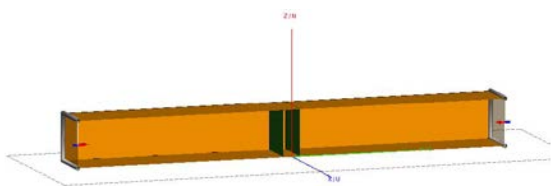

Fig 6. FEKO MoM model of a three layer fairing blanket sample.

The permittivity and conductivity of each Kapton layer was characterized as a dielectric with the thickness accounted for in the TDS implementation. The foam was represented by air as in the three layer fairing model.

It is straight forward to convert the separate layer model into a multilayer TDS which only uses one face in the geometry representation. However, the multilayer TDS cannot be represented as a coating to a metal. Hence, representation of the material in a single TDS is pursued.

The finite element method (FEM) was employed to verify that the NRW derived equivalent properties derived with (3) represent the S parameters when the waveguide is filled with a homogeneous dielectric block. The FEM model in Fig. 7 effectively reproduced the results as shown in Fig. 9 with some parameter optimization in the model. In this instance, the regions defining the boundary of the block are represented as the dielectric material and implemented with permittivity parameters with respective loss tangents.

The parameters were then implemented with a TDS single layer as shown in Fig. 8 for final implementation into the fairing fixture.

When meshing constraints require a reduced thickness in the TDS layer, a thinner layer can be established by changing the sample length in (3) to achieve a corresponding permittivity. Figure 9 shows a comparison of test, MoM separate layer model, FEM dielectric block model, and the final single layer TDS with original and reduced sample thicknesses. The material parameters can then be adjusted to provide a closer match to the original S_{21} measurements.

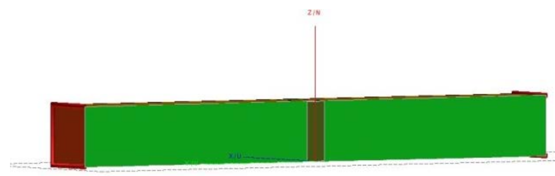

Fig. 7. Equivalent homogeneous dielectric block.

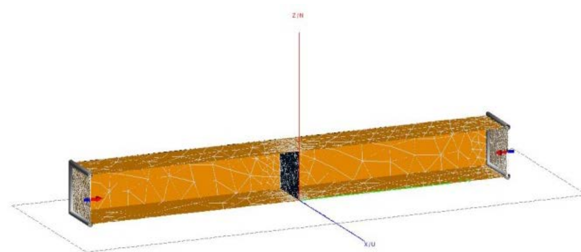

Fig. 8. TDS layer in waveguide.

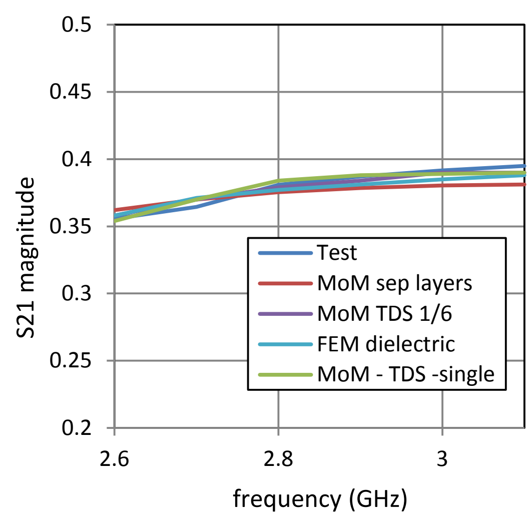

Fig. 9. Comparison of the waveguide S-parameter test data to the FEKO models.

D. Equivalent one-layer vehicle model

Results in Fig. 10 show that incorporation of the permittivity and loss tangent derived from the NRW waveguide technique into a TDS coating of a single metal layer in the vehicle model provides a reasonable correlation to the test data, as does the three layer model. First, the original sample thickness results are applied directly to the coating properties. Due to layer wavelength related constraints, however, the thickness of the coating is set at three skin depths of the Kapton layer. A closer approximation is achieved by using (3) to provide a different permittivity and loss tangent to correspond to a sample thickness adjusted to a smaller value. Results shown are for a TDS length of 1/6 of the original sample which varied from the test results an average of only 2.5 dB.

The upper and lower bounds represented in Fig. 10 are based on cavity Q equations for aluminum and blanketed walls [17].

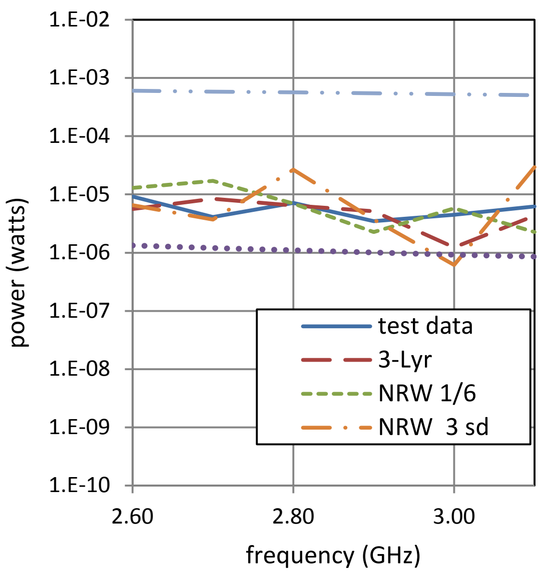

Fig. 10. Comparison of received power using the single layer and the three layer fairing models with the test data.

It is evident that the FEKO models provide significantly better results than approximation results that are generally relied upon. It should be noted that the primary intent of the Q related approximations are to evaluate chambers with very conductive walls with small absorbers present, but the application of these equations are often extended to cavities with more complex material configurations.

The efficiency benefits of using MLFMM in a three and one layer model as compared to MoM are shown in Table 1.

Table 1: Memory/run time comparison/2.6 GHz

Method	# Un - knowns	CPU Time/ process (hrs)	CPU Time total	Peak Memory (GB)
Mom 1 layer	124,377	21.2	339	115
MLFMM 3 layer	372,622	3.9	60.9	10
MLFMM 1 layer	124,377	0.066	1.1	2.2

V. CONCLUSION

This paper shows that fairing structures with complex blanketing materials can be modeled effectively with equivalent impedance techniques in a multilayer MLFMM model within the FEKO solution environment by establishing the eigenmodes within the cavity verses an average power approximation. This is important because quantifying fields due to transmission within a vehicle fairing has largely relied on general reverberation chamber average power approximation. The MLFMM more accurately depicts the actual RF energy within the cavity structure. The techniques explored here were the three layer and one layer models. From this data set, both methods appeared to have an improvement over the power approximation techniques for a launch vehicle with simulated acoustic blankets. The equivalent one-layer approach utilized a novel application of NRW formulations to derive an equivalent permittivity of the three layer configuration. Future work includes extending the frequency range beyond S-Band and the application of this technique to other layered materials such as composite vehicle structures.

REFERENCES

[1] R. Brewer and D. Trout, “Modern Spacecraft, Antique Specifications,” *2006 IEEE International Symposium on Electromagnetic Compatibility*, pp. 213-218, Aug, 2006.

[2] K. Bahadori and Y. Rahmat-Samii, “Estimation of blockage effects of complex structures on the performance of the spacecraft reflector antennas by a hybrid PO/NF-FF Method,” *Applied Computational Electromagnetic Society (ACES) Journal*, March 2007, vol. 22, no. 1, pp. 31-38.

[3] I. Gonzalez, E. Garcia, F. Saez de Adana, and M. F. Catedra, “MONURBS: A Parallelized Fast

Multipole Multilevel Code for Analyzing Complex Bodies Modeled by NURBS Surfaces," *Applied Computational Electromagnetic Society (ACES) Journal*, January 2008, vol. 23, no. 2, pp. 134-142.

[4] D. H. Trout, J . E. Stanley, and P. F. Wahid, "Electromagnetic Launch Vehicle Fairing and Acoustic Blanket Model of Received Power using FEKO," ACES Conference, March 2011.

[5] D. H. Trout, P. F. Wahid, and J. E. Stanley, "Electromagnetic Cavity Effects from Transmitters Inside a Launch Vehicle Fairing," IEEE EMC Symposium Austin: IEEE, 2009, in *Proc of IEEE EMC Symp. on EMC*, Austin, 2009, pp. 70-74.

[6] M. Kandula, K. Hammad, and P. Schallhorn, "CFD Validation with LDV Test Data for Payload/Fairing Internal Flow," *Proc. AIAA*, 2005-4910-9151.

[7] ETS Lindgren Website on double ridged waveguide horn, EMCO 3115, User Manual. [Online]. Available: http://www.ets-lindgren.com/manuals/3115.pdf.

[8] FEKO User's Manual, July 2008.

[9] U. Jakobus, "Comparison of Different Techniques for the Treatment of Lossy Dielectric/Magnetic Bodies within the Method of Moments Formulation," *AE¨U International Journal of Electronics and Communications*, 2000, iss. 3, vol. 54, pp. 163-173.

[10] U. Jakobus, J. Tonder, and M. Schoeman, "Advanced EMC Modeling by Means of a Parallel MLFMM and Coupling Network Theory," IEEE Internaltion Symposium on EMC, August 2008, pp. 1-5.

[11] J . E. Stanley, D. H. Trout, S. K. Earles, I. N. Kostanic, and P F. Wahid, "Analysis of Multi-Layer Composite Cavity Using FEKO," *Applied Computational Electromagnetic Society (ACES) Journal*, January 2010, iss. 1, vol. 25, pp. 69-74.

[12] Y. Tsunemitsu, J. Hirokawa, M. Ando, Y. Miura, Y. Kazama, and N. Goto, "Polarization Isolation Characteristics Between Two Center-Feed Single-Layer Waveguide Arrays Arranged Side-by-Side," *Applied Computational Electromagnetic Society (ACES) Journal*, November 2006, vol. 25, no. 3, pp. 240-247.

[13] S. D. Keller, "Coplanar Waveguide Slot-coupled Ka-band Patch Antenna for Integration with Wafer-scale Beam-steering MEMS Control Board," *Applied Computational Electromagnetic Society (ACES) Journal*, June 2008, vol. 23, no. 2, pp. 177-183.

[14] W. C. Chew, J. M. Jin, E. Michielssen, and J. Song, *Fast and Efficient Algorithms in Computational Electromagnetics*, Artech House, Inc., Norwood, MA, 2001.

[15] Rhode & Schwarz, *Measurement of dielectric material properties.* s.l.: Application Center Asia/Pacific, 2006. RAC0607-0019.

[16] M. D. Deshpande and C. J. Reddy, "Application of FEM to Estimate Complex Permittivity of Dielectric Material at Microwave Frequency using Waveguide Measurements," NASA, Langley Research Center, 1995.

[17] D. A. Hill, M. T. Ma, A. R. Ondrejka, B. F. Riddle, M. L. Crawford, and R. T. Jonk, "Aperture Excitation of Electrically Large, Lossy Cavities," *IEEE Trans. Electromagn. Compat.*, vol. 36, no. 3, pp. 169–177, Aug. 1994.

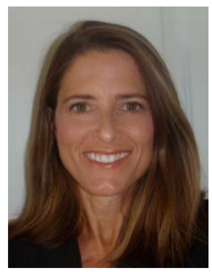

Dawn H. Trout (M'95) has been a member of IEEE since 1995. She received her B.S. degree in Electrical Engineering from Memphis State University in 1989 and her Masters in Electrical Engineering from the University of Alabama in Huntsville in 1995. She is currently pursuing her Ph.D. in Electrical Engineering at University of Central Florida through the Kennedy Space Center Graduate Fellowship Program.

She has worked at NASA in the area of electromagnetic compatibility for twenty years. She has served as lead of electromagnetic teams at Marshall Space Flight Center in Alabama and at Kennedy Space Center in Florida. She has initiated multiple electromagnetic related studies in her career and her current research interests include electromagnetic fields in large composite cavities and indirect lightning effects.

Ms. Trout has served on multiple EMC standards committees and led the development of ISO 14302, Electromagnetic Compatibility, Space Systems Standard for which she received an AIAA award.

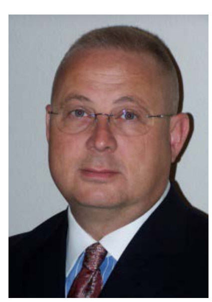

Dr. James E. Stanley (M'87) has been a member of IEEE since 1987. He received his B.E.E. from Auburn University in 1988 and his Masters of Science in Engineering (Electrical Engineering) from Mercer University in 1997. He received his Ph.D. in Electrical Engineering from the Florida Institute of Technology in 2010.

He has worked in DoD on multiple airframes and subsystems. After moving to the commercial sector with General Electric and communication companies, he is contributing to the Qinetiq-North America team as a NASA contractor. For the last five years, he has been the lead in electromagnetic analysis for the Kennedy Space Center Launch Services Program. He has received numerous commendations for bringing the Electromagnetic Compatibility Team from a purely back-of-the-envelope approach to one with intensive numerical analytical analysis capability. His skills are increasingly in demand to evaluate mission integration issues with antennas in cavities. He has done extensive research on layered materials and modeling these layers with impedance sheets. He also has expertise in developing computer systems and writing electromagnetic modeling codes.

Dr. PARVEEN F. WAHID received her B.S. degree in Mathematics and Physics in 1969, her M.S. degree in Physics from the University of Mysore, India in 1971 and her Ph.D. in Electrical Communication Engineering from the Indian Institute of Science, India, in 1979.

She was a Research Associate at the Electrical Engineering Department, University of Utah from 1980-1982 and at the Electrical Engineering Department, University of Nebraska, Lincoln from 1982-1983. Since 1984, she has been with the University of Central Florida, where she is now a Professor in the department of Electrical Engineering. She teaches electromagnetics, antenna theory and design, and microwave engineering courses. Her research interests are in the area of the design of microstrip antennas and arrays and adaptive arrays for wireless applications and she has over 50 technical publications.

In 1989, Dr. Wahid was named the Tau Beta Pi Professor of the Year. She received the College of Engineering Excellence in Teaching Award in 1994 and 1999. In 1991, she received the University of Central Florida Excellence in Advising Award and in 1997, the University of Central Florida Excellence in Professional Service Award. In 2000, she was awarded the IEEE Region 3 Outstanding Engineer Educator Award and the IEEE Florida Council Outstanding Educator Award. She is a recipient of the IEEE Millennium Award. She was the Technical Program Chair for the 1999 IEEE International AP/URSI symposium and the General Chair for the 1998 IEEE Region 3 Southeastcon conference. She has served many times on the technical program committee for the IEEE AP/URSI conferences. Dr. Wahid is a Senior Member of the IEEE and a member of the Eta Kappa Nu and the Tau Beta Pi Societies.

Evaluation of Lightning Induced Effects in a Graphite Composite Fairing Structure

Dawn H. Trout [1,2], James E. Stanley [2], and Parveen F. Wahid[1]

[1] Department of Electrical Engineering and Computer Science
University of Central Florida, Orlando, FL32816, USA
dawn.h.trout@knights.ucf.edu, Parveen.Wahid@ucf.edu

[2] Kennedy Space Center
KSC, FL 32899, USA
dawn.h.trout@nasa.gov
james.e.stanley@nasa.gov

Abstract ─ Defining the electromagnetic environment inside a graphite composite fairing due to near-by lightning strikes is of interest to spacecraft developers. This effort develops a transmission-line-matrix (TLM) model with CST Microstripes to examine induced voltages on interior wire loops in a composite fairing due to a simulated near-by lightning strike. A physical vehicle-like composite fairing test fixture is constructed to anchor a TLM model in the time domain and a FEKO method of moments model in the frequency domain. Results show that a typical graphite composite fairing provides attenuation resulting in a significant reduction in induced voltages on high impedance circuits despite minimal attenuation of peak magnetic fields propagating through space in near-by lightning strike conditions.

Index Terms ─ Composite, Lightning, Magnetic, Method of Moments, Shielding, Transmission Line Method.

I. INTRODUCTION

A. Background

Direct strike lightning effects have been thoroughly evaluated for composite aircraft structures [1]. In the space industry, launch commit criteria and ground protection systems such as catenary wires shift the focus for launch vehicle protection to indirect effects from a near-by strike. Note that the use of the term indirect effects based on a nearby strike is different than that of the aircraft industry where the effects on internal circuitry from a strike to the airframe is indicated [2]. Aircraft avionics are typically hardened to this environment, but such hardening is not characteristic of typical spacecraft systems that are sensitive by design. Much work in the launch vehicle industry has concentrated on lightning coupling analysis of the large umbilical cable connecting ground support equipment to vehicle/spacecraft power and data circuits as illustrated in Fig. 1. Accordingly, any protection of spacecraft afforded by the composite structure is not well characterized [3].

Minimal shield transfer impedance is required to reduce the common mode coupling to a differential circuit [1]. When design criteria constraints prohibit adequate shielding, voltages induced into sensitive circuitry are primarily driven by the loop area, magnetic field amplitude, and the transient rise time. Thermal constraints can also limit the application of wire twisting, which makes the cancellation of the magnetic field via loop area reduction impractical.

In the event of a near-by lightning strike the spacecraft system must evaluate the retest criteria. This retest criteria is important because only minimal on-pad testing is possible due to limited interface controls. Triggering of this criteria can lead to payload destack and return to processing facilities where mission specific testing can ensue.

Submitted On: August 6, 2011
Accepted On: January 23, 2012

False indications of this trigger based on the assumption of zero shielding in composite fairings is costly from a budget and schedule standpoint. Albeit, the consequences of unneccessary retest are severe, the repercussions of an undetected failure are irreversible. As there is no possibility to retrieve a payload on orbit, a conservative, yet easily implementable prediction of attenuation of indirect lightning effects is desired.

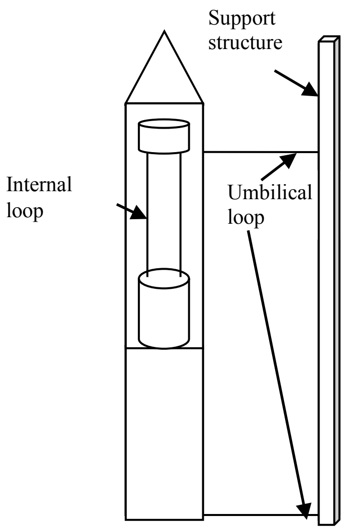

Fig. 1. Launch vehicle and umbilical tower.

B. Lightning Induced Effects

The time varying magnetic and electric fields lead to induced voltages and currents in vehicle and spacecraft circuitry. The governing equation used to approximate the magnetic field from a nearby lighting strike ignoring ohmic losses is given by

$$\oint H \cdot dl = I_i + I_d$$
$$= \iint_A J_i \cdot da + \iint_A \frac{\partial}{\partial t}(\varepsilon_0 E) da$$
$$\begin{aligned} &Where: \\ &E, H = Electric\ and\ magnetic\ fields, \\ &A, l = loop\ area\ and\ length, \\ &I, J = current\ and\ current\ density, \\ &\varepsilon_0 = permittivity\ of\ free\ space, and \\ &i, d = lightning\ source\ and\ displacement. \end{aligned} \tag{1}$$

MIL-STD-464 gives the change in the electric field contributed by a near lightning strike 10 m away as 6.8 x 10^{11} volts/meter/second (V/m/s) [4]. Assuming a reasonable worst case circuit area, A, of 4 m x 0.05 m = 0.2 m^2, the contributing portion of the magnetic field due to the displacement current (I_d) is 1.2 A/m [1]. This displacement current is relatively insignificant compared to the contribution of the lightning channel, allowing the magnetostatics assumptions to be applied [1], [5,6]. Hence, an approximation of the magnetic field simplifies to $I_i/(2\pi r)$, where r is the distance from the strike and $2\pi r$ represents the circumference of the circle with radius, r. For instance, a 50 kA strike at 10 meters would contribute a magnetic field of 795 (amperes/meter) A/m. To determine the induced voltage that arises due to a lightning related magnetic field, the rise time is key as depicted in (2). This rise time varies from 1.4 μs to 50 ns depending on which component of lightning is active (initial severe stroke, return stroke, multiple stroke, or multiple burst). For most launch sites, the range data includes strike magnitude and location (within a 250 to 500m accuracy), but does not include rise time information. MIL-STD-464 [4] reports the change of magnetic field with respect to time for a near lightning strike 10 m away as 2.2 x 10^9 A/m/s and using this, we get

$$\begin{aligned} &Max\, V_{oc} = \frac{d(\mu_0 \mathrm{HA})}{\mathrm{dt}} = \mu(2.2\times10^9)(0.2) = 552.9V \\ &Where: \\ &\mu_0 = free\, space\ permeability = 4\pi\times10^{-7}\ H/m. \end{aligned} \tag{2}$$

The differential circuit voltage will be less than predicted by (2) due to actual circuit impedances and common mode rejection; however, the remaining voltage is undesirable for most spacecraft instrumentation cirucuits. Spacecraft retest criteria of 10 – 50 volts is common; however, lower sensitivities have been reported by design constrained spacecraft payloads.

C. Motivation

Test data and two-dimensional numerical models presented in the literature for a single composite panel in otherwise conductive enclosures, show greater than 40 dB reduction in dB/dt levels with a composite panel as compared to a fiberglass panel when a nearby transient lightning pulse is simulated [7-9]. The diffusion of direct strikes through composite walls is addressed in evaluation of composite aircraft in [1]. Spacecraft developers and launch vehicle providers have questioned the applicability of panel only studies to the launch vehicle fairing structure. In this study the attenuation of a composite graphite fairing-like structure to the induced effects of nearby lighting strikes is addressed. A physical fairing fixture model is built and test validation is performed as a baseline for the model. Both frequency and time domain testing are performed to anchor the model.

II. FAIRING MODEL

A. Test Fixture

The scaled fairing fixture model shown in Fig. 2 and used for all simulations in this work is ½ to $^1/_7$ the size of typical launch vehicles. The 1.8 m by 0.6 m fairing fixture is made of two composite fairing halves with tabs at the edges for clamping the fairing enclosure. Two 1 mm 4 ply layers of carbon composite material sandwich a 6.35 mm Rohacell®WF foam core. Rohacell®WF is a closed-cell rigid foam based on polymethacrylimide chemistry, which does not contain any carbon fiber composites (CFC's) and is often utilized in manufacturing advanced composites for aerospace applications [10]. The surface resistivity was measured as 161 mohms. The composite fairing structure was grounded via a metallic flat plate which interfaced with the bottom edges of the fixture.

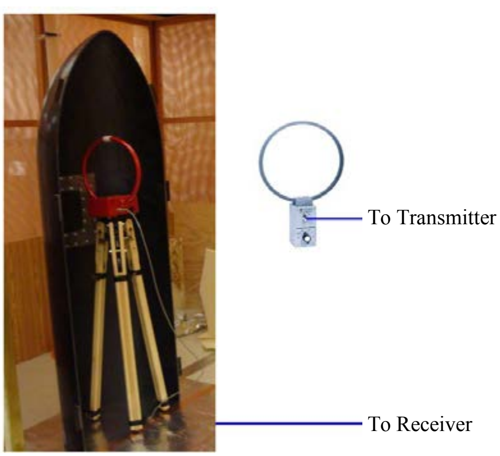

Fig. 2. Test fixture.

B. Composite Structure Model

Modeling the layers of the composite fairing individually requires the mesh to be small with respect to the thickness of each layer and is computationally prohibitive with respect to the entire model size. However, although CFC structures are inhomogeneous and tensor formation of permittivity and permeability are needed for accurate representation of electromagnetic shielding, the frequency range of lightning is generally below the interlayer resonance of composite structures, allowing an effective one layer representation of the composite fairing [11,12]. Literature supports modeling composite materials as a single layer if the period of the structure is small with respect to wavelength [11]. This criterion is clearly met with a thin structure and lightning frequency content below 30 MHz [1]. Several composite builds can effectively be modeled as one layer into the GHz frequency range [11]. Each composite 4 ply build was represented as an electromagnetically penetrable thin film with conductivity parameters developed from surface resistivity measurements [13].

In addition, composite material is not uniform in all directions; hence, the volume conductivity cannot entirely be determined from the surface conductivity and thickness. However, if there are several layers of composite materials, then multiple orientations of the fibers will exist allowing the standard volume resistivity calculated from surface resistance to approximate the actual conductivity of the structure [14]. The conductivity for the graphite composite layer was modeled with the uniform material assumption and calculated using (3) shown below

$$\sigma = \frac{1}{\rho}, \quad \rho = R_s t,$$

$$\sigma = \frac{1}{(161 mohm)(1 mm)} = 6211\, s/m \tag{3}$$

Where:

σ = *conductivity in s/m,*

ρ = *volume resistivity,*

R_s = *surface resistivity, and*

t = *thickness.*

III. MODEL CHARACTERIZATION

Before examining the induced voltages with precise industry lightning models, a characterization of the composite structure was performed with a lab implementable test set-up. The thin layer approach to model the composite fairing was anchored with test data in both the frequency and time domain.

A. Frequency domain

Initially, an industry standard magnetic shielding test was performed [15]. The test set-up was then simulated in the frequency domain using the method of moments (MoM) solver in the electromagnetic simulation software, EM Software & System's FEKO [16], and an imported Pro-E fairing model. Although time domain computational methods dominate lightning related literature, use of the MoM with post-processing has been shown effective [17]. The equivalent layer model was implemented with an infinitely thin impedance sheet based on the direct surface impedance measurement. The impedance sheet represents the relationship between the tangential electric field on the surface and the electric surface current [18].

For both the modeling and test, a sensor is placed 1 meter high in the center of the fairing (see Fig. 2). The baseline case is obtained from measurements with no fairing in place. A small loop was used to provide external excitation and internal sensing at specific frequencies.

Both test and simulation results, shown in Table 1, indicate an increase in magnetic field shielding effectiveness with increasing frequency upto 10 MHz.

Table 1: Frequency domain shielding comparisons

Frequency	Shielding Effectiveness (Test Data) dB	Shielding Effectiveness (Model Data) dB	Difference dB
150 kHz	2	0.9	1.1
300 kHz	5	0.8	4.2
2 MHz	11	10	1
5MHz	17	19.5	2.5
10 MHz	21	21.9	0.9

B. Time Domain

Given the limited frequency content in lightning transient pulses, the TLM tool in CST Microstripes is optimally applied for this electrically small structure. Adaptations can be made to the TLM process to account for edge effects, especially for higher frequency applications [19]. TLM divides the physical space into circuits that can be solved for voltages and currents that are related to fields through analogies to Maxwell's equations [20]. The current source is proximally placed with respect to the composite fairing structure to represent a low impedance magnetic field associated with near field conditions and thus worst case (minimal) shielding of the composite fairing structure. The distal leg of current loop is selected as far as possible away from the fairing in order to limit field cancellation effects as shown in Fig. 3 [13].

The transient source was implemented with a 2 m square PVC structure supporting a 16 gauge wire. An Electrometrics, EM 3410, spike generator was placed at the base of the structure to drive a 10 μsec pulse into the loop. The closest side of the loop was placed 0.5 meters from the fairing, as depicted in the model shown in Fig. 3. This transient current loop was selected rather than a high voltage source for feasibility of implementation in the laboratory setting.

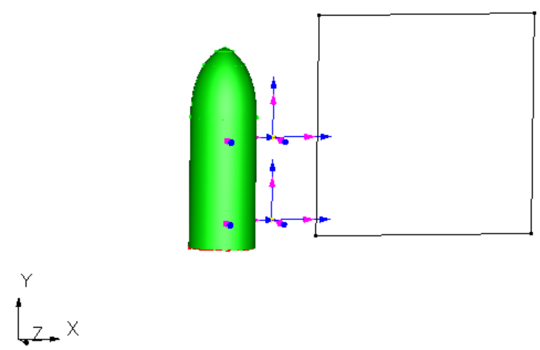

Fig. 3. Laboratory and simulation set-up.

A B-dot sensor (ELGAL MDM-0) was employed in conjunction with a digital oscilloscope, to measure the change in magnetic field with respect to time in the test case. For simulation, this change was determined by examining the time response of the magnetic field data. The baseline comparison case is obtained from measurements with no fairing in place.

The current source in the model was designed to closely characterize the transient generator pulse that could be implemented with a spike generator into an inductive loop. The laboratory loop was modeled with a 10 ohm load impedance to partially account for the inductance created by the loop. A 100 volt transient pulse source was applied to a loop with a wire conductivity of 5.87×10^7 s/m and a radius of 0.15 cm.

The difference in the change in magnetic field with respect to time with and without the fairing was 8.06 dB in simulation and 7.4 dB in test, revealing model and test case agreement.

IV. INDUCED EFFECTS MODEL

First, to represent a nearby lighting strike, a 1MV/1Mohm source at the top of a 30 foot long simulated lightning channel was substituted for the loop in the model characterization phase as shown in Fig. 4 [21]. To reduce electric field contributions, the source was shielded with a graphite epoxy box as in [21].

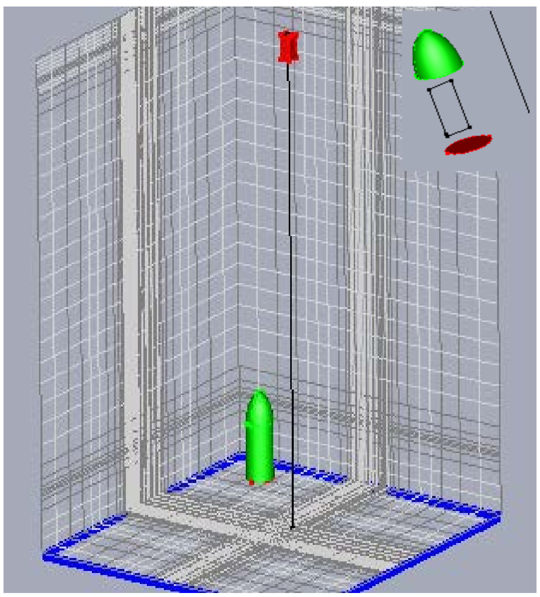

Fig. 4. Composite vehicle with a simulated lightning strike.

The source was driven by the double exponential source characteristics given in (4) which are based on MIL-STD-464 [4].

$$i(t) = I_0(e^{-\alpha t} - e^{-\beta t}) \quad (4)$$

Where: $I_0 = 218{,}810$ A, $\alpha = 11{,}354$ s^{-1}, and $\beta = 647{,}265$ s^{-1} .

The TLM model frequency span is set to 20 MHz for broad band evaluations, and the structure mesh size is driven by this frequency. The run time duration is extended beyond the default settings to account for the total waveform time.

In addition, a loop was added in the simulated vehicle to examine currents and voltages on low and high impedance circuitry with respect to magnetic field peak reduction. The emphasis of this paper is the composite fairing attenuation of induced lightning effects. More detailed studies of the lightning induced effects related to loop ground and termination impedances, loop height above ground, and structure surge impedance modeling can be found in recent studies [22-23].

V. RESULTS

Figure 5 depicts the low resistance circuit response excited by a simulated nearby (1 m away) lightning strike with and without a composite fairing surrounding the loop.

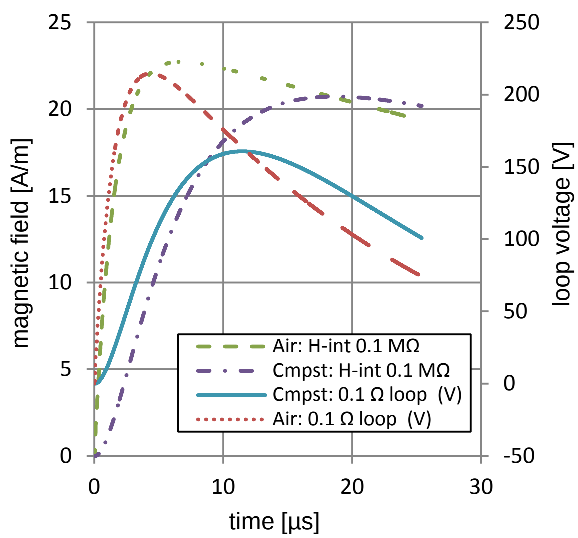

Fig. 5. Composite fairing to air comparison with low impedance loop coupling.

Figure 6 indicates the high impedance circuit response for the same case. Although peak magnetic field coupling is similar with and without the fairing in place, the rise time is longer with the fairing in place leading to lower induced voltages in interior circuits. As evident in (2), Fig. 6 reveals a much sharper peak in induced voltage for the air (no-fairing) case due to the derivative relationship between this voltage and the magnetic field rise time. When the coupled voltage is dominant, as in high impedance circuits, the variation in induced effects is influenced by the diffusion process which slows the rise of the magnetic field [24]. The effect is much less dominant in the low impedance circuit.

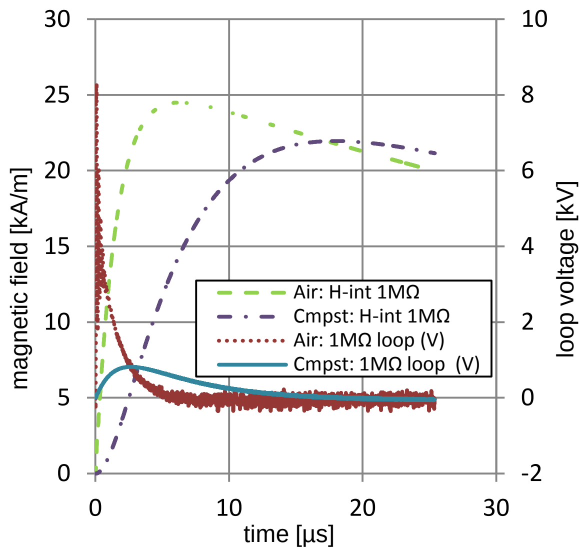

Fig. 6. Composite fairing to air comparison with high impedance loop coupling.

Table 2 provides the composite fairing attenuation effects on magnetic field and coupled loop voltage. It also includes the effects of source distance on the internal magnetic field and the coupled voltages.

Table 2: Comparison of fairing attenuation of induced effects for varying internal loop impedance and distance from source

Loop Impedance Ohms	0.1	1M			
Distance (m)	1	1	3	10	Plane Wave
Induced Voltage Attenuation (dB)	1.5	20.1	20	18.22	31
Magnetic Field Attenuation (dB)	0.8	1.04	.93	1.06	0.87

The plane wave case provides the greatest attenuation due to the higher source impedance of the field with respect to the composite structures. Nevertheless, significant attenuation of induced voltage in the high impedance loop is achieved at close distances where the source impedance is lower than a plane wave.

VI. CONCLUSION

The results presented show that the TLM thin film modeling of the composite structure is effective for the evaluation of attenuation from frequency based and transient based magnetic fields.

The model was modified to align with the industry approach for lightning induced electromagnetic effects. Results shown indicate a typical graphite composite fairing provides significant reduction in induced voltages on high impedance circuits despite minimal attenuation of peak magnetic fields. The energy in the pulse is spread by the diffusion process through the composite material. This spreading slows the incident pulse rise time which in turn reduces the coupling to the circuit.

This study provides a good insight into the differences between literature that specifies attenuation of lightning induced effects and account for any lightning related attenuation for composite structures. The data from this effort is useful for evaluating spacecraft/launch vehicle destack criteria.

ACKNOWLEDGMENT

The ingenuity of Dr. Ellen Lackey and Dr. Elliott Hutchcraft from University of Mississippi who developed this low cost composite fairing was essential in this task.

REFERENCES

[1] F. A. Fisher, R.A. Perala, J. A. Plumer, *Lightning Protection of Aircraft*, Lightning Technologies Inc., 1990, pp. 306-331.

[2] M. Apra, M. D'Amore, K. Gigliotti, M.S. Sarto, and V. Volpi, "Lightning Indirect Effects Certification of a Transport Aircraft by Numerical Simulation," *Electromagnetic Compatibility, IEEE Transactions on*, vol. 50, no.3, pp.513-523, Aug. 2008.

[3] D. H. Trout, J. E. Stanley, and P. F. Wahid, "Evaluation of lightning induced effects in a graphite fairing composite structure (Parts 1 and 2), Annual Review of Progress in Applied Computation Electromagnetics, March 2011.

[4] *Electromagnetic Environmental Effects Requirements for Systems*, Mil-Std-464, Department of Defense, December 2010.

[5] V.A. Rakov, M.A. Uman, *Lightning Physics and Effect,* Cambridge University Press, 2003.

[6] C. A. Balanis, *Advanced Engineering Electromagnetics,* John Wiley and Sons, New York, 1989.

[7] R.W. Evans, *NASA Contractor Report 4783, Test Report – Direct and Indirect Lightning Effects on Composite Materials*, Space Environment Effects Program, July 1997.

[8] M. S. Sarto, "A new model for the FDTD analysis of shielding performance of composite structures," *IEEE Transactions on EMC*, vol. 41, no. 4, pp. 298-306, Nov. 1999.

[9] M. S. Sarto, "Hybrid MFIE/FDTD analysis of the shielding effectiveness of a composite enclosure excited by a transient plane wave," *IEEE Trans. on Magnetics,* vol. 36, no. 4, pp. 946-950, July 2000.

[10] J. Stanley, *Indirect Lightning Effects Analysis for A Graphite Composite Structure*," Center Director Discretionary Fund Report, Analex Corporation, Sep. 2009.

[11] C. L. Holloway, M. S. Sarto, and M. Johansson, "Analyzing carbon-fiber composite materials with equivalent-layer models," *IEEE Trans. on EMC*, vol. 47, no. 4, pp. 833 – 844, Nov. 2005.

[12] J. E. Stanley, D. H. Trout, S. K. Earles, I. N. Kostanic, and P. F. Wahid, "Analysis of multi-layer composite cavity using FEKO," 25th Annual Review of Progress in Applied Computation Electromagnetics, pp. 643-647, March 8-12, 2009.

[13] *CST Microstripes Reference Manual*, CST Computer Simulation Technology AG, 2009.

[14] R.W. Evans, *Design Guidelines for Shielding Effectiveness, Current Carrying Capability and the Enhancement of Conductivity of Composite Materials,* NASA Contractor Report 4784, Space Environment Effects Program, August 1997.

[15] *IEEE Standard Method for Measuring the Effectiveness of Electromagnetic Shielding Enclosures*, IEEE STD 299, 2006.

[16] FEKO Quarterly, Field computations involving objects of arbitrary shape, March 2005.

[17] M. O. Goni, M. S. I. Hossaini, "Numerical Electromagnetic Analysis of GSM Tower under the Influence of Lightning Over-voltage," *Applied Computational Electromagnetics Society (ACES) Journal,* vol. 24, no. 3, pp. 344 – 351, June 2009.

[18] FEKO User's Manual, July 2008.

[19] M. Rajabi, N. Komjani, "Improvement of Transmission Line Matrix Method Algorithm Frequency Response Based on Modification of Cell Impedance," *Applied Computational Electromagnetics Society (ACES) Journal,* vol. 26, no. 4, pp. 319 – 324, April 2011.

[20] M. N.O. Sadiku, *Numerical Techniques in Electromagnetics, Second Edition*, pp. 467-529, CRC Press, Boca Raton, FL, 2001.

[21] C. Baldwin, "Full-wave EM modeling and test verification in aerospace applications," *IEEE EMC Symposium*, MO-PM-1-2, Austin, TX, August 17-21, 2009.

[22] M. O. Goni, E. Kaneko, A. Ametani, "Simulation of Lightning Return Stroke Currents and Its Effect to Nearby Overhead Conductor," *Applied Computational Electromagnetics Society (ACES) Journal,* vol. 24, no. 5, pp. 469 – 477, October 2009.

[23] M. O. Goni, A. Ametani, "Analysis and Estimation of Surge Impedance of Tower," *Applied Computational Electromagnetics Society (ACES) Journal,* vol. 24, no. 1, pp. 72 – 78, February 2009.

[24] F. M. Tesche, M. Ianoz, and T. Karlsson, *EMC Analysis Methods and Computational Models*, John Wiley and Sons, Dec. 1996, pp. 510-535.

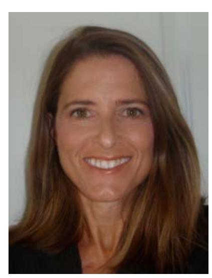

Dawn H. Trout (M'95) has been a member of IEEE since 1995. She received her B.S.E.E from Memphis State University in 1989 and her Masters in Electrical Engineering from the University of Alabama in Huntsville in 1995. She is currently pursuing her PhD in Electrical Engineering at University of Central Florida through the Kennedy Space Center Graduate Fellowship Program.

In her twenty years at NASA, she has served as lead of electromagnetic teams at Marshall Space Flight Center in Alabama and at Kennedy Space Center in Florida. She has initiated multiple electromagnetic related studies in her career and her current research interests include electromagnetic fields in large composite cavities and indirect lighting effects. She has also served on multiple EMC standards committees and led the development of an EMC Space Systems Standard for which she received an AIAA award.

James E. Stanley (M'87) has been a member of IEEE since 1987. He received his B.E.E. from Auburn University in 1988 and his Masters of Science in Engineering (Electrical Engineering) from Mercer University in 1997. He received his Ph.D. in Electrical Engineering from the Florida Institute of Technology in 2010.

He has worked in DoD on multiple airframes and subsystems. After moving to the commercial sector with General Electric and communication companies, he is contributing to the Qinetiq-North America team as a NASA contractor. For the last five years he has been the lead in electromagnetic analysis for the Kennedy Space Center Launch Services Program. He has received numerous commendations for bringing the Electromagnetic Compatibility Team from a purely back-of-the-envelope approach to one with intensive numerical analytical analysis capability. His skills are increasingly in demand to evaluate mission integration issues with antennas in cavities. He has done extensive research on layered materials and modeling these layers with impedance sheets. He also has expertise in developing computer systems and writing electromagnetic modeling codes.

Parveen F. Wahid received her B.S. degree in Mathematics and Physics in 1969, her M.S. degree in Physics from the University of Mysore, India in 1971 and her Ph.D. in Electrical Communication Engineering from the Indian Institute of Science, India, in 1979. She was a Research Associate at the Electrical Engineering Department, University of Utah from 1980-1982 and at the Electrical Engineering Department, University of Nebraska, Lincoln from 1982-1983. Since 1984 she has been with the University of Central Florida, where she is now a Professor in the department of Electrical Engineering. She teaches electromagnetics, antenna theory and design and microwave engineering courses. Her research interests are in the area of the design of microstrip antennas and arrays and adaptive arrays for wireless applications and she has over 50 technical publications.

In 1989 Dr. Wahid was named the Tau Beta Pi Professor of the Year. She received the College of Engineering Excellence in Teaching Award in 1994 and 1999. In 1991 she received the University of Central Florida Excellence in Advising Award and in 1997 the University of Central Florida Excellence in Professional Service Award In 2000 she was awarded the IEEE Region 3 Outstanding Engineer Educator Award and the IEEE Florida Council Outstanding Educator Award. She is a recipient of the IEEE Millennium Award. She was the Technical Program Chair for the 1999 IEEE International AP/URSI symposium and the General Chair for the 1998 IEEE Region 3 Southeastcon conference. She has served many times on the technical program committee for the IEEE AP/URSI conferences. Dr. Wahid is a Senior Member of the IEEE and a member of the Eta Kappa Nu and the Tau Beta Pi Societies.

Analysis of Transient Electromagnetic Scattering from an Overfilled Cavity Embedded in an Impedance Ground Plane

Robert S. Callihan and Aihua W. Wood

Department of Mathematics and Statistics
Air Force Institute of Technology, Wright-Patterson AFB, Ohio 45433-7765, USA
robert.callihan@us.af.mil, aihua.wood@afit.edu

Abstract **─** In this paper, we consider the time-domain scattering problem of a two-dimensional overfilled cavity embedded in an impedance ground plane. An artificial boundary condition is introduced on a semicircle enclosing the cavity that couples the fields from the infinite exterior domain to those fields inside. The problem is first discretized in time using the Newmark scheme, and at each time step, we derive the variational formulation for the TM polarization, and establish well-posedness. Numerical implementation of the method for both the planar and overfilled cavity models is also presented.

Index Terms **─** Impedance boundary conditions, overfilled cavity, time domain.

I. INTRODUCTION

Electromagnetic scattering of cavity-backed apertures has been examined by numerous researchers in the engineering community (for example [1-6]) and the mathematical community (for example [7-10]). For overfilled cavities, we mention the works [11-14]. We note that most of the published work deals with either cavities with PEC ground planes or time-harmonic problems. Here, we consider transient overfilled cavities with impedance boundary conditions. Our approach is unique in that we develop a hybrid finite element - boundary integral mathematical model that incorporates an overfilled cavity with impedance boundary conditions. It will be more mathematically challenging yet more physically realistic and, as a result, has numerous applications.

We organize the paper as follows. In Section II, we introduce the problem setting and geometry. In Section III, we discretize the PDE via the Newmark scheme, first decomposing the entire solution domain into two sub-domains via an artificial semicircle, $\mathcal{B}_R$, which entirely encloses the overfilled cavity. This requires solving a nonhomogeneous modified Helmholtz equation with nonhomogeneous impedance boundary conditions at each time step via a generalized Green's function approach to obtain an integral representation. In Section IV, we present the integral representation, the Green's function for an impedance ground plane, and the properties of the Steklov-Poincaré operator. We conclude in Section V, by producing a variational formulation of the problem that is well-posed. In Section VI, we provide numerical results for a simplified planar cavity and an overfilled cavity that demonstrates the analysis can be implemented.

II. PROBLEM SETTING

Let $\Omega \subset \mathbb{R}^2$ be the cross-section (cavity interior) of a z-invariant cavity in the infinite ground plane, and the infinite homogenous, isotropic region above the cavity as $\mathcal{U} = \mathbb{R}^2_+ \setminus \Omega$. Furthermore, let $\mathcal{B}_R$ be a semicircle of radius R, centered at the origin and surrounded by free space, large enough to completely enclose the overfilled portion of the cavity. We denote the region bounded by $\mathcal{B}_R$ and the cavity wall S as Ω_R, so that Ω_R consists of the cavity itself and the homogeneous part between $\mathcal{B}_R$ and Γ. Let $\mathcal{U}_R$ be the homogeneous region outside of Ω_R; that is, $\mathcal{U}_R = \{(r,\theta) : r > R, 0 < \theta < \pi\}$. Refer to Fig. 1 for the complete problem geometry.

Submitted On: June 19, 2011
Accepted On: August 9, 2011

1054-4887 © 2011 ACES

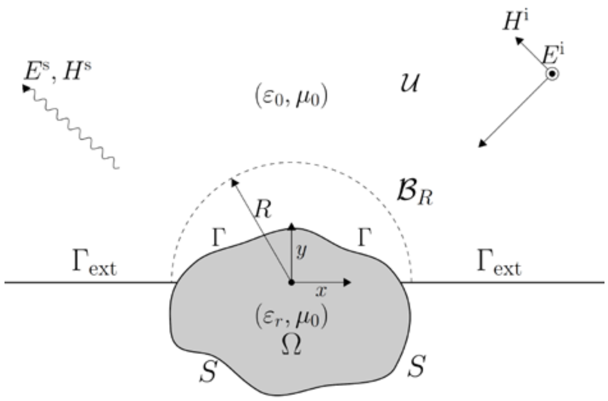

Fig. 1. Problem geometry – TM polarization depicted.

The following formulation is modeled after Van and Wood [13]. In this case, the magnetic field H is transverse to the z-axis so that E and H are of the form $E = (0, 0, E_z)$ and $H = (H_x, H_y, 0)$. In this case, the nonzero component of the total electric field E_z satisfies the following boundary value problem:

$$\begin{aligned} &-\Delta E_z + \varepsilon_r \frac{\partial^2 E_z}{\partial t^2} = 0 && \text{in } \Omega \cup \mathcal{U} \times (0,\infty), \\ &\frac{\partial E_z}{\partial t} = -\frac{\eta}{\mu}\frac{\partial E_z}{\partial \mathbf{n}} && \text{on } S \cup \Gamma_{\text{ext}} \times (0,\infty), \quad (1) \\ &E_z\big|_{t=0} = E_0, \\ &\frac{\partial E_z}{\partial t}\Big|_{t=0} = E_{t,0} && \text{in } \Omega \cup \mathcal{U} \end{aligned}$$

where $\varepsilon_r = \varepsilon / \varepsilon_0$ is the relative electric permittivity, E_0 and $E_{t,0}$ are the given initial conditions and $\eta = \sqrt{\mu_r / \varepsilon_r}$ is the normalized intrinsic impedance of the infinite ground plane. We are assuming that we have a non-dispersive material in the cavity, or that the permittivity is not a function of frequency, but could vary with respect to position. That is, we are assuming that the impedance is constant in the time domain. We observe the scattered field E_z^s solves:

$$\begin{aligned} -\Delta E_z^s + \frac{\partial^2 E_z^s}{\partial t^2} &= 0 \quad \text{in } \mathcal{U} \times (0,\infty), \\ \frac{\partial E_z^s}{\partial t} + \frac{\eta}{\mu}\frac{\partial E_z^s}{\partial \mathbf{n}} &= -\left(\frac{\partial E_z^i}{\partial t} + \frac{\eta}{\mu}\frac{\partial E_z^i}{\partial \mathbf{n}}\right), \quad (2) \\ &\text{on } \Gamma_{\text{ext}} \cup \Gamma \times (0,\infty), \end{aligned}$$

and also satisfies the appropriate radiation condition at infinity.

The homogeneous region $\mathcal{U}$ above the protruding cavity is assumed to be air and hence, its permittivity is $\varepsilon_r = 1$. In $\mathcal{U}$, the total field can be decomposed as $E_z = E_z^i + E_z^s$ where E_z^i is the incident field, and E_z^s the scattered field.

III. SEMIDISCRETE PROBLEM

We will first decompose the entire solution domain to two sub-domains via an artificial semicircle, $\mathcal{B}_R$, which entirely encloses the overfilled cavity (refer to Fig. 2). These two sub-domains consist of the infinite upper half plane over the impedance plane exterior to the semicircle, denoted $\mathcal{U}_R$, and the cavity plus the interior region of the semicircle, denoted Ω_R.

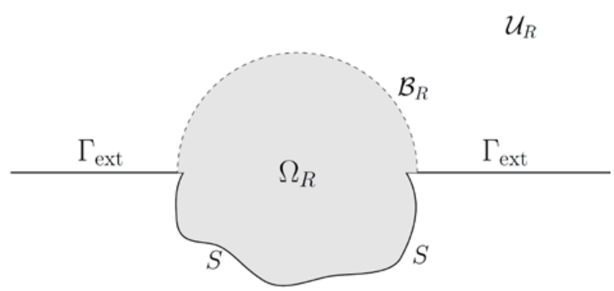

Fig. 2. Sub-domains.

For this problem, as in [13], we will choose to use the Newmark scheme, an implicit time-stepping method that offers the advantage of stability. It is defined by the following: let N be a positive integer, T be the time interval, $\delta t = T / N$ be the temporal step size, and $t_{n+1} = (n+1)\delta t$ for $n = 0, 1, 2, \ldots, N-1$. The following are approximations at $t = t_{n+1}$:

$$u^{n+1} \approx u, \qquad \dot{u}^{n+1} \approx \frac{\partial u}{\partial t}, \qquad \ddot{u}^{n+1} \approx \frac{\partial^2 u}{\partial t^2}.$$

We further define γ and β as parameters to be determined to guarantee stability of the scheme, $\alpha^2 = \frac{1}{(\delta t)^2 \beta}$, and $\tilde{u}$ denotes predicted values.

Therefore, it can be shown that the scattered field $u^{s,n+1}$ satisfies the following *exterior problem*:

$$\begin{aligned} &-\Delta u^{s,n+1} + \alpha^2 u^{s,n+1} = \alpha^2 \tilde{u}^{s,n+1} \quad \text{in } \mathcal{U}_\mathrm{R}, \\ &u^{s,n+1}(R,\theta) = g(R,\theta) \quad \text{on } \mathcal{B}_\mathrm{R}, \\ &\delta t\gamma\alpha^2 u^{s,n+1} + \frac{\eta}{\mu}\frac{\partial u^{s,n+1}}{\partial n} = \\ &\qquad \delta t\gamma\alpha^2 \tilde{u}^{s,n+1} - \tilde{\dot{u}}^{s,n+1} \ \text{on}\, \Gamma_\mathrm{ext}, \end{aligned} \tag{3}$$

where $g \overset{def}{=} u^{n+1} - u^{i,n+1}$ and the radiation condition is satisfied.

Therefore, we seek the solution for the nonhomogeneous modified Helmholtz equation $-\Delta u(\mathbf{r}) + \alpha^2 u(\mathbf{r})) = f((\mathbf{r}))$, where $\mathbf{r}$ denotes location and $f(\mathbf{r}) = \alpha^2 \tilde{u}^{s,n+1}(\mathbf{r})$. This equation is subject to nonhomogeneous boundary conditions of the form $Au(\mathbf{r}_s) + B\frac{\partial u(\mathbf{r}_s)}{\partial \mathbf{n}} = h(\mathbf{r}_s)$, where $\mathbf{r}_s$ is on the surface and $\mathbf{n}$ is the outward unit normal, A and B are constants defined as $A = \Delta t\gamma\alpha^2$ and $B = \frac{\eta}{\mu}$, and $h(\mathbf{r}_s) = \Delta t\gamma\alpha^2 \tilde{u}^{s,n+1} - \tilde{\dot{u}}^{s,n+1}$.

IV. INTEGRAL REPRESENTATION OF SOLUTION AND GREEN'S FUNCTION

The integral representation of the solution in the exterior domain (the annular sector depicted in Fig. 3) can be shown to be, for $\mathrm{r} \in \mathcal{U}_R$ and source location at r':

$$\begin{aligned} u(r) = &\iint_{\mathcal{U}_R} f(r')G(r\,|\,r')dS' - \\ &\frac{1}{A}\int_{\Gamma_\mathrm{ext}} h(r')\frac{\partial G(r\,|\,r')}{\partial n'}dr' + \\ &\int_{\mathcal{B}_R}\left(G(r\,|\,r')\frac{\partial u(r')}{\partial n'} - u(r')\frac{\partial G(r\,|\,r')}{\partial n'}\right)d\theta'. \end{aligned} \tag{4}$$

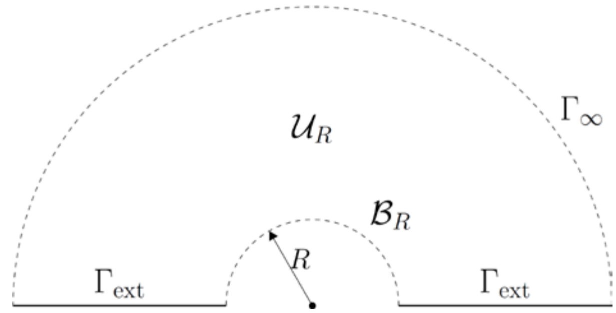

Fig. 3. Exterior domain.

The Green's function has been developed from several sources for an impedance half-plane, see for example, [15-17]. We follow Durán, *et al.*, in [11] to obtain the following, noting the integral expression may be simplified through residue analysis:

$$\begin{aligned} G(r\,|\,r') = &\frac{1}{2\pi}K_0(\alpha R) - \frac{1}{2\pi}K_0(\alpha R^*) \\ &-\frac{2B}{4\pi}\int_{-\infty}^{\infty}\frac{e^{-\sqrt{\xi^2+\alpha^2}\,(y'+y)}}{(A - B\sqrt{\xi^2+\alpha^2})}e^{i(x'-x)\xi}d\xi. \end{aligned} \tag{5}$$

We note $R = \sqrt{(x'-x)^2 + (y'-y)^2}$ and $R^* = \sqrt{(x'-x)^2 + (y'+y)^2}$. At this point, we implement an integral equation method along the artificial boundary, $\mathcal{B}_R$, to couple the solution along the artificial boundary through the Dirichlet-to-Neumann mapping, or Steklov-Poincaré operator. Following Hsiao, *et al.*, in [18], where we define $\varphi(r') = \frac{\partial u(r')}{\partial n_{r'}}$, all of the boundary integral operators for $r \in \mathcal{B}_R$ are expressed as follows:

$$(S\varphi)(r) = \int_{\mathcal{B}_R} G(r\,|\,r')\varphi(r')d\theta',$$

$$(Du)(r) = \int_{\mathcal{B}_R} u(r')\frac{\partial G(r\,|\,r')}{\partial n'}d\theta',$$

$$(A\varphi)(r) = \int_{\mathcal{B}_R}\frac{\partial G(r\,|\,r')}{\partial n}\varphi(r')d\theta',$$

$$(Hu)(r) = -\int_{\mathcal{B}_R} u(r')\frac{\partial}{\partial n}\frac{\partial G(r\,|\,r')}{\partial n'}d\theta.$$

We further define the Newton Potential to consist of the following terms, for $r \in \mathcal{B}_R$:

$$(Nf)(r) = \iint_{\mathcal{U}_R} f(r')G(r \mid r')dS',$$

$$(Ph)(r) = -\frac{1}{A}\int_{\Gamma_{\text{ext}}} h(r')\frac{\partial G(r \mid r')}{\partial n'}dx'.$$

The mapping properties are well-established for the preceding boundary integral operators. As a result, as in [18] or [19], we define $\mathcal{T}_R : H^{1/2}(\mathcal{B}_R) \to H^{-1/2}(\mathcal{B}_R)$ as a bounded Steklov-Poincaré operator as follows:

$$(\mathcal{T}_R u)(r) = S^{-1}(\frac{1}{2}I + D)u(r)$$
$$= \left[(\frac{1}{2}I + A)S^{-1}(\frac{1}{2}I + D) + H\right]u(r).$$

The second expression is the symmetric expression of the operator. In addition, the following theorem, similar to Cakoni and Colton's Theorem 5.20 in [20], also applies:

Theorem 1 *The Steklov-Poincaré operator,* $\mathcal{T}_R$ *, is a bounded, linear operator from* $H^{1/2}(\mathcal{B}_R) \to H^{-1/2}(\mathcal{B}_R)$*. Also, the principal part of* $\mathcal{T}_R$ *, referred to as* $\mathcal{T}_{R,P}$ *, satisfies the coercivity estimate:*

$$-\langle \mathcal{T}_{R,P}u, u\rangle \geq C\ \|u\|^2_{H^{1/2}(\mathcal{B}_R)}$$

for some $C > 0$*, such that the difference* $\mathcal{T}_R - \mathcal{T}_{R,P}$ *is a compact operator from* $H^{1/2}(\mathcal{B}_R) \to H^{-1/2}(\mathcal{B}_R)$.

V. VARIATIONAL FORMULATION

Instead of enforcing the boundary conditions on the test function space V as in [1], we choose to define the subspace V simply as $H^1(\Omega_R)$. The variational formulation will then be to find $u \in V$ such that:

$$b_{TM}(u,v) = F(v) \qquad \forall v \in V. \tag{6}$$

We define the sesquilinear term:

$$\begin{aligned} b_{TM}(u,v) = &\int_{\Omega_R} \nabla u \cdot \nabla \bar{v}\, dxdy - \int_{\mathcal{B}_R} \mathcal{T}_R u\bar{v}\, d\ell \\ &+ \frac{\mu}{\eta}\Delta t\gamma\alpha^2 \int_S u\bar{v}\, d\ell \\ &+ \alpha^2 \int_{\Omega_R} \varepsilon_r u\bar{v}\, dxdy, \end{aligned} \tag{7}$$

as well as the bounded conjugate linear functional term:

$$\begin{aligned} F(v) = &\int_{\mathcal{B}_R} J\bar{v}\, d\ell - \int_{\mathcal{B}_R} \Psi\tilde{u}^s\bar{v}\, d\ell \\ &+ \frac{\mu}{\eta}\Delta t\gamma\alpha^2 \int_S \tilde{u}\bar{v}\, d\ell \\ &- \frac{\mu}{\eta}\int_S \tilde{\tilde{u}}\bar{v}\, d\ell + \alpha^2 \int_{\Omega_R} \varepsilon_r \tilde{u}\bar{v}\, dxdy, \end{aligned} \tag{8}$$

and we further define the bounded terms:

$$(\Psi_R \tilde{u}^{s,n+1})(r) = S^{-1}((N\tilde{u}^{s,n+1})(r) + (P\tilde{u}^{s,n+1})(r))$$

and $\qquad J = \dfrac{\partial u^i}{\partial r}\Big|_{r=R} - \mathcal{T}_R u^i.$

Theorem 2 *The variational problem (6) is well-posed: a solution* $u \in V$ *exists, is unique, and for* $C > 0$*:*

$$\|u\| \leq C\left[\|u^i\| + \|\tilde{u}^s\| + \|\tilde{u}\| + \|\tilde{\tilde{u}}\| + \|\varepsilon_r\tilde{u}\|\right].$$

Using the results of the previous section, and writing $b_{TM}(u,v)$ as the sum of a coercive operator and compact operator, (6) can be shown to be well-posed through variational methods.

VI. NUMERICAL RESULTS

A. Planar cavity results

We ran a numerical study on a planar cavity to provide a context for the theory. We ran the data for two separate cases: a perfect electrical conducting (PEC) surface on the plane Γ_{ext} and PEC surface on the cavity walls, S, and a PEC plane and impedance boundary conditions (IBC) on the cavity walls. The idea is to see the progression as we introduce IBC on a strict PEC surface, in which we would expect more attenuation as the surface changes.

The numerical model was set up as depicted in Fig. 4, using an incident Gaussian Pulse with $\delta t = 0.0625$, $\varepsilon_r = 2$, $\mu_0 = 1$, and Newmark parameters $\gamma = 0.95$ and $\beta = 0.5256$ to ensure stability. The visual depictions of the electric field are plotted against time as measured in light meters (LM), which is the amount of time light travels in one meter of free space.

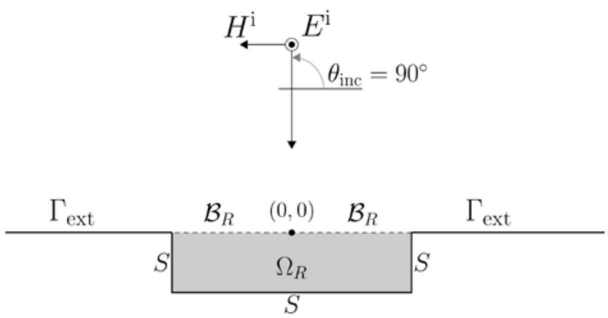

Fig. 4. Shallow cavity (1m by 0.25m).

The first run is depicted in Fig. 5. With the PEC plane and PEC cavity walls as a benchmark, we observe that the case with IBC enforced at the cavity walls ($\eta = 0.8$) exhibits more attenuated characteristics. We also observe the stability of the Newmark scheme over time.

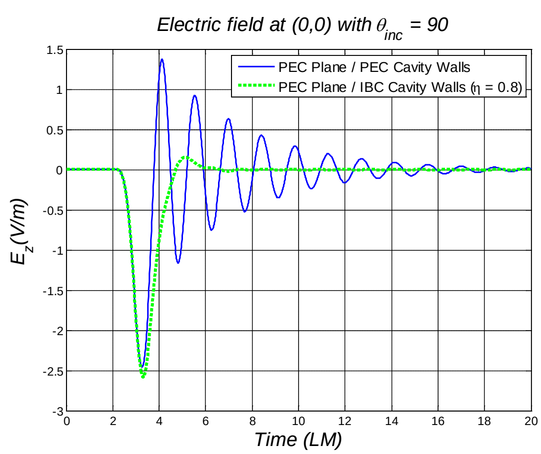

Fig. 5. Shallow cavity with $\eta = 0.8$.

We also want to observe the effects as $\eta \rightarrow 0$, as we would expect the field to exhibit the characteristics of a strict PEC on the plane and cavity walls. This is clearly evident in Fig. 6 with the PEC plane and IBC cavity walls simulation showing more oscillatory behavior as in the strict PEC case. Again, we observe the stability of the Newmark scheme over time.

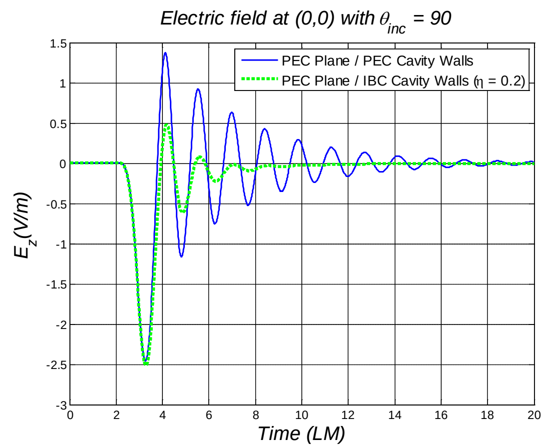

Fig. 6. Shallow cavity with $\eta = 0.2$.

We also wanted to observe the effects of changing boundary conditions on the radar cross section of the cavity model. We ran two simulations, at the selected frequencies of 289.5 MHz and 480.45 MHz, as depicted in Fig. 7 and Fig. 8.

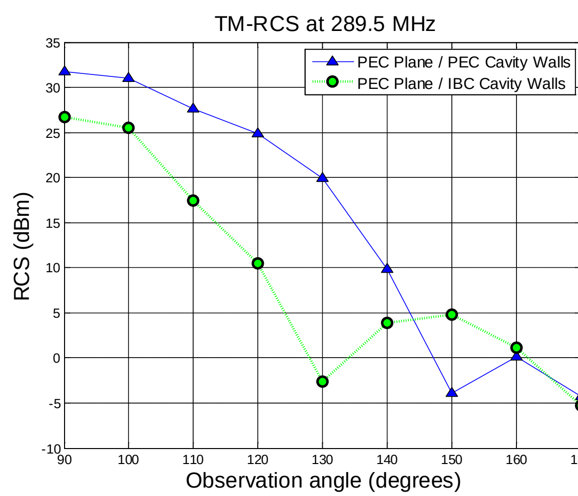

Fig. 7. Shallow cavity RCS at 289.5 MHz.

In both cases, we observe the expected lobing, and note the fact that as the frequency is increased to 480.45 MHz, the separation in RCS values between the two cases is more apparent. More specifically, for 480.45 MHz, the RCS values are lower as the boundary conditions approach a complete IBC on the cavity walls.

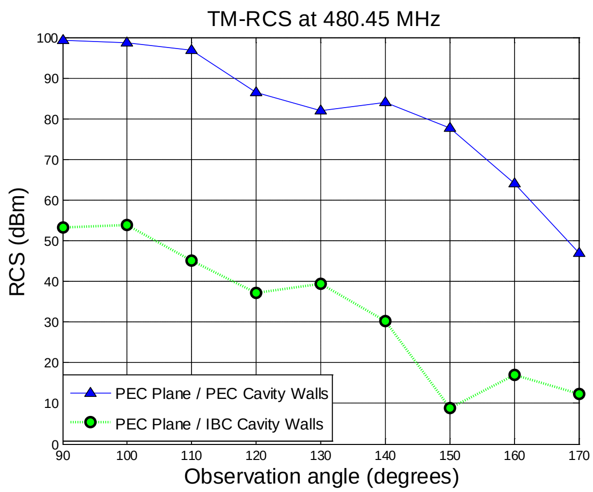

Fig. 8. Shallow cavity RCS at 480.45 MHz.

B. Overfilled cavity results

As with the planar cavity, we used the same set of parameters for the overfilled cavity depicted in Fig. 9.

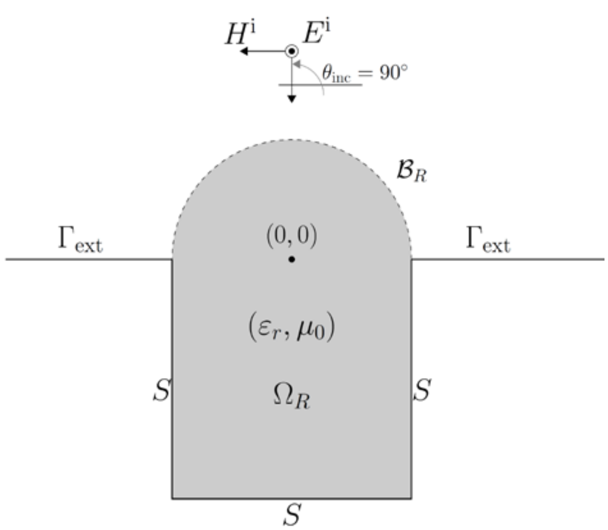

Fig. 9. Overfilled cavity (1m deep; 0.5m radius).

However, in this model, we add a third case of an IBC on both the cavity walls and plane. We also chose an observation point at the origin. We note in both Fig. 10 and Fig. 11 that the depicted scattered field becomes more attenuated as the boundary conditions for the plane and cavity walls approach an IBC surface. The observation is truncated at 50 LM for scaling, but the simulations exhibit the same stability as with the planar case beyond this point. It is also evident that the fields are more oscillatory than the shallow cavity due to the presence of more material both above and below the observation point. We also note in Fig. 11 that as $\eta \rightarrow 0$ the field begins to exhibit the characteristics of a strict PEC surface, as seen in the more oscillatory behavior of the IBC plane and IBC cavity walls condition.

We also present the RCS data in Fig. 12 for 289.5 MHz and Fig. 13 for 480.45 MHz. Again, we notice similar behavior at the lower frequency for all three cases; however, at a higher frequency, we observe both the expected lobing and the more attenuated results as the IBC is enforced on both the cavity walls and the plane.

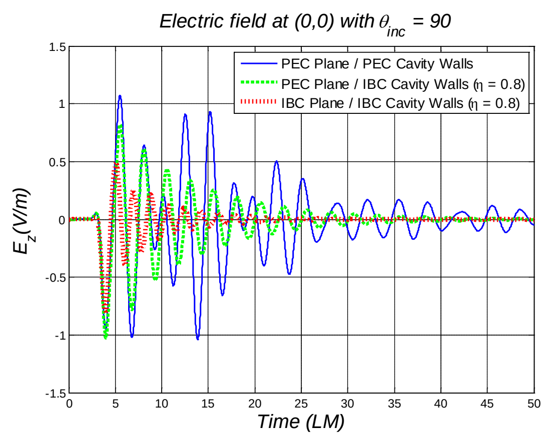

Fig. 10. Overfilled cavity with $\eta = 0.8$.

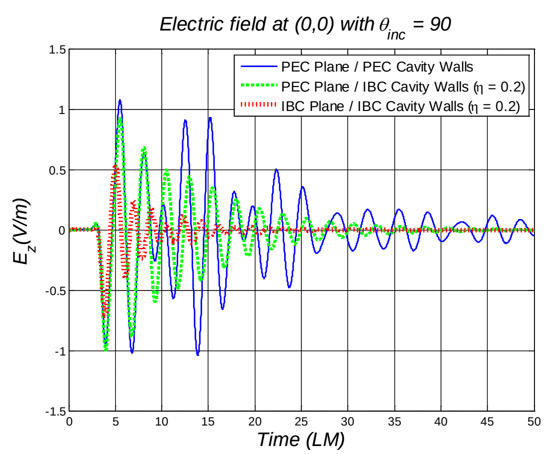

Fig. 11. Overfilled cavity with $\eta = 0.2$.

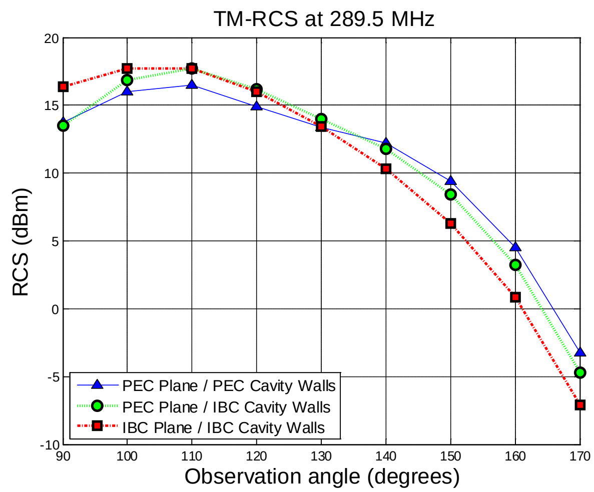

Fig. 12. Overfilled cavity RCS at 289.5 MHz.

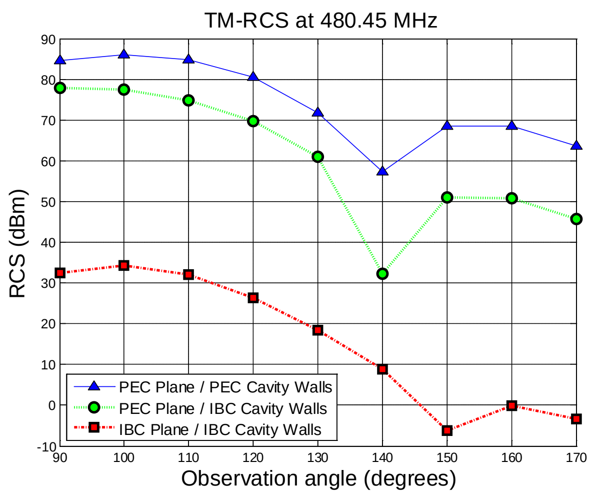

Fig. 13. Overfilled cavity RCS at 480.45 MHz.

VII. CONCLUSION

We present a mathematical model for analyzing transient electromagnetic scattering induced by an overfilled cavity embedded in an impedance ground plane. We have established the well-posedness of the problem through a variational formulation, and this sets the foundation for numerical implementation through a hybrid finite element - boundary integral technique. We present electric field and RCS data for both a simplified planar cavity as well as the overfilled cavity model, which both exhibit expected results.

ACKNOWLEDGMENT

The views expressed in this article are those of the authors and do not reflect the official policy or position of the United States Air Force, Department of Defense, or the U. S. Government.

REFERENCES

[1] J. M. Jin, S. Ni, and S. W. Lee, "Hybridization of SBR and FEM for Scattering by Large Bodies with Cracks and Cavities," *IEEE Trans. Antennas Propag.*, vol. 43, no. 10, pp. 1130-1139, 1995.

[2] L. C. Kempel and J. L. Volakis, "Scattering by Cavity-Backed Antennas on a Circular Cylinder," *IEEE Trans. Antennas Propag.*, vol. 42, no. 10, pp. 1268-1279, 1994.

[3] J. Liu and J. M. Jin, "A Special Higher Order Finite-Element Method for Scattering by Deep Cavities," *IEEE Trans. Antennas Propag.*, vol. 48, no. 5, pp. 694-703, 2000.

[4] W. D. Wood and A. W. Wood, "Development and Numerical Solution of Integral Equations for Electromagnetic Scattering from a Trough in a Ground Plane," *IEEE Trans. Antennas Propag.*, vol. 47, no. 8, pp. 1318-1322, 1999.

[5] C. J. Reddy, M. D. Deshpande, B. R. Cockrell, and F. B. Beck, "Fast Frequency Response Calculations of Cavity-Backed Aperture Antennas using Hybrid FEM/MoM Technique in Conjunction with Model Based Parameter Estimation," *Applied Computational Electromagnetic Society (ACES) Journal*, vol. 13, no. 3, pp. 283-290, 1998.

[6] D. Caratelli and A. Yarovoy, "Design and Full-Wave Analysis of Cavity-Backed Resistively Loaded Circular-End Bow-Tie Antennas for GPR Applications – Part I," *Applied Computational Electromagnetic Society (ACES) Journal*, vol. 25, no. 10, pp. 809-817, 2010.

[7] H. Ammari, G. Bao, and A. Wood, "A Cavity Problem for Maxwell's Equations," *Meth. Math. Appl.*, vol. 9, no. 2, pp. 249-260, 2002.

[8] T. Van and A. Wood, "Analysis of Time-Domain Maxwell's Equations for 3-D Cavities," *Adv. Comput. Math.*, vol. 16, nos. 2-3, pp. 211-228, 2002.

[9] T. Van and A. Wood, "A Time-Marching Finite Element Method for an Electromagnetic Scattering Problem," *Math. Meth. Appl. Sci.*, vol. 26, no. 12, pp. 1025-1045, 2003.

[10] T. Van and A. Wood, "A Time-Domain Finite Element Method for Maxwell's Equations," *SIAM J. Numer. Anal.*, vol. 42, no. 4, pp. 1592-1609, 2004.

[11] M. Durán, I. Muga, and J.-C. Nédélec, "The Helmholtz Equation in a Locally Perturbed Half-Plane with Passive Boundary," *IMA J. Appl. Math.*, vol. 71, no. 6, pp. 853-876, 2006.

[12] A. W. Wood, "Analysis of Electromagnetic Scattering from an Overfilled Cavity in the Ground Plane," *J. Comput. Phys.*, vol. 215, no. 2, pp. 630-641, 2006.

[13] T. Van and A. W. Wood, "Analysis of Transient Electromagnetic Scattering from Overfilled Cavities," *SIAM J. Appl. Math.*, vol. 64, no. 2, pp. 688-708, 2004.

[14] J. Huang, A. W. Wood, and M. J. Havrilla, "A Hybrid Finite Element-Laplace Transform Method for the Analysis of Transient Electromagnetic Scattering by an Over-Filled Cavity in the Ground Plane," *Commun. Comput. Phys.*, vol. 5, no. 1, pp. 126-141, 2009.

[15] M. Durán, I. Muga, and J.-C. Nédélec, "The Helmholtz Equation in a Locally Perturbed Half-Space with Non-Absorbing Boundary," *Arch. Ration. Mech. An.*, vol. 191, no. 1, pp. 143-172, 2009.

[16] R. O. Hein-Hoernig, *Green's Functions and Integral Equations for the Laplace and Helmholtz Operators in Impedance Half-Spaces*, Ph.D. Thesis, École Polytechnique, 2010.

[17] C. G. Politis, M. V. Papalexandris, and G. A. Athanassoulis, "A Boundary Integral Equation Method for Oblique Water-Wave Scattering by Cylinders Governed by the Modified Helmholtz Equation," *Appl. Ocean Res.*, vol. 24, no. 4, pp. 215-233, 2002.

[18] G. C. Hsiao, O. Steinbach, and W. L. Wendland, "Domain Decomposition Methods via Boundary Integral Equations," *J. Comput. Appl. Math.*, vol. 125, no. 1, pp. 521-537, 2000.

[19] O. Steinbach and W. L. Wendland, "On C. Neumann's Method for Second-Order Elliptic Systems in Domains with Non-Smooth Boundaries," *J. Math. Anal. Appl.*, vol. 262, no. 2, pp. 733-748, 2001.

[20] F. Cakoni and D. Colton, *Qualitative Methods in Inverse Scattering Theory*, Springer-Verlag, Berlin, Germany, 2006.

Robert S. Callihan received his B.S. from the U. S. Air Force Academy in mathematics, and his M.B.A. from Georgia College and State University. He currently is a Ph.D. candidate at the Air Force Institute of Technology. He has served 18 years in the Air Force, primarily as a trainer pilot and KC-135 tanker pilot. He most recently served on the faculty as an Assistant Professor of Mathematical Sciences at the U. S. Air Force Academy, and will return to that assignment following his dissertation. Lieutenant Colonel Callihan's research interests are partial differential equations and Green's functions.

Aihua W. Wood received her B.S. from Beijing University and Ph.D. from the University of Connecticut in Mathematics. She served as an Assistant Professor at the Naval Postgraduate School for three years and the Pennsylvania State University at Erie for one year before joining the faculty at the Air Force Institute of Technology in 1994. She has been a Professor of Mathematics since 2002 and is currently the institute's Equity Advisor. Dr. Wood's research interests include partial differential equations, electromagnetic wave propagation, and rarefied gas dynamics.

Coupled Electromagnetic Field Computation with External Circuit for the Evaluation the Performance of Electric Motor Designs

A. Sarikhani and O. A. Mohammed

Energy Systems Research Laboratory
Department of Electrical and Computer Engineering
Florida International University, Miami, FL 33174, USA
mohammed@.fiu.edu

***Abstract* --** In this paper, a set of PM machine's designs, having the similar level of nominal input and outputs i.e. voltage, torque, and speed were compared to evaluate the effectiveness of a computational design procedure. The designs include the machines with distributed winding arrangements, different number of slots, different pole widths, and different slot opening shapes. The physical characteristics of machines such as the cogging torque, back emf, flux linkages, and inductances were calculated from a 2D nonlinear transient finite element analysis with motion. The torque and speed profiles of all of the machines were calculated from the phase variable modeling approach. The phase variable model is a database representation of the machine's numerical model and it allows computationally efficient dynamic simulation of the coupled problem with realistic physics-based design. The phase variable models of the machines were linked to the driving circuit to determine the mutual effect of machine design parameter and the drive topology on the performance measures of machines.

Index terms-- Cogging torque, electromagnetic field computation, finite element analysis, motor design, phase variable model, PM machines.

I. INTRODUCTION

Electric machines play an essential role in many industries. PM synchronous motors are widely utilized due to their high power density, low maintenance costs, and high efficiency. From a structural point of view, depending on the setting of the magnets on the rotor, the synchronous motors can be constructed by either burying the magnets within the rotor iron or by mounting them on the rotor surface. Most PM synchronous motors can be categorized into three general categories; surface mounted PM synchronous motors (SPM) which have their permanent magnets mounted on the surface of the rotor, inset PM synchronous motors in which the permanent magnets are inset or partially inset into the rotor, and interior PM synchronous motors which have the permanent magnets completely buried inside the rotor [1]. From machine winding point of view, concentrated windings versus distributed winding for PM motors are widely used because of the low manufacturing cost. Comparisons and quantitative analysis of these two types of windings for two motors with same stator were studied [2, 3]. Nevertheless, it is recognized that in the case of design of the PM motor, infinite number of combinations would result in acceptable outputs. Depending on such outputs and the planned application, different designs could be achieved.

One of the intrinsic characteristics of PM motors is the pulsating torque. This ripple torque is parasitic, and can produce acoustic noise, mechanical vibration, and other problems in electric machine drive systems such as increased iron losses and total harmonic distortion [4]. Therefore, the machine designer must consider these issues in the design process [4, 5]. The study of pulsating torque is important for the application of constant speed or high-precision position control, especially at low speed applications. The torque pulsations are due to the cogging torque and the electromagnetic torque ripple. Many techniques for mitigating the cogging torque were proposed in the literature [6-8]. Some of the methods manipulate the stator or rotor separately or both of them together. This includes employing a fractional number of slots per pole, skewing of the magnets, slots, and/or the opening of slots, shifting and shaping of the main magnets, shifting the slots opening, optimizing the magnet pole-arc to

Submitted On: April 24, 2011
Accepted On: September 25, 2011

pole-pitch ratio, and introducing supplementary slots or teeth [6, 7, 8]. The fractional number of slots/pole can change both the amplitude and the frequency of the cogging torque to a desirable value. It also increases the fundamental order of the magnetic flux density in the air gap due to the different relative circumferential positions of the stator slots with respect to the edges of the magnets when this topology is used. On the other hand, the actual back emf waveform of PM motors depends on the conductor distributions and flux density. This in turn is a function of the magnetization characteristic of the magnet stator teeth, and slot structures.

PM machines with trapezoidal back emf have been widely used due to the simplicity in their control [9]. The skew of magnets is effective in reducing the harmonic content in the flux linkage and back EMF waveform, as well as in reducing the cogging torque [8].

As discussed above, different practical and theoretical methods have been proposed for mitigating the cogging torque, and also manipulating the back emf waveform for a simpler and cheaper driving strategy. In fact most of these strategies increase the cost because they alter the conventional manufacturing processes. In this paper, sets of designs representing studied cases were obtained from classic design procedure. Following this step, a finite element analysis was completed on each of the designed geometries. This was done to calculate the cogging torque, back emf, and flux linkage for all of the cases. Finally, a phase variable model was used to simulate the output torque and speed of the machine [11, 12]. The phase variable model is a data base table look up model of the nonlinear transient finite element solution of the motor to enable dynamic simulation.

II. CASE OF STUDIES

A. Preparation of case studies for field computation

The goal of this section is the preparation of a set of machines with different number of slots, pole widths, different slot opening shape, but with the same range of speed, input power, and voltage. Four different sets of machines were designed where the designs vary in the number of slots and pole widths. The totals of twenty one different machine designs were considered. A schematic view of the designed machine is shown in figures 1(a) and 1(b). All of the machine designs created from a classic design procedure [1, 10] for a WYn winding, 2-hp, 1200-rpm, 6-pole, phase voltage of 111.5-Volt, and current density of 3 A/mm^2.

The difference in the designs of the machines is shown in Table 1. In the first set, we have eighteen slots with four different pole widths which make four different machines, and all of the coils in the stator are in series together in each phase. In the second set, the number of slots were changed to thirty six, and four different poles width make four different machines, where there is two parallel paths for currents in each phase. The other sets were designed for fifty four and seventy two slots, respectively as shown in Table 1. In this table N_p, S_p, and C_s stand for number of parallel paths, number of slot per pole, and coil span, respectively. The design details for the various sets were illustrated in Tables 2 and 3. The used magnetic material for all of the machines is Sm2Co17. The magnets are radically magnetized. After a classic design procedure, each machine was prepared for an FE analysis as shown in Figure 2 (b). Here, the accuracy of manufacturing tolerance is assumed as 0.05 millimeter. Therefore all of the design parameters are rounded to the nearest real value.

Another test set was prepared where the influence of the slot opening geometry on the physical behavior of the machine and its performance measure was investigated. In order to examine the influence of the slot opening geometry, the five 36-slot/6-pole machine designs shown in Figure 1(c) were considered. The details of stator geometry are shown in Table 3. The inter pole angles in all of the designs were two degrees while the rotor geometry remain the same for these five test shown in Table 4. In this set of tests, Design 1 has tapered tooth tips and parallel slot opening. Design 2 has straight tooth tips and parallel slot opening, Design 3 has straight tooth tips and no slot opening, Design 4 has tapered tooth tips and non-parallel slot opening, and Design 5 has straight tooth tips and non-parallel slot opening. All the other stator design parameter remains the same for all of the designs. It is mentioned that, the chosen current density for this range of machine ensure us the thermal limitations; however for a secure and optimal design, a thermoelectric design procedure will be a superior solution.

Here, depending to the voltage value of the DC bus before the conventional 6-switch, 3-phase

DC/AC inverter and also control strategy of the inverter, the maximum amplitude of the back emf should be chosen otherwise the desired speed and torque characteristics will not be achieved. The four well-known, modulation strategies for the inverter connected to the motors are: six-step inverter control, sinusoidal PWM, space vector PWM, harmonic elimination, hysteresis, Delta and Third harmonic injections. The respective phase-neutral DC bus utilization of each of these control strategy are $2V_{dc}/\pi$,$V_{dc}/2$ with modulation factor equal to one, $V_{dc}/\sqrt{3}$, $2\,V_{dc}/\pi$, $V_{dc}/2$, $V_{dc}/2$, and $V_{dc}/\sqrt{3}$. The rule is that the maximum amplitude of the back emf voltage of each of the phases should be always lower than the phase-neutral voltage in order to ensure us a proper speed control. If this rule is ignored then unwanted fluctuations will appear in the torque and speed profiles and more probably the speed control will lost. Therefore, in this paper the number of coil's turns per phase is chosen based upon this criterion. In this work, the voltage of the DC bus for the inverter is chosen as 300-V, and the control strategy is chosen as Hysteresis current regulated control, therefore the maximum back emf voltage is limited to a value lower than 150-V. However, for a secure current hysteresis control for a wide speed range, the maximum back emf should be chosen with a good security margin. Here, it is assumed that the drive is not equipped with the flux weakening control therefore in the designs the maximum amplitude of the fundamental component of the back emf were limited to 100-V to offer more security margin for over speed conditions, likely 150% of the nominal speed. The hysteresis band in the hysteresis current control is fixed as 0.3 Ampere.

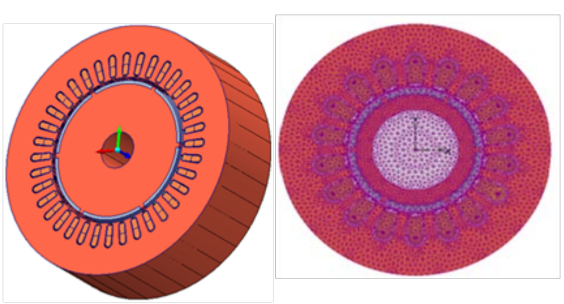

Fig. 1. (a) A schematic 2D view of the studied case.

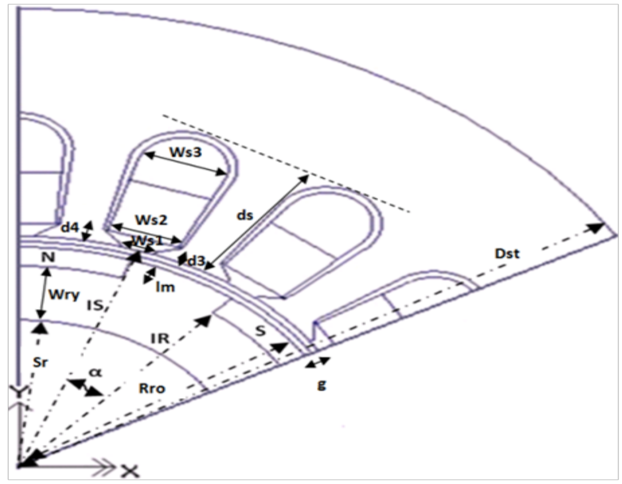

Fig. 1. (b) A schematic 2D view of the studied.

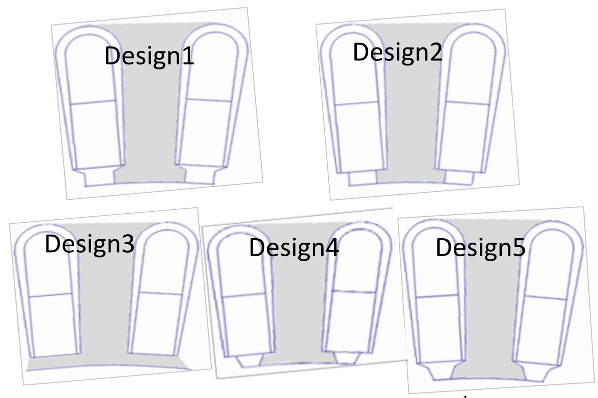

Fig. 1. (c) Slot opening changes in the 5th test set.

Table 1: Winding arrangements and inter pole angle of studied cases

(N_s)	Np	Slot/pole	Sp	Cs	α° (degree)	Coil/phase
18	1	3	60	3	(0°,2°,5°,10°)	17
36	2	6	30	5	(0°,2°,5°,10°)	17
54	3	9	20	8	(0°,2°,5°,10°)	17
72	4	12	15	10	(0°,2°,5°,10°)	17

Table 2: Stator geometry of 1th to 4th sets (in mm)

Set	N_s	W_{s3}	W_{s2}	W_{s1}	d_3	d_4	d_s	D_{st}	L_{st},
1st	18	22.2	16.8	7.4	3	0.8	37	138	50
2nd	36	11	8.4	3.6	3	0.8	37	138	50
3rd	54	5.6	4.2	1.8	3	0.8	37	138	50
4th	72	2.8	2.1	1	3	0.8	37	138	50

Table 3: Stator geometry of 5th set (in mm)

	Ns	W_{s3}	W_{s2}	W_{s1}	d_3	d_4	d_s	D_{st}	L_{st},
1	36	8.15	6.4	3.6	0.75	1.9	19.8	126.6	74.5
2	36	8.15	6.4	3.6	0	1.9	19.1	126.6	74.5
3	36	8.15	6.4	0	0	2.3	19.4	126.6	74.5
4	36	8.15	6.4	2.1	0.76	1.9	19.8	126.6	74.5
5	36	8.15	6.4	2.1	0	1.9	19.1	126.6	74.5

Table 4: Rotor geometry of studied case (mm)

Set number	Rro	Sr	Wry	Lm	g
All sets	66.6	44.1	16.4	5.8	3

III. THE PHASE VARIABLE MODEL

The phase variable model of PM machines is an accurate and fast model for the purpose of integrated drive system simulations. This model uses transient FE solutions to establish a detailed block description of the implemented machines in a Simulink environment as shown in Figure 2(a). This model accounts for flux weakening as well as other performances [11, 12, and 14]. The model is essentially a database representation of the nonlinear transient operation of the machine to allow the use of a detailed computational model for dynamic simulation.

The creation of the phase variable model consists of two discrete steps. In the first step, a linear transient FE analysis is performed to calculate the cogging torque, back emf, flux linkage, and the inductance matrix of the machine. The FE-based phase variable model is rotor –position dependent, therefore, the FE analysis must take the transient analysis and the motion of rotor into account. In the FE domain, the corresponding magnetic vector potential formulation is calculated as:

$$-\nabla.\left(\sigma\frac{\partial A}{\partial t} - \sigma\vartheta \times (\nabla \times A) - J^e\right) = 0 \qquad (1)$$

$$\sigma\frac{\partial A}{\partial t} + \nabla \times (\mu^{-1}\nabla \times A - M) - \sigma\vartheta \times (\nabla \times A) = J^e \qquad (2)$$

where σ is the conductivity, A is the vector potential, ϑ is the velocity of the modeled object, J^e is the external current density, μ is the permeability, and M is the magnetisation. The constitutive relation considering ferromagnetic saturation is:

$$B = \mu_0(H + M) \qquad (3)$$

where B is the flux density, H is the field strength, and μ_0 is the permeability of air.

Following the FE analysis, the FE output parameters are collected into lookup tables in the circuit environment. The second step is the implementation of the machine equations, equations (4) - (8), in the circuit environment. The values are retrieved via look-up tables to create the database and implement it. In the circuit environment, the back emf, and the flux linkage, cogging torque as well as the Inductances are updated for each rotation position varying with the speed of the machine. Rotor-position-dependent inductance matrix is calculated by the incremental method [13]. Following the implementation of the phase variable model in Simulink, a hysteresis current regulated drive with speed controller were linked with the phase variable model of the machine to control the speed as given in Figure 2 (b).

$$V_{abc} = R_{abc}i_{abc} + {d\varphi_{abc}(i_{abc}\,,\theta)}/{dt} \qquad (4)$$

$$\varphi_{abc}(i_{abc},\theta) = \varphi_{sabc}(\theta) + \varphi_{rabc}(\theta) = L_{abc}(\theta)i_{abc} + \varphi_{rabc}(\theta) \qquad (5)$$

$$T_M = [p(0.5i_{abc}^T dL_{abc}(\theta)/d\theta).\,i_{abc} + i_{abc}^T d\varphi_{rabc}(\theta)/d\theta] + T_{cog}(\theta) \qquad (6)$$

$$\frac{Jd\omega}{dt} = T_m - F\omega - T_L \qquad (7)$$

$$\omega = d\theta/dt \qquad (8)$$

In the above equations, V_{abc}, $R_{abc,}$ and i_{abc} are the terminal voltage, resistance, and current of the stator winding, respectively. The flux linkage φ_{abc} is composed of two parts, see Eq. (5). The first part is related to the inductance L_{abc} of the stator winding, while the other part is contributed by the permanent magnets on the rotor, represented by φ_{abc}. The cogging torque T_{cog} is added to obtain the total output torque T_m, as shown in Eq. (7). The rotation angle of the rotor position is represented by θ. Here, L_{abc}, φ_{abc} and T_{cog} are considered as rotor-position-dependent parameters. Also, in these equations p, J, ω and F are the number of pole pairs, inertia, angular speed, and friction factor, respectively. The load torque is T_L in Eq. (7).

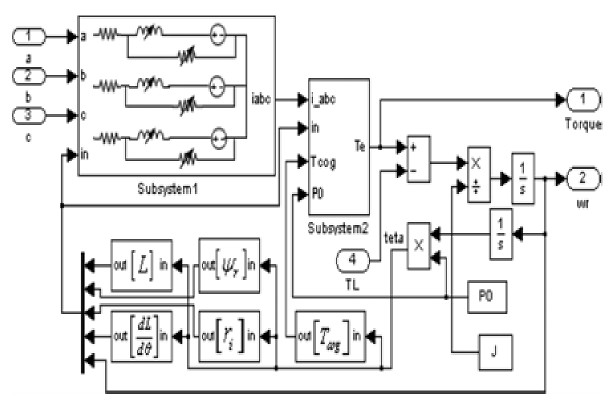

Fig. 2. (a) Phase-variable model of PM machine [14].

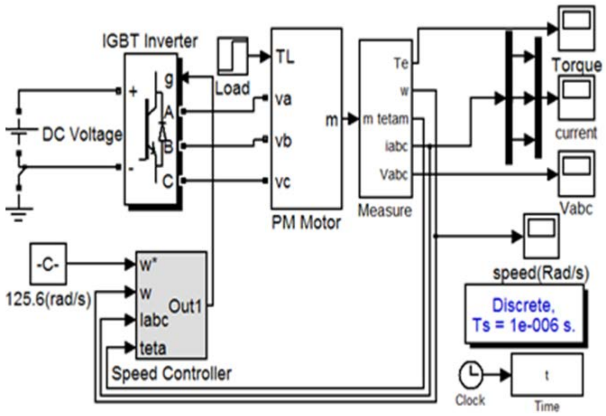

Fig. 2. (b) Phase variable model with hysteresis IGBT driver and speed controller.

IV. SIMULATION RESULTS

A. The cogging torque

The cogging torque is the consequence of the interaction between the permanent magnet fields and the stator in the neighbor of the air gap that is because of the reluctance variations with the rotor position and that is independent of the stator current [11]. Figure 3 (A) to (D) show the simulated cogging torque for different angle α. It can be observed that the maximum value of cogging torque and its frequency is dependent to the number of slots and pole widths. In this study, as α is changed, the inner radius of the poles are kept unchanged. From Figure 3, it is concluded that for the eight slots and by decreasing the pole width, the maximum of the cogging torque is reduced, but its frequency increases. Therefore, it is concluded that a change in the angle α would change the cogging torque to a better value. As can be seen in Figures 3 (a) to (d), it is concluded that the cogging torque can be a function of (α, Ns) which has a minimum that, in this case, occur at α=2 degree. Moreover, by comparison of Figures 3 (a) to (d), it is concluded that the number of slots in the design procedure would highly have an influence on the maximum amplitude of the cogging torque.

The cogging torque calculation in the 5th set, Figure 3 (e), shows that the 2nd design has the highest cogging torque and the 3th design has the lowest cogging torque. The cogging torques of the 1st, 4th, and 5th designs are almost similar with the maximum amplitude equal to 0.6 (n. m).

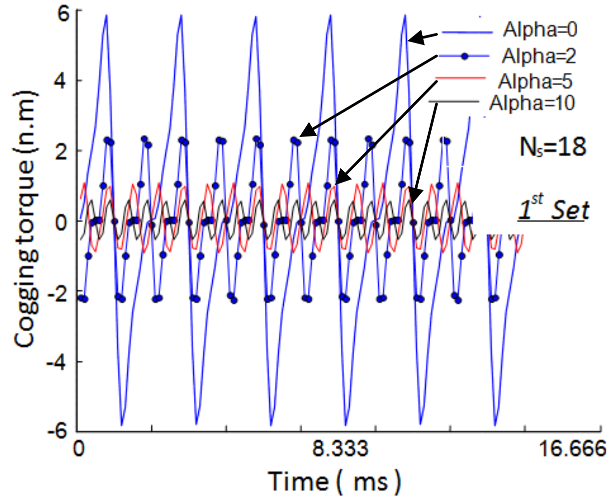

Fig. 3. (a) Cogging torque of the 1st set.

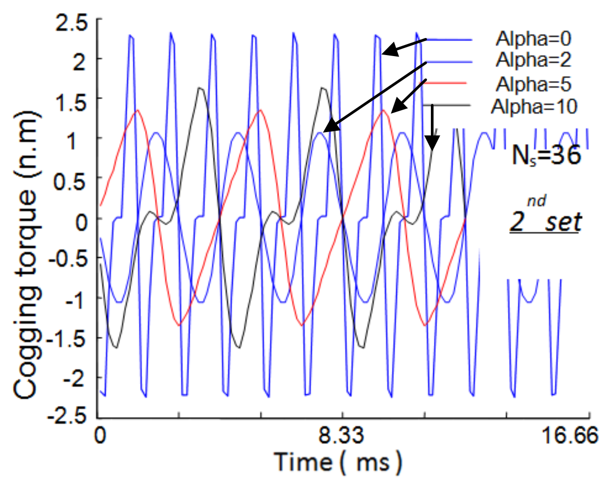

Fig. 3. (b) Cogging torque of the 2nd set.

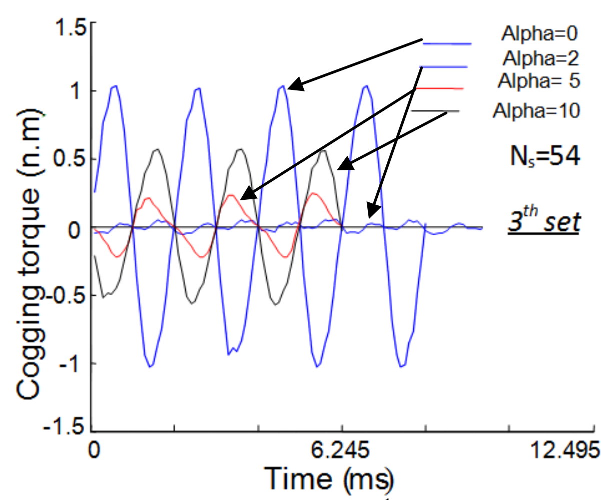

Fig. 3. (c) Cogging torque of the 3th set.

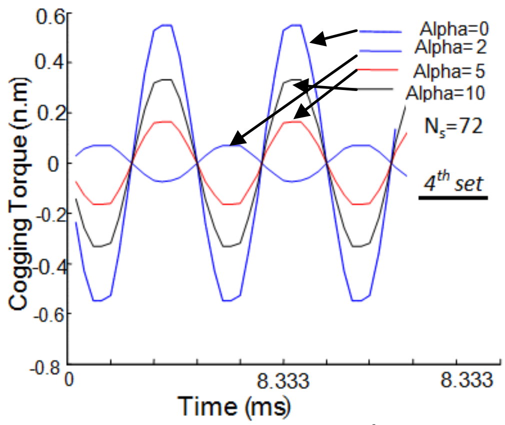

Fig. 3. (d) Cogging torque of the 4th set.

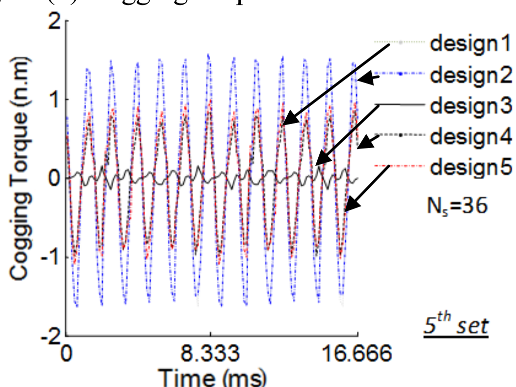

Fig. 3. (e) Cogging torque of the 5th set.

B. The back emf and flux linkage as a function of design parameters:

The back emf is the consequence of the induced voltage in the coils due to the rotation of the magnetic field produced by the magnets. The waveform of the back emf has a direct influence on the machine current and therefore the torque ripple [11-12]. As can be seen from Figure 4, as the pole width is decreased, i.e. when α is increased, the flux opens a new path through the iron of the inter-pole to the rotor yoke. Therefore, the concentration of flux inside the coils is decreased and therefore the root mean square value of the induced back emf in the coils is reduced.

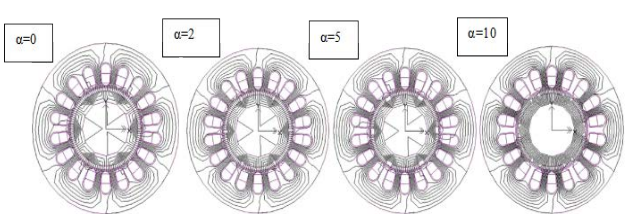

Fig. 4. The flux picture as a function for the 1th set.

Figures 5 (a) to 5 (d) show the back emfs for different pole width and number of slots. As can be seen from these figures, when the number of slots is increased the influence of the pole width becomes more visible. For example, for 72 stator slots, as the angle α increase, the back emf waveforms become more similar to a sinusoidal waveform than for the 36 slots machine. Also one can observe that the maximum value of the back emf is independent of the angle α. Therefore, it is concluded that the back emf of a motor with a higher number of slots is more sensitive to the pole width. In fact the shape of the back emf has an essential role for choosing the driving strategy. By comparison of Figures 8(a) to (d) it can be concluded that, if a trapezoidal waveform of the back emf is required, the lower inter-pole angle is preferable and if a sine waveform of the back emf is required, a higher inter-pole angle would be preferable although this conclusions is almost validated for radial and parallel magnetized permanent magnets with equal inter-pole angles [1]. Moreover, by comparison of the Figures 5(a) to (d) concerning different number of slots it is seen that the machines with higher number of slots can provide the drive circuit with better trapezoidal or sine back emf waveform; for example, in Figure 5 (a) it is seen that achievement of a pure sine or a pure trapezoidal back emf waveform is indeed unachievable. In fact, creation of a proper current for ripple free performance with the used drive topology and winding arrangement maybe not be feasible.

On the other hand, a closer look at the effect of the number of slots reveals that with smaller number of slots, a smaller number of coils are required. However, the number of turns per coil and the size of the slot would be larger. A small number of slots may lead to a small savings in cost. However, the effect of the stator slots on the air gap flux and therefore back emf in small machines is considerable.

Figure 6 (a) show the flux linkage of the 1st to 4th set. As can be seen from this Figure, the number of slots has minor influence on the maximum amplitude of flux linkage, but as the pole width is decreased the maximum amplitude of the flux is decreased. Moreover, the flux linkage of the 5th set, Figure 6 (b), shows that, the 3rd set has the lowest flux linkage that the reason is that the flux closes its path in the added iron to the slot openings area. The flux linkages of other test set are relatively remained unchanged.

Figures 7 (a) and 7 (b) show the self and mutual inductances of the 5th set. As it is seen from the inductance profiles, the 3rd design has the highest self and the lowest mutual inductance. The self and the mutual inductance of the other designs are at the same level. It is evident that the slot opening geometry has a noticeable effect on the inductances. This shows that, the machines with the highest inductances have higher start-up time but have lowest speed fluctuations. Moreover, the inductance study of the 1th to 4th set show that, the higher number of slot/pole ratio, the lower will be the winding inductance ratio. This is due to the number of the series turns per phase reduces in order to achieve a given back emf.

Figures 8(a) and 8 (b) show the total output torque against different number of slots and slot openings shapes respectively. The output torque is obtained from simulation of the phase variable model. All of the simulations had the same drive system. A hysteresis band speed controller was used to control the speed. The torque is calculated for the pole width in which the cogging torque has minimum values in all of the cases, i.e. the value of α is equal to 2. As illustrated in Figure 8 (a), as the number of slots is increased, the torque ripples and the setting time of the torque is decreased. In figure 8 (b) less torque ripple compared to other designs is seen.

Figures 9(a) and 9(b) show the speed profile with different number of slots and slot openings shapes, respectively. From Figure 9 (a), it is concluded that the higher number of slots has lower speed fluctuations which can be an important factor for some special application. In Figure 9 (b), design 3, lower speed fluctuation but higher start-up time compared to other machines is seen. The hysteresis current loop control used for the speed control of the machine has higher dynamic comparing to other modulation strategies such as SVPWM, SPWM, harmonic elimination, etc. This method is also sensitive to the inductance of the electrical load. As the inductance of the machine is increased the current ripple is decreased. As a result, the electrical torque ripple and the speed fluctuations is decreased. However, the higher inductance the start-up time of the machine and the setting time of the speed during start-up or any change in speed reference is increased.

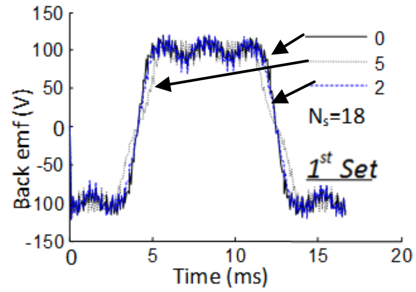

Fig. 5. (a) Back emf of the 1st set.

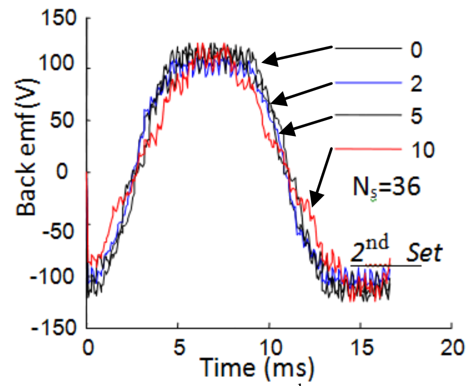

Fig. 5. (b) Back emfs of the 2nd set.

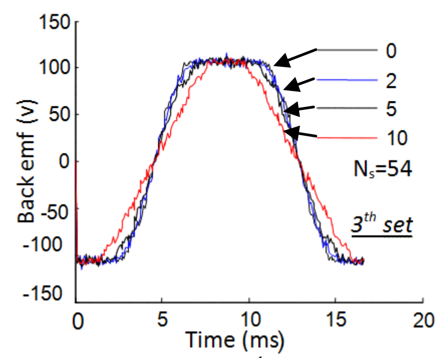

Fig. 5. (c) Back emfs of the 3th set.

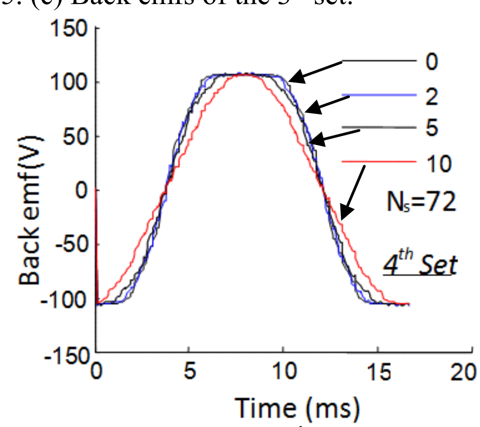

Fig. 5. (d) Back emfs of the 4th set.

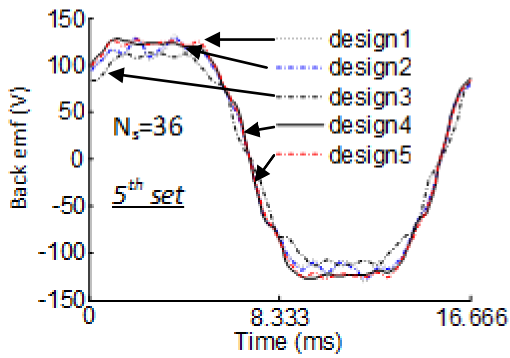

Fig. 5. (e) Back emfs of the 5th set.

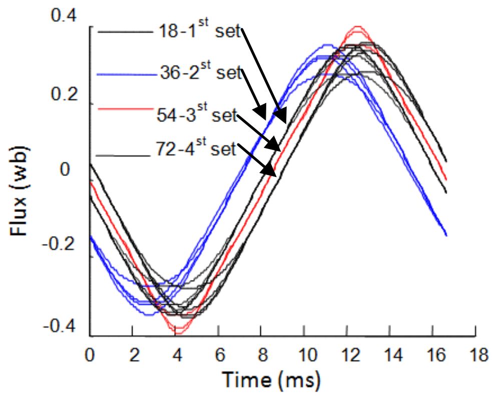

Fig. 6. (a) Flux linkage of the 1st to 4th set.

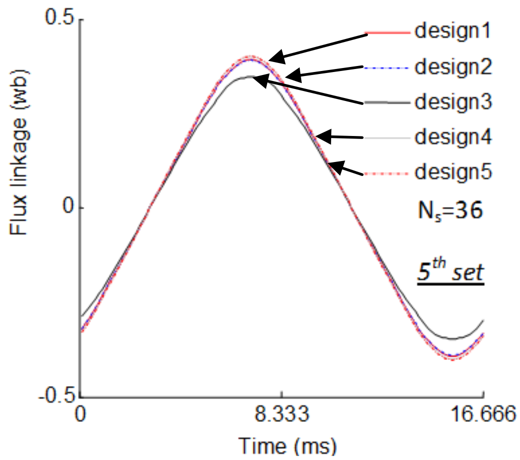

Fig. 6. (b) Flux linkage of the 5th set.

V. CONCLUSION

We investigated the effect of the number of slots, pole width, and slot openings shape as design parameters on the cogging torque, back emf, flux linkage, total torque, and speed for various PM motors controlled by a sinusoidal current regulated drive. The study was performed on twenty one different machines with similar nominal range of inputs/output. The simulation results shown that as the number of slots was increased, the cogging torque was generally decreased. In addition, it was shown that the pole width has a good potential to effectively change the cogging torque. It was found that a minimum cogging torque can be found for a specific pole width. Moreover, it was shown that a machine with higher number of slots has lower setting time compared to a machine with lower number of slots where the speed fluctuations and torque ripples were also relatively reduced. It can be concluded that a machine with higher number of slots can show better performance measures than a machine with lower number of slots, although it may increase the cost and require more accuracy in manufacturing tolerances.

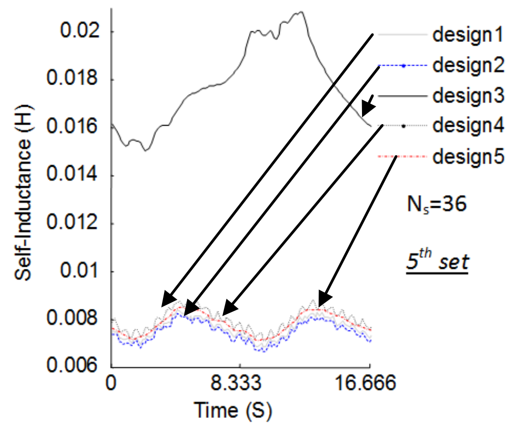

Fig. 7. (a) Self-inductances of the 5th set.

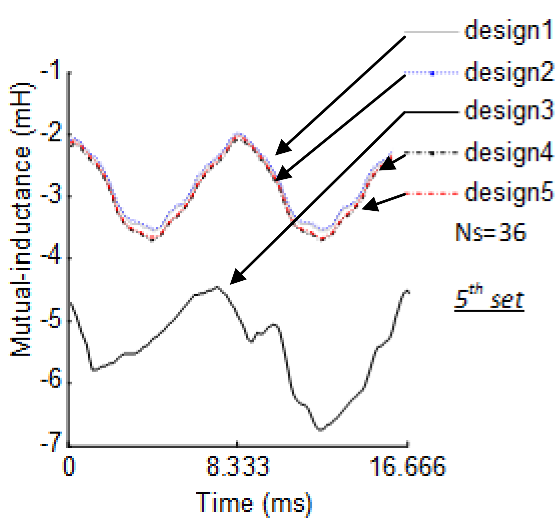

Fig. 7. (b) Mutual inductances of the 5th set.

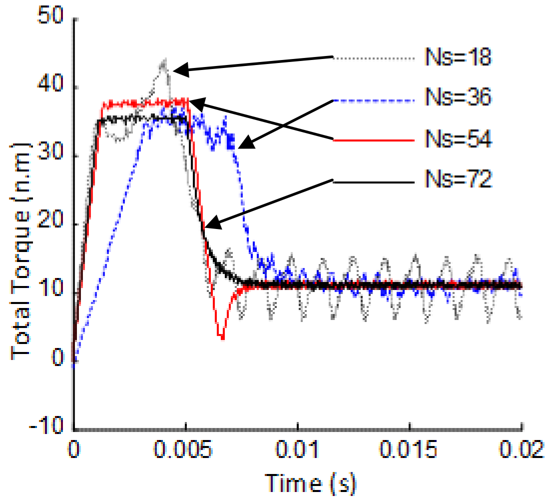

Fig. 8. (a) Total torque for α equal to 2 degree concerning different number of slots.

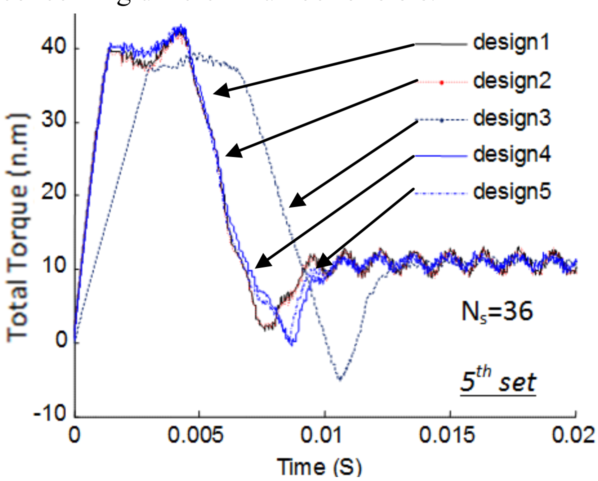

Fig. 8. (b) Total torque for α equal to 2 degree concerning different slot opening shape.

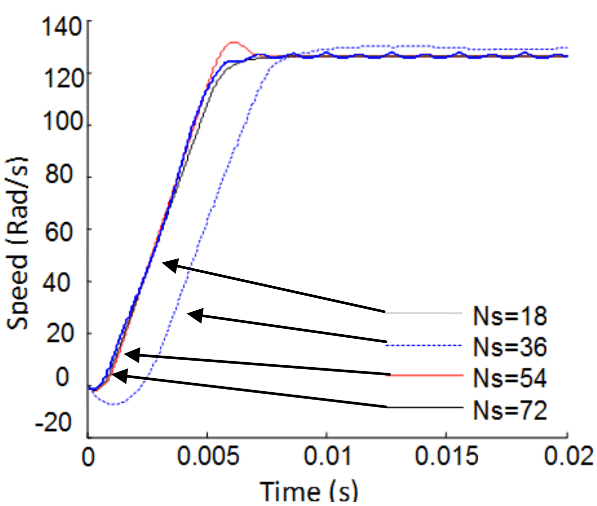

Fig. 9 (a) Speed for α equal to 2 degree concerning different number of slots.

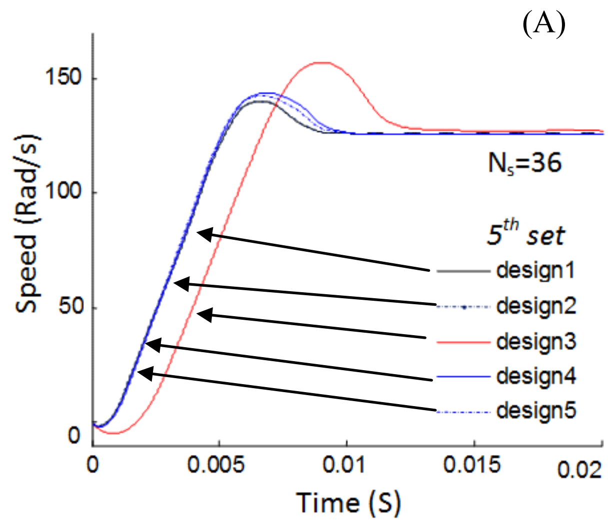

Fig. 9. (b) Speed for α equal to 2 degree concerning different slot opening shape.

ACKNOWLEDGMENTS

Part of this work is supported by a grant from the Office of Naval Research.

REFERENCES

[1] Duan Hanselman, *Brushless Permanent Magnet Motor Design*, Manga Physics, pp. 68-160 and 352-360, March 2003.

[2] F. Magnussen, P. Thelin, and C. Sadarangani, "Performance Evaluation of Permanent Magnet Synchronous Machines with Concentrated and Distributed Windings Including the Effect of Field-Weakening," *2nd IEE Inter. Conf. on Power Elec., Machines and Drives*, Edinburgh, UK, vol. 2, pp. 679-85, 2004.

[3] M. El-Refaie, T. M. Jahns, and D. W. Novotny, "Analysis of Surface Permanent Magnet Machines with Fractional-Slot Concentrated Windings," *IEEE Trans. Energy Conversion*, vol. 21, no. 1, pp. 34-43, Mar. 2006.

[4] L. Dosiek and P. Pillay, "Cogging Torque Reduction in Permanent Magnet Machines," *IEEE trans. on Industry application*, vol. 43, no. 6, pp. 1656–1571, 2007.

[5] Z. Q. Zhu and D. Howe, "Influence of Design Parameters on Cogging Torque in Permanent Magnet Machines," *IEEE Trans. Energy Conversion*, vol. 15, no. 4, pp. 407-412, 2000.

[6] Z. Q. Zhu, S. Ruangsinchaiwanich, and D. Howe, "Synthesis of Cogging Torque Waveform form Analysis of a Single Stator Slot," *IEEE Trans Industry App.*, vol. 42, no. 3, pp. 650-657, 2006.

[7] P. Salminen, J. Pyrhönen, F. Libert, and J. Soulard, "Torque Ripple of Permanent Magnet Machines with Concentrated Windings," ISEF *International*

Symposium on Electromagnetic Fields in Mechatronics, Electrical and Electronic Engineering, Baiona, Spain, 2005.

[8] S. A. Saied and K. Abbaszadeh "Cogging Torque Reduction in Brushless DC Motors Using Slot-Opening Shift," *Advances in Electrical and Computer Engineering*, vol. 9, no. 1, 2009.

[9] S. Tomy and G. Vineeta, "Analysis of Induced EMF Waveforms and Torque Ripple in a Brushless Permanent Magnet Machine," *IEEE Trans. On Indr. App.*, vol. 32, no. 1, January 1996.

[10] M. G. Say, "Performance and Design of AC Machines," 3ed. 1958.

[11] O. A. Mohammed, Z. Liu, and S. Liu, "Stator Power Factor Adjustable Direct Torque Control of Doubly-Fed Induction Machines," Proceedings of the *International Electric Machines and Drives Conference IEMDC'05*, pp. 572-578, May 2005.

[12] O. A. Mohammed, S. Liu, and Z. Liu, "A Phase Variable Model of Brushless DC Motor Based on Physical FE Model and its Coupling with External Circuits," *IEEE Transactions on Magnetics*, vol. 41, no. 5, pp. 1576-1579, May 2005.

[13] M. Gyimesi and D. Ostergaard, "Inductance Computation by Incremental Finite Element Analysis," *IEEE Trans. On Magnetics*, vol. 35, pp. 1119-1122, May 1999.

[14] S. Liu, O. A. Mohammed, and Z. Liu, "An Improved FE-Based Phase Variable Model of PM Synchronous Machines Including Dynamic Core Losses," *IEEE Trans. On Magnetics*, vol. 43, no. 4, April 2007.

Ali Sarikhani started his bachelor in Transmission and Distribution Engineering in Power and Water University of Technology, Iran. He followed his Master in Power Electrical Engineering in Shahrood University of Technology, Iran. He is now a Ph.D. candidate of electrical engineering at Energy Systems Research Laboratory, Florida International University, USA. His current interests are the computational design prototyping, design adaptation and fault diagnosis of electrical apparatus by standard and intelligent systems.

Osama A. Mohammed (S'79, SM'84, F'94) is a Professor of Electrical and Computer Engineering and the Director of the Energy Systems Research Laboratory at Florida International University. He received his M.S. and Ph.D. degrees in Electrical Engineering from Virginia Polytechnic Institute and State University. He published numerous journal articles over the past 30 years in areas relating to power systems, electric machines and drives, computational electromagnetics and in design optimization of electromagnetic devices, artificial intelligence applications to energy systems. He authored and co-authored more than 300 technical papers in the archival literature. He has conducted research work for government and research laboratories in shipboard power conversion systems and integrated motor drives. He is also interested in the application communication and wide area networks for the distributed control of smart power grids. He has been successful in obtaining a number of research contracts and grants from industries and Federal government agencies for projects related to these areas. Professor Mohammed also published several book chapters including; Chapter 8 on direct current machinery in the Standard Handbook for Electrical Engineers, 15th Edition, McGraw-Hill, 2007 and a book Chapter entitled " Optimal Design of Magnetostatic Devices: the genetic Algorithm Approach and System Optimization Strategies," in the Book entitled: Electromagnetic Optimization by Genetic Algorithms, John Wiley & Sons, 1999.

Professor Mohammed is a Fellow of IEEE and is the recipient of the IEEE PES 2010 Cyril Veinott Electromechanical Energy Conversion Award. Dr. Mohammed is also a Fellow of the Applied Computational Electromagnetic Society. He is Editor of IEEE Transactions on Energy Conversion, IEEE Transactions on Magnetics, Power Engineering Letters and also an Editor of COMPEL. Professor Mohammed is the past President of the Applied Computational Electromagnetic Society (ACES). He received many awards for excellence in research, teaching and service to the profession and has delivered numerous invited lectures at scientific organizations around the world.

Professor Mohammed has been the general chair of several international conferences including; ACES 2006, IEEE-CEFC 2006, IEEE-IEMDC 2009, IEEE-ISAP 1996 and COMPUMAG-1993. He has also chaired technical programs for other major international conferences including; IEEE-CEFC 2010, IEEE-CEFC-2000 and the 2004 IEEE Nanoscale Devices and System Integration. Dr. Mohammed also organized and taught many short courses on power systems, Electromagnetics and intelligent systems in the U.S.A and abroad. Professor Mohammed has served ACES in various capacities for many years. He also serves IEEE in various Boards, committees and working groups at the national and international levels.

Adaptive Design Specifications and Coarsely-Discretized EM Models for Rapid Optimization of Microwave Structures

Slawomir Koziel

Engineering Optimization & Modeling Center, School of Science and Engineering
Reykjavik University, 101 Reykjavik, Iceland
koziel@ru.is

Abstract **─** A simple and efficient procedure for EM-simulation-driven design optimization of microwave devices is discussed. Our approach exploits recently introduced adaptively adjusted design specifications technique that shifts the optimization burden into a relaxed-accuracy and computationally cheap (low-fidelity) model of the structure under consideration, evaluated using the same EM solver as the original (high-fidelity) model but with coarse discretization. The unavoidable misalignment between the low- and high-fidelity models is accounted for by suitable adjustments of the design specifications. The presented method is simple to implement and allows rapid design improvement as demonstrated through examples.

Index Terms **─** Adaptive design specifications, computer-aided design (CAD), electromagnetic simulation, simulation-driven design.

I. INTRODUCTION

Simulation-driven design and design optimization is ubiquitous in contemporary microwave engineering. For many classes of microwave structures no systematic design procedures are available so that EM-based design becomes the only option. Examples include ultrawideband (UWB) antennas [1], dielectric resonator antennas [2] and substrate integrated circuits [3]. On the other hand, increasing complexity of microwave devices and the demand for high accuracy make the direct optimization involving numerous electromagnetic (EM) simulations impractical because of the computational cost of such a process. Co-simulation [4-6] is only a partial solution because the circuit models with embedded EM components are still directly optimized.

A cost-efficient design of microwave structures exploiting EM solvers can be realized using surrogate-based optimization (SBO) [7, 8]. In SBO, the direct optimization of the CPU-intensive EM-evaluated structure of interest (high-fidelity model) is replaced by iterative updating and re-optimization of its computationally cheap representation, the surrogate. The successful SBO approaches in microwave area are space mapping (SM) [9-16] and various forms of tuning [17, 18] as well as combinations of both [19, 20]. Other SBO methods used in microwave engineering include manifold mapping [28] as well as techniques exploiting variable-fidelity EM simulations [29, 30]. Space mapping builds the surrogate using a physically-based low-fidelity model, typically an equivalent circuit. Tuning approaches are based on embedding circuit-theory-based tuning elements into the structure of interest using properly located internal ports [18]. Both approaches can be very efficient and yield satisfactory designs after a few full-wave EM simulations of the structures under consideration [9, 18].

Unfortunately, implementation of both SM and tuning may not be straightforward. In particular, modification of the structure being optimized and engineering experience may be required (tuning), additional mapping and more or less complicated interaction between various auxiliary models is necessary (SM). In order to take advantage of space mapping, the low-fidelity model should be computationally much cheaper

Submitted On: January 21, 2011
Accepted On: October 18, 2011

than the high-fidelity model, therefore, equivalent-circuit models are preferred [9]. Reliable equivalent-circuit models, however, may be difficult to develop for certain types of microwave devices (e.g., antennas). Also, an extra simulator must be involved in the process and linked to the optimization algorithm. Moreover, space mapping performance heavily depends on the selection of the SM transformations used to construct the surrogate. On the other hand, tuning cannot be directly applied to radiating structures.

In this paper, an efficient technique for simulation-driven design of EM-simulated structures is discussed that is based on the SBO principle, coarsely-discretized EM low-fidelity models, and adaptive adjustment of the design specifications [21]. Original design specifications are modified to take into account the difference between the high-fidelity and low-fidelity model responses at the current design. The low-fidelity model is then optimized with respect to the modified specifications to produce a new design that—assuming sufficient quality of the low-fidelity model—gives a good prediction of the optimal high-fidelity model design with respect to the original specifications. The above assumption is typically satisfied for coarsely-discretized EM models. The presented method is simple to implement, and, as demonstrated through examples, it is able to yield a satisfactory design after a few high-fidelity EM simulations of the structure under considerations.

II. SIMULATION-DRIVEN DESIGN METHODOLOGY

In this section, we formulate the optimization problem (Section II. A), describe the concept of adaptively adjusted design specifications technique (Section II. B), as well as comment upon the use of coarse-discretization EM simulations as the low-fidelity model guiding the optimization process (Section II. C).

A. Design optimization problem

Let $\boldsymbol{R}_f(\boldsymbol{x})$ and $\boldsymbol{R}_c(\boldsymbol{x})$ denote the response vectors of a high- and low-fidelity models of the microwave structure of interest at the design vector x. For example, $\boldsymbol{R}_f(\boldsymbol{x})$ may consist of the values of $|S_{21}|$ evaluated at a set of frequencies. The high-fidelity model is evaluated using CPU-intensive electromagnetic simulation. The low-fidelity model is a relaxed-accuracy and computationally cheap representation of $\boldsymbol{R}_f$. In particular, $\boldsymbol{R}_c$ may be evaluated using the same solver as $\boldsymbol{R}_f$ but with coarser mesh.

We want to optimize the high-fidelity model with respect to a given set of design specifications. Figure 1(a) shows the high- and low-fidelity model responses at the optimal design of $\boldsymbol{R}_c$, corresponding to the microstrip bandstop filter [21] used here as an illustration example; design specifications are indicated using horizontal lines.

B. Optimization through adaptively adjusted design specifications

The optimization procedure based on adaptively adjusted design specifications, originally introduced in [21], consists of the following two simple steps that can be iterated if necessary:

1. Modify the original design specifications in order to take into account the difference between the responses of $\boldsymbol{R}_f$ and $\boldsymbol{R}_c$ at their characteristic points.
2. Obtain a new design by optimizing the low-fidelity model with respect to the modified specifications.

Characteristic points of the responses should correspond to the design specification levels. They should also include local maxima/minima of the respective responses at which the specifications may not be satisfied. Figure 1(b) shows characteristic points of $\boldsymbol{R}_f$ and $\boldsymbol{R}_c$ for our bandstop filter example. The points correspond to –3 dB and –30 dB levels as well to the local maxima of the responses. As one can observe in Fig. 1(b), the selection of points is rather straightforward.

In the first step of the optimization procedure, the design specifications are modified so that the level of satisfying/violating the modified specifications by the low-fidelity model response corresponds to the satisfaction/violation levels of the original specifications by the high-fidelity model response. More specifically, for each edge of the specification line, the edge frequency is shifted by the difference of the frequencies of the corresponding characteristic points, e.g., the left edge of the specification line of –30 dB is moved to the right by about 0.7 GHz, which is equal to the length of the line connecting the corresponding characteristic points in Fig. 1(b). Similarly, the specification levels are shifted by the difference between the local maxima/minima values for the respective points, e.g., the –30 dB level is shifted down by about 8.5 dB because of the difference of the local maxima of the corresponding characteristic points of $\boldsymbol{R}_f$ and $\boldsymbol{R}_c$. Modified design specifications are shown in Fig. 1(c).

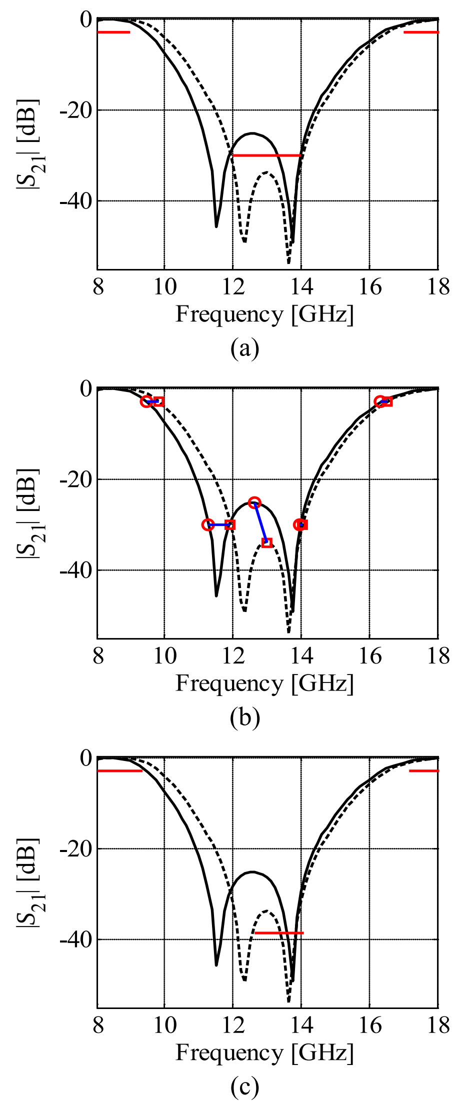

Fig. 1. Bandstop filter example (responses of $\boldsymbol{R}_f$ and $\boldsymbol{R}_c$ are denoted using solid and dashed line, respectively) [21]: (a) responses at the initial design (low-fidelity model optimum) as well as the original design specifications, (b) characteristic points of the responses corresponding to the specification levels (here, -3 dB and -30 dB) and to the local maxima, (c) responses at the initial design as well as the modified design specifications.

The low-fidelity model is subsequently optimized with respect to the modified specifications and the new design obtained this way is treated as an approximated solution to the original design problem (i.e., optimization of the high-fidelity model with respect to the original specifications). Steps 1 and 2 can be repeated if necessary. As demonstrated in Section III, substantial design improvement is typically observed after the first iteration, however, additional iterations may bring further enhancement. In practice, the algorithm is terminated once the current iteration does not bring further improvement of the high-fidelity model design.

Figure 2 shows the flow diagram of the optimization procedure. It should be emphasized, that unlike in case of other simulation-driven techniques popular in microwave engineering (particularly space mapping [9]), the low-fidelity model is not modified or corrected in any way. The discrepancy between the models is “absorbed” by means of modifying the design specifications.

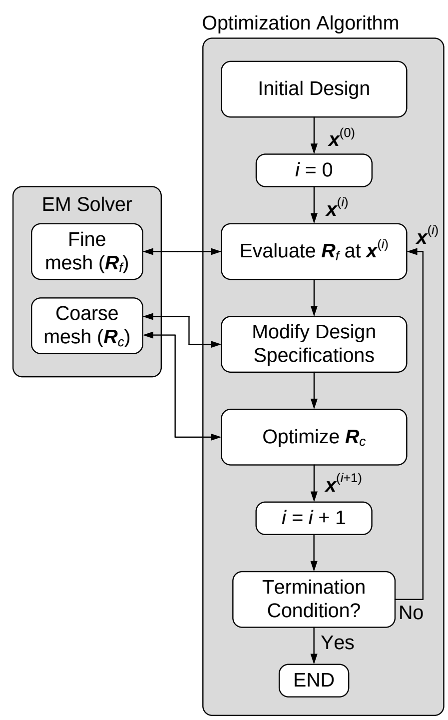

Fig. 2. A flow diagram of the optimization procedure exploiting adaptively adjusted design specifications and coarse-discretization EM models.

The operation of the adaptively adjusted design specifications technique can probably be best explained using the example. Figure 3 illustrates an iteration of the procedure used for design of a CBCPW-to-SIW transition [31]. One can observe that the absolute matching between the low- and high-fidelity models is not as important as the shape similarity.

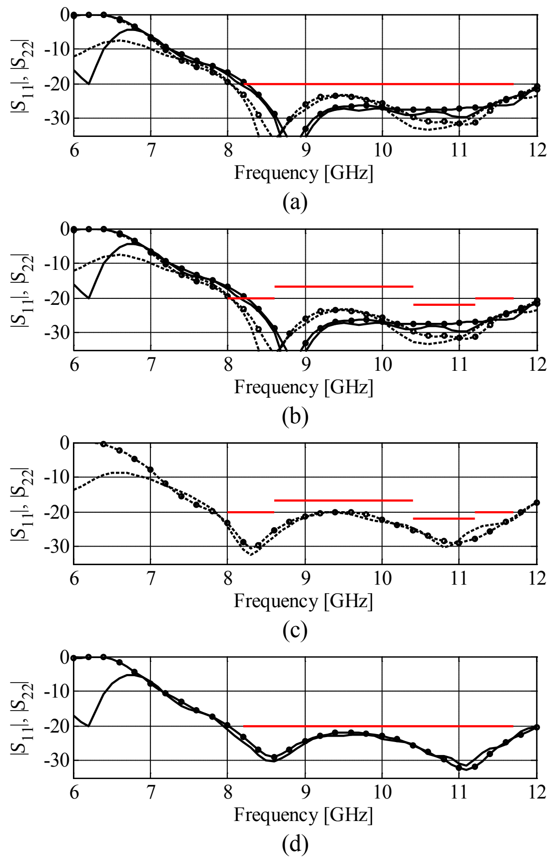

Fig. 3: Adaptively adjusted design specification technique applied to optimize CBCPW-to-SIW transitions. High- and low-fidelity model response denoted as solid and dashed lines, respectively. $|S_{22}|$ distinguished from $|S_{11}|$ using circles. Design specifications denoted by thick horizontal lines. (a) High- and low-fidelity model responses at the beginning of the iteration as well as original design specifications; (b) high- and low-fidelity model responses and modified design specifications that reflect the differences between the responses; (c) low-fidelity model optimized to meet the modified specifications; (d) high-fidelity model at the low-fidelity model optimum shown versus original specifications. Thick horizontal lines indicate the design specifications.

It should be stressed that the low-fidelity model is not modified in any way, that is, no changes are applied to it in order to align it with the high-fidelity model. The discrepancy between the high- and low-fidelity model responses is accounted for by modifying the design specifications.

C. Coarsely-discretized EM-simulation models

While in general, the low-fidelity model can be any physically-based model that is available (e.g., equivalent circuit [9]), the coarse-discretization EM models are used here. This has several advantages: (i) coarse-discretization models using the same EM solvers as corresponding fine models are typically more accurate than any other models of a given structure (e.g., equivalent circuits), (ii) optimization procedure is easy to implement because it exploits one software package (in the case of circuit-based low-fidelity models, an extra simulator is necessary which complicates the algorithm implementation because interaction the simulators has to be realized), (iii) coarse-discretization EM model typically provides better initial design than any other conceivable low-fidelity model type, (iv) coarse-discretization model is available for any microwave structure; in particular, the optimization can performed for devices where finding equivalent circuit model may be problematic (e.g., antennas).

One of the possible problems is that coarse-discretization EM models are relatively expensive so that minimizing the number of low-fidelity model evaluations is crucial in reducing the computational cost of the optimization process. It should be emphasized, however, that the procedure described here is quite efficient with this respect. In particular, it does not have a parameter extraction step—typical for space mapping approaches [12]—that normally requires consumes a substantial number of low-fidelity model evaluations.

D. Practical issues

The adaptively adjusted design specifications technique is very simple to implement and quite efficient as demonstrated in Section III. It should be emphasized, however, that the quality of the low-fidelity model is essential for the performance of this design procedure. More specifically, it is necessary that the high- and low-fidelity models are similar in shape (as functions of frequency) so that modification of the design specifications can be a relevant tool reflecting their misalignment. This requires that the discretization density for the low-fidelity model is sufficient; otherwise, the method may fail to find a satisfactory design. In practice, a parametric study of the mesh density and visual comparison of the high- and low-fidelity model responses are necessary to select the meshing parameters for the latter.

III. EXAMPLES

A. Double annular ring antenna [22]

Consider the stacked probe-fed printed annular ring antenna [22] shown in Fig. 4. The antenna is printed on a printed circuit board (PCB) with electrical permittivity $\varepsilon_{r1} = 2.2$, and height $d_1 = 6.096$ mm for the lower substrate, and $\varepsilon_{r2} = 1.07$, $d_2 = 8.0$ mm for the upper substrate. The radius of the feed pin is $r_0 = 0.325$ mm. The design parameters are $\boldsymbol{x} = [a_1\ a_2\ b_1\ b_2\ \rho_1]^T$.

The fine model is evaluated using FEKO [23]. Its response is the modulus of the reflection coefficient, $|S_{11}|$, evaluated over the frequency band 1.75 GHz to 2.15 GHz. The number of meshes for $\boldsymbol{R}_f$ is 1480 and its evaluation time is 2 hours and 5 minutes. The design specifications are $|S_{11}| \leq -10$ dB for 1.75 GHz $\leq \omega \leq$ 2.15 GHz. The coarse model $\boldsymbol{R}_c$ is also simulated in FEKO. The number of meshes for $\boldsymbol{R}_c$ is 300. The coarse model evaluation time is 6 minutes and 30 seconds. Initial design $\boldsymbol{x}^{(0)} = [10\ 8\ 30\ 30\ 20]^T$ mm.

Optimization of the antenna was performed using the adaptively adjusted design specifications technique described in Section II. Figure 5 shows the fine and coarse model responses at the initial design (minimax specification error +6.0 dB), as well as the fine model response at the final design $\boldsymbol{x}^{(2)} = [10.81\ 5.75\ 28.5\ 32.25\ 19.5]^T$ mm (specification error is –0.2 dB) obtained after two iterations of our procedure. The total number of evaluations of the coarse model in the optimization process is 87. Table 1 shows the computational cost of the optimization: the total optimization time corresponds to only 6.5 evaluations of the fine model. For comparison purposes, the direct optimization of the fine model using Matlab's *fminimax* routine was performed using $\boldsymbol{x}^{(0)}$ as a starting point. A slightly better design was obtained (with the specification error of –0.5 dB) at much higher cost of 55 fine model evaluations (almost 115 hours of CPU time).

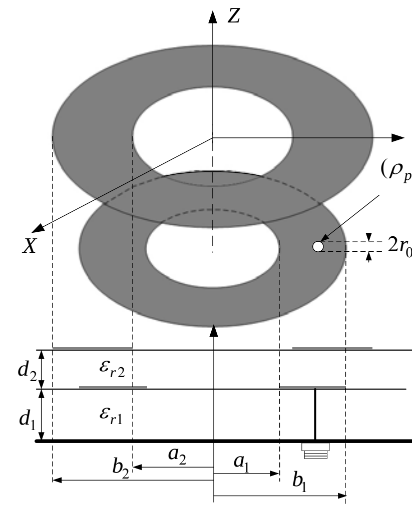

Fig. 4. Geometry of a stacked probe-fed printed double annular ring antenna [22].

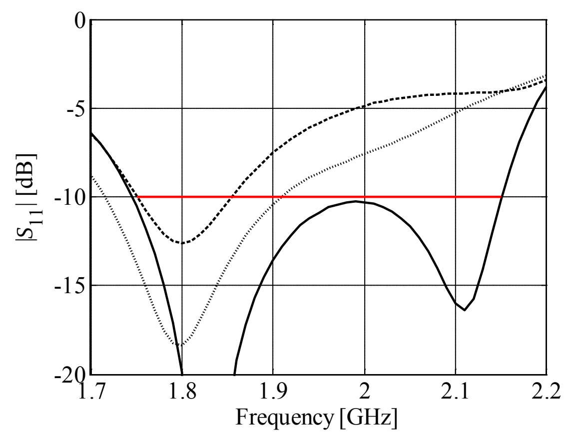

Fig. 5. Double annular ring antenna: High- (- - -) and low-fidelity (· · ·) model responses at the initial design $\boldsymbol{x}^{(0)}$, and the high-fidelity model response at the final design found by the adaptive design specifications technique (—).

Table 1: Computational cost of optimizing the double annular ring antenna

Algorithm Component	Number of Model Evaluations	Optimization Time	
		Absolute [min]	Relative#
Evaluation of $\boldsymbol{R}_c$	87	565	4.5
Evaluation of $\boldsymbol{R}_f$	2*	250	2.0
Total optimization time	N/A	815	6.5

* Excluded evaluation of the fine model at the initial design
# Number of high-fidelity model evaluations

B. Miniature dual-mode bandpass microstrip filter [24]

Consider the miniature dual-mode bandpass filter [24] shown in Fig. 6. The design parameters are $\boldsymbol{x} = [L\ s\ p\ g]^T$; W = 1 mm, W_c = 0.5 mm. Both the fine and coarse models are evaluated in FEKO [23]. The total mesh number for the fine model is 646 (evaluation time 20 min), the total mesh number for the coarse model is 68 (evaluation time 26 seconds). The design specifications are $|S_{21}| \geq -1$ dB for 2.35 GHz $\leq \omega \leq$ 2.45 GHz, $|S_{21}| \leq -20$ dB for 1.6 GHz $\leq \omega \leq$ 2.2 GHz and for 2.6 GHz $\leq \omega \leq$ 3.2 GHz. The initial design is $\boldsymbol{x}^{(0)} = [12.0\ 2.0\ 2.0\ 0.2]^T$ mm.

The adaptively adjusted design specifications technique of Section 2 was used to optimize the filter. Figure 7 shows the fine model and coarse model responses at the initial design (minimax specification error +19.6 dB), as well as the fine model response at the final design $\boldsymbol{x}^{(3)} = [12.65\ 1.99\ 1.38\ 0.145]^T$ mm (specification error is –0.2 dB) obtained after three iterations of the optimization procedure. The total number of evaluations of the coarse model in the optimization process is 137. The total cost of the design process corresponds to only 5.9 evaluations of the fine model (Table 2). For comparison purposes, the direct optimization of the fine model using Matlab's *fminimax* routine was performed using $\boldsymbol{x}^{(0)}$ as a starting point. This direct optimization failed to find a design satisfying the specifications (algorithm terminated after 120 function evaluations, i.e., 40 hours of CPU time, best design found corresponds to +5.2 dB). Optimization of the fine model using pattern search algorithm [25] resulted in the satisfactory design (specification error –0.4 dB); however, the cost was quite high (97 fine model evaluations, over 32 hours of CPU time).

C. UWB monopole antenna

The monopole is on a 0.508 mm thick Rogers RO3203 substrate. Design variables are $\boldsymbol{x} = [h_0\ w_0\ a_0\ s_0\ h_1\ w_1\ l_{gnd}\ w_s]^T$ (Fig. 8). Other parameters: l_s = 25, w_m = 1.25, h_p =0.75 (all in mm). The microstrip input of the monopole is fed through an edge mount SMA connector [26] having a hex nut. The ground of the monopole has a profiled edge. Both high- and low-fidelity models are evaluated using the time-domain solver of CST Microwave Studio [27]. Simulation time of $\boldsymbol{R}_c$ (152,640 mesh cells) is 2 min, and that of $\boldsymbol{R}_f$ (1,151,334 mesh cells) is 45 min (both at the initial design). The design specifications for reflection are $|S_{11}| \leq -10$ dB for 3.1 GHz to 10.6 GHz. Additionally, the radiation pattern of the monopole is to be omnidirectional in the *XOY* plane.

Initial design $\boldsymbol{x}^{(0)} = [18\ 12\ 2\ 0\ 5\ 1\ 15\ 40]^T$ mm. Optimization performed using the adaptively adjusted design specifications technique yields the final design $\boldsymbol{x}^{(3)} = [18.27\ 19.41\ 2.02\ 1.34\ 1.95\ 5.83\ 15.74\ 35.75]^T$ mm ($|S_{11}| < -14.5$ dB in the frequency band of interest) obtained after three iterations of our procedure. Figure 9 shows reflection responses of the high- and low-fidelity models at the initial design as well as the $\boldsymbol{R}_f$ response at the final design. The far-field response of the final design is shown in Fig. 10. The total number of evaluations of $\boldsymbol{R}_c$ in the optimization process is 252. Table 3 shows the computational cost of the optimization: the total optimization time corresponds to about 14 evaluations of the high-fidelity model.

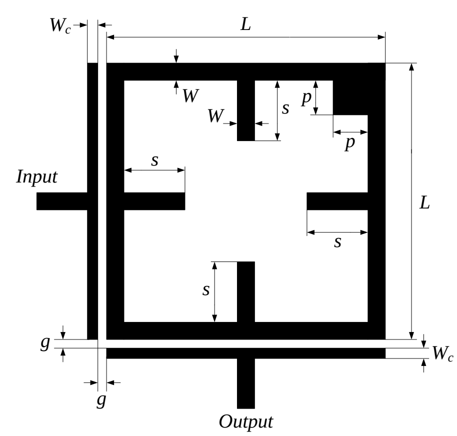

Fig. 6. Miniature dual-mode bandpass filter: geometry [24].

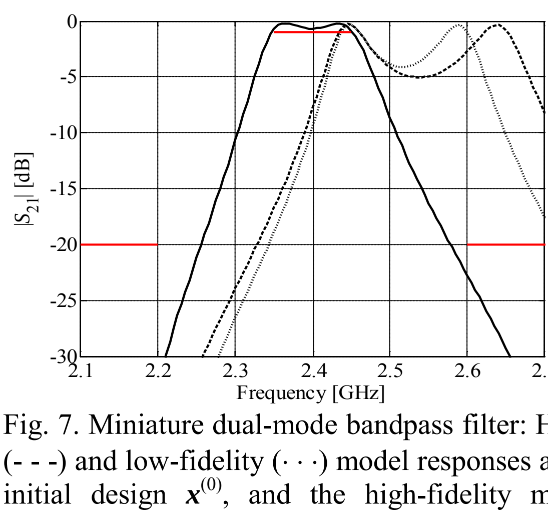

Fig. 7. Miniature dual-mode bandpass filter: High- (- - -) and low-fidelity (· · ·) model responses at the initial design $\boldsymbol{x}^{(0)}$, and the high-fidelity model response at the final design found by the adaptive design specifications technique (—).

Table 2: Computational cost of optimizing the miniature dual-mode bandpass filter

Algorithm Component	Number of Model Evaluations	Optimization Time	
		Absolute [min]	Relative#
Evaluation of $\boldsymbol{R}_c$	137	59	2.9
Evaluation of $\boldsymbol{R}_f$	3*	60	3.0
Total optimization time	N/A	119	5.9

* Excluded evaluation of the fine model at the initial design
\# Number of high-fidelity model evaluations

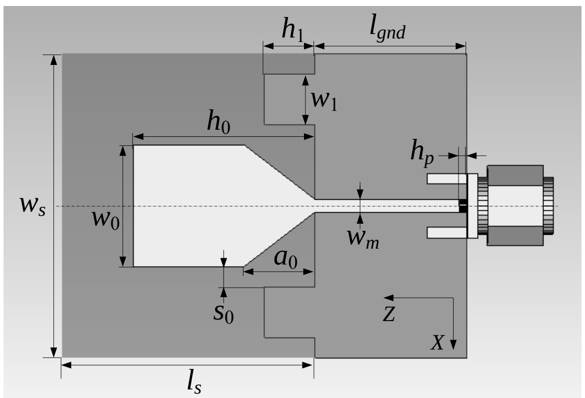

Fig. 8. UWB monopole: top view, substrate shown transparent. H-symmetry wall is shown with the dash-dot line.

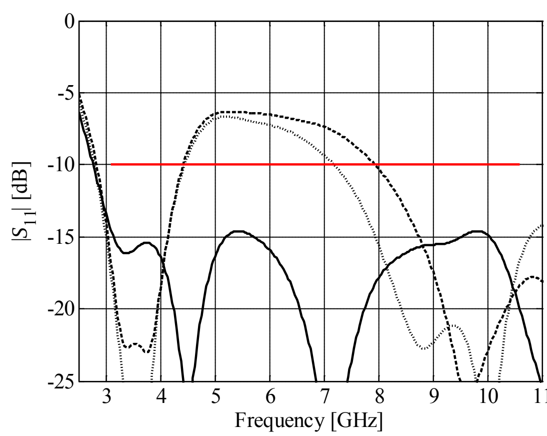

Fig. 9. UWB monopole antenna: High- (dashed line) and low-fidelity (dotted line) model responses at the initial design $\boldsymbol{x}^{(0)}$, and the high-fidelity model response at the final design found by the adaptive design specifications technique (solid line).

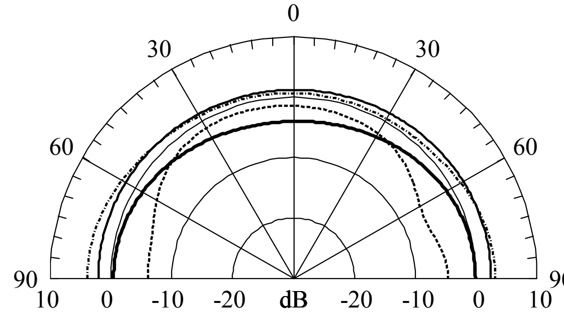

Fig. 10. Realized gain (x-pol.) of the UWB monopole: pattern cut in XOY plane at 3 GHz (—), 5 GHz (▬), 7 GHz (- · · · -), and 9 GHz (- - -). 90^0 on the left, 0^0, and 90^0 on the right are for Y, X, and $-Y$ directions, respectively.

Table 3: Computational cost of optimizing the UWB monopole antenna

Algorithm Component	Number of Model Evaluations	Optimization Time	
		Absolute [hours]	Relative#
Evaluation of $\boldsymbol{R}_c$	252	8.4	11.2
Evaluation of $\boldsymbol{R}_f$	3*	2.3	3.0
Total optimization time	N/A	10.7	14.2

* Excluded evaluation of the fine model at the initial design
\# Number of high-fidelity model evaluations

IV. CONCLUSION

An efficient procedure for design optimization of EM-simulated microwave devices is discussed. The presented approach exploits a computationally cheap model of the structure under consideration, evaluated using the same electromagnetic solver but with coarse discretization. The misalignment between the low- and high-fidelity EM models is absorbed by suitable adjustments of the design specifications. The performance of the presented technique is demonstrated through the design of the double annular ring antenna, the microstrip bandpass filter, and the UWB monopole antenna. Satisfactory designs are obtained at the computational cost corresponding to a few high-fidelity EM simulations of the respective structures.

ACKNOWLEDGMENT

This work was supported in part by the Icelandic Centre for Research (RANNIS) Grant 110034021.

REFERENCES

[1] H. Schantz, *The Art and Science of Ultrawideband Antennas*, Artech House, 2005.

[2] A. Petosa, *Dielectric Resonator Antenna Handbook*, Artech House, 2007.

[3] K. Wu, "Substrate Integrated Circuits (SiCs) – A New Paradigm for Future Ghz and Thz Electronic and Photonic Systems," *IEEE Circuits and Systems Society Newsletter,* vol. 3, no. 2, Apr. 2009.

[4] R. V. Snyder, "Practical Aspects of Microwave Filter Development," *IEEE Microwave Magazine*, vol. 8, no. 2, pp. 42-54, Apr. 2007.

[5] S. Shin and S. Kanamaluru, "Diplexer Design using EM and Circuit Simulation Techniques," *IEEE Microwave Magazine*, vol. 8, no. 2, pp. 77-82, Apr. 2007.

[6] V. Rizzoli, A. Costanzo, D. Masotti, and P. Spadoni, "Circuit-Level Nonlinear/Electromagnetic Co-Simulation of an Entire Microwave Link," *IEEE MTT-S Int. Microwave Symp. Dig.*, Long Beach, CA, pp. 813-816, June 2005.

[7] N. V. Queipo, R. T. Haftka, W. Shyy, T. Goel, R. Vaidynathan, and P. K. Tucker, "Surrogate-Based Analysis and Optimization," *Progress in Aerospace Sciences*, vol. 41, no. 1, pp. 1-28, Jan. 2005.

[8] A. I. J. Forrester and A. J. Keane, "Recent Advances in Surrogate-Based Optimization," *Prog. in Aerospace Sciences*, vol. 45, no. 1-3, pp. 50-79, Jan.-April 2009.

[9] J. W. Bandler, Q. S. Cheng, S. A. Dakroury, A. S. Mohamed, M. H. Bakr, K. Madsen, and J. Søndergaard, "Space Mapping: The State of the Art," *IEEE Trans. Microwave Theory Tech.*, vol. 52, no. 1, pp. 337-361, Jan. 2004.

[10] D. Echeverria and P. W. Hemker, "Space Mapping and Defect Correction," *CMAM The International Mathematical Journal Computational Methods in Applied Mathematics,* vol. 5, no. 2, pp. 107-136, 2005.

[11] S. Amari, C. LeDrew, and W. Menzel, "Space-Mapping Optimization of Planar Coupled-Resonator Microwave Filters," *IEEE Trans. Microwave Theory Tech.*, vol. 54, no. 5, pp. 2153-2159, May 2006.

[12] S. Koziel, Q. S. Cheng, and J. W. Bandler, "Space Mapping," *IEEE Microwave Magazine*, vol. 9, no. 6, pp. 105-122, Dec. 2008.

[13] G. Crevecoeur, P. Sergeant, L. Dupre, and R. Van de Walle, "Two-Level Response and Parameter Mapping Optimization for Magnetic Shielding," *IEEE Trans. on Magnetics*, vol. 44, no. 2, pp. 301-308, Feb. 2008.

[14] M. F. Pantoja, P. Meincke, and A. R. Bretones, "A Hybrid Genetic-Algorithm Space-Mapping Tool for the Optimization of Antennas," *IEEE Trans. Antennas and Propagation*, vol. 55, no. 3, Part 1, pp. 777-781, March 2007.

[15] T. V. Tran, S. Brisset, and P. Brochet, "A New Efficient Method for Global Multilevel Optimization Combining Branch-and-Bound and Space Mapping," *IEEE Trans. Magn.*, vol. 45, no. 3, pp. 1590-1593, 2009.

[16] J. Quyang, F. Yang, H. Zhou, Z. Nie, and Z. Zhao, "Conformal Antenna Optimization with Space Mapping," *J. of Electromagn. Waves and Appl.*, vol. 24, no. 2-3, pp. 251-260, 2010.

[17] D. Swanson and G. Macchiarella, "Microwave Filter Design by Synthesis and Optimization," *IEEE Microwave Magazine*, vol. 8, no. 2, pp. 55-69, Apr. 2007.

[18] J. C. Rautio, "Perfectly Calibrated Internal Ports in EM Analysis of Planar Circuits," *IEEE MTT-S Int. Microwave Symp. Dig.*, Atlanta, GA, pp. 1373-1376, June 2008.

[19] S. Koziel, J. Meng, J. W. Bandler, M. H. Bakr, and Q. S. Cheng, "Accelerated Microwave Design Optimization with Tuning Space Mapping," *IEEE Trans. Microwave Theory and Tech.*, vol. 57, no. 2, pp. 383-394, 2009.

[20] Q. S. Cheng, J. W. Bandler, and S. Koziel, "Space Mapping Design Framework Exploiting Tuning Elements," *IEEE Trans. Microwave Theory and Tech.*, vol. 58, no. 1, pp. 136-144, 2010.

[21] S. Koziel, "Efficient Optimization of Microwave Structures through Design Specifications Adaptation," *IEEE Int. Symp. Antennas Prop.*, Toronto, Canada, 2010.

[22] D. M. Kokotoff, J. T. Aberle, and R. B. Waterhouse, "Rigorous Analysis of Probe-Fed Printed Annular Ring Antennas," *IEEE Trans. Antennas Propagat*, vol. 47, no. 2, pp. 384-388, Feb. 1999.

[23] FEKO, Suite 5.3, EM Software & Systems-S.A. (Pty) Ltd, 32 Techno Lane, Technopark, Stellenbosch, 7600, South Africa, 2008.

[24] Y. F. Lin, C. H. Chen, K. Y. Chen, H. M. Chen, and K. L. Wong, "A Miniature Dual-Mode Bandpass Filter using Al_2O_3 Substrate," *IEEE Microw. Wireless Compon. Lett.*, vol. 17, no. 8, pp. 580-582, Aug. 2007.

[25] T. G. Kolda, R. M. Lewis, and V. Torczon, "Optimization by Direct Search: New Perspectives on Some Classical and Modern Methods," *SIAM Review*, vol. 45, no. 3, pp. 385-482, 2003.

[26] SMA Edge Mount P.C. Board Receptacles, Catalog, Applied Engineering Products, New Haven, CT, USA.

[27] CST Microwave Studio, ver. 2009, CST AG, Bad Nauheimer Str. 19, D-64289 Darmstadt, Germany, 2009.

[28] D. Echeverria and P.W. Hemker, "Space mapping and defect correction," *CMAM Int. Mathematical Journal Computational Methods in Applied Mathematics,* vol. 5, pp. 107-136, 2005.

[29] S. Koziel, "Multi-Fidelity Optimization of Microwave Structures using Response Surface Approximation and Space Mapping," *Applied Computational Electromagnetic Society (ACES) Journal*, vol. 24, no. 6, pp. 600–608, December 2009.

[30] S. Koziel, "Computationally Efficient Multi-fidelity Multi-Grid Design Optimization of Microwave Structures," *Applied Computational Electromagnetic Society (ACES) Journal*, vol. 25, no. 7, pp. 578–586, July 2010.

[31] D. Deslandes and K. Wu, "Analysis and Design of Current Probe Transition from Grounded Coplanar to Substrate Integrated Rectangular Waveguides," *IEEE Trans. Microw. Theory Tech.*, vol. 53, no. 8, Aug. 2005, pp. 2487-2494.

Slawomir Koziel received the M.Sc. and Ph.D. degrees in Electronic Engineering from Gdansk University of Technology, Poland, in 1995 and 2000, respectively. He also received the M.Sc. degrees in Theoretical Physics and in Mathematics, in 2000 and 2002, respectively, as well as the Ph.D. in Mathematics in 2003, from the University of Gdansk, Poland. He is currently an Associate Professor with the School of Science and Engineering, Reykjavik University, Iceland. His research interests include CAD and modeling of microwave circuits, surrogate-based optimization, space mapping, circuit theory, analog signal processing, evolutionary computation and numerical analysis.

Direct Field and Mixed Potential Integral Equation Solutions by Fast Fourier Transform Accelerated Multilevel Green's Function Interpolation for Conducting and Impedance Boundary Objects

Dennis T. Schobert and Thomas F. Eibert

Lehrstuhl für Hochfrequenztechnik
Technische Universität München
Arcisstr. 21, 80333 München, Munich, Germany
schobert@ieee.org

Abstract ─ A fast solver based on multilevel Lagrange interpolation of homogenous space electric and magnetic field Green's functions is discussed. Broadband applications are possible due to a wavelength adaptive multilevel scheme. By an FFT-technique, the pertinent translation operators are diagonalized. An impedance boundary condition (IBC) is employed considering electric and magnetic currents for the approximate treatment of non-metallic objects. The common mixed-potential integral equation and a direct field formulation are both discussed. In general, the direct field formulation leads to more accurate results in conjunction with interpolated Green's functions, especially for low frequency problems. The efficiency of the algorithm is shown in several numerical examples.

Index Terms ─ Electromagnetic radiation, electromagnetic scattering, fast integral solvers, integral equations.

I. INTRODUCTION

Surface integral equation methods belong to the most efficient techniques for solving electromagnetic scattering or radiation problems. When employing method of moments (MoM) discretization, the integral equation (IE) operators are converted into matrix vector products [1, 2]. Unfortunately, these IE operators are in general fully populated, causing bad numerical complexities. This makes the computation of problems with many unknowns very challenging. Hierarchical fast solvers have been introduced to overcome this problem. One of the most popular methods is the multilevel fast multipole method (MLFMM) [2]. In this method, discretization elements with small separations are grouped hierarchically and far-range interactions are computed among groups of basis functions on appropriate levels in the accordant hierarchy. Interactions between the single basis/testing functions are just contained in the translation operators between elements, which are very close to each other. Due to the strongly increasing magnitude of the Hankel functions, the MLFMM suffers a low frequency breakdown. This makes the numerical evaluation of the MLFMM diagonal plane wave based translation operators very difficult [2]. Hence, other approaches have to be found. One possibility to overcome this drawback is to include evanescent waves within the respective translation operators to better capture reactive fields [3]. Furthermore, it is also possible to work with the standard multipole-based translation operators at low frequencies [4], which are full operators. With respect to the diagonal MLFMM, both approaches have increased computational complexity.

For approximating smoother fields at lower frequencies, polynomial field representations appear to be very appropriate as low interpolation orders may be sufficient. One popular method working with a non-hierarchical approximation on a grid of equally spaced points covering all objects is the adaptive integral method (AIM) [7]. Although the approximation itself is non-hierarchical, a hierarchical acceleration of the translation step is performed by an FFT. Due to the AIM grid structure, empty portions of the solution domain are also covered causing unnecessary computations.

A hierarchical method employing multilevel Taylor series expansion of the respective Green's functions is presented in [5]. In [6], a method based on Lagrange interpolation of the Green's functions is proposed. The advantage of Lagrange interpolation is its rather constant approximation

Submitted On: June 29, 2011
Accepted On: September 12, 2011

error throughout the interpolation domain due to several interpolation points, whereas the approximation error of the Taylor expansion increases with distance from the single expansion point.

In this contribution, a method working with multilevel Lagrange interpolation based polynomial factorization of Green's functions, which is fully compatible with the well-known MLFMM oct-tree is presented. Firstly introduced in [8] for perfectly electric conducting (PEC) objects and mixed-potential electric field integral equation (MPIE) formulation, the method has been expanded for the treatment of IBC objects. The method is also applied to magnetic field integral equation (MFIE). Mixed-potential and dyadic integral equation formulations for electric and magnetic currents are considered and compared. The translations are only performed between non-empty boxes within the multilevel configuration. On the various levels, translations are accelerated by FFT without loss of accuracy. Due to the involved oct-tree structure, near-couplings can be computed by direct-MoM. Hence, no pre-correction step is necessary as in AIM or other pre-corrected FFT methods. The excellent performance of the algorithm, especially for low-frequency applications, is demonstrated in several examples.

II. INTEGRAL EQUATION FORMULATION

Consider a time-harmonic (time dependence $e^{j\omega t}$ suppressed) discretized surface integral equation (IE)

$$\left[Z_J\right]\left\{J\right\}+\left[Z_M\right]\left\{M\right\}=\left\{e\right\}. \tag{1}$$

$\{J\}$ and $\{M\}$ are the unknown electric and magnetic surface current expansion coefficient vectors and $\{e\}$ is the excitation vector due to an incident plane wave or a delta-gap source [1, 2]. Rao-Wilton-Glisson (RWG) vector basis functions $\mathbf{b}_n(\mathbf{r}')$ and either RWG or $\hat{n}$ ×RWG testing functions $\mathbf{a}_m(\mathbf{r}) = \hat{n} \times \mathbf{b}_m(\mathbf{r})$, $\hat{n}$ being the respective surface normal vector, are employed.

The respective MoM matrix entries are given by

$$\begin{aligned} Z_{mn,J}^{direct} &= -j\omega\mu\alpha\left\langle \mathbf{b}_m(\mathbf{r}),\mathbf{L}\left(\mathbf{b}_n(\mathbf{r}')\right)\right\rangle \\ &\quad +\frac{Z}{2}(1-\alpha)\left[\left\langle \mathbf{a}_m(\mathbf{r}),\mathbf{a}_n(\mathbf{r})\right\rangle\right. \\ &\quad \left. +2\left\langle \mathbf{a}_m(\mathbf{r}),\mathbf{K}\left(\mathbf{b}_n(\mathbf{r}')\right)\right\rangle\right], \end{aligned} \tag{2}$$

$$\begin{aligned} Z_{mn,M}^{direct} &= -\frac{\alpha}{2}\left[\left\langle \mathbf{b}_m(\mathbf{r}),\mathbf{a}_n(\mathbf{r})\right\rangle\right. \\ &\quad \left. +2\left\langle \mathbf{b}_m(\mathbf{r}),\mathbf{K}\left(\mathbf{b}_n(\mathbf{r}')\right)\right\rangle\right] \\ &\quad -j\omega Z\varepsilon\left(1-\alpha\right)\left\langle \mathbf{a}_m(\mathbf{r}),\mathbf{L}\left(\mathbf{b}_n(\mathbf{r}')\right)\right\rangle, \end{aligned} \tag{3}$$

with the inner product

$$\left\langle \mathbf{v}(\mathbf{r}),\mathbf{w}(\mathbf{r})\right\rangle = \iint_A \mathbf{v}(\mathbf{r})\cdot\mathbf{w}(\mathbf{r})da \tag{4}$$

and the operators

$$\begin{aligned} \mathbf{L}\left(\mathbf{v}(\mathbf{r}')\right) &= \iint_{A'} \bar{\mathbf{G}}(\mathbf{r},\mathbf{r}')\cdot\mathbf{v}(\mathbf{r}') \\ \mathbf{K}\left(\mathbf{v}(\mathbf{r}')\right) &= \iint_{A'} \nabla G(\mathbf{r},\mathbf{r}')\times\mathbf{v}(\mathbf{r}'). \end{aligned} \tag{5}$$

The excitation vector elements are

$$\begin{aligned} e_m(\mathbf{r}) &= -\iint_A \left\{\mathbf{b}_m(\mathbf{r})\cdot\alpha\left[\mathbf{E}^{inc}(\mathbf{r})\right.\right. \\ &\quad \left.\left. +Z(1-\alpha)(\hat{n}\times\mathbf{H}^{inc}(\mathbf{r}))\right]\right\}da. \end{aligned} \tag{6}$$

The parameters $\boldsymbol{\mu}$, $\boldsymbol{\varepsilon}$, $\boldsymbol{k}$ and $\boldsymbol{Z} = \sqrt{\boldsymbol{\mu}/\boldsymbol{\varepsilon}}$ are the permeability, permittivity, wavenumber and wave impedance of free-space. $\boldsymbol{G}(\mathbf{r},\mathbf{r}') = \boldsymbol{e}^{-\boldsymbol{j}\boldsymbol{k}|\mathbf{r}-\mathbf{r}'|}/(\mathbf{4}\boldsymbol{\pi}|\mathbf{r}-\mathbf{r}'|)$ is the homogeneous space scalar Green's function, $\bar{\mathbf{G}}(\mathbf{r},\mathbf{r}') = \left(\bar{\mathbf{I}} + \mathbf{1}/\boldsymbol{k}^{\mathbf{2}}\,\nabla\nabla\right)\boldsymbol{G}(\mathbf{r},\mathbf{r}')$ the electric field dyadic Green's function, and $\boldsymbol{\alpha}$ the so-called combined field integral equation (CFIE) combination parameter with $\mathbf{0} \leq \boldsymbol{\alpha} \leq \mathbf{1}$. $\mathbf{E}^{\boldsymbol{inc}}(\mathbf{r})$ and $\mathbf{H}^{\boldsymbol{inc}}(\mathbf{r})$ are the electric and magnetic field strength due to the respective excitation.

No magnetic surface currents $\mathbf{M}_{\boldsymbol{A}}$ with the expansion coefficients $\{\boldsymbol{M}\}$ occur at the respective Huygens' surface if a PEC object is analyzed and equations (1) and (2) determine a unique solution for $\{\boldsymbol{J}\}$. However, in general this set of equations is under-determined and additional equations are required. For this purpose, the common impedance boundary condition [10] is utilized for dielectrically coated PEC objects. The IBC is defined on the boundary between the exterior of the coating and the surrounding medium. It is formulated as

$$\mathbf{M}_A = Z_A(\mathbf{J}_A\times\hat{\boldsymbol{n}}). \tag{7}$$

$\boldsymbol{Z_A}$ is the characteristic surface impedance which can be approximated according to [10] as $\boldsymbol{Z_A} \approx \boldsymbol{jZ}\sqrt{\boldsymbol{\mu_r}/\boldsymbol{\varepsilon_r}}\,\mathbf{tan}(\boldsymbol{kd}\sqrt{\boldsymbol{\mu_r}\boldsymbol{\varepsilon_r}})$ with the relative permeability and permittivity $\boldsymbol{\mu_r}$ and $\boldsymbol{\varepsilon_r}$ and the thickness $\boldsymbol{d}$ of the coating. The IBC (7) is then discretized according to [11] and the resulting equations are directly considered within an iterative solver.

The hyper-singular integrals in (2) and (3) can be avoided by the so-called mixed-potential formulation which has only weak $\mathbf{1/R}$-singularities with $\boldsymbol{R} = |\mathbf{r} - \mathbf{r}'|$. After applying some vector-analytic manipulations to (2) and (3), especially the surface divergence theorem [1], the inner products involving $\boldsymbol{\nabla\nabla G}(\mathbf{r}, \mathbf{r}')$ are rewritten in the following manner [11]:

$$\begin{aligned} \left\langle \mathbf{a}(\mathbf{r}), \mathbf{L}_{\nabla\nabla}\left(\mathbf{b}(\mathbf{r}')\right)\right\rangle &= \oint_{C_m} \mathbf{a}(\mathbf{r}) \cdot \hat{u}_m L_S\left(\nabla \cdot \mathbf{b}(\mathbf{r}')\right) dC_m \\ \left\langle \mathbf{b}(\mathbf{r}), \mathbf{L}_{\nabla\nabla}\left(\mathbf{b}(\mathbf{r}')\right)\right\rangle &= \left\langle \nabla \cdot \mathbf{b}(\mathbf{r}), L_S\left(\nabla \cdot \mathbf{b}(\mathbf{r}')\right)\right\rangle, \end{aligned} \tag{8}$$

with the operators

$$\begin{aligned} \mathbf{L}_{\nabla\nabla}\left(\mathbf{v}(\mathbf{r}')\right) &= \iint_{A'} \nabla\nabla G(\mathbf{r}, \mathbf{r}') \cdot \mathbf{b}(\mathbf{r}') da' \\ L_s\left(s(\mathbf{r}')\right) &= \iint_{A'} G(\mathbf{r}, \mathbf{r}') s(\mathbf{r}') da'. \end{aligned} \tag{9}$$

$\boldsymbol{C_m}$ is the boundary curve of the test domain and $\boldsymbol{\hat{u}_m}$ is the unit vector in the tangent plane and perpendicular to $\boldsymbol{C_m}$. The mixed-potential coupling integrals with (8) and (9) applied to (2) and (3), respectively, are named $\boldsymbol{Z_{mn,J}^{mixed}}$ and $\boldsymbol{Z_{mn,M}^{mixed}}$ in the following.

For reducing redundancy of the discretized IE operators, which are in general fully-populated with respect to the contained far-interactions, an appropriate basis change is performed for these far-interactions. The basis change is achieved by multilevel Lagrange interpolation of the pertinent Green's functions, where the current basis functions are mapped on the interpolation samples. A further speed-up is reached by FFT acceleration for the computation of the multilevel interactions among the interpolation samples.

III. LAGRANGE INTERPOLATION OF GREEN'S FUNCTIONS

The electric field dyadic Green's function $\overline{\mathbf{G}}(\mathbf{r}, \mathbf{r}')$, the scalar Green's function $G(\mathbf{r}, \mathbf{r}')$ and its gradient $\nabla G(\mathbf{r}, \mathbf{r}')$ can be factorized by Lagrange interpolation with respect to $\mathbf{r}$ and $\mathbf{r}'$ employing Lagrange interpolation factors according to

$$\begin{aligned} \tilde{\overline{\mathbf{G}}}(\mathbf{r}, \mathbf{r}') &= \sum_{i=1}^{N_p^3} \sum_{j=1}^{N_p^3} \Lambda_i(\mathbf{r}) \Lambda_j(\mathbf{r}') \overline{\mathbf{G}}_{ij}(\mathbf{r}_i, \mathbf{r}_j') \\ \tilde{G}(\mathbf{r}, \mathbf{r}') &= \sum_{i=1}^{N_p^3} \sum_{j=1}^{N_p^3} \Lambda_i(\mathbf{r}) \Lambda_j(\mathbf{r}') G_{ij}(\mathbf{r}_i, \mathbf{r}_j') \\ (\widetilde{\nabla G})(\mathbf{r}, \mathbf{r}') &= \sum_{i=1}^{N_p^3} \sum_{j=1}^{N_p^3} \Lambda_i(\mathbf{r}) \Lambda_j(\mathbf{r}') \nabla G_{ij}(\mathbf{r}_i, \mathbf{r}_j'), \end{aligned} \tag{10}$$

with $\Lambda_i(\mathbf{r})$ being the respective Lagrange polynomials and N_p the number of interpolation points. When inserted in equations (2) and (3), the resulting integrals can be pre-computed and do not have to be evaluated in every matrix-vector product within an iterative solver.

By this Lagrange interpolation point representation, an accelerated evaluation of the discretized IE operators can be achieved in two ways. First, the necessary number of interpolation points can be considerably smaller than the number of basis functions. This is in particular the case for low-frequency applications where very many discretization steps per wavelength are needed in order to represent fine geometrical details. Second, the coupling computation effort can be considerably reduced when employing an FFT-based coupling computation.

IV. DIAGONALIZATION OF THE TRANSLATION OPERATOR

The computational effort of the presented Lagrange interpolation based integral equation representation has a disadvantageous large computational effort for the far-interactions of $O\left(N_p^3 N_p^3\right) = O\left(N_p^6\right)$ for one pair of interpolation domains (3D cubes) with N_p being the number of interpolation points. This is because the interpolations must in general be performed in three dimensions, even if a surface integral equation is considered. Furthermore, the corresponding translation operators are still full operators.

To overcome this drawback, an FFT-based method for diagonalizing the corresponding translation operators is employed. In particular the formulation for $Z_{mn,J}^{direct}$ according to (1) and (2) is considered but everything applies in similar form also for $Z_{mn,J}^{mixed}$ and all other matrices. The approximated matrix $\tilde{Z}_{mn,J}$ with the interpolated dyadic Green's function according to (10) can be formulated as

$$\tilde{Z}_{mn,J} = \sum_{i=1}^{N_p^3} \iint_A \Lambda_i(\mathbf{r})\mathbf{b}_m(\mathbf{r})da \cdot \sum_{j=1}^{N_p^3} \bar{\mathbf{G}}(\mathbf{r}_i,\mathbf{r}_j') \cdot \iint_{A'} \Lambda_j(\mathbf{r}')\mathbf{b}_n(\mathbf{r}')da'. \quad (11)$$

As it can be seen, the Green's function is factorized by the Lagrange interpolation with respect to $\mathbf{r}$ and $\mathbf{r}'$ so that the integrals in (11) can be pre-computed.

Employing tensor notation with third order tensors, each order corresponding to one Cartesian dimension, the j summation in (11) can be rewritten as

$$[\mathbf{R}]^3_{ix,iy,iz} = \sum_{ix'}^{N_p}\sum_{iy'}^{N_p}\sum_{iz'}^{N_p} \bar{\mathbf{G}}\left(\Delta i_x, \Delta i_y, \Delta i_z\right) \cdot [\mathbf{S}]^3_{ix',iy',iz'}, \quad (12)$$

with the third order tensors $[\mathbf{S}]^3$ and $[\mathbf{R}]^3$ containing the source or receive integrals, respectively, and $\Delta i_k = i_k - i'_k$. This discrete convolution in space domain with equidistant sampling can efficiently be computed in spectral domain according to

$$\begin{aligned}[\mathbf{R}]^3_{ix,iy,iz} &= \sum_{ix'=1}^{2N_p-1}\sum_{iy'=1}^{2N_p-1}\sum_{iz'=1}^{2N_p-1} \left[\bar{\mathbf{G}}\right]^3_{\Delta(ix,iy,iz)} \cdot [\mathbf{S}]^3_{ix',iy',iz'} \\ &= F^{-1}\left\{F\left\{\left[\bar{\mathbf{G}}\right]^3\right\} \otimes F\left\{[\mathbf{S}]^3\right\}\right\}.\end{aligned} \quad (13)$$

Zero-padding has to be performed in order to avoid aliasing errors. The symbol "$\otimes$" denotes the Hadamard (tensor element-wise) dyadic-vector product in the discrete Fourier domain. It is essential, that the necessary forward transformations F and backward transformations F^{-1} are performed by FFT to obtain enhanced computational efficiency when employing (13) instead of (11). In the end, the receive contributions in $[\mathbf{R}]^3$ must be multiplied with the test integrals. Since the translations are computed as Hadamard products in the discrete Fourier domain, diagonalization of the translation operators has been achieved. However, the computational complexity is then dominated by the transformations instead of the coupling computations itself. Together with the necessary zero-padding, the overall procedure appears to be efficient only for relatively large numbers of interpolation points, as e.g. obtained if the whole radiation or scattering object is covered with one regular grid.

By numerical experiments it was found that employing (13) is advantageous even for the small number of 3 interpolation points per Cartesian dimension. For cubic interpolation with $N_p = 4$, which is mostly a good choice for accurate computations, there is a reduction in translation time by a factor of about 7. Due to this observation, FFT-based translations are employed within this fast solver. The complexity of the translation is $O\left(N_p^3 \log N_p^3\right) = O\left(N_p^3 \log N_p\right)$ with respect to the number of interpolation points N_p instead of $O\left(N_p^6\right)$ for direct translation in space domain.

VI. MULTILEVEL ALGORITHM

One major drawback of grid based fast solvers is the general necessity to work with 3 dimensional grids although the problem itself is a 2 dimensional surface problem. Especially dominant is this drawback in AIM or pre-corrected FFT techniques. There, all coupling computations are performed by a global 3D FFT on a single grid covering the whole computation domain. Hence, most computations are performed for grid points located in the empty space inside the computation domain. To relieve this problem, a multilevel algorithm following a hierarchical oct-tree grouping strategy is developed, where regular grids within the individual groups are considered and where the translations among non-empty groups are computed by employing FFT-acceleration.

A cubic oct-tree structure as known from the MLFMM algorithm [2] is assumed. The distances d between different box centers on a given level lev are found to be

$$\begin{aligned} d_{lev}^{near} &= n_1 a_{lev} \\ d_{lev}^{far} &= n_2 a_{lev}. \end{aligned} \quad (14)$$

d_{lev}^{near} is the near-coupling range for each level lev, where the necessary interactions are computed on finer levels or by direct MoM integration. d_{lev}^{far} is the far-coupling range up to which far translations are performed on the corresponding level and a_{lev} is the edge length of each cube in the pertinent level. On all levels, the relation $a_{lev+1} = 2\, a_{lev}$ is valid.

The described Lagrange interpolation algorithm with FFT acceleration is employed for boxes with separations $d_{lev}^{near} \leq d \leq d_{lev}^{far}$. Interactions among boxes with $d > d_{lev}^{far}$ are computed on the next coarser level $lev + 1$. For levels with a small box-size as compared to wavelength, the number of interpolation points per dimension N_p^{lev} on a certain level lev can be kept constant on different levels as suggested in [12]. As the resulting impedance matrix is then an $\mathbf{H}^2$ -matrix [12], computational and storage complexity per matrix-vector product are $O(N)$. This strategy is only valid for fine levels with box sizes significantly smaller than the wavelength. Hence, we use this strategy if a_{lev+1}/λ is below a constant threshold r^{const}. Following this strategy, a coarser level source tensor $[\mathbf{S}^{lev+1}]^3$ is Lagrange anterpolated for aggregation case

$$\left[\mathbf{S}^{lev+1}\right]^3_{ix',iy',iz'} = \sum_{i_x=1}^{N_p}\sum_{i_y=1}^{N_p}\sum_{i_z=1}^{N_p} \Lambda_{ix,iy,iz,ix',iy',iz'} \left[\mathbf{S}^{lev}\right]^3_{ix,iy,iz}, \quad (15)$$

where the interpolation points on all levels are equally spaced in each dimension in order to realize a regular grid. The disaggregation procedure is performed in the same manner by interpolating finer level receive contributions from corresponding coarser level receive contributions. All aggregation factors can be pre-computed before evaluating the matrix-vector product. Due to the orthogonality of the Lagrange polynomials, the operators contain a lot of zero entries, which leads to computation time and memory reduction.

If the box size is not small compared to the wavelength, the absolute interpolation point distance is maintained on coarser levels. No Lagrange interpolation is necessary as all coarser level points are at the same position as at least one finer level interpolation point and the accordant Lagrange polynomials are orthogonal. Hence, (15) reduces to

$$\left[\mathbf{S}^{lev+1}\right]^3_{ix+\Delta ix,y+\Delta iy,z+\Delta iz} = \left[\mathbf{S}^{lev}\right]^3_{ix,iy,iz}, \quad (16)$$

for the aggregation case, whereas $N_p^{lev} = N_p$ at the finest level following this strategy and $N_p^{lev+1} = 2N_p^{lev} - 1$ for all subsequent coarser levels. $\Delta ix, \Delta iy,$ and Δiz are index offsets dependent on the position of the finer level group within the coarser level group.

For disaggregation case, the pertinent receive contributions from the coarser level have just to be copied on the finer level. Following this strategy, the computational complexity increases as the required number of interpolation points roughly doubles in each direction. The computational complexity following this strategy is $O\left(N^{3/2}\log(N)\right)$ in conjunction with FFT-based translations and is thus significantly worse compared to fast high frequency solvers like MLFMM with $O(N\log(N))$ complexity. The proposed algorithm is thus especially suited for low-frequency problems where the fine-level strategy can be employed for most levels.

VI. Dyadic versus mixed-potential MLIPFFT

The presented multilevel interpolatory FFT accelerated method (MLIPFFT) is employed to direct field integral equations according to (2) and (3) as well as to the more common mixed potential integral equations (MPIE) according to (8)-(10). In a previous work [9] it has been shown, that the MPIE is preferable for interpolation in well-conditioned problems as the computation time per matrix-vector product is smaller than for the EFIE and MFIE with dyadic Green's function formulation. For ill-conditioned problems, the direct field EFIE and MFIE with dyadic Green's functions are preferable as the isolated electric scalar potential and the superposition of the potential contributions of the MPIE usually need a higher interpolation accuracy.

VII. NUMERICAL RESULTS

The efficiency of the presented algorithm is shown for several computation examples. All computations shown in this section have been carried out on one core of a Dell Precision T7500 workstation (2.53 GHz clock speed, 96 GByte RAM).

As a linear equation system solver, a flexible generalized minimal residual solver with Given's rotations was used. As an iteration stop criterion, a residual error of 10^{-4} was configured.

A. Sphere with dielectric coating

A PEC sphere with diameter 1 m and a dielectric coating of 2.5 cm thickness ($\varepsilon_r = 4 - j100$) is computed as a first example. It is discretized by 176 472 unknowns (88 236 electric and magnetic current unknowns, respectively). The object is illuminated by a plane wave with a frequency of 500 MHz. In Fig. 1a, the bistatic radar cross section (RCS) of the sphere is depicted for an MLIPFFT computation employing the IBC (direct field formulation) compared to an analytical Mie series solution. As can be seen, both results show excellent agreement. Figure 1b shows the object and the resulting magnetic current distribution. For the MLIPFFT, the total solution time was 2 171 sec with a memory consumption of 1 522 MByte.

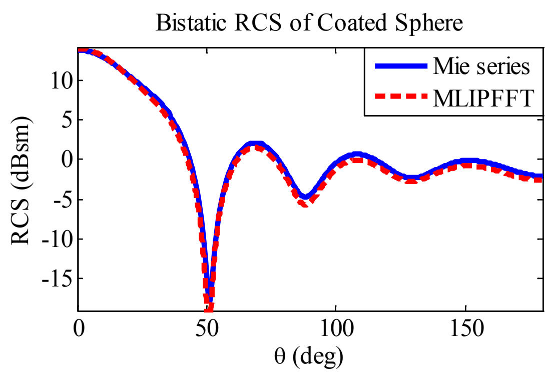

Fig. 1a. Bistatic RCS of a sphere with dielectric coating.

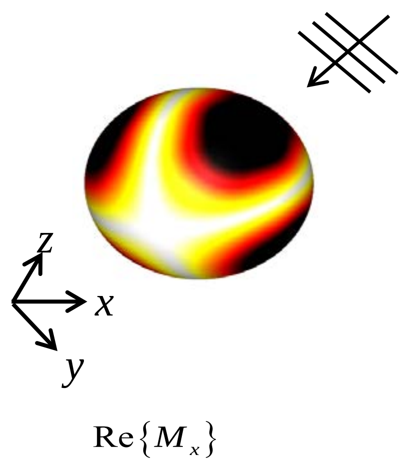

Fig. 1b. x-component of magnetic current distribution on dielectric sphere (real part).

B. Parabolic reflector

The second example is a 3λ PEC parabolic reflector, which is vertically illuminated by a plane wave. The reflector is densely discretized resulting in 222 583 unknowns. The MLIPFFT computation employing a mixed-potential EFIE was performed within 5 577 sec and with a total memory consumption of 1 873 MByte. For comparison, the computation was also performed by an MLFMM within 9 066 sec and with 9 475 MByte memory consumption. Both RCS results are shown in Fig. 2a and the accordant current distribution in Fig. 2b.

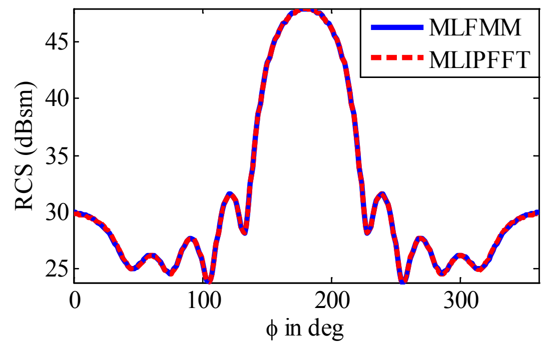

Fig. 2a. Bistatic θφ-RCS of a parabolic reflector.

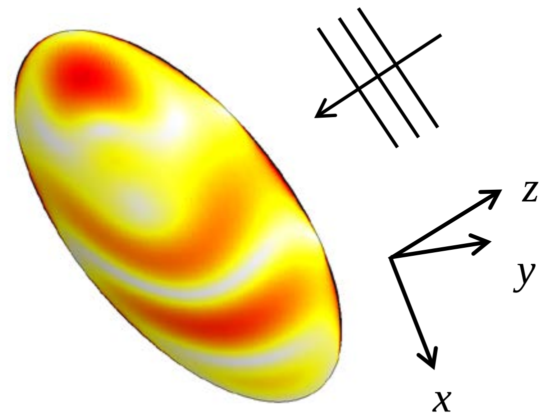

Fig. 2b. Electric current distribution on parabolic reflector (real part).

C. P3-Orion

The last example is the flight object "P3-Orion" with a length of 35 m. At first, the object's surface material is PEC. The object is discretized with 536 250 electric current unknowns and illuminated by a plane wave incident from $\theta_i = 90°, \varphi_i = 20°$ with a wavelength of 36 m. The accordant MLIPFFT computation time was 12 675 sec and the required memory 7 718 MByte. Second, the problem was computed for a finite conducting coating ($\sigma = 10^{-1}$ S/m) of the object employing IBC. The computation time was 18 793 sec and the memory demand 13 610 MByte. The accordant bistatic φθ-RCS results are depicted in Fig. 3a. Figure 3b shows the object and the electric current distribution.

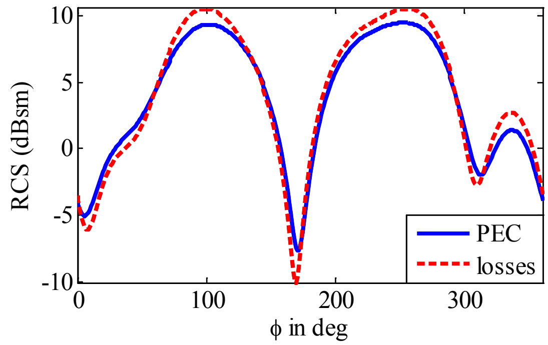

Fig. 3a. Bistatic RCS of P3-Orion.

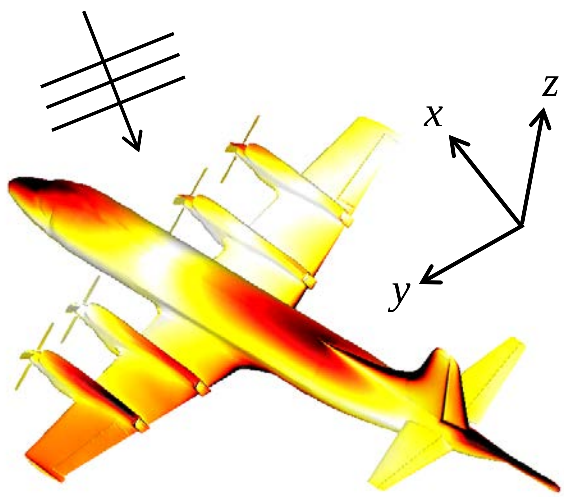

Fig. 3b. Electric current distribution on P3-Orion.

VIII. CONCLUSIONS

A fast integral equation fast solver, which is especially suited for low frequencies, has been presented. By 3D FFT, the accordant translation operators are diagonalized. Even for small numbers of interpolation points, this FFT-based technique has shown to be effective. Furthermore, an oct-tree based adaptive multilevel scheme reduces the computation of empty space and makes the algorithm useful for broadband applications and combinable with a high-frequency fast solver. The interpolation-based fast solver has demonstrated excellent efficiency and accuracy for PEC and impedance boundary body problems.

REFERENCES

[1] S. M. Rao, D. R. Wilton, and A. W. Glisson, "Electromagnetic Scattering by Surfaces of Arbitrary Shape", *IEEE Trans. Antennas Propagat.*, vol. 30, no. 3, pp. 409–418, May 1982.

[2] W. C. Chew, J. Jin, E. Michielssen, and J. Song, *Fast and Efficient Algorithms in Computational Electromagnetics*, Boston, MA: Artech House, 2001.

[3] D. Wulf and R. Bunger, "An Efficient Implementation of the Combined Wideband MLFMA/LF-FIPWA," *IEEE Trans. Antennas Propagat.*, vol. 57, no. 12, pp. 467–474, Feb 2009.

[4] L. J. Jiang and W. C. Chew, "A Mixed-Form Fast Multipole Algorithm," *IEEE Trans. Antennas Propagat.,* vol. 53, no. 12, pp. 4145–4156, Dec. 2005.

[5] M. Vikram, H. Huang, B. Shanker, and T. Van, "A Novel Wideband FMM for Fast Integral Equation Solution of Multiscale Problems in Electromagnetics," *IEEE Trans. Antennas Propagat.*, vol. 57, no. 7, pp. 2094–2104, July 2009.

[6] H. Wang and C. Chan, "The Implementation of Multilevel Green's Function Interpolation Method for Full-Wave Electromagnetic Problems," *IEEE Trans. Antennas Propagat.*, vol. 55, no. 5, pp. 1348 –1358, May 2007.

[7] E. Bleszynski, M. Bleszynski, and T. Jaroszewicz, "AIM: Adaptive Integral Method for Solving Large-Scale Electromagnetic Scattering and Radiation Problems," *Radio Sci.,* vol. 31, pp. 1225–1251, 1996.

[8] D. Schobert and T. Eibert, "A Multilevel Interpolating Fast Integral Solver with Fast Fourier Transform Acceleration," *URSI EMTS*, pp. 539–542, 2010.

[9] D. T. Schobert, T. F. Eibert, and C. H. Schmidt, "Fast Fourier Transform Accelerated Multilevel Green's Function Interpolation for Mixed Potential and Direct Field Surface Integral Equations," *EUCAP Conference*, pp. 3208 -3211, 2011.

[10] J. Jin, *The Finite Element Method in Electromagnetics*, New York: John Wiley & Sons, 2002.

[11] Ismatullah and T. F. Eibert, "Surface Integral Equation Solutions by Hierarchical Vector Ba- sis Functions and Spherical Harmonics Based Multilevel Fast Multipole Method," *IEEE Trans. Antennas Propagat.*, vol. 57, no. 7, pp. 2084 –2093, July 2009.

[12] W. Hackbusch and S. Boerm, "$\mathbf{H}^2$ −Matrix Approximation of Integral Operators by Interpolation," *Applied Numerical Mathematics*, vol. 43, no. 1-2, pp. 129 – 143, 2002.

[13] M. Li, H. Chen, C. Li, R. Chen, and C. Ong, "Hybrid UV/MLFMA Analysis of Scattering by PEC Targets above a Lossy Half-Space," *Applied*

Computational Electromagnetic Society (ACES) Journal, vol. 26, no. 1, pp. 17 – 25, January 2011.

[14] S. Seo, C. Wang, and J. Lee, "Analyzing PEC Scattering Structure Using an IE-FFT Algorithm," *Applied Computational Electromagnetic Society (ACES) Journal*, vol. 24, no. 2, pp. 116 – 128, April 2009.

[15] C. Luo and C. Lu, "Electromagnetic Scattering Computation Using a Hybrid Surface and Volume Integral Equation Formulation," *Applied Compuational Electromagnetic Society (ACES) Journal*, vol. 22, no. 3, pp. 340 – 349, November 2007.

[16] X. Xu, Q. Liu, and Z. Zhang, "The Stabilized Biconjugate Gradient Fast Fourier Transform Method for Electromagnetic Scattering," *Applied Computational Electromagnetic Society (ACES) Journal*, vol. 17, no. 1, pp. 97 – 103, March 2002.

Dennis T. Schobert received his Dipl.-Ing. (M.Sc.) degree in Electrical Engineering from Technische Universität Dresden, Dresden, Germany, in 2009. Since 2009, he is with the Lehrstuhl für Hochfrequenztechnik at Technische Universität München, Munich, Germany as a research assistant. His major research interests include fast integral equation solvers and novel automotive communication techniques.

Thomas F. Eibert received the Dipl.-Ing. (FH) degree from Fachhochschule Nürnberg, Nürnberg, Germany, the Dipl.-Ing. degree from Ruhr-Universität Bochum, Bochum, Germany, and the Dr.-Ing. degree from Bergische Universität Wuppertal, Wuppertal, Germany, in 1989, 1992, and 1997, all in Electrical Engineering. From 1997 to 1998, he was with the Radiation Laboratory, EECS Department of the University of Michigan, Ann Arbor, MI, USA from 1998 to 2002, he was with Deutsche Telekom, Darmstadt, Germany, and from 2002 to 2005, he was with the Institute for High-frequency Physics and Radar Techniques of FGAN e.V., Wachtberg, Germany, where he was head of the department Antennas and Scattering. From 2005 to 2008, he was a Professor for radio frequency technology at Universität Stuttgart, Stuttgart, Germany.

Since October 2008, he has been a Professor for high-frequency engineering at the Technische Universität München, Munich, Germany. His major areas of interest are numerical electromagnetics, wave propagation, measurement techniques for antennas and scattering as well as all kinds of antenna and microwave circuit technologies for sensors and communications.

An Implementation of King's Green Functions in Thin Wire Scattering Problems

Ömer Zor[1] and Burak Polat[2]

[1] Electronics Engineering Department
Uludağ University, Bursa, TR-16059, Turkey
omerzor@uludag.edu.tr

[2] Electrical and Electronics Engineering Department
Trakya University, Edirne, TR-22030, Turkey
burakpolat@trakya.edu.tr

Abstract **─** We investigate electromagnetic scattering from metallic thin wire structures located over planar and spherical lossy dielectric half-spaces by applying Green's function formulation and method of moments in the resonance region and under "high contrast approximation" (HCA). For this purpose, in the calculations of the impedance matrix and the potential column of the moment system, we employ the Green functions of King valid for arbitrary range under HCA and the asymptotic (far field) Green functions for planar and spherical impedance surfaces delivered by Norton and Wait, respectively. For a verification of the developed codes, the current distributions obtained under plane wave illumination on the arms of a cross shaped thin wire structure are compared to the same results obtained by the commercial software SNEC™. Various illustrations for the scattered electrical field from a thin wire plate located over planar and spherical half-spaces are also presented.

Index Terms **─** Electromagnetic scattering, method of moments, Sommerfeld problem, thin wires.

I. INTRODUCTION

Ever since the pioneering work [1] by Sommerfeld over a century ago the interest in the derivation of computationally efficient solutions for the radiation fields of a Hertzian dipole in inhomogeneous media has constantly grown in parallel to their applications in diverse areas of electrical engineering. While it is impossible to provide a satisfactory list of all such attempts in literature to date, a wide account can be reached in [2]. The class of solutions to the Sommerfeld problem that constitute the topic of the present investigation is the Green functions derived by King in 1982 [3] for Hertzian dipoles radiating over a planar lossy dielectric half-space. The most distinctive aspect of King's fully analytical solutions, which have been collected in [4] for various different properties of ambient medium, is that they apply for arbitrary range under high contrast approximation (HCA). Following 1999 to date, King's method has been applied to many new geometries involving stratified spherical grounds in numerous works [5-17] initiated by his co-workers.

The thin wire mesh electromagnetic model of an arbitrarily shaped conducting body was first introduced and tested experimentally in 1966 by Richmond [18]. This pioneering work was followed by numerous theoretical as well as experimental investigations [19-27] to specify the ranges of validity of wire mesh models for certain canonical structures. Following the development of the method of moments (MoM) in 1967 by Harrington [28], there has appeared many papers through the 70's on the MoM formulation of scattering problems for the wire mesh structures over a dielectric half-space due to their importance in radar applications [29] Since a computationally efficient analytical solution of the Sommerfeld problem was not available until 1982 [3], in such

Submitted On: July 4, 2011
Accepted On: October 15, 2011

works the surface wave components of Green functions were generally ignored (as called "reflection coefficient method") for a practical computation of the impedance matrix without estimating the relative error. This gap was then filled by the famous open software NEC-2 [30], which was developed in 1981 in Lawrence Livermore National Laboratory, CA with extensive numerical/asymptotic libraries.

In the present work, we provide the analytical backbone of a software which incorporates the Green functions of King alternative to a similar role of the extensive numerical/asymptotic libraries of NEC-2 whenever HCA applies. While the developed codes equally have the ability to read NEC-2 formatted input files, their main advantage lies in the capability to evolve by proper substitutions of Green functions to take into account various terrain features in any scenario. Accordingly, in Section 2 we provide the MoM formulation of the scattering problem, while the details of the calculation of the elements of the impedance matrix are presented in Section 3. In Section 4 the elements of the potential column in MoM formulation are provided for three different scenarios of propagation over planar and spherical impedance surfaces, and their numerical implementations are presented in Section 5. For a verification of the developed codes we provide the amplitude and phase distributions of currents on the arms of a crossed wire over a planar lossy ground with reference to the same results obtained by the commercial software SNEC™ [31].

A time convention $\exp(-i\omega t)$ is assumed and suppressed.

II. FORMULATION

Let regions I ($z>0$) and II ($z<0$) be free-space and a simple lossy dielectric with constitutive parameters and wave numbers given as (ε_0,μ_0), $k_1=\omega\sqrt{\mu_0\varepsilon_0}$ and $(\varepsilon_2,\mu_0,\sigma_2)$, $k_2=\omega\sqrt{\mu_0(\varepsilon_2+i\sigma_2/\omega)}$, respectively. The complex refractivity of ground is defined by $N=k_2/k_1=\sqrt{\varepsilon_r+i\sigma_2/(\omega\varepsilon_0)}$ with $\varepsilon_r=\varepsilon_2/\varepsilon_0$. The HCA is defined as $|N|^2>>1$ (or equivalently $|N|\geq 3$). Analytically, the lowest value that $|N|$ can take in any simple medium is limited by $\sqrt{\varepsilon_r}$. Therefore, in any medium with $\varepsilon_r\geq 9$ (especially seawater with $\varepsilon_r\approx 75-80$), it can always be satisfied regardless of conductivity and the operating frequency.

Under HCA, the King formulation of Green functions for a Hertzian dipole located at $\vec{r}'=(x',y',z')$ and calculated at $\vec{r}=(x,y,z)$ constitutes "direct" (d), "perfect image" (i), and "surface wave" (s) components, which can be represented in tensorial form by

$$\overline{\overline{G}}(\vec{r},\vec{r}')=\overline{\overline{G}}^{d}(\vec{r},\vec{r}')+\overline{\overline{G}}^{i}(\vec{r},\vec{r}')+\overline{\overline{G}}^{s}(\vec{r},\vec{r}'),$$

$$\begin{aligned}\overline{\overline{G}}^{(d,i,s)}&=\hat{x}\hat{x}g_x^{x(d,i,s)}+\hat{y}\hat{x}g_y^{x(d,i,s)}+\hat{z}\hat{x}g_z^{x(d,i,s)}\\&+\hat{x}\hat{y}g_x^{y(d,i,s)}+\hat{y}\hat{y}g_y^{y(d,i,s)}+\hat{z}\hat{y}g_z^{y(d,i,s)}\\&+\hat{x}\hat{z}g_x^{z(d,i,s)}+\hat{y}\hat{z}g_y^{z(d,i,s)}+\hat{z}\hat{z}g_z^{z(d,i,s)}\ .\end{aligned}$$

Here, g_b^a stands for the total b-axis electrical field component of the Hertzian dipole with unit moment directed along a-axis. The entire set is given for $z,z'>0$ as follows:

$$\begin{aligned}g_x^x&=\frac{e^{ik_1R_1}}{4\pi R_1}\left[\xi_1-\frac{(x-x')^2}{R_1^2}\xi_2\right]\\&-\frac{e^{ik_1R_2}}{4\pi R_2}\left[\eta_1-\frac{(x-x')^2}{R_2^2}\eta_2\right]\\&+\frac{e^{ik_1R_2}}{2\pi R_2}\frac{1}{N}\left\{\frac{z+z'}{R_2}\eta_3-\frac{\eta_1}{N}+\frac{(y-y')^2}{R_2^2}\frac{\eta_2}{N}\right.\\&\left.-\frac{\Xi}{N^2}\frac{R_2}{P^3}\left[ik_1R_2(x-x')^2+\frac{R_2^2}{P^2}(y-y')^2\right]\right\},\end{aligned}$$

$$\begin{aligned}g_y^x&=-\frac{(x-x')(y-y')}{R_1^2}\frac{e^{ik_1R_1}}{4\pi R_1}\xi_2\\&+\frac{(x-x')(y-y')}{R_2^2}\frac{e^{ik_1R_2}}{4\pi R_2}\eta_2\\&-\frac{(x-x')(y-y')}{R_2^2}\frac{e^{ik_1R_2}}{2\pi R_2}\\&\times\frac{\Xi}{N^2}\left[\eta_2+\frac{1}{N}\frac{R_2^3}{P^3}\left(ik_1R_2-\frac{R_2^2}{P^2}\right)\right],\end{aligned}$$

$$g_z^x = -\frac{(x-x')(z-z')}{R_1^2}\frac{e^{ik_1R_1}}{4\pi R_1}\xi_2 + \frac{(x-x')(z+z')}{R_2^2}\frac{e^{ik_1R_2}}{4\pi R_2}\eta_2 - \frac{x-x'}{R_2}\frac{e^{ik_1R_2}}{2\pi R_2}\frac{1}{N}\left[\eta_3 + \frac{\Xi}{N} ik_1R_2\frac{R_2}{P}\right],$$

$$g_x^y = g_y^x ,$$

$$g_y^y = \frac{e^{ik_1R_1}}{4\pi R_1}\left[\xi_1 - \frac{(y-y')^2}{R_1^2}\xi_2\right] - \frac{e^{ik_1R_2}}{4\pi R_2}\left[\eta_1 - \frac{(y-y')^2}{R_2^2}\eta_2\right] + \frac{e^{ik_1R_2}}{2\pi R_2}\frac{1}{N}\left\{\begin{array}{l} \dfrac{z+z'}{R_2}\eta_3 - \dfrac{\eta_1}{N} \\ +\dfrac{\eta_2}{N}\dfrac{(x-x')^2}{R_2^2} - \dfrac{\Xi}{N^2}\dfrac{R_2}{P^3} \\ \times\left[ik_1R_2(y-y')^2 + \dfrac{R_2^2}{P^2}(x-x')^2\right]\end{array}\right\},$$

$$g_z^y = -\frac{(y-y')(z-z')}{R_1^2}\frac{e^{ik_1R_1}}{4\pi R_1}\xi_2 + \frac{(y-y')(z+z')}{R_2^2}\frac{e^{ik_1R_2}}{4\pi R_2}\eta_2 - \frac{y-y'}{R_2}\frac{e^{ik_1R_2}}{2\pi R_2}\frac{1}{N}\left[\eta_3 + \frac{\Xi}{N} ik_1R_2\frac{R_2}{P}\right],$$

$$g_x^z = -\frac{(x-x')(z-z')}{R_1^2}\frac{e^{ik_1R_1}}{4\pi R_1}\xi_2 - \frac{(x-x')(z+z')}{R_2^2}\frac{e^{ik_1R_2}}{4\pi R_2}\eta_2 + \frac{x-x'}{R_2}\frac{e^{ik_1R_2}}{2\pi R_2}\frac{1}{N}\left[\eta_3 + \frac{\Xi}{N} ik_1R_2\frac{R_2}{P}\right],$$

$$g_y^z = -\frac{(y-y')(z-z')}{R_1^2}\frac{e^{ik_1R_1}}{4\pi R_1}\xi_2 - \frac{(y-y')(z+z')}{R_2^2}\frac{e^{ik_1R_2}}{4\pi R_2}\eta_2 + \frac{y-y'}{R_2}\frac{e^{ik_1R_2}}{2\pi R_2}\frac{1}{N}\left[\eta_3 + \frac{\Xi}{N} ik_1R_2\frac{R_2}{P}\right],$$

$$g_z^z = \frac{e^{ik_1R_1}}{4\pi R_1}\left[\xi_1 - \frac{(z-z')^2}{R_1^2}\xi_2\right] + \frac{e^{ik_1R_2}}{4\pi R_2}\left[\eta_1 - \frac{(z+z')^2}{R_2^2}\eta_2\right] + \frac{\Xi}{N} ik_1P\frac{e^{ik_1R_2}}{2\pi R_2},$$

with

$$R_{1,2}(\vec{r},\vec{r}') = \left|\vec{r} \mp \vec{r}'\right| = \left[(x-x')^2 + (y-y')^2 + (z\mp z')^2\right]^{1/2},$$

$$P = \left[(x-x')^2 + (y-y')^2\right]^{1/2},$$

$$U = \frac{k_1R_2}{2N^2}\left[\frac{R_2 + N(z+z')}{P}\right]^2,$$

and the dimensionless parameters

$$\xi_1 = 1 - \frac{1}{ik_1R_1} - \frac{1}{k_1^2R_1^2}\ ,\ \ \xi_2 = 1 - \frac{3}{ik_1R_1} - \frac{3}{k_1^2R_1^2}\ ,$$

$$\eta_1 = 1 - \frac{1}{ik_1R_2} - \frac{1}{k_1^2R_2^2}\ ,\ \ \eta_2 = 1 - \frac{3}{ik_1R_2} - \frac{3}{k_1^2R_2^2}\ ,$$

$$\eta_3 = 1 - \frac{1}{ik_1R_2}\ ,\ \ \Xi = \left(\frac{\pi}{k_1R_2}\right)^{1/2} e^{-iU}F(U)\ ,$$

where

$$F(U) = 1 + i(\pi U)^{1/2}e^{-U}erfc(-iU^{1/2}),$$

is known as the Norton attenuation function. The surface wave components vanish in the limit $|N| \to \infty$.

In thin wire approximation, we assume the wire mesh structure comprises cylindrical segments with fixed length $\ell << \lambda$ and radius $a << \ell$, where λ is the wavelength in the ambient medium, as depicted in Fig. 1.

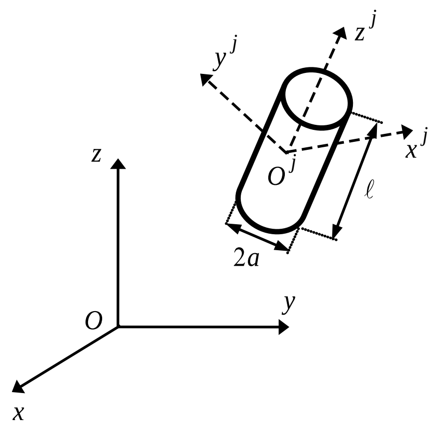

Fig. 1. *j-th* thin wire segment with outer and local reference systems.

In virtue of our choice of pulse basis functions in MoM formulation, we may assume the *j-th* thin wire segment supports a constant current I_j, whose density function can be expressed in the local cylindrical coordinates $O^j\rho^j\phi^j z^j$ through the Dirac delta distribution δ and the unit step function H as

$$\vec{J}_j(\rho^j,\phi^j,z^j)=\hat{z}^j I_j\frac{\delta(\rho^j-a)}{2\pi a}\times\left[H(z^j+\ell/2)-H(z^j-\ell/2)\right].$$

The radiation field of *j-th* segment is given by the volume integral

$$\vec{E}_j(\vec{r})=i\omega\mu_0\int\overline{\overline{G}}(\vec{r};\vec{r}^{\,j\prime})\cdot\vec{J}_j(\vec{r}^{\,j\prime})d\vartheta^{j\prime}=I_j\vec{f}_j(\vec{r}), \tag{1}$$

and the total radiatied field by a total of M segments in a mesh is expressed by

$$\vec{E}(\vec{r})=\sum_{j=1}^{M}\vec{E}_j(\vec{r})=\sum_{j=1}^{M}I_j\vec{f}_j(\vec{r})\ ,$$

based on the principle of superposition. Accordingly, the total electrical field at any point in space reads

$$\vec{E}^{tot}(\vec{r})=\vec{E}^{inc}(\vec{r})+\vec{E}(\vec{r}),$$

where $\vec{E}^{inc}(\vec{r})$ is the total field calculated at any point in the absence of the scatterer. Applying the collocation method, the boundary condition on the segments yields the linear system of equations

$$\sum_{j=1}^{M}Z_{mj}I_j=V_m\ ,\ \ m=1,2,...,M\ ,$$

$$Z_{mj}=i\omega\mu_0\int_{-\ell/2}^{\ell/2}\int_{0}^{2\pi}\hat{\ell}_m\cdot\overline{\overline{G}}(\vec{r}_m;\vec{r}^{\,j\prime})\cdot\hat{z}^j\Big|_{\rho^{j\prime}=a}\frac{d\phi^{j\prime}}{2\pi}dz^{j\prime}\ , \tag{2}$$

$$V_m=-\vec{E}^{inc}(\vec{r}_m)\cdot\hat{\ell}_m\ . \tag{3}$$

Here, $\vec{r}_m=(x_m,y_m,z_m)$ denotes the central point and (x_m^I,y_m^I,z_m^I) & $(x_m^{II},y_m^{II},z_m^{II})$, the starting & end points of *m-th* segment in the presumed direction of current flow. Then, its unit tangential vector can be written as

$$\hat{\ell}_m=\ell_{mx}\hat{x}+\ell_{my}\hat{y}+\ell_{mz}\hat{z}=\left[(x_m^{II}-x_m^I)\hat{x}+(y_m^{II}-y_m^I)\hat{y}+(z_m^{II}-z_m^I)\hat{z}\right]\big/\ell,$$

where

$$\ell=\left[(x_m^{II}-x_m^I)^2+(y_m^{II}-y_m^I)^2+(z_m^{II}-z_m^I)^2\right]^{1/2},\ \forall m\,.$$

At each junction the corresponding junction condition on currents increases the dimension of the linear system by one. In case of L junctions in a wire mesh, the currents are calculated by multiplying the extended system $[Z]_{(M+L)\times M}\cdot[I]_{M\times 1}=[V]_{(M+L)\times 1}$ by the Hermitian transpose $[Z]^*_{M\times(M+L)}$ of the extended impedance matrix before inversion as follows:

$$[I]_{M\times 1}=\left([Z]^*_{M\times(M+L)}\cdot[Z]_{(M+L)\times M}\right)^{-1}\times\left([Z]^*_{M\times(M+L)}\cdot[V]_{(M+L)\times 1}\right).$$

Alternative models for junctions can be reached at [32-34].

The total radiation (far) field of the wire mesh can be approximated as the superposition of the fields generated by Hertzian dipoles with moment $p_j=I_j\ell$ centered at $\vec{r}=\vec{r}_j$ and directed along $\hat{\ell}_j$ as

$$\vec{E}(\vec{r})=i\omega\mu_0\sum_{j=1}^{M}p_j\overline{\overline{G}}(\vec{r};\vec{r}_j)\cdot\hat{\ell}_j\ .$$

III. CALCULATION OF THE ELEMENTS OF IMPEDANCE MATRIX

The elements of the impedance matrix comprise three components

$$Z_{mj}=Z_{mj}^d+Z_{mj}^i+Z_{mj}^s\ ,$$

which require to be calculated separately through

$$Z_{mj}^{(d,i,s)} = i\omega\mu_0 \int_{-\ell/2}^{\ell/2}\int_0^{2\pi} \hat{\ell}_m \cdot \overline{\overline{G}}^{(d,i,s)}(\vec{r}_m;\vec{r}^{\,j\prime})\cdot \hat{z}^j \bigg|_{\rho^{j\prime}=a} \frac{d\phi^{j\prime}}{2\pi} dz^{j\prime} . \tag{4}$$

Since Z_{mj}^d and Z_{mj}^i are space wave components, their calculations can be carried out directly in the local reference frame $O^j x^j y^j z^j$. Regarding Z_{mj}^d, the expressions of the difference vector directed from the central point of j-*th* to *m-th* segment in local and outer reference frames are given as

$\vec{r}^{\,m} = (x^m, y^m, z^m)$,

$\vec{r}_m - \vec{r}_j = (x_m - x_j, y_m - y_j, z_m - z_j)$,

while they are related by

$$\vec{r}^{\,m} = \overline{\overline{T}}_j \cdot (\vec{r}_m - \vec{r}_j) \quad \text{or} \quad \vec{r}_m - \vec{r}_j = \overline{\overline{T}}_j^{TR} \cdot \vec{r}^{\,m} ,$$

through the Euler transformation matrix $\overline{\overline{T}}_j$

$$\overline{\overline{T}}_j = \begin{bmatrix} \cos\alpha_j \cos\beta_j & \sin\alpha_j \cos\beta_j & -\sin\beta_j \\ -\sin\alpha_j & \cos\alpha_j & 0 \\ \cos\alpha_j \sin\beta_j & \sin\alpha_j \sin\beta_j & \cos\beta_j \end{bmatrix},$$

whose inverse is equal to its transpose: $\overline{\overline{T}}_j^{-1} = \overline{\overline{T}}_j^{TR}$. The explicit expressions of the 3-D transformation angles α_j ve β_j are as follows:

$$\sin\alpha_j = (y_j^{II} - y_j^I) \big/ [(x_j^{II} - x_j^I)^2 + (y_j^{II} - y_j^I)^2]^{1/2} ,$$

$$\cos\alpha_j = (x_j^{II} - x_j^I) \big/ [(x_j^{II} - x_j^I)^2 + (y_j^{II} - y_j^I)^2]^{1/2} ,$$

$$\sin\beta_j = [(x_j^{II} - x_j^I)^2 + (y_j^{II} - y_j^I)^2]^{1/2} \big/ \ell ,$$

$$\cos\beta_j = (z_j^{II} - z_j^I) \big/ \ell .$$

Accordingly, under the thin wire approximation one has

$$R_1^2(\vec{r}^{\,m};\vec{r}^{\,j\prime}) \cong (x^m)^2 + (y^m)^2 + (z^m)^2 + a^2 - 2z^m z^{j\prime} + (z^{j\prime})^2 ,$$

and the $\hat{z}^j$ -directed Green functions read

$$g_{x^j}^{z^j d}(\vec{r}^{\,m},\vec{r}^{\,j\prime}) = -\frac{(x^m - x^{j\prime})(z^m - z^{j\prime})}{R_1^2}\frac{e^{ik_1R_1}}{4\pi R_1}\xi_2 , \tag{5}$$

$$g_{y^j}^{z^j d}(\vec{r}^{\,m},\vec{r}^{\,j\prime}) = -\frac{(y^m - y^{j\prime})(z^m - z^{j\prime})}{R_1^2}\frac{e^{ik_1R_1}}{4\pi R_1}\xi_2 , \tag{6}$$

$$g_{z^j}^{z^j d}(\vec{r}^{\,m},\vec{r}^{\,j\prime}) = \frac{e^{ik_1R_1}}{4\pi R_1}\left[\xi_1 - \frac{(z^m - z^{j\prime})^2}{R_1^2}\xi_2\right] .$$

Substituting the polar transformations $x^{j\prime} = a\cos\phi^{j\prime}$ ve $y^{j\prime} = a\sin\phi^{j\prime}$ in (5) and (6), a full period integration in (4) yields the resultant regular integral

$$Z_{mj}^d = i\omega\mu_0 \int_{-\ell/2}^{\ell/2} \begin{bmatrix} \ell^{mx} t_{x^j}^{z^j d}(\vec{r}^{\,m},\vec{r}^{\,j\prime}) \\ +\ell^{my} t_{y^j}^{z^j d}(\vec{r}^{\,m},\vec{r}^{\,j\prime}) \\ +\ell^{mz} g_{z^j}^{z^j d}(\vec{r}^{\,m},\vec{r}^{\,j\prime}) \end{bmatrix} dz^{j\prime} ,$$

with

$$t_{x^j}^{z^j d}(\vec{r}^{\,m},\vec{r}^{\,j\prime}) = -\frac{x^m(z^m - z^{j\prime})}{R_1^2}\frac{e^{ik_1R_1}}{4\pi R_1}\xi_2 ,$$

$$t_{y^j}^{z^j d}(\vec{r}^{\,m},\vec{r}^{\,j\prime}) = -\frac{y^m(z^m - z^{j\prime})}{R_1^2}\frac{e^{ik_1R_1}}{4\pi R_1}\xi_2 ,$$

$$\hat{\ell}^m = \ell^{mx}\hat{x}^j + \ell^{my}\hat{y}^j + \ell^{mz}\hat{z}^j = \overline{\overline{T}}_j \cdot \hat{\ell}_m ,$$

which is a calculated numerically. Similar considerations hold for the calculation of Z_{mj}^i.

In calculating the surface wave components Z_{mj}^s, we express the source points in the local reference frame and the observation points in the outer reference frame. For this purpose, we set $\vec{r} = \vec{r}_m$, $\vec{r}' = \vec{r}_j' = \vec{r}_j + \overline{\overline{T}}_j^{TR} \cdot \vec{r}^{\,j\prime}$ in King's Green functions, where $\vec{r}_j' = (x_j', y_j', z_j')$ and $\vec{r}^{\,j\prime} = (x^{j\prime}, y^{j\prime}, z^{j\prime})$ (see Fig. 2).

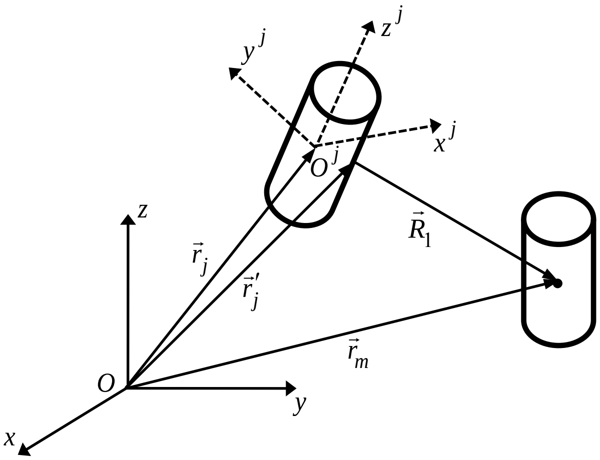

Fig. 2. *j-th* and *m-th* thin wire segments and position vectors.

Under the thin wire approximation one has

$$R_{1,2}^2(\vec{r}_m;\vec{r}^{\,j\prime}) \cong (x_m-x_j)^2+(y_m-y_j)^2 + (z_m-z_j)^2+a^2+z^{j\prime 2} - 2z^{j\prime}\begin{bmatrix}(x_m-x_j)\cos\alpha_j\sin\beta_j\\ +(y_m-y_j)\sin\alpha_j\sin\beta_j\\ +(z_m\mp z_j)\cos\beta_j\end{bmatrix},$$

$$P^2 \cong (x_m-x_j)^2+(y_m-y_j)^2 - 2z^{j\prime}\sin\beta_j\begin{bmatrix}(x_m-x_j)\cos\alpha_j\\ +(y_m-y_j)\sin\alpha_j\end{bmatrix} + (z^{j\prime})^2\sin^2\beta_j\,,$$

$$U \cong \frac{k_1R_2}{2N^2}\left(\frac{R_2+NI_z}{P}\right)^2\,,$$

$$I_z = z_m+z_j' \cong z_m+z_j+z^{j\prime}\cos\beta_j\,.$$

By describing the following parameters

$$I_x=\int_0^{2\pi}(x_m-x_j')\frac{d\phi^{j\prime}}{2\pi}=x_m-x_j-z^{j\prime}\cos\alpha_j\sin\beta_j\,,$$

$$I_{xx}=\int_0^{2\pi}(x_m-x_j')^2\frac{d\phi^{j\prime}}{2\pi} =(x_m-x_j-z^{j\prime}\cos\alpha_j\sin\beta_j)^2 +(a^2/2)(\cos^2\alpha_j\cos^2\beta_j+\sin^2\alpha_j),$$

$$I_{xy}=\int_0^{2\pi}(x_m-x_j')(y_m-y_j')\frac{d\phi^{j\prime}}{2\pi} =(x_m-x_j-z^{j\prime}\cos\alpha_j\sin\beta_j) \times(y_m-y_j-z^{j\prime}\sin\alpha_j\sin\beta_j) -(a^2/2)\sin\alpha_j\cos\alpha_j\sin^2\beta_j\,,$$

$$I_y=\int_0^{2\pi}(y_m-y_j')\frac{d\phi^{j\prime}}{2\pi}=y_m-y_j-z^{j\prime}\sin\alpha_j\sin\beta_j\,,$$

$$I_{yy}=\int_0^{2\pi}(y_m-y_j')^2\frac{d\phi^{j\prime}}{2\pi} =(y_m-y_j-z^{j\prime}\sin\alpha_j\sin\beta_j)^2 +(a^2/2)(\sin^2\alpha_j\cos^2\beta_j+\cos^2\alpha_j),$$

$$t_x^{xs}=\int_0^{2\pi}g_x^{xs}\frac{d\phi^{j\prime}}{2\pi} =\frac{e^{ik_1R_2}}{2\pi R_2}\frac{1}{N}\begin{bmatrix}\dfrac{I_z}{R_2}\eta_3-\dfrac{\eta_1}{N}+\dfrac{I_{yy}}{R_2^2}\dfrac{\eta_2}{N}\\ -\dfrac{\Xi}{N^2}\dfrac{R_2}{P^3}\left(ik_1R_2I_{xx}+\dfrac{R_2^2}{P^2}I_{yy}\right)\end{bmatrix},$$

$$t_y^{xs}=\int_0^{2\pi}g_y^{xs}\frac{d\phi^{j\prime}}{2\pi} =-\frac{I_{xy}}{R_2^2}\frac{e^{ik_1R_2}}{2\pi R_2}\frac{1}{N^2}\left[\eta_2+\frac{\Xi}{N}\frac{R_2^3}{P^3}\left(ik_1R_2-\frac{R_2^2}{P^2}\right)\right],$$

$$t_z^{xs}=\int_0^{2\pi}g_z^{xs}\frac{d\phi^{j\prime}}{2\pi}=-\frac{I_x}{R_2}\frac{e^{ik_1R_2}}{2\pi R_2}\frac{1}{N} \times\left[\eta_3+\frac{\Xi}{N}ik_1R_2\frac{R_2}{P}\right],$$

$$t_x^{ys}=t_y^{xs}\,,$$

$$t_y^{ys}=\int_0^{2\pi}g_y^{ys}\frac{d\phi^{j\prime}}{2\pi} =\frac{e^{ik_1R_2}}{2\pi R_2}\frac{1}{N}\begin{bmatrix}\dfrac{I_z}{R_2}\eta_3-\dfrac{\eta_1}{N}+\dfrac{\eta_2}{N}\dfrac{I_{xx}}{R_2^2}\\ -\dfrac{\Xi}{N^2}\dfrac{R_2}{P^3}\left(ik_1R_2I_{yy}+\dfrac{R_2^2}{P^2}I_{xx}\right)\end{bmatrix},$$

$$t_z^{ys}=\int_0^{2\pi}g_z^{ys}\frac{d\phi^{j\prime}}{2\pi}=-\frac{I_y}{R_2}\frac{e^{ik_1R_2}}{2\pi R_2}\frac{1}{N} \times\left[\eta_3+\frac{\Xi}{N}ik_1R_2\frac{R_2}{P}\right],$$

$$t_x^{zs}=\int_0^{2\pi}g_x^{zs}\frac{d\phi^{j\prime}}{2\pi}=\frac{I_x}{R_2}\frac{e^{ik_1R_2}}{2\pi R_2}\frac{1}{N}\times\left[\eta_3+\frac{\Xi}{N}ik_1R_2\frac{R_2}{P}\right],$$

$$t_y^{zs}=\int_0^{2\pi}g_y^{zs}\frac{d\phi^{j\prime}}{2\pi}=\frac{I_y}{R_2}\frac{e^{ik_1R_2}}{2\pi R_2}\frac{1}{N}\times\left[\eta_3+\frac{\Xi}{N}ik_1R_2\frac{R_2}{P}\right],$$

$$t_z^{zs}=\int_0^{2\pi}g_z^{zs}\frac{d\phi^{j\prime}}{2\pi}=\frac{\Xi}{N}ik_1P\frac{e^{ik_1R_2}}{2\pi R_2}\,,$$

which emerge from the full period integration of the surface wave components of the Green tensor, one reaches the resultant regular integral

$$Z^{s}_{mj} = i\omega\mu_0 \times \int_{-\ell/2}^{\ell/2} \begin{bmatrix} \ell_{mx} t_x^{xs} z_{jx} + \ell_{mx} t_x^{ys} z_{jy} + \ell_{mx} t_x^{zs} z_{jz} \\ +\ell_{my} t_y^{xs} z_{jx} + \ell_{my} t_y^{ys} z_{jy} + \ell_{my} t_y^{zs} z_{jz} \\ +\ell_{mz} t_z^{xs} z_{jx} + \ell_{mz} t_z^{ys} z_{jy} + \ell_{mz} t_z^{zs} z_{jz} \end{bmatrix} dz^{j\prime},$$

with $\hat{z}_j = z_{jx}\hat{x} + z_{jy}\hat{y} + z_{jz}\hat{z} = \overline{\overline{T}}_j^{TR} \cdot \hat{z}^j$, which requires to be calculated numerically.

IV. THREE DIFFERENT SCENARIOS

The influence of the geometrical and physical properties of the ambient medium in scattering phenomenon appears in the expression (3), which is determined by the incident field. In this section, we consider three different scenarios for the incident field and the ambient medium for a numerical investigation.

A. Scenario I: Homogeneous plane wave incidence and planar ground

Let the electrical field of an incoming homogeneous plane wave in an arbitrary direction $\hat{n}_i$ in region I be given by

$$\vec{E}^i = \hat{e}_i e^{ik_0 \hat{n}_i \cdot \vec{r}} .$$

The normal of the interface is $\hat{n} \equiv \hat{z}$, while the normal of the incidence plane is calculated as $\hat{q} = \hat{n} \times \hat{n}_i$. By use of the identity $\hat{e}_i = \hat{q}(\hat{q}\cdot\hat{e}_i) - \hat{q}\times(\hat{q}\times\hat{e}_i)$ one can decompose the incident wave into TE and TM components as

$$\vec{E}^i = \vec{E}^i_{TE} + \vec{E}^i_{TM} ,$$

where

$$\vec{E}^i_{TE} = -\hat{q}\times(\hat{q}\times\hat{e}_i)\, e^{i\vec{k}\cdot\vec{r}} = (\hat{q}\times\hat{e}_i)\times\hat{q}\, e^{i\vec{k}\cdot\vec{r}} ,$$

$$\vec{E}^i_{TM} = \hat{q}(\hat{q}\cdot\hat{e}_i)\, e^{i\vec{k}\cdot\vec{r}} ,$$

while their reflected components read

$$\vec{E}^r_{TE} = (\hat{q}\times\hat{e}_i)\times\hat{q}\,\Gamma_{TE}\, e^{i\vec{k}\cdot\vec{r}} , \vec{E}^r_{TM} = \hat{q}(\hat{q}\cdot\hat{e}_i)\Gamma_{TM}\, e^{i\vec{k}\cdot\vec{r}} ,$$

with the Fresnel coefficients

$$\Gamma_{TE} = \frac{N\cos\psi - (N - \sin^2\psi)^{1/2}}{N\cos\psi + (N - \sin^2\psi)^{1/2}} ,$$

$$\Gamma_{TM} = \frac{\cos\psi - (N - \sin^2\psi)^{1/2}}{\cos\psi + (N - \sin^2\psi)^{1/2}} .$$

Here, $\psi \in [0, \pi/2)$ stands for the angle between the unit vectors $\hat{n}$ and $\hat{n}_i$. Accordingly, the total incident field can be expressed by

$$\vec{E}^{inc} = \vec{E}^i_{TE} + \vec{E}^r_{TE} + \vec{E}^i_{TM} + \vec{E}^r_{TM} .$$

B. Scenario II: A monopole antenna and planar impedance ground

In virtue of (1), the incident far field of a monople antenna located at $\vec{r} = \vec{r}\,'$ along $\hat{\ell}_M$ direction with moment p_M can be expressed as

$$\vec{E}^{inc}(\vec{r}) = i\omega\mu_0 p_M \overline{\overline{G}}(\vec{r};\vec{r}\,')\cdot\hat{\ell}_M . \tag{7}$$

The elements of the Green tensor can be specified as the Green functions delivered by Norton [35] under HCA and grazing wave incidence as follows:

$$g_x^x = \frac{e^{ik_1R_1}}{4\pi R_1}\left[1 - \frac{(x-x')^2}{R_1^2}\right] + \frac{e^{ik_1R_2}}{4\pi R_2}\left[R_h \frac{(y-y')^2}{P^2} - R_v (x-x')^2 \left(\frac{1}{P^2} - \frac{1}{R_2^2}\right)\right] + \frac{e^{ik_1R_2}}{4\pi R_2}\begin{bmatrix} \frac{(y-y')^2}{P^2}(1-R_h)F(q) \\ -\frac{(x-x')^2}{P^2}\Delta_N^2(1-R_v)F(W_N) \end{bmatrix},$$

$$g_y^x = -\frac{(x-x')(y-y')}{R_1^2}\frac{e^{ik_1R_1}}{4\pi R_1} - (x-x')(y-y')\frac{e^{ik_1R_2}}{4\pi R_2}\left[\frac{R_h}{P^2} + R_v\left(\frac{1}{P^2} - \frac{1}{R_2^2}\right)\right] - \frac{(x-x')(y-y')}{P^2}\frac{e^{ik_1R_2}}{4\pi R_2} \times\left[(1-R_h)F(q) + \Delta_N^2(1-R_v)F(W_N)\right],$$

$$g_z^x = -\frac{(x-x')(z-z')}{R_1^2}\frac{e^{ik_1R_1}}{4\pi R_1} + \frac{(x-x')(z+z')}{R_2^2}R_v\frac{e^{ik_1R_2}}{4\pi R_2} - \frac{x-x'}{R_2}\Delta_N(1-R_v)F(W_N)\frac{e^{ik_1R_2}}{4\pi R_2} ,$$

$$g_x^y = g_y^x,$$

$$g_y^y = \frac{e^{ik_1R_1}}{4\pi R_1}\left[1-\frac{(y-y')^2}{R_1^2}\right] + \frac{e^{ik_1R_2}}{4\pi R_2}\left[\begin{array}{l} R_h \dfrac{(x-x')^2}{P^2} \\ -R_v (y-y')^2\left(\dfrac{1}{P^2}-\dfrac{1}{R_2^2}\right)\end{array}\right] + \frac{e^{ik_1R_2}}{4\pi R_2}\left[\begin{array}{l} \dfrac{(x-x')^2}{P^2}(1-R_h)F(q) \\ -\dfrac{(y-y')^2}{P^2}\Delta_N^2(1-R_v)F(W_N)\end{array}\right],$$

$$g_z^y = -\frac{(y-y')(z-z')}{R_1^2}\frac{e^{ik_1R_1}}{4\pi R_1} + \frac{(y-y')(z+z')}{R_2^2}R_v\frac{e^{ik_1R_2}}{4\pi R_2} - \frac{y-y'}{R_2}\Delta_N(1-R_v)F(W_N)\frac{e^{ik_1R_2}}{4\pi R_2},$$

$$g_x^z = -\frac{(x-x')(z-z')}{R_1^2}\frac{e^{ik_1R_1}}{4\pi R_1} - \frac{(x-x')(z+z')}{R_2^2}R_v\frac{e^{ik_1R_2}}{4\pi R_2} + \frac{x-x'}{R_2}\Delta_N(1-R_v)F(W_N)\frac{e^{ik_1R_2}}{4\pi R_2},$$

$$g_y^z = -\frac{(y-y')(z-z')}{R_1^2}\frac{e^{ik_1R_1}}{4\pi R_1} - \frac{(y-y')(z+z')}{R_2^2}R_v\frac{e^{ik_1R_2}}{4\pi R_2} + \frac{y-y'}{R_2}\Delta_N(1-R_v)F(W_N)\frac{e^{ik_1R_2}}{4\pi R_2},$$

$$g_z^z = \frac{P^2}{R_1^2}\frac{e^{ik_1R_1}}{4\pi R_1} + \frac{P^2}{R_2^2}R_v\frac{e^{ik_1R_2}}{4\pi R_2} + \frac{P^2}{R_2^2}(1-R_v)F(W_N)\frac{e^{ik_1R_2}}{4\pi R_2},$$

In Norton's formulation the ground is modeled by a scalar impedance boundary condition (cf.[36, Sec.1.15]) with normalized surface impedance

$$\Delta_N = (1/N)\left[1-(1/N^2)(P/R_2)^2\right]^{1/2},$$

With respect to free space characteristic impedance $Z_0 = 120\pi$, while the reflection coefficients and ground parameters therein are given as

$$R_v = \frac{z+z'-R_2\Delta_N}{z+z'+R_2\Delta_N}, \quad R_h = \frac{z+z'-R_2\delta_0}{z+z'+R_2\delta_0},$$

$$W_N = \frac{ik_1R_2}{2}\left(\frac{z+z'+R_2\Delta_N}{P}\right),$$

$$\delta_0 = N^2\Delta_N, \quad q = \frac{ik_1R_2}{2}\left(\frac{z+z'+R_2\delta_0}{P}\right).$$

C. Scenario III: A monopole antenna and spherical impedance ground

In this case, the expression (7) still applies, while the Green functions can be adopted as the set given by Wait 37,38] which are derived based on the Pol and Bremmer theory [39,40]. Accordingly, the z, x, and y axes of the outer Cartesian coordinates in the vicinity of the scatterer can be coincided respectively with the spherical coordinate curves r, θ, ϕ of the globe, whose origin is the central point as depicted in Fig. 3.

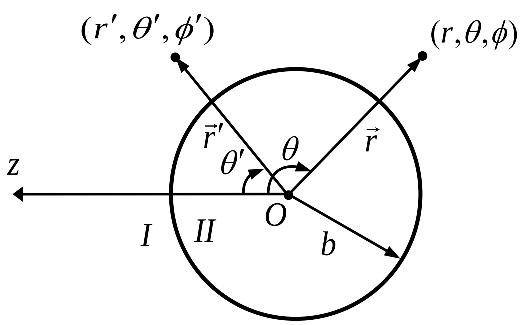

Fig. 3. Spherical earth and its global coordinate system $Or\theta\phi$.

Thereby, the Cartesian tensor components of the Green functions are suitable for our purposes with $\theta' = 0$ can be calculated as

$$g_x^x = e^{i\pi/4}\cos\phi \frac{(\pi A\theta)^{1/2}}{A^2}\frac{e^{ik_1 b\theta}}{2\pi b\theta} \times \sum_{s=1}^{\infty}\frac{e^{iA\theta t_s} w'(t_s - y_1) w'(t_s - y_2)}{(t_s - q^2) w^2(t_s)},$$

$$g_y^x = -e^{i\pi/4}\sin\phi (\pi A\theta)^{1/2}\frac{e^{ik_1 b\theta}}{2\pi b\theta} \times \sum_{m=1}^{\infty}\frac{e^{iA\theta \overline{t}_m} w(\overline{t}_m - y_1) w(\overline{t}_m - y_2)}{(\overline{t}_m - q_1^2) w^2(\overline{t}_m)},$$

$$g_z^x = ie^{i\pi/4}\cos\phi \frac{(\pi A\theta)^{1/2}}{A}\frac{e^{ik_1 b\theta}}{2\pi b\theta} \times \sum_{s=1}^{\infty}\frac{e^{iA\theta t_s} w'(t_s - y_1) w(t_s - y_2)}{(t_s - q^2) w^2(t_s)},$$

$$g_x^y = e^{i\pi/4}\sin\phi \frac{(\pi A\theta)^{1/2}}{A^2}\frac{e^{ik_1 b\theta}}{2\pi b\theta} \times \sum_{s=1}^{\infty}\frac{e^{iA\theta t_s} w'(t_s - y_1) w'(t_s - y_2)}{(t_s - q^2) w^2(t_s)},$$

$$g_y^y = e^{i\pi/4}\cos\phi (\pi A\theta)^{1/2}\frac{e^{ik_1 b\theta}}{2\pi b\theta} \times \sum_{m=1}^{\infty}\frac{e^{iA\theta \overline{t}_m} w(\overline{t}_m - y_1) w(\overline{t}_m - y_2)}{(\overline{t}_m - q_1^2) w^2(\overline{t}_m)},$$

$$g_z^y = ie^{i\pi/4}\sin\phi \frac{(\pi A\theta)^{1/2}}{A}\frac{e^{ik_1 b\theta}}{2\pi b\theta} \times \sum_{s=1}^{\infty}\frac{e^{iA\theta t_s} w'(t_s - y_1) w(t_s - y_2)}{(t_s - q^2) w^2(t_s)},$$

$$g_x^z = -ie^{i\pi/4}\frac{(\pi A\theta)^{1/2}}{A}\frac{e^{ik_1 b\theta}}{2\pi b\theta} \times \sum_{s=1}^{\infty}\frac{e^{iA\theta t_s} w(t_s - y_1) w'(t_s - y_2)}{(t_s - q^2) w^2(t_s)},$$

$$g_y^z = 0 ,$$

$$g_z^z = e^{i\pi/4}(\pi A\theta)^{1/2}\frac{e^{ik_1 b\theta}}{2\pi b\theta} \times \sum_{s=1}^{\infty}\frac{e^{iA\theta t_s} w(t_s - y_1) w(t_s - y_2)}{(t_s - q^2) w^2(t_s)},$$

where $\Delta = (1/N)\left[1-(1/N^2)\right]^{1/2}$ represents the surface impedance normalized w.r.t. free space characteristic impedance $Z_0 = 120\pi$; $b = (4/3)\times 6378\ [km]$ is the effective radius of earth taking into account first order tropospheric refractions; $A = (k_1 b/2)^{1/3}$, $q = iA\Delta$, and $q_1 = N^2 q$ are ground constants; $h_1 = r' - b$ and $h_2 = r - b$ are the heights of the source and observation points above the ground; $y_1 = k_1 h_1/A$; $y_2 = k_1 h_2/A$; and $w(t) = \sqrt{\pi}\left[B_i(t) + iA_i(t)\right]$ with $A_i(t)$, $B_i(t)$ denoting standard Airy functions. The Green functions are derived under the natural assumption $h_{1,2} << b$ and the Rayleigh hypothesis $|\Delta|^2 << 1$, which fits well with HCA. The parameters t_s and $\overline{t}_m$ correspond to the discrete complex roots of the Stokes equations $w'(t) - qw(t) = 0$ and $w'(t) - q_1 w(t) = 0$, respectively. They are the eigenvalues of the ground wave modes which are located in the first quadrant of the complex plane and their magnitudes increase with index number. In their determination, we apply the algorithm available in [41, pp. 340-343].

The critical distance, beyond which the influence of the curvature of earth on wave propagation cannot be disregarded, has been determined by Houdzoumis [42] as $\rho_C = b(k_1 b/2)^{-1/3}$.

In order to enrich any scenario by including any terrain feature, either land to sea transitions or obstacles (“islands”) along the propagation path as devised by Furutsu [43-49] or layered media, it is sufficient to substitute the appropriate set of Green functions into (2) and (3).

The oceanographic parameters such as mean wind speed, fetch length, and wave directionality as described in any sea spectrum [50], [51, pp. 386-403], [52, pp. 109-139], [53-55] can also be taken into account by modifying the normalized surface impedance as $\overline{\Delta} = \Delta + \Delta_{add}$, where the additional term Δ_{add} was first calculated analytically by Barrick [56] as a 2-D spectral integral involving the sea spectrum using perturbation technique and the Rayleigh hypothesis.

V. NUMERICAL IMPLEMENTATIONS

In this section, we provide certain numerical results for the three scenarios in Sec. 4 in the frequency range $3-45\,[MHz]$ for propagation over seawater with $\varepsilon_r = 80$, $\sigma = 4\,[S/m]$. First, for a verification of the developed codes we consider the case depicted in Fig. 4 where a crossed wire above planar sea surface is illuminated by a homogeneous plane wave with incidence angle $\psi = 45^{\circ}$ and unit electrical field amplitude.

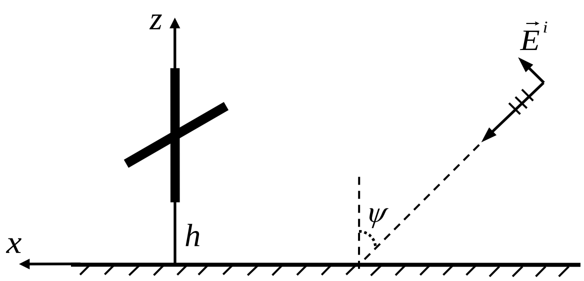

Fig. 4. A crossed wire located above planar sea surface and illuminated by a homogeneous plane wave.

The four arms of the cross are assumed to have the same length $3.33\,[m]$ while the height of the bottom arm from ground is $h = 8\,[m]$. The horizontal arms are assumed to lie along the y-axis.

In the first set of illustrations, the operating frequency is taken $f = 3\,[MHz]$ ($\lambda = 100\,[m]$) for which each arm length is $\lambda/30$ and $h = 2\lambda/25$. In virtue of thin wire approximation, the geometrical parameters of the segments are picked as $\ell = 0.5\,[m] = \lambda/200\,[m]$ and $a = 1/40\,[m] = \lambda/4000\,[m] = \ell/20$. They fall into the range in which the values of the computed fields remain insensitive. Under this parameterization, the total number of segments read 27.

In Figs. 5 and 6, we provide the amplitude and phase distributions of currents on the arms of the crossed wire and relative errors calculated by $\%100\,|(\text{SNEC™} - CODE)/\text{SNEC™}|$ with reference to the same results obtained by the commercial software SNEC™.

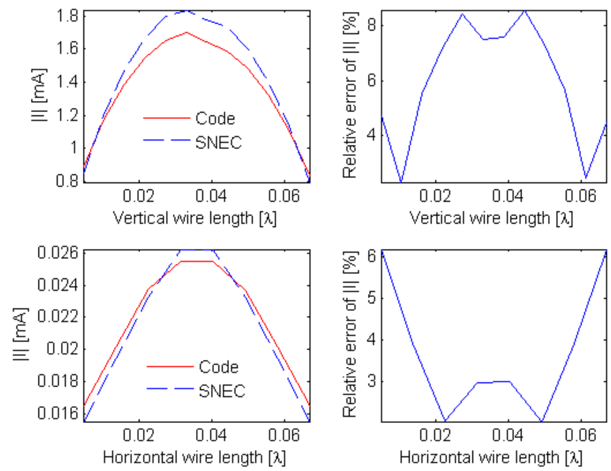

Fig. 5. The amplitude distributions of currents on vertical and horizontal arms and relative errors at $3\,[MHz]$.

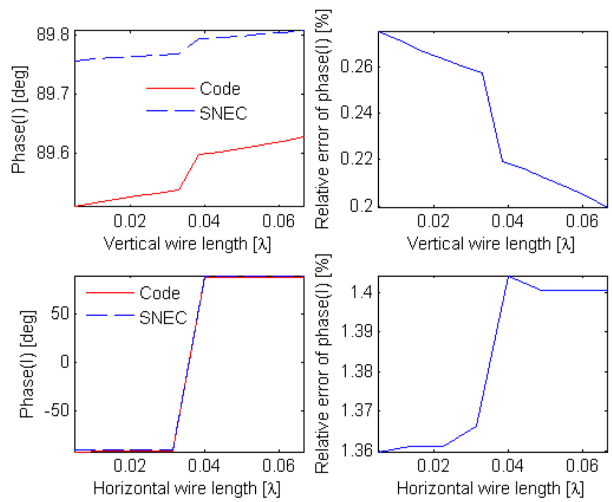

Fig. 6. The phase distributions of currents on vertical and horizontal arms and relative errors at $3\,[MHz]$.

In the second set of illustrations in Figs. 7 and 8, the operating frequency is taken $f = 15\,[MHz]$ ($\lambda = 20\,[m]$) for which the arm length is $\lambda/6$ and $h = 2\lambda/5$, while $\ell = 0.5[m] = \lambda/40\,[m]$ and $a = 1/40\,[m] = \lambda/800\,[m] = \ell/20$.

The relative errors in the two sets of illustrations, which are restricted by 10%, stem from the choice of poorly converging pulse basis functions in the MoM scheme, as opposed to the more realistic sinusoidal basis functions employed in SNEC™. It is seen that the error due to theoretical failure of pulse basis functions in satisfying the zero current tip condition reflects on the entire geometry through matrix inversion in the current calculation.

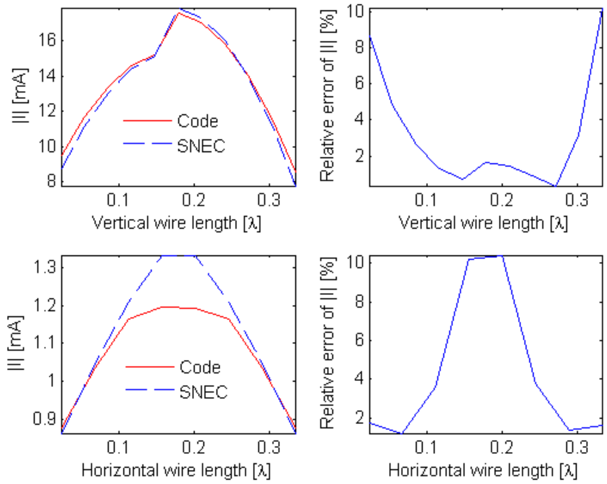

Fig. 7. The amplitude distributions of currents on vertical and horizontal arms and relative errors at $15\ [MHz]$.

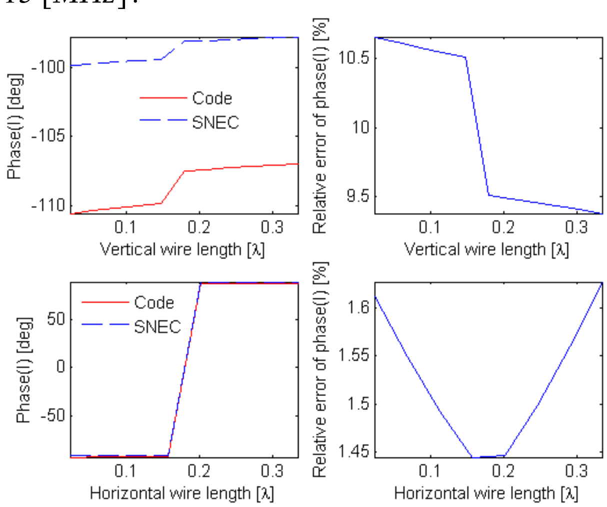

Fig. 8. The phase distributions of currents on vertical and horizontal arms and relative errors at $15\ [MHz]$.

As an application of the second scenario, a wire mesh plate with side length $7\ [m]$ and diagonal length $D \cong 10\ [m]$ is illuminated by a monopole with unit moment at a distance of $10\ [km]$ as depicted in Fig. 9.

In Figs. 10 and 11, we plot the elevation (Oxz) and azimuth (Oxy) patterns of the total (normalized) scattered field $10\log_{10}(4\pi r^2 |\vec{E}|^2)$ at $15, 30, 45\ [MHz]$ for which the operating wavelength corresponds to $2D, D, 2D/3$, respectively. The symmetries observed in the patterns are due to the symmetric structure of the plate as well as the thin wire approximation that the current flows only along longitudinal direction in every segment.

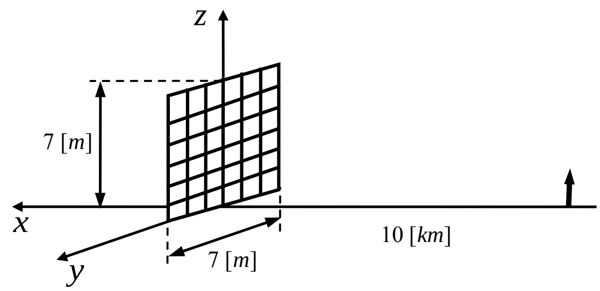

Fig. 9. A wire mesh plate illuminated by a monopole residing on planar sea surface.

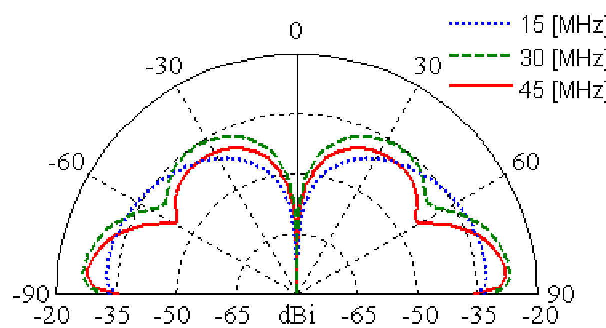

Fig. 10. Elevation patterns for the total scattered field at a) 15, b) 30, c) 45 $[MHz]$.

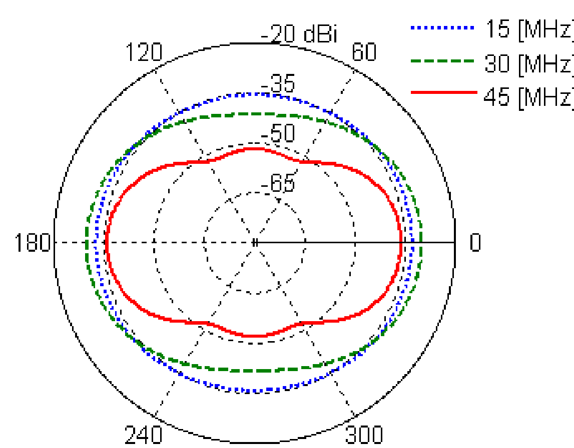

Fig. 11. Azimuth patterns for the total scattered field at a) 15, b) 30, c) 45 $[MHz]$.

In Fig. 12, we consider the same scatterer and source as in Fig. 9 on the spherical sea surface illuminated from a distance $10^3\,[km]$.

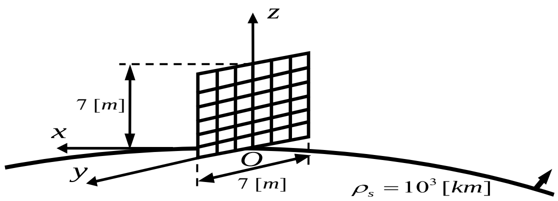

Fig. 12. A wire mesh plate illuminated by a monopole on spherical sea surface.

The total scattered field $20\log_{10}|\vec{E}|$ measured over the sea surface from the origin in the direction of the monopole is plotted in Fig. 13 at $15, 30, 45\,[MHz]$, for which the critical distances are calculated respectively as $77.216\,[km]$, $61.287\,[km]$, $53.539\,[km]$. As expected physically, there is an increased attentuation beyond the critical distances proportional with frequency.

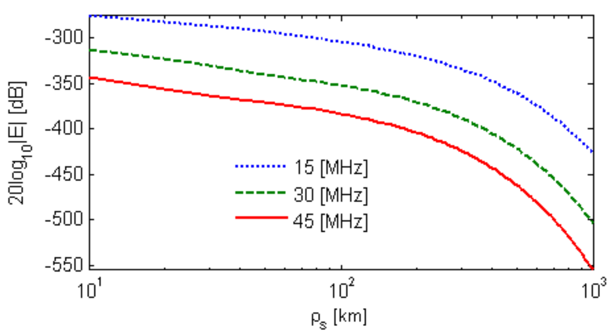

Fig. 13. The total scattered field by a wire mesh plate calculated over sea surface at $15, 30, 45\,[MHz]$.

VI. CONCLUDING REMARKS

In the present work, we provided a MoM formulation for thin wire structures located over a lossy dielectric ground under HCA employing King's range independent Green functions. Since we are focused on the analytical aspects of the formulation in the first place, our choice of pulse basis functions as the simplest option in a MoM scheme has resulted in a predictable and unavoidable relative error in current calculation as compared to the same results by the commercial software SNEC™, which employs (more realistic) sinusoidal pulse basis functions. Since such a deficiency is not associated with the success of the analytical calculations, the relative error can totally be removed by picking the same set of sinusoidal basis functions as in NEC softwares. While the current codes equally have the ability to read NEC-2 formatted input files, they are developed in the MATLAB™ environment with no commercial concern on total computational time at the time being. However, the numerical implementations put it very clearly that an electromagnetic simulation software that incorporates the Green functions of King may not only provide an alternative to the similar role of the extensive numerical/asymptotic libraries of NEC-2 whenever HCA applies (see also [57,58]), but also provides a capability to evolve by proper substitutions of Green functions to take into account various terrain features in any scenario. This is especially important since the physical (antenna) measurements around critical distances over earth have been reported to diverge seriously from those calculated by NEC-3 and NEC-4 while they follow the analytical results derived by King smoothly (see [59, Sec. 1] and the references cited therein). In light of the expertise gained the research is planned to pursue along the following areas of investigation:

i) Replacing the pulse basis functions in MoM scheme with sinusoidal basis functions following reference works as [60] to eliminate the current relative error with reference to NEC based softwares completely;
ii) Providing a time domain analysis ability to investigate the scattering of actual radar wave forms (as in [61-63]) from mesh structures above sea surface;
iii) Extending the impedance matrix for dielectric coated mesh structures for stealth applications. This is managed by reformulating the MoM matrix by describing a first order impedance boundary condition on each wire segment. For an analytical demonstration of the validity of the impedance boundary condition on arbitrarily shaped surfaces one may refer to [64];
iv) Incorporating Green functions of layered and complex media available in literature ([4-17]) for arbitrary range;
v) Investigation of most efficient NEC2 pre-processors (cf.[65]), modeling guidelines (cf.[66,67]), programming platforms and

algorithms to minimize the computational time for integration and linear algebraic operations at the stage of developing a commercial product.

ACKNOWLEDGMENT

This work is supported by Uludağ University Research Fund Project No. F-2007/37.

REFERENCES

[1] A. Sommerfeld, "Propagation of Waves in Wireless Telegraphy," *Ann. Phys.*, vol. 28, pp. 665-736, 1909.

[2] Y. R. Samii, R. Mittra and P. Parhami, "Evaluation of Sommerfeld Integrals for Lossy Half-Space Problems," *Electromagnetics*, vol. 1, no. 1, pp. 1-28, 1981.

[3] R. W. P. King, "New Formulas for the Electromagnetic Field of a Vertical Electric Dipole in a Dielectric or Conducting Half-Space Near its Horizontal Interface," *J. Appl. Phys.*, vol. 53, pp. 8476-8472, 1982 (Erratum: vol. 56, pp. 33-66, 1984).

[4] R. W. P. King, M. Owens, and T. T. Wu, *Lateral Electromagnetic Waves: Theory and Applications to Communications, Geophysical Exploration, and Remote Sensing*, Springer Verlag, New York, 1992.

[5] V. A. Houdzoumis, "Vertical Electric Dipole Radiation Over a Sphere: Character of the Waves that Propagate Through the Sphere," *J. Appl. Phys.*, vol. 86, pp. 3939-3942, 1999.

[6] V. A. Houdzoumis, "Two Modes of Wave Propagation Manifested in Vertical Electric Dipole Radiation Over a Sphere," *Radio Science*, vol. 35, no.1, pp. 19-29, 2000.

[7] D. Margetis and T. T. Wu, "Exactly Calculable Field Components of Electric Dipoles in Planar Boundary," *J. Math. Phys.*, vol. 42 (2), pp. 713-745, 2001.

[8] D. Margetis, "Radiation of Horizontal Electric Dipole on Large Dielectric Sphere," *J. Math. Phys.*, vol. 43, pp. 3162-3201, 2002.

[9] K. Li and S. O. Park, "Electromagnetic Field in the Air Generated by a Horizontal Electric Dipole Located in the Spherical Electrically Earth Coated with a Dielectric Layer," *J. Electromagn. Waves Applicat.*, vol. 17, no. 10, pp. 1399-1417, 2003.

[10] W. Y. Pan and H. Q. Zhang, "Electromagnetic Field of a Vertical Electric Dipole on the Spherical Conductor Covered with a Dielectric Layer," *Radio Sci*., vol. 38, no. 3, p. 1061, 2003.

[11] K. Li, S. O. Park, and H. Q. Zhang, "Electromagnetic Field in the Presence of a Three-Layered Spherical Region," *Progress in Electromagnetics Research*, vol. 45, pp. 103–121, 2004.

[12] K. Li, S. O. Park, and H. Q. Zhang, "Electromagnetic Field over the Spherical Earth Coated with n-Layered Dielectric," *Radio Science*, vol. 39, 2004.

[13] H. Q. Zhang, K. Li, and W. Y. Pan, "The Electromagnetic Field of a Vertical Dipole on the Dielectric-Coated Imperfect Conductor," *J. of Electromag. Waves and Appl.*, vol. 18, no. 10, pp. 1305-1320, 2004.

[14] K. Li and Y. L. Lu, "Electromagnetic Field from a Horizontal Electric Dipole in the Spherical Electrically Earth Covered with n-Layered Dielectrics," *Progress In Electromagnetics Research*, vol. 54, pp. 221-244, 2005.

[15] J. P. Mei and K. Li, "Electromagnetic Field from a Horizontal Electric Dipole on the Surface of a High Lossy Dielectric Coated with a Uniaxial Layer," *Progress in Electromagnetics Research*, vol. 73, pp. 71-91, 2007.

[16] T. Fei, L. W. Li, T. S. Yeo, H. L. Wang, and Q. Wu, "A Comparative Study of Radio Wave Propagation Over the Earth Due to a Vertical Electric Dipole," *IEEE Trans. Antennas Propagat.*, vol. 55, no. 10, pp. 2723-2732, 2007.

[17] L. Liang and K. Li, "Radiation from a Vertical Electric Dipole in the Presence of a Three-Layered Region," *IEEE Trans. Antennas Propagat.*, vol. 55, no. 12, pp. 3469-3475, 2007.

[18] J. H. Richmond, "A Wire-Grid Model for Scattering by Conducting Bodies," *IEEE Trans. Antennas Propagat.*, vol. AP-14, no. 6, pp. 782-786, 1966.

[19] J. L. Lin, W. L. Curtis, and M. C. Vincent, "On the Field Distribution of an Aperture," *IEEE Trans. Antennas Propagat.*, vol. AP-22, pp. 467-471, 1974.

[20] K. S. H. Lee, L. Martin, and J. P. Castillo, "Limitations of Wire-Grid Modeling of a Closed Surface," *IEEE Trans. Electromag. Compat.,* vol. 18, no. 3, pp. 123-129, 1976.

[21] A. C. Ludwig, "Wire Grid Modeling of Surface," *IEEE Trans. Antennas Propagat.,* vol. AP-14, no. 9, pp. 1045-1048, 1987.

[22] A. F. Peterson, "Difficulties Encountered when Attempting to Validate Thin Wire Formulations for Linear Dipole Antennas," *Applied Computational Electromagnetic Society (ACES) Journal*, vol. 4, no. 3, pp. 25-40, 1990.

[23] T. H. Hubing and J. F. Kauffman, "Modeling Electrically Small, Thin Surfaces with Wire Grids," *Applied Computational Electromagnetic Society (ACES) Journal*, vol. 5, no. 1, pp. 19-24, 1990.

[24] J. T. Mayhan, "Characteristic Modes and Wire Grid Modeling," *IEEE Trans. Antennas Propagat.*, vol. 38, no. 4, pp. 457-469, 1990.

[25] S. Kashyap, "Wire Grid and Surface Patch Modelling for EMP Interaction," *IEEE and Propagation Society International Symposium*, AP-S, 1990.

[26] R. Paknys, "The Near Field of a Wire Grid Model," *IEEE Trans. Antennas Propagat.,* vol. 39, no. 7, pp. 994-999, 1991.

[27] R. Paknys and L. R. Raschkowan, "Moment Method Surface Patch and Wire Grid Accuracy in the Computation of Near Fields," *Applied Computational Electromagnetic Society (ACES) Journal*, vol. 12, no. 3, pp. 16-25, 1997.

[28] R. F. Harrington, "Moment Methods for Field Problems," *Proc. of the IEEE*, vol. 55, no. 2, pp. 136-149, 1967.

[29] T. K. Sarkar and R. F. Harrington, "Radar Cross Sections of Conducting Bodies over a Lossy Half Space," *Radio Science*, vol. 15, no. 3, pp. 581-585, 1980.

[30] G. J. Burke and A. J. Poggio, "Numerical Electromagnetics Code (NEC)-Method of Moments," *Lawrence Livermore Laboratory*, Jan. 1981.

[31] SuperNec, Poynting Software (Pty) Ltd., South Africa. http://www.supernec.com/

[32] T. T. Crow and T. H. Shumpert, "Electromagnetic Scattering from Configurations of Thin Wire with Multiple Junctions," *Interaction Note 99*, 1972.

[33] R. W. P. King and T. T. Wu, "Analysis of Crossed Wires in a Plane-Wave Field," *Interaction Note 216*, 1975.

[34] A. R. Bretones, A. S. Extrema, R. M. Gómes, and J. F. Callejón, "About the Study in the Time Domain of Junctions Between Thin Wires," *Applied Computational Electromagnetic Society (ACES) Journal,* vol. 6, no. 2, pp. 2-20, 1991.

[35] K. A. Norton, "The Propagation of Radio Waves over the Surface of the Earth and in the Upper Atmosphere," *Proc. IRE*, vol. 25, pp. 1203-1236, 1937.

[36] T. S. M. Maclean and Z. Wu, *Radiowave Propagation over Ground*, Chapman & Hall, 1993.

[37] J. R. Wait, "Radiation from a Vertical Antenna over a Curved Stratified Ground," *J. Res. Natl. Bur. Stand.*, vol. 56D, no. 4, pp. 237-244, 1956.

[38] J. R. Wait, *Electromagnetic Surface Waves*, in Advances in Radio Research, ed. J.A. Saxton, vol. 1, Academic Press, New York, pp. 157-217, 1964.

[39] B. Van Der Pol, "Theory of Reflection of the Light from a Point Source by a Finite Conducting Flat Mirror, with an Application to Radiotelegraphy," *Physica*, vol. 2, pp. 843-853, 1935.

[40] H. Bremmer, T*errestrial Radio Waves*, New York, Elsevier, 1949.

[41] J. Galejs, *Terresterial Propagation of Long Electromagnetic Waves*, Pergamon Press, New York, 1972.

[42] V. A. Houdzoumis, "Scattering of Electromagnetic Missiles-Part I; Vertical Electric Dipole Radiation over Spherical Earth- Part II," Ph.D. Dissertation, Harvard Univ., 1994.

[43] K. Furutsu, "On the Theory of Radio Wave Propagation over Inhomogeneous Earth," *J. Res. Natl. Bur. Stand.,* vol. 67D, no. 1, pp. 39-62, 1963.

[44] K. Furutsu, "On the Statistical Theory of Electromagnetic Waves in a Fluctuating Medium (I)," *J. Res. Natl. Bur. Stand.*, vol. 67D, no. 3, pp. 303-323, 1963.

[45] K. Furutsu, R. E. Wilkerson, and R. F. Hartmann, "Some Numerical Results Based on the Theory of Radio Wave Propagation over Inhomogeneous Earth," *J. Res. Natl. Bur. Stand.*, vol. 68D, no. 7, pp. 827-846, 1964.

[46] K. Furutsu, "Calculated Curves for Groundwave Propagation over Inhomogeneous Earth with Pronounced Topographical Features," *J. Res. Natl. Bur. Stand.*, vol. 69D, no. 7, pp. 1011-1025, 1965.

[47] K. Furutsu and R. E. Wilkerson, "Optical Approximation for Residue Series of Terminal Gain in Radiowave Propagation over Inhomogeneous Earth," *Proc. IEE*, vol. 118, pp. 1197-1202, 1971.

[48] K. Furutsu, "A Systematic Theory of Wave Propagation over Irregular Terrain," *Radio Science*, vol. 17, no. 5, pp. 1037-1050, 1982.

[49] B. Polat, "Ground Wave Attenuation Curves in the Presence of Successive 2-D Islands," *Bulletin of the Technical University of Istanbul (ARI)*, vol. 54, no. 2, pp. 34-39, 2004.

[50] M. K. Ochi, *Ocean Waves – The Stochastic Approach*, Cambridge University Press, 1998.

[51] G. Kinsman, *Wind Waves: Their Generation and Propagation on the Ocean Surface*, Prentice Hall, Englewood Cliffs, New Jersey, 1965.

[52] O. M. Phillips, *Dynamics of the Upper Ocean*, Cambridge University Press, New York, 1966.

[53] W. J. Pierson and L. Moskowitz, "A Proposed Spectral Form for Fully Developed Wind Seas Based on the Similarity Theory of S. A. Kitaigorodski," *J. Geophys. Res.*, vol. 69, pp. 5181-5190, 1964.

[54] D. E. Hasselmann, M. Dunckel, and J. A. Ewing, "Directional Wave Spectra Observed during

JONSWAP 1973," *J. Phys. Oceanogr.*, vol. 10, pp. 1264-1280, 1980.
[55] F. Berizzi and E. Dalle Mese, "Sea-Wave Fractal Spectrum for SAR Remote Sensing," *IEE Proc.-Radar, Sonar Navig.*, vol. 148, no. 2, pp. 56-66, 2001.
[56] D. E. Barrick, "Theory of HF and VHF Propagation Across the Rough Sea: 1, The Effective Surface Impedance for a Slightly Rough Highly Conducting Medium at Grazing Impedance; 2, Application to HF and VHF Propagation Above the Sea," *Radio Science*, vol. 6, no. 5, pp. 517-533, 1971.
[57] M. M. Weiner, "Validation of the Numerical Electromagnetics Code (NEC) for Antenna Wire Elements in Pproximity to Earth," *Applied Computational Electromagnetic Society (ACES) Journal,* vol. 8, no. 2, pp. 44-71, 1993.
[58] D. B. Davidson and H. T. Mouton, "Validation of and Limitations on the Use of NEC-4 for Radiation from Antennas Buried within a Homogeneous Half-Space," *Applied Computational Electromagnetic Society (ACES) Journal,* vol. 13, no. 3, pp. 302–309, 1998.
[59] R. W. P. King, "Electromagnetic Ground Wave Field of Vertical Antennas for Communication at 1 to 30 MHz," *IEEE Trans. Electromag. Compatibility,* vol. 40, no. 4, pp. 337-342, 1998.
[60] E. H. Newman, "Simple Examples of the Method of Moments in Electromagnetics," *IEEE Trans. Education.,* vol. 31, no. 3, pp. 193-200, 1988.
[61] R. W. P. King and T. T. Wu, "The Propagation of a Radar Pulse in Sea Water," *J. Appl. Phys.*, vol. 73, no. 4, pp. 1581-1590, 1993 (Erratum: *J. Appl. Phys.*, vol. 77, no. 7, pp. 3586-3587, 1995.)
[62] R. W. P. King, "The Propagation of a Gaussian Pulse in Sea Water and its Application to Remote Sensing," *IEEE Trans. Geoscience and Remote Sensing*, vol. 31, no. 3, pp. 595-605, 1993.
[63] R. W. P. King, "Propagation of a Low Frequency Rectangular Pulse in Sea Water," *Radio Science*, vol. 28, no. 3, pp. 299-307, 1993.
[64] B. Polat, "Approximate Boundary Conditions on Anisotropic Sheets," *Progress in Electromagnetics Research-B,* vol. 29, pp. 355–392, 2011.
[65] C. F. du Toit and D. B. Davidson, "Wiregrid: a NEC2 Pre-Processor," *Applied Computational Electromagnetic Society (ACES) Journal,* vol. 10, no. 1, pp. 31–39, 1995.
[66] C. W. Trueman and S. J. Kubina, "Verifying Wire-Grid Model Integrity with Program CHECK," *Applied Computational Electromagnetic Society (ACES) Journal*, vol. 5, no. 2, pp. 17–42, 1990.
[67] L. A. Oyekanmi and J. Watkins, "Selecting Wire Radius for Grid/Mesh Models," *Applied Computational Electromagnetic Society (ACES) Journal*, vol. 5, no. 2, pp. 43–57, 1990.

Ömer Zor received B.S. and M.S. degrees in Electronics Engineering from Uludağ University in 2003 and 2006, respectively. Currently, he is a Ph.D. student and works as a research assistant at the same university. His research interests are on analytical and computational methods in electromagnetic theory.

Burak Polat received the B.S., M.S., and Ph.D. degrees in Electronics and Communications Engineering from Istanbul Technical University, Istanbul, Turkey in 1993, 1995, and 1997, respectively. In 1998, he was awarded the title of Associate Professor by the Council of Higher Education, Turkey. Between 1994-2000, he worked in Gebze Institute of Technology as a research assistant and Istanbul University as an associate professor. In 2000, he was on leave from Istanbul University to join Applied Electromagnetics Group at Electrical and Computer Engineering Department, Clemson University, SC, USA as a visiting researcher. Between 2000-2001, he worked as a postdoctoral research fellow at the Department of Electromagnetic Systems, Technical University of Denmark and between 2001-2003, he was a senior researcher at Marmara Research Center, Turkish Scientific and Technical Research Council, where he served in military electromagnetic simulation projects. Between May 2003 and October 2005, he worked as an Associate Professor at Department of Electronics and Communications Engineering, Istanbul Technical University (ITU) and Co-Director of ITU-Center for Satellite Communications and Remote Sensing. In 2004, he was at Electromagnetic Compatibility Lab., Electrical and Computer Engineering Department, Concordia University, Montreal, Canada on a 3 months sabbatical leave from ITU. Between 2005-2010, he worked as a full professor at Electronics Engineering and Mathematics Departments of Uludağ University, Turkey. Since September 2010, he serves as the Chair of Electrical and Electronics Department, Trakya University, Turkey. He is also an Associate Editor of Selçuk Journal of Applied Mathematics.

Dr. Polat's research interests include analytical, asymptotic and computational methods in electromagnetic theory.

Simulation and Design of a Tunable Patch Antenna

Benjamin D. Horwath and Talal Al-Attar

Department of Electrical Engineering, Center for Analog Design and Research
Santa Clara University, Santa Clara, CA 95053-0569, USA
bhorwath@scu.edu, talattar@scu.edu

Abstract **–** A method for designing a tunable microstrip patch antenna is presented, suggesting cooperation between a theoretical transmission line model and a professional electromagnetic simulation tool. Tunable impedance elements are used to perturb the microstrip patch to alter the tuning range of the antenna. Results show excellent correlation between theoretical calculations and simulation data from Sonnet. Finally, guidelines for designing an antenna to be excited by an IMPATT diode are discussed.

Index Terms **–** Tunable Antenna, IMPATT Diode, Sonnet, Microstrip, Patch Antenna

I. INTRODUCTION

Tunable antennas offer several intriguing properties for wireless communications [1-5], ranging from cost savings by combining several analog components into one to introducing new uses, such as an adaptive element for smart antenna systems. The ideal element would offer dynamic control of a significant tuning range of resonance frequencies and bandwidths on a single antenna. To date, attempts to design a truly tunable antenna have been rudimentary, attaining a piece of the goal, such as a shift in resonance frequency at the cost of bandwidth, or vice versa. Some focus is needed to determine the type of excitation that offers total control over the electrical properties of an antenna.

Previously, a theoretical method was explored for tuning microstrip patch antennas by way of a dynamic "black box" impedance element: an ideal component with an unlimited set of values for both resistance and reactance [6]. Such an idealistic approach helped find the bounds of tunability with respect to the antenna's field pattern and identify the most useful implementations of tunable antenna elements. Subsequently, the transmission line model previously used has been improved to include the impact of feedline width and mutual effects, which in turn allows for more accurate design simulations.

The transmission line model offers enough accuracy to quickly optimize not only the antenna dimensions, but also to search for tuning features such as complex impedance values and diode locations to meet design specifications. While more rigorous optimization techniques are available, (such as demonstrated for patch antenna sensitivity analysis with a method of moments [7]) these tools focus specifically on evaluating changes to the physical structure of the antenna only. Significant effort would be needed to modify this technique to include perturbations from an active tunable impedance device, as modeled in this presented research.

As a check against this work, a professional software tool, Sonnet, was used to evaluate the antenna baseline and tuning results derived from the theoretical model. Sonnet uses a method of moments [8] to analyze the electromagnetic properties from the physical dimensions of a circuit. By using Sonnet for this comparison, the previous work can be confirmed with a different computer-aided design methodology. It was found that the two design tools offered complementary benefits, so a natural conclusion was to create a cooperative procedure for designing tunable antennas. This new procedure takes advantage of the optimization flexibility of the theoretical model and the analytical rigor from the easy-to-use Sonnet package.

While the basis of the work was an ideal impedance "black box", the IMPact Avalanche

Submitted On: June 27, 2011
Accepted On: February 9, 2012

Transit Time (IMPATT) diode [9-11] has shown significant promise as a real-world means for achieving tunable antennas. Sonnet design and simulation considerations for integrating an IMPATT diode with a microstrip patch antenna are also discussed.

II. THEORY

The cornerstone of the tunable antenna model is the classic Pues and Van de Capelle [12-14] transmission line model for microstrip antennas. This method uses the dimensions as well as four imaginary radiating slots to represent the radiation properties of the antenna, and is well-known for being simple yet accurate. The model allows one to visualize the antenna as a network of elements as seen in Fig. 1.

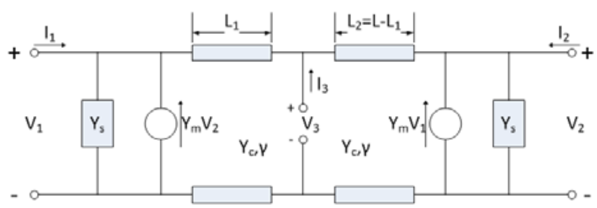

Fig. 1. Three-port network diagram for Pues transmission line model.

Procedurally, the Pues model computes effective parameters for line width W_e, length L_e, dielectric constant ε_{eff}, and loss tangent δ_e that have been adjusted to compensate for the total dimensions of the strip, the strip thickness, and dispersion at the operating frequency. These parameters are then used to find the appropriate characteristic admittance Y_c, propagation constant γ, self-admittance Y_s of the equivalent radiating slot, and mutual admittance effects Y_m. They combine via:

$$Y_{in} = \frac{Y_c^2 + Y_s^2 - Y_m^2 + 2Y_sY_c\coth(\gamma L) - 2Y_mY_c\,\mathrm{csch}(\gamma L)}{Y_s + Y_c\coth(\gamma L)}, \quad (1)$$

to yield an input admittance for the designed antenna at a microstrip feedline located at one edge of the patch.

The relationship in (1) leads directly to the input impedance of the patch antenna, but can be somewhat simplified by use of the transmission line admittance transfer function [5]:

$$Y_i = Y_c\frac{Y_c + Y_l\coth(\gamma L)}{Y_l + Y_c\coth(\gamma L)}, \quad (2)$$

where Y_c is still the characteristic admittance, Y_l is a load admittance at a distance L from an intermediate location, and Y_i is the transferred admittance at that intermediate point. If Y_l is set as the sum of Y_m and Y_s, (2) can be used to find a Y_i at the input edge that has been transferred from the slot and mutual effects of the far edge of the antenna. Then slot and mutual admittances from the input edge can be added to yield the expected input admittance.

In regards to tunability, the transfer function in (2) can be exploited to introduce a tunable element along the length of the patch, connecting the radiating slots of the antenna. For instance, consider some Y_d that represents the admittance of a tunable diode placed at distance L/2 from the patch input. This becomes a new intermediate point, and the transfer function needs to be used twice. First, the far edge admittance, $Y_{l,far}$, is "rolled" a distance L/2 with (2). This creates a $Y_{i,diode}$ that can be added with Y_d (a shunt device) to give a $Y_{l,diode}$. Then, (2) is used again to "roll" the remaining L/2 to the near edge, where it is added with the near edge admittance $Y_{l,input}$ to give a new Y_{in} for the tuned antenna.

This effort suggests another factor impacting antenna tunability: the location of the "black box" on the patch at design time. The addition of another parameter to the design considerations evolves the simple L and W search of the standard patch antenna design procedure to a new process requiring an optimization routine that takes into account not only the antenna dimensions, but Y_d and its location as well.

Generally speaking, the tunable impedance element (or admittance based on preference) provides a perturbation that, in turn, modifies the input impedance to the patch. With the relationship between input impedance and patch dimensions {in light of the documented Pues model and (2)}, this tuned antenna system behaves like a static antenna but with a new W and L at the operating frequency. It is as if the tunable "black box" impedance can electrically stretch or squeeze the patch antenna.

For the tunable microstrip patch antenna designer, the following process is recommended:

i. *Design a basic microstrip patch antenna to establish a baseline for the design using (1)*
ii. *Set design goal(s) for the complete tunable antenna system, such as frequency operating range or a desired Z_{in}*
iii. *Begin iterative loop to step through different locations and tuning values for the tunable impedance (admittance) element*

iv. *Use (2) to find the transferred shunt admittance of the radiating slot plus mutual effects at the location of the "black box"*
v. *Combine the tunable and transferred admittances; use (2) to transfer to the input*
vi. *Combine the new transferred admittance with the near radiating slot and mutual effects to get the new input admittance*
vii. *Repeat the design process in reverse if the 'tuned' width and length are desired*
viii. *Compare to design goal(s) and continue iterations until desired effects are achieved*

This procedure can be used to evaluate the impact of the tuned impedance values from the "black box" at several different locations on the baseline antenna. Checking this work against an accepted software tool is vital to ensuring its reliability. Comparison with results from Sonnet is presented below.

III. RESULTS

As a baseline, a microstrip patch antenna is designed with a resonance frequency at f_o = 2.4 GHz. The dimensions of the patch are W = 2.42259 cm and L = 4.15922 cm with strip thickness t = 35 μm on a substrate having ε_r = 2.2 and height h = 0.15875 cm. These substrate parameters mimic Rogers RT/duroid 5880, a well-known, commercially available copper substrate. The feedline is matched to 50 Ω at 2.4 GHz with a width of 0.484517 cm. Fig. 2 illustrates the antenna layout with a "black box" at the input.

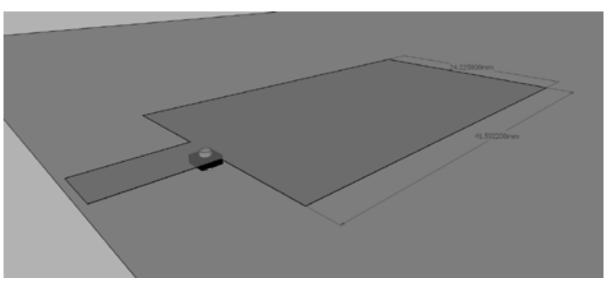

Fig. 2. Physical layout of microstrip patch antenna with black box element at the input.

Using the implemented model based on Pues [12-14], the baseline antenna is calculated to have Z_{in} = 979.58 Ω, Z_c = 14.3269 Ω, Z_s = 15.432 - j185.92 Ω, Z_m = 1150.1 + j4130.6 Ω, and γ = 0.0326 + j72.3651. Sonnet simulated this antenna to resonate slightly higher at 2.404 GHz with Z_{in} = 979.9 Ω. The nearly identical Z_{in} responses for the theoretical model and Sonnet are plotted in Fig. 3.

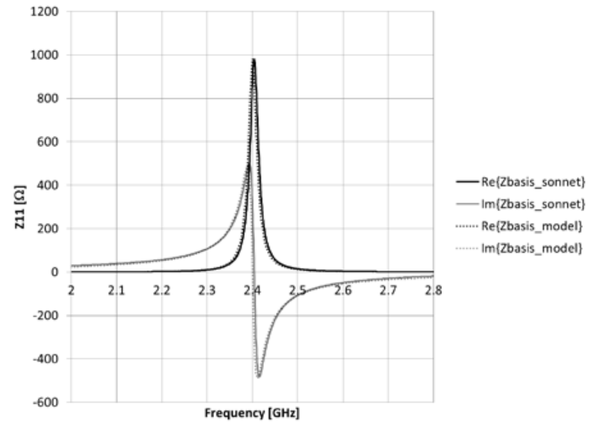

Fig. 3. Comparison of input impedance vs. frequency for designed patch antenna from the theoretical model and equivalent in Sonnet.

To evaluate the impact of placing the tuning element at various locations along the midline of the patch antenna, the Sonnet geometry for the patch was modified to include a via port at the desired locations. It is at this port the "black box" will be added in shunt to perturb the antenna. The first step was to choose a cell size for Sonnet since it is desirable to make the via as small as possible to reduce parasitic capacitance, yet shrinking the cell multiplies the memory requirement for Sonnet's calculations. For a single cell implementation, the final dimensions of the via were 202.889 μm long by 230.723 μm wide by 158.75 μm deep (10% of the dielectric height).

A new geometry was created to include the via port along the midline at one-tenth increments of the patch length from the feedline input to the far edge of the antenna. The net parasitic capacitance is seemingly significant, shifting the resonance frequency of the new geometries lower by about 10-15 MHz, yet the field patterns are comparable at 2.4 GHz, as shown in Figs. 4a and b. By comparing the Z_{in} responses for the basis and via-port geometries, it was determined the shunt capacitance introduced averages about 64 fF around the 2.4 GHz operating range.

Analyzing the impact of the tuning elements was carried out by stepping through values within a desired impedance range for the "black box" and one-tenth increments of the antenna length. It is assumed that the tunable "black box" has two extremes: 1) positive resistance with inductance (extreme value of 30 + j190 Ω), 2) negative resistance with capacitance (extreme value of -5 - j100 Ω). The tuning range bounds were chosen to provide a bit of reality to this theoretical search, as it is hoped to replicate these results in the lab. Thus, the values were picked to emulate measurement results from previous IMPATT diode work [9-11], and also result in a good degree of tunability for the proposed antenna system.

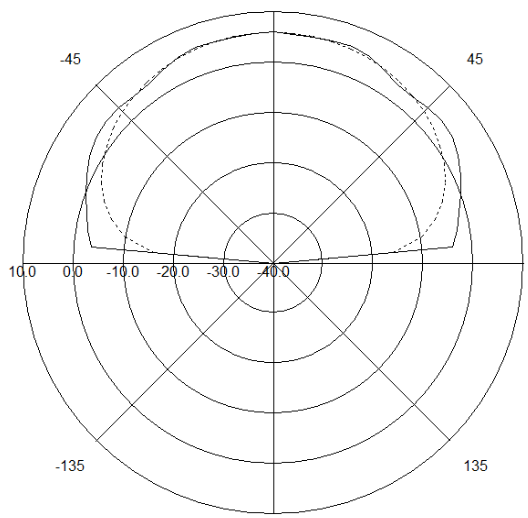

Fig. 4a. Field pattern for basis antenna. Solid line: E-plane, Dashed line: H-plane.

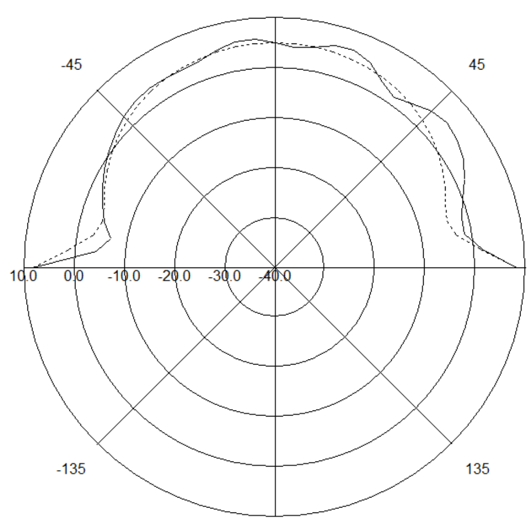

Fig. 4b. Field pattern for antenna with via @ 0.2L. Solid line: E-plane, Dashed line: H-plane.

Using the procedure given in Section II for an element tuned to -5 - j100 Ω and placed at the input to the patch, the resultant Z_{in} is calculated and plotted in Fig. 5, highlighting a downward resonance frequency shift of 107 MHz to 2.293 GHz. Correspondingly, the Sonnet Netlist function is used to combine the antenna with a .z1p data file and plot the results in Figs. 6 and 7.

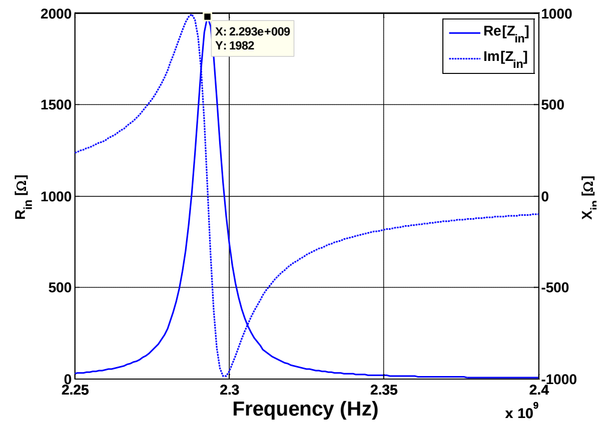

Fig. 5. Input impedance versus frequency for patch antenna tuned with Z_d = -5-j100Ω from theoretical model with resonance frequency at 2.293 GHz.

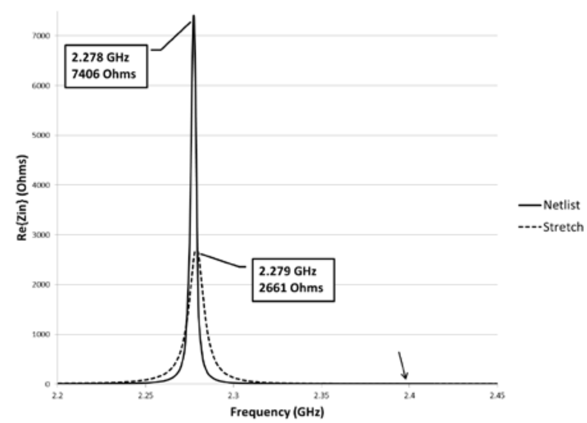

Fig. 6. Input resistance vs. frequency for tuned antenna (Z_d=-5-j100Ω) in Sonnet: networked components vs. stretched dimensions. Arrow indicates match at frequency of 2.4 GHz.

Additionally, Figs. 6 and 7 display a "stretched" antenna based on the tuned input impedance at 2.4 GHz (labeled 'stretch'). For this scenario, the equivalent patch dimensions are a 7.4% longer length of 4.46902 cm and a 28.2% shorter width of 1.74059 cm, demonstrating the ability to tune beyond the physical area of the antenna. The Netlist and "stretched" curves differ, with comparable resonance frequencies at 2.278 and 2.279 GHz, respectively, but have a significant discrepancy in input impedance. It should also be noted that the Netlist curve included the additional capacitance from the via port, while the 'stretched' analysis does not.

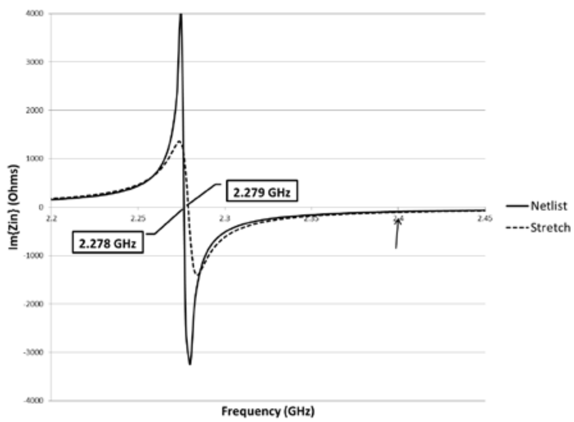

Fig. 7. Input reactance vs. frequency for tuned antenna (Z_d=-5-j100Ω) in Sonnet: networked components vs. stretched dimensions. Arrow indicates match at frequency of 2.4 GHz.

The difference between the Netlist and "stretched" input impedance results highlights an initial flaw in the proposed analysis procedure: there is an important distinction between the operating range and the designed resonance frequency. Subsequent research will focus on the equivalent "tuned" dimensions over an entire desired operating range, and reporting how well that range is met for the "new" length and width.

To summarize the comparison, results from the two extreme tuning scenarios, -5-j100Ω and 30+j190Ω, at each of the predetermined locations are captured in Table 1 to assess the impact to moving the tuning element along the midline of the patch antenna. The first observation to be made is to note that adding -5-j100Ω anywhere causes the resonance frequency to shift towards DC, while 30+j190Ω moves f_{res} higher. Next, the shift seen due to the inclusion of the via port in the Sonnet geometries was consistent through all results: not only in the difference of the 2 tuning scenarios, but also as the delta between the model and Sonnet. There is an excellent correlation between the results of the model and those of Sonnet, validating the use of the model as a design guide for placing tunable elements.

Table 1: Impact of tuning at several locations – no load (nl), -5-j100Ω (nrc), and 30+j190Ω (prl)

	Model/Sonnet	
Case	**f_{res} (GHz)**	**Z11 (Ω)**
Basis	2.4/2.404	979.6/979.9
0.0L, nl	2.4/2.394	979.6/1102
0.0L, nrc	2.293/2.278	1982/7406
0.0L, prl	2.456/2.445	541/505
0.4L, nl	2.4/2.392	979.6/969.8
0.4L, nrc	2.39/2.381	982.4/958.6
0.4L, prl	2.405/2.397	932/933.2
0.6L, nl	2.4/2.391	979.6/1023
0.6L, nrc	2.391/2.381	1068/1148
0.6L, prl	2.405/2.395	896.2/935.1
1.0L, nl	2.4/2.394	979.6/971.5
1.0L, nrc	2.294/2.273	2046/2843
1.0L, prl	2.456/2.448	538.8/553.0

A third observation can be seen from Table 1 that the closer the location is to 0.5L, the lesser the impact to the f_{res} shift. There may be other benefits to placing the tuning element at these inner locations such as dynamic input impedance tuning, but this was not evaluated during the analysis. For this work, the input feedline meets the patch at the very edge (as seen in Fig. 2 and not indented), creating an impedance mismatch. The input may be notched further inside to provide a better Z match in subsequent work.

The final observation is that there is symmetry about the 0.5L point, as can be seen by comparing the results between 0.0L and 1.0L as well as 0.4L and 0.6L in Table 1. Each case offers very similar results whether it is on the near or far side of the midpoint, and analysis of the impedance response in the surrounding spectrum confirms comparable results. In a way, this makes the choice of tuning location a bit easier, since the impact on one side mirrors the other side. In turn, this may offer more degrees of freedom to choose locations that bring other benefits such as system layout convenience.

The largest discrepancies in the results can be seen in the magnitude of Z_{in} at resonance. Of strongest note is the difference in Z_{in} at the 0.0L location for the -5-j100Ω scenario. Much of the disparity can be linked to the resolution of the calculations, as the input impedance behaves asymptotically near resonance.

As a final remark, the work presented intuitively leads to a design procedure that leverages the advantages of the two models. The designer can begin constructing the dimensions of the desired antenna and tuning characteristics with an optimization tool like the theoretical transmission line model presented. Once a framework is determined, Sonnet's advanced layout and simulation features can be used to verify performance and establish a design feedback loop with physical data such as area and boundaries. Such a complementary effort between the two tools could be integrated via SonnetLab, which offers a link between MATLAB and Sonnet for automating their interaction.

IV. IMPATT DIODES

Several methods for tuning antenna elements have been proposed over the years, most notably the usage of varactors and/or specially-biased FETs [15]. These are often limited to just resistance or capacitance and tend to fall short for improving antenna robustness.

The tuning range chosen for this investigation is based on values that have been achieved with the IMPATT diode [9-11], a promising method for achieving a range of impedance values through a single device. A DC bias, which should be well isolated from the RF signal, controls the avalanche frequency, and, hence, the diode impedance. Fig. 8 shows the model for the IMPATT diode before and after the avalanche frequency.

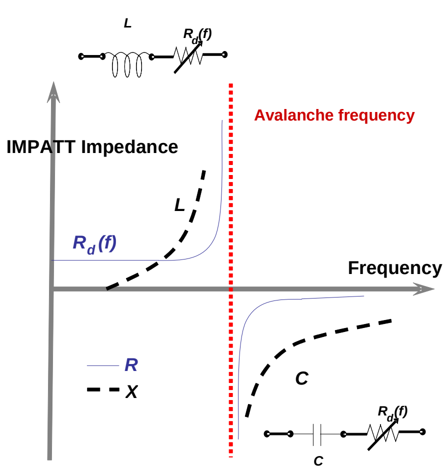

Fig. 8. Model for IMPATT impedance vs. frequency, for both sides of avalanche frequency.

The impedance capabilities of the IMPATT diode range from R + jωL to –R + 1/jωC, as modeled with the "black box". The necessary tuning range can be achieved by careful design of the diode dimensions. This means that when combined with a patch antenna, the properties can be tuned solely by the biasing of the IMPATT diode. Using the model to find ideal locations for IMPATT diodes along the patch, designers could quickly layout and analyze a tunable antenna with co-located IMPATT diodes in Sonnet.

V. CONCLUSIONS AND REMARKS

In summary, the work presented demonstrates a good marriage between results from the transmission line model and Sonnet. This relationship naturally leads to a collaborative design procedure for tunable patch antennas. To further advance the study of exciting a microstrip patch with impedance elements, Sonnet could improve the means of locating shunt impedances inside a structure (not just at edges) for evaluation. Finally, it should be pointed out that the final step of implementing the proposed tunable antenna with an IMPATT diode is made significantly simpler with the advanced layout and analysis features of the Sonnet tool.

REFERENCES

[1] J. C. Liberti and T.S. Rappaport, *Smart Antennas for Wireless Communications: IS-95 and Third Generation CDMA Applications,* Upper Saddle River, NJ: Prentice Hall PTR, pp. 81-116, 1999.

[2] W. L. Stutzman and G. A. Thiele, *Antenna Theory and Design*, New York, NY: John Wiley & Sons, 1981.

[3] S. J. Orfanidis, *Electromagnetic Waves and Antennas*, Piscataway, NJ: Electrical and Computer Engineering Department, Rutgers University, 2008. http://www.ece.rutgers.edu/~orfanidi/ewa/

[4] C. A. Balanis, *Antenna Theory*, Hoboken, NJ: John Wiley & Sons, pp. 811-843, 2005.

[5] D. K. Cheng, *Field and Wave Electromagnetics*, Reading, MA: Addison-Wesley Publishing Company, 1989.

[6] B. D. Horwath and T. Al-Attar, "Evaluating the Robustness of Tunable Adaptive Antenna Arrays," *IEEE 11th Annual Wireless and Microwave Technology Conference (WAMICON),* pp.1-5, 12-13 April 2010.

[7] Y. Zhang, N. K. Nikolova, and M. H. Bakr, "Input Impedance Sensitivity Analysis of Patch

Antenna with Discrete Perturbations on Method-of-Moment Grids," *Applied Computational Electromagnetics Society (ACES) Journal*, vol. 25, no. 10, pp. 867 – 876, October 2010.

[8] J. C. Rautio and R. F. Harrington, "An Electromagnetic Time-Harmonic Analysis of Shielded Microstrip Circuits," *IEEE Trans. Microwave Theory Tech.*, vol. MTT-35, pp. 726-730, Aug. 1987.

[9] T. Al-Attar and T. H. Lee, "Monolithic Integrated Millimeter-Wave IMPATT Transmitter in Standard CMOS Technology," *IEEE Transactions on Microwave Theory and Techniques*, vol. 53, issue 11, pp. 3557-3561, November 2005.

[10] T. Al-Attar, M.D. Mulligan, and T.H. Lee, "Lateral IMPATT Diodes in Standard CMOS Technology," *IEEE International Electron Devices Meeting*, pp. 459-462, December 13-15, 2004.

[11] T. Al-Attar, "Simulation and Layout of On-Chip Microstrip Patch Antenna in Standard CMOS Technology," *Applied Computational Electromagnetics Society (ACES), 26th Annual Review of Progress in*, pp. 866-871, April 26-29, 2010.

[12] H. Pues and A. van de Capelle, "Accurate transmission-line model for the rectangular microstrip antenna," *Microwaves, Optics and Antennas, IEE Proceedings H*, vol. 131, no. 6, pp. 334-340, December 1984.

[13] E. Hammerstad and O. Jensen, "Accurate Models for Microstrip Computer-Aided Design," *Microwave symposium Digest, 1980 IEEE MTT-S International*, pp. 407-409, 28-30 May 1980.

[14] M. Kirschning, R. H. Jansen, and N.H.L. Koster, "Accurate Model for Open End Effect of Microstrip Lines," *Electronics Letters*, vol. 17, no. 3, pp. 123-125, February 5, 1981.

[15] Libo Huang and P. Russer, "Electrically Tunable Antenna Design Procedure for Mobile Applications," *IEEE Transactions on Microwave Theory and Techniques,* vol. 56, no. 12, pp. 2789-2797, Dec. 2008.

Benjamin D. Horwath is a 2nd year Ph.D. student in the Department of Electrical Engineering at Santa Clara University. Ben has held engineering, marketing, and business development positions with Corning Incorporated, Phaethon Communications, and his own start-up, AirRay Systems. Prior to his doctorate education, Ben obtained his B.Sc. in Chemical Engineering at Penn State University and M.Sc. in Electrical Engineering at Santa Clara University. His primary research is currently focused on smart antenna systems for mobile devices.

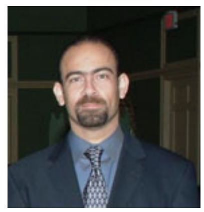

Dr. Talal Al-Attar has over 10 years in teaching experience in Electrical Engineering between Kuwait University, Stanford University and Santa Clara University. He received the B.S., M.S. from Kuwait University and his Ph.D degree from Stanford University. His doctoral work focused on IMPATT modeling at millimeter-wave range, on-chip integration of microstrip patch antennas and transmission lines in standard CMOS Technology.

He worked as a senior design and device engineer at Volterra Semiconductor [2004 - 2007], and a senior member of consulting staff at Sabio Labs [2007]. Dr. Al-Attar joined Magma Design Automation in 2008 when it acquired Sabio Labs. He joined SCU in 2006 as an adjunct professor, then lecturer, and finally as a full-time assistant professor.

His primary research interests includes IMPATT Modeling and scaling in Standard CMOS Technology, Analog design optimization, Microstrip Patch Antenna on-chip for 60GHz and 77GHz applications, Data Converters, LDMOS modeling for RF applications, and UWB measurements.

Dr. Al-Attar contributed to two books in CMOS RFIC and Planar Microwave Engineering. He currently serves on the committees of Radio and Wireless Symposium (RWS) as a student paper competition chair, and he is a member of the IEEE and the ASEE.

2011 INSTITUTIONAL MEMBERS

DTIC-OCP LIBRARY
8725 John J. Kingman Rd, Ste 0944
Fort Belvoir, VA 22060-6218

AUSTRALIAN DEFENCE LIBRARY
Northcott Drive
Canberra, A.C.T. 2600 Australia

BEIJING BOOK CO, INC
701 E Linden Avenue
Linden, NJ 07036-2495

DARTMOUTH COLLEGE
6025 Baker/Berry Library
Hanover, NH 03755-3560

DSTO EDINBURGH
AU/33851-AP, PO Box 830470
Birmingham, AL 35283

SIMEON J. EARL – BAE SYSTEMS
W432A, Warton Aerodome
Preston, Lancs., UK PR4 1AX

ENGINEERING INFORMATION, INC
PO Box 543
Amsterdam, Netherlands 1000 Am

ETSE TELECOMUNICACION
Biblioteca, Campus Lagoas
Vigo, 36200 Spain

GA INSTITUTE OF TECHNOLOGY
EBS-Lib Mail code 0900
74 Cherry Street
Atlanta, GA 30332

TIMOTHY HOLZHEIMER
Raytheon
PO Box 1044
Rockwall, TX 75087

HRL LABS, RESEARCH LIBRARY
3011 Malibu Canyon
Malibu, CA 90265

IEE INSPEC
Michael Faraday House
6 Hills Way
Stevenage, Herts UK SG1 2AY

INSTITUTE FOR SCIENTIFIC INFO.
Publication Processing Dept.
3501 Market St.
Philadelphia, PA 19104-3302

LIBRARY – DRDC OTTAWA
3701 Carling Avenue
Ottawa, Ontario, Canada K1A OZ4

LIBRARY of CONGRESS
Reg. Of Copyrights
Attn: 407 Deposits
Washington DC, 20559

LINDA HALL LIBRARY
5109 Cherry Street
Kansas City, MO 64110-2498

MISSOURI S&T
400 W 14th Street
Rolla, MO 56409

MIT LINCOLN LABORATORY
Periodicals Library
244 Wood Street
Lexington, MA 02420

NATIONAL CHI NAN UNIVERSITY
Lily Journal & Book Co, Ltd
20920 Glenbrook Drive
Walnut, CA 91789-3809

JOHN NORGARD
UCCS
20340 Pine Shadow Drive
Colorado Springs, CO 80908

OSAMA MOHAMMED
Florida International University
10555 W Flagler Street
Miami, FL 33174

NAVAL POSTGRADUATE SCHOOL
Attn:J. Rozdal/411 Dyer Rd./ Rm 111
Monterey, CA 93943-5101

NDL KAGAKU
C/0 KWE-ACCESS
PO Box 300613 (JFK A/P)
Jamaica, NY 11430-0613

OVIEDO LIBRARY
PO BOX 830679
Birmingham, AL 35283

DAVID PAULSEN
E3Compliance
1523 North Joe Wilson Road
Cedr Hill, TX 75104-1437

PENN STATE UNIVERSITY
126 Paterno Library
University Park, PA 16802-1808

DAVID J. PINION
1122 E Pike Street #1217
SEATTLE, WA 98122

KATHERINE SIAKAVARA
Gymnasiou 8
Thessaloniki, Greece 55236

SWETS INFORMATION SERVICES
160 Ninth Avenue, Suite A
Runnemede, NJ 08078

YUTAKA TANGE
Maizuru Natl College of Technology
234 Shiroya
Maizuru, Kyoto, Japan 625-8511

TIB & UNIV. BIB. HANNOVER
DE/5100/G1/0001
Welfengarten 1B
Hannover, Germany 30167

UEKAE
PO Box 830470
Birmingham, AL 35283

UNIV OF CENTRAL FLORIDA
4000 Central Florida Boulevard
Orlando, FL 32816-8005

UNIVERSITY OF COLORADO
1720 Pleasant Street, 184 UCB
Boulder, CO 80309-0184

UNIVERSITY OF KANSAS – WATSON
1425 Jayhawk Blvd 210S
Lawrence, KS 66045-7594

UNIVERSITY OF MISSISSIPPI
JD Williams Library
University, MS 38677-1848

UNIVERSITY LIBRARY/HKUST
Clear Water Bay Road
Kowloon, Honk Kong

CHUAN CHENG WANG
8F, No. 31, Lane 546
MingCheng 2nd Road, Zuoying Dist
Kaoshiung City, Taiwan 813

THOMAS WEILAND
TU Darmstadt
Schlossgartenstrasse 8
Darmstadt, Hessen, Germany 64289

STEVEN WEISS
US Army Research Lab
2800 Powder Mill Road
Adelphi, MD 20783

YOSHIHIDE YAMADA
NATIONAL DEFENSE ACADEMY
1-10-20 Hashirimizu
Yokosuka, Kanagawa,
Japan 239-8686

APPLIED COMPUTATIONAL ELECTROMAGNETICS SOCIETY JOURNAL
http://aces.ee.olemiss.edu

INFORMATION FOR AUTHORS

PUBLICATION CRITERIA

Each paper is required to manifest some relation to applied computational electromagnetics. **Papers may address general issues in applied computational electromagnetics, or they may focus on specific applications, techniques, codes, or computational issues.** While the following list is not exhaustive, each paper will generally relate to at least one of these areas:

1. **Code validation.** This is done using internal checks or experimental, analytical or other computational data. Measured data of potential utility to code validation efforts will also be considered for publication.

2. **Code performance analysis.** This usually involves identification of numerical accuracy or other limitations, solution convergence, numerical and physical modeling error, and parameter tradeoffs. However, it is also permissible to address issues such as ease-of-use, set-up time, run time, special outputs, or other special features.

3. **Computational studies of basic physics.** This involves using a code, algorithm, or computational technique to simulate reality in such a way that better, or new physical insight or understanding, is achieved.

4. **New computational techniques** or new applications for existing computational techniques or codes.

5. **"Tricks of the trade"** in selecting and applying codes and techniques.

6. **New codes, algorithms, code enhancement, and code fixes.** This category is self-explanatory, but includes significant changes to existing codes, such as applicability extensions, algorithm optimization, problem correction, limitation removal, or other performance improvement. **Note: Code (or algorithm) capability descriptions are not acceptable, unless they contain sufficient technical material to justify consideration.**

7. **Code input/output issues.** This normally involves innovations in input (such as input geometry standardization, automatic mesh generation, or computer-aided design) or in output (whether it be tabular, graphical, statistical, Fourier-transformed, or otherwise signal-processed). Material dealing with input/output database management, output interpretation, or other input/output issues will also be considered for publication.

8. **Computer hardware issues.** This is the category for analysis of hardware capabilities and limitations of various types of electromagnetics computational requirements. Vector and parallel computational techniques and implementation are of particular interest.

Applications of interest include, but are not limited to, antennas (and their electromagnetic environments), networks, static fields, radar cross section, inverse scattering, shielding, radiation hazards, biological effects, biomedical applications, electromagnetic pulse (EMP), electromagnetic interference (EMI), electromagnetic compatibility (EMC), power transmission, charge transport, dielectric, magnetic and nonlinear materials, microwave components, MEMS, RFID, and MMIC technologies, remote sensing and geometrical and physical optics, radar and communications systems, sensors, fiber optics, plasmas, particle accelerators, generators and motors, electromagnetic wave propagation, non-destructive evaluation, eddy currents, and inverse scattering.

Techniques of interest include but not limited to frequency-domain and time-domain techniques, integral equation and differential equation techniques, diffraction theories, physical and geometrical optics, method of moments, finite differences and finite element techniques, transmission line method, modal expansions, perturbation methods, and hybrid methods.

Where possible and appropriate, authors are required to provide statements of quantitative accuracy for measured and/or computed data. This issue is discussed in "Accuracy & Publication: Requiring, quantitative accuracy statements to accompany data," by E. K. Miller, *ACES Newsletter,* Vol. 9, No. 3, pp. 23-29, 1994, ISBN 1056-9170.

SUBMITTAL PROCEDURE

All submissions should be uploaded to ACES server through ACES web site (http://aces.ee.olemiss.edu) by using the upload button, journal section. Only pdf files are accepted for submission. The file size should not be larger than 5MB, otherwise permission from the Editor-in-Chief should be obtained first. Automated acknowledgment of the electronic submission, after the upload process is successfully completed, will be sent to the corresponding author only. It is the responsibility of the corresponding author to keep the remaining authors, if applicable, informed. Email submission is not accepted and will not be processed.

EDITORIAL REVIEW

In order to ensure an appropriate level of quality control, papers are peer reviewed. They are reviewed both for technical correctness and for adherence to the listed guidelines regarding information content and format.

PAPER FORMAT

Only camera-ready electronic files are accepted for publication. The term **"camera-ready" means that the material is neat, legible, reproducible, and in accordance with the final version format listed below.**

The following requirements are in effect for the final version of an ACES Journal paper:

1. The paper title should not be placed on a separate page.

The title, author(s), abstract, and (space permitting) beginning of the paper itself should all be on the first page. The title, author(s), and author affiliations should be centered (center-justified) on the first page. The title should be of font size 16 and bolded, the author names should be of font size 12 and bolded, and the author affiliation should be of font size 12 (regular font, neither italic nor bolded).

2. An abstract is required. The abstract should be a brief summary of the work described in the paper. It should state the computer codes, computational techniques, and applications discussed in the paper (as applicable) and should otherwise be usable by technical abstracting and indexing services. The word "Abstract" has to be placed at the left margin of the paper, and should be bolded and italic. It also should be followed by a hyphen (—) with the main text of the abstract starting on the same line.

3. All section titles have to be centered and all the title letters should be written in caps. The section titles need to be numbered using roman numbering (I. II. ….)

4. Either British English or American English spellings may be used, provided that each word is spelled consistently throughout the paper.

5. Internal consistency of references format should be maintained. As a guideline for authors, we recommend that references be given using numerical numbering in the body of the paper (with numerical listing of all references at the end of the paper). The first letter of the authors' first name should be listed followed by a period, which in turn, followed by the authors' complete last name. Use a coma (,) to separate between the authors' names. Titles of papers or articles should be in quotation marks (" "), followed by the title of journal, which should be in italic font. The journal volume (vol.), issue number (no.), page numbering (pp.), month and year of publication should come after the journal title in the sequence listed here.

6. Internal consistency shall also be maintained for other elements of style, such as equation numbering. Equation numbers should be placed in parentheses at the right column margin. All symbols in any equation have to be defined before the equation appears or right immediately following the equation.

7. The use of SI units is strongly encouraged. English units may be used as secondary units (in parentheses).

8. Figures and tables should be formatted appropriately (centered within the column, side-by-side, etc.) on the page such that the presented data appears close to and after it is being referenced in the text. When including figures and tables, all care should be taken so that they will appear appropriately when printed in black and white. For better visibility of paper on computer screen, it is good to make color figures with different line styles for figures with multiple curves. Colors should also be tested to insure their ability to be distinguished after black and white printing. Avoid the use of large symbols with curves in a figure. It is always better to use different line styles such as solid, dotted, dashed, etc.

9. A figure caption should be located directly beneath the corresponding figure, and should be fully justified.

10. The intent and meaning of all text must be clear. For authors who are not masters of the English language, the ACES Editorial Staff will provide assistance with grammar (subject to clarity of intent and meaning). However, this may delay the scheduled publication date.

11. Unused space should be minimized. Sections and subsections should not normally begin on a new page.

ACES reserves the right to edit any uploaded material, however, this is not generally done. It is the author(s) responsibility to provide acceptable camera-ready files in pdf and MSWord formats. Incompatible or incomplete files will not be processed for publication, and authors will be requested to re-upload a revised acceptable version.

COPYRIGHTS AND RELEASES

Each primary author must execute the online copyright form and obtain a release from his/her organization vesting the copyright with ACES. Both the author(s) and affiliated organization(s) are allowed to use the copyrighted material freely for their own private purposes.

Permission is granted to quote short passages and reproduce figures and tables from and ACES Journal issue provided the source is cited. Copies of ACES Journal articles may be made in accordance with usage permitted by Sections 107 or 108 of the U.S. Copyright Law. This consent does not extend to other kinds of copying, such as for general distribution, for advertising or promotional purposes, for creating new collective works, or for resale. The reproduction of multiple copies and the use of articles or extracts for commercial purposes require the consent of the author and specific permission from ACES. Institutional members are allowed to copy any ACES Journal issue for their internal distribution only.

PUBLICATION CHARGES

All authors are allowed for 8 printed pages per paper without charge. Mandatory page charges of $75 a page apply to all pages in excess of 8 printed pages. Authors are entitled to one, free of charge, copy of the printed journal issue in which their paper was published. Additional reprints are available for $ 50. Requests for additional re-prints should be submitted to the managing editor or ACES Secretary.

Corresponding author is required to complete the online form for the over page charge payment right after the initial acceptance of the paper is conveyed to the corresponding author by email.

ACES Journal is abstracted in INSPEC, in Engineering Index, DTIC, Science Citation Index Expanded, the Research Alert, and to Current Contents/Engineering, Computing & Technology.